



Universität Hamburg  
DER FORSCHUNG | DER LEHRE | DER BILDUNG

# Energy Transfer Between Chromophores Bound to Layered Silicate Surfaces

Thesis Submitted for the Fulfilment of the Degree

Doctor rerum Naturalium  
(Dr. rer. nat.)

*By*

Hongxiao Xiang

*To*

Department of Chemistry  
Institute of Physical Chemistry  
University of Hamburg  
Hamburg

2024

Reviewers of Dissertations: Prof. Dr. Volker Abetz  
Dr. Eric H. Hill

Oral Defense Committee: Prof. Dr. Volker Abetz  
Prof. Dr. Chris Meier  
Prof. Dr. Alf Mews

Date of Disputation: 18.10.2024

This Dissertation was carried out in the period from January 2021 to August 2024 in  
Hamburg.

## I. List of Publications

### **First Author Publications:**

1: Xiang, H., Hill, E. H. (2024). Cascade Förster Resonance Energy Transfer Between Layered Silicate Edge-linked Chromophores. *Journal of Colloid and Interface Science*, 676, 543-550.

2: Xiang, H., Valandro, S. R., & Hill, E. H. (2023). 2D Nanomaterial-Directed Molecular Aggregation and Energy Transfer between Edge-Bound Donor–Acceptor Pairs. *The Journal of Physical Chemistry C*, 127(31), 15416-15422.

3: Xiang, H., Valandro, S. R., & Hill, E. H. (2023). Layered silicate edge-linked perylene diimides: Synthesis, self-assembly and energy transfer. *Journal of Colloid and Interface Science*, 629, 300-306.

### **Publications as Contributing Author:**

1: Valandro, S. R., Herber, M., Xiang, H., & Hill, E. H. (2024). The Role of Aggregation on Energy Transfer in Layered Rare-Earth Hydroxide/Naphthalene Diimide Hybrid Materials. *The Journal of Physical Chemistry C*, 128(6), 2529-2535.

2: Jatav, S., Xiang, H., Herber, M., Paineau, E., & Hill, E. H. (2023). In2S3 Growth Templated by Aluminogermanate Double-Walled Imogolite Nanotubes Toward Efficient Visible Light Photocatalysts. *Solar RRL*, 7(4), 2200947.

3: Jatav, S., Herber, M., Xiang, H., & Hill, E. H. (2022). Layered double hydroxide–bismuth molybdate hybrids toward water remediation via selective adsorption of anionic species. *ACS Applied Materials & Interfaces*, 14(46), 51921-51930.

4: Jatav, S., Herber, M., Xiang, H., & Hill, E. H. (2022). Surface-Encapsulated Bismuth Molybdate-Layered Silicate Hybrids as Sorbents for Photocatalytic Filtration Membranes. *ACS Applied Materials & Interfaces*, 14(20), 22790-22798.



## II. Table of Contents

I.	List of Publications .....	I
II.	Table of Contents .....	II
III.	List of Abbreviations .....	IV
	<b>ZUSAMMENFASSUNG</b> .....	V
	<b>ABSTRACT</b> .....	VI
<b>1.</b>	<b>Introduction</b> .....	1
<b>1.1.</b>	<b>Fluorescence</b> .....	1
<b>1.1.1.</b>	<b>History of Fluorescence</b> .....	1
<b>1.1.2.</b>	<b>The Perri-Jablonski Diagram</b> .....	2
<b>1.1.3.</b>	<b>The Stokes Shift</b> .....	4
<b>1.1.4.</b>	<b>Fluorescence Lifetime and Quantum Yield</b> .....	4
<b>1.2.</b>	<b>Organic Chromophores</b> .....	5
<b>1.2.1.</b>	<b>Molecular Orbital Transitions</b> .....	5
<b>1.2.2.</b>	<b>Rylene Diimides</b> .....	7
<b>1.2.2.1.</b>	<b>Naphthalene Diimides</b> .....	7
<b>1.2.2.2.</b>	<b>Perylene Diimides</b> .....	9
<b>1.2.2.3.</b>	<b>Molecular Self-Assembly</b> .....	12
<b>1.3.</b>	<b>Electronic Energy Transfer</b> .....	13
<b>1.2.1.</b>	<b>Förster Resonance Energy Transfer</b> .....	14
<b>1.2.2.</b>	<b>Förster Resonance Energy Transfer in Supramolecular Systems</b> .....	16
<b>1.2.3.</b>	<b>Förster Resonance Energy Transfer in Organic-Inorganic Hybrids</b> .....	17
<b>1.4.</b>	<b>Laponite</b> .....	18
<b>1.4.1.</b>	<b>Clay Minerals</b> .....	18
<b>1.4.2.</b>	<b>Smectites</b> .....	19
<b>1.4.3.</b>	<b>Physical Properties of Laponite</b> .....	20
<b>1.4.4.</b>	<b>Organic Modification of Laponite</b> .....	21
<b>1.5.</b>	<b>Motivation</b> .....	23
<b>2.</b>	<b>Layered silicate edge-linked perylene diimides: Synthesis, self-assembly and energy transfer</b> .....	24
<b>3.</b>	<b>2D Nanomaterial-Directed Molecular Aggregation and Energy Transfer between Edge-Bound Donor-Acceptor pairs</b> .....	32
<b>4.</b>	<b>Cascade Förster resonance energy transfer between layered silicate edge-linked chromophores</b> .....	40
<b>5.</b>	<b>Discussion and Outlook</b> .....	49

<b>5.1. Discussion</b> .....	49
<b>5.2. Outlook</b> .....	50
<b>5.2.1. Modifications on One-Dimensional Clay</b> .....	50
<b>5.2.2. Development of Chromophore-Modified Laponite Thin Films</b> .....	51
<b>Bibliography</b> .....	52
<b>Appendix I</b> .....	67
<b>Chemicals</b> .....	67
<b>Appendix II</b> .....	73
<b>Supplementary Information for Chapter 2</b> .....	73
<b>Appendix III</b> .....	89
<b>Supplementary Information for Chapter 3</b> .....	89
<b>Appendix IV</b> .....	104
<b>Supplementary Information for Chapter 4</b> .....	104
<b>ACKNOWLEDGEMENTS</b> .....	118
<b>DECLARATION</b> .....	119

### III. List of Abbreviations

Förster Resonance Energy Transfer	FRET
Laponite	Lap
Internal Conversion	IC
Intersystem Crossing	ISC
Lowest Unoccupied Molecular Orbital	LUMO
Highest Occupied Molecular Orbital	HOMO
Naphthalene Diimide	NDI
1,4,5,8-Naphthalene Tetracarboxylic Dianhydride	NTCDA
Dimethylformamide	DMF
Perylene Diimide	PDI
3,4,9,10-Perylene Tetracarboxylic Dianhydride	PTCDA
Perylene Monoimide	PMI
Aggregation-Caused Quenching	ACQ
Aggregation-Induced Emission	AIE
Metal-Organic Framework	MOF
Covalent Organic Framework	COF
Rhodamine 6G	R6G
Cation Exchange Capacity	CEC
Montmorillonite	MMT
Cetyltrimethylammonium Bromide	CTAB
Aminopropyldimethylethoxysilane	APES
3-Aminopropyltrimethoxy Silane	APTES
Poly(N-vinylpyrrolidone)	PVP
Doxorubicin	DOX
4',6-Diamidino-2-Phenylindole	DAPI

## ZUSAMMENFASSUNG

Der Förster-Resonanzenergietransfer (FRET) beschreibt den Prozess, bei dem die überschüssige Energie eines angeregten Donormoleküls durch nichtstrahlende Dipol-Dipol-Kopplung auf ein nahe gelegenes, ruhendes Akzeptormolekül übertragen wird. Da sich das Akzeptormolekül in unmittelbarer Nähe des Donormoleküls befinden muss, ist FRET empfindlich gegenüber dem Abstand und der Ausrichtung zwischen Donor- und Akzeptormolekülen, was die Bedeutung eines definierten Systems zur Optimierung der FRET-Effizienz unterstreicht. Die Einbindung von Nanopartikeln als Matrizie bietet einen strategischen Vorteil bei der Immobilisierung von Akzeptor- und Donormolekülen. In dieser Dissertation die Verknüpfung organischer Chromophore mit einem Schichtsilikat und die Entwicklung von drei verschiedenen FRET-Systemen auf der Grundlage der resultierenden organisch-anorganischen Hybride untersucht.

Im ersten System wurde ein Perylendiimid kovalent an die Randoberfläche von Laponit (Lap) als Akzeptor gebunden, gefolgt von der Assoziation eines Donor-Moleküls mit der basalen Oberfläche durch Ionenaustausch. Es wurde ein FRET von dem an der Basalfläche von Lap befindlichen Donor zu dem an die Lap-Kante gebundenen Akzeptor beobachtet. Im zweiten System wurden ein Naphthalindiimid-Donor und ein Perylendiimid-Akzeptor kovalent an die Randoberflächen von zwei separaten LAP-Teilchen gebunden. Beide Chromophore an den Randflächen von Lap bildeten in einem Lösungsmittelgemisch mit hohem Wassergehalt Aggregate, und es wurde FRET zwischen diesen randgebundenen Chromophoren beobachtet. Die Verwendung eines kationischen Tensids zur Bildung einer organisierten Stapelung von Lap-Teilchen führte zu einer günstigen Ausrichtung zwischen Donor- und Akzeptormolekülen für FRET, was zu einer erheblichen Steigerung der FRET-Effizienz führte. Das letzte System konzentrierte sich auf eine zweistufige FRET-Kaskade, bei der FRET von einem kantengebundenen Lap-Donor zum intermediären Donor/Akzeptor auf der basalen Oberfläche stattfindet, gefolgt von FRET vom intermediären Donor/Akzeptor auf der basalen Oberfläche zu einem anderen kovalent kantengebundenen Akzeptor. Zusätzlich zur Beobachtung von Kaskaden-FRET führten bestimmte Lösungsmittelzusammensetzungen zu einer erhöhten FRET-Effizienz.

In dieser Dissertation wird die Synthese von chromophor-modifiziertem Lap vorgestellt und es werden drei verschiedene FRET-Systeme untersucht, die auf nanoskopischen organisch-anorganischen Hybriden basieren. Die Verwendung eines Schichtsilikatons als Nanomaterialvorlage mit anisotroper Oberflächenchemie ermöglicht eine vielseitige Synthese, die zu einer präzisen Kontrolle über die Immobilisierung organischer Chromophore für den Energietransfer und zu einem verbesserten Energietransfer bei einer relativ niedrigen Chromophorkonzentration führt. Diese Studien stellen einen neuartigen Ansatz für die Synthese von organisch-anorganischen hybriden Nanomaterialien mit abstimmbaren physikalischen und photophysikalischen Eigenschaften dar und erweitern die potenziellen Anwendungen von FRET und Materialien auf Nanopartikelbasis, wie etwa Leuchtdioden, Energiespeicher, Photovoltaik und Biosensoren.

## ABSTRACT

Förster resonance energy transfer (FRET) describes the transfer of excess energy from an excited donor molecule to a nearby acceptor molecule through nonradiative dipole-dipole coupling. As the acceptor molecule must be in close proximity to the donor molecule, FRET is sensitive to distance and orientation between donor and acceptor molecules, indicating the importance of a well-defined system for optimizing FRET efficiency. The incorporation of nanoparticles as a template provides a strategic advantage in the immobilization of both acceptor and donor molecules. This dissertation explores the linkage of organic chromophores to a layered silicate clay and the development of three distinct FRET systems based on the resulting organic-inorganic hybrids.

In the first system, a perylene diimide derivative was covalently linked to the edge surface of Laponite (Lap) as an acceptor, followed by the association of a donor molecule to the basal surface via ion exchange. FRET was observed from the Lap basal surface located donor to the Lap edge-bound acceptor. In the second system, a naphthalene diimide donor and a perylene diimide acceptor were covalently linked to the edge surfaces of two separate Lap particles. Both chromophores at the edge surfaces of Lap formed aggregates in a solvent mixture with high water content, and FRET between these edge-bound chromophores, was observed. Employing a cationic surfactant to form organized stacking of Lap particles led to a favorable orientation between donor and acceptor molecules for FRET, resulting in significant enhancement of FRET efficiency. The final system focused on a two-step FRET cascade, which involved FRET from a Lap edge-bound donor to the intermediate donor/acceptor on the basal surface, followed by FRET from the intermediate donor/acceptor on the basal surface to another covalently edge-bound acceptor. In addition to the observation of cascade FRET, certain solvent compositions led to enhanced FRET efficiency.

This dissertation introduces the synthesis of chromophore-modified Lap and investigates three distinct FRET systems based on nanoscopic organic-inorganic hybrids. The employment of a layered silicate clay as a nanomaterial template with anisotropic surface chemistry enables versatile synthesis, leading to an advance in precise control over immobilizing organic chromophores for energy transfer, and enhanced energy transfer at a relatively low chromophore concentration. These studies represent a novel approach for synthesizing organic-inorganic hybrid nanomaterials with tunable physical and photophysical properties, extending potential applications of FRET and nanoparticle-based materials, such as light-emitting diodes, energy storage devices, photovoltaics, and biosensors.

# 1. Introduction

Organic-inorganic hybrid materials can combine the physicochemical properties of both organic molecules and inorganic materials, providing a strategic advantage for expanding the applications of both organic and inorganic materials. Förster resonance energy transfer (FRET) is a crucial distance-dependent photophysical phenomenon that has been widely applied to study macromolecular interactions in diverse fields such as biological sensors, photovoltaics, and dye-sensitized solar cells. Various supramolecular templates such as organic linkers, polymer networks, and metal-organic frameworks have been utilized to immobilize donor-acceptor pairs with optimal distances and orientations to achieve efficient FRET. However, inorganic layered clay as a template for FRET exhibits advantages in terms of versatile synthesis, low cost, and great physicochemical stability. This dissertation focuses on the attachment of organic chromophores to specific surfaces of a layered silicate clay and investigations of FRET building on chromophores-modified layered silicate clay.

This chapter provides the essential theoretical background in fluorescence, organic chromophores, FRET, and layered silicate clays. It also introduces FRET in supramolecular systems and organic-inorganic systems and concludes with the motivation behind this dissertation.

## 1.1. Fluorescence

### 1.1.1. History of Fluorescence

In 1565, the Spanish physician Nicolas Monnardes made a groundbreaking discovery when he observed blue light emission from an infusion of *Lignum nephriticum* (see Figure 1.1). This optical phenomenon was first introduced as luminescence in 1888 by the physicist and science historian Eilhardt Wiedemann. Luminescence describes the spontaneous emission of radiation from an electronically excited species or a vibrationally excited species not in thermal equilibrium with its environment, distinct from incandescence.<sup>1</sup> Luminescence has various classifications based on the excitation mechanism, including electric field-induced electroluminescence, chemical reaction-induced chemiluminescence, ultrasound-induced sonoluminescence, etc.<sup>2,3</sup> Light absorption-induced luminescence falls under the classification of photoluminescence, involving fluorescence, phosphorescence, and delayed fluorescence.<sup>3</sup>

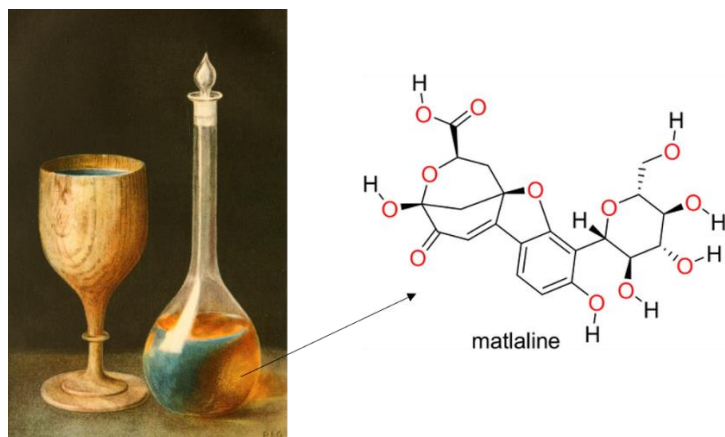


Figure 1.1: The first reported observation of fluorescence: absorption (brown) and fluorescence (blue) of infusion of *Lignum nephriticum* due to the matlaline composition.<sup>4-6</sup>

The physicist Sir George Gabriel Stokes introduced the term “Fluorescence” in 1853 at Cambridge. Fluorescence consists of “fluor-”, representing minerals containing calcium fluorite, and “-rescence” linked to the term opalescence.<sup>7,8</sup> While pure calcium fluorite was found to be colorless and non-fluorescent, the observed fluorescence in Fluorspar was attributed to impurities of the rare-earth family.<sup>9</sup> Stokes observed blue light emission from quinine sulfate solution upon the ultraviolet irradiation, apart from observed transparent solution in the visible light. Based on this observation, Stokes stated that the emission wavelength is consistently longer than the exciting wavelength, and this statement was known as Stokes' law.<sup>3,7,8</sup>

Fluorescence is categorized under photoluminescence alongside phosphorescence and delayed fluorescence. What distinguishes between fluorescence and phosphorescence? Becquerel proposed that fluorescence and phosphorescence are the same emission phenomenon differing primarily in the emission duration, which is short in fluorescence and long in phosphorescence.<sup>10</sup> However, long-lived fluorescence with comparable decay times to those of short-lived phosphorescence (around 0.1 to 1 $\mu$ s) had been detected. Jean Perrin and Francis Perrin first studied and provided the theoretical distinction between fluorescence and phosphorescence. In essence, fluorescence emission arises from electronic transitions with retention of spin multiplicity, and phosphorescence emission results from electronic transitions involving a different spin multiplicity.<sup>11</sup>

### 1.1.2. The Perri-Jablonski Diagram

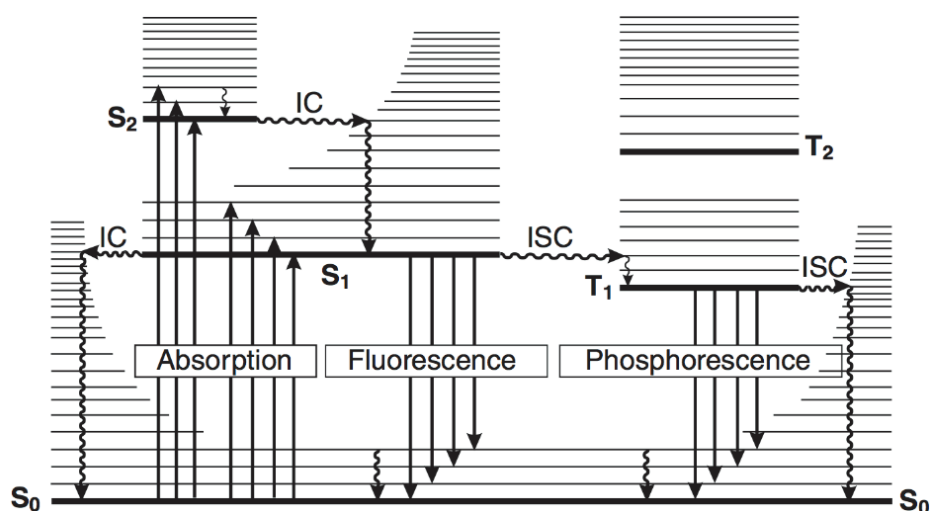
The Perri-Jablonski Diagram is frequently employed to describe the successive processes involved in light absorption-induced excitation of a molecule (Scheme 1.2).<sup>3,11,12</sup> According to the Perri-Jablonski Diagram, electrons in a molecule at the singlet ground state  $S_0$  absorb energy of light and transition to higher energy singlet states, such as  $S_1$  and  $S_2$ . To return to  $S_0$ , electrons undergo various relaxation processes. One such process is internal conversion (IC), which describes the nonradiative transition between two electronic states with the same spin

multiplicity, for instance, from  $S_2$  to  $S_1$ . The IC from  $S_1$  to  $S_0$  is significantly less efficient due to its large energy gap.

The relaxation from  $S_1$  to  $S_0$  can also occur through the emission of photons, leading to the phenomenon known as fluorescence emission. Since fluorescence arises from the  $S_1$  state, the emission characteristics are intrinsic to the molecule and remain independent of excitation wavelength. According to Stokes' law, and as illustrated in the Perri-Jablonski diagram, the energy of fluorescence emission is lower than the absorbed energy, leading to a location of emission band at a longer wavelength compared to the excitation wavelength.<sup>7</sup>

Intersystem crossing (ISC) describes the nonradiative transition between two isoenergetic vibrational levels with different spin multiplicities.<sup>13</sup> Commonly, it involves an excited molecule transitioning from the  $S_1$  to the triplet state  $T_1$ , followed by vibrational relaxation to the lowest energy level in  $T_1$ . In principle, transitions between vibrational levels of different spin multiplicities are forbidden. However, spin-orbit coupling, which describes the interaction between the orbital magnetic moment and the spin magnetic moment, can be efficient enough to facilitate these transitions.<sup>14</sup> For instance, in the presence of heavy atoms, such as bromine or platinum, spin-orbit coupling can be enhanced, resulting in efficient ISC.<sup>15</sup> A reverse ISC, such as from  $T_1$  to  $S_1$ , can occur if their energy gap is small enough and the triplet lifetime is sufficiently long. This process is followed by radiative emission from  $S_1$  to  $S_0$  with a longer lifetime, known as delayed fluorescence. This type of fluorescence is thermally activated, and its efficiency varies with temperature changes.<sup>13</sup>

Phosphorescence arises from the radiative relaxation from triplet state  $T_1$  to singlet ground state  $S_0$  due to spin-orbit coupling at a low temperature or in a rigid matrix.<sup>13</sup> Since the energy level of  $T_1$  is lower than that of  $S_1$ , the phosphorescence emission band is located at a longer wavelength than the fluorescence emission band. Moreover, phosphorescence generally has a much longer lifetime (seconds to minutes) than fluorescence (picoseconds to nanoseconds) due to the involvement of triplet states and the spin-forbidden nature of electronic transitions.





Scheme 1.2.1: The Perri-Jablonski Diagram: IC refers to internal conversion, ISC refers to intersystem crossing, straight arrows upwards refer to radiative absorption, straight arrows downwards refer to radiative emission, and curved arrows represent nonradiative processes.<sup>13</sup>

Intermolecular photophysical processes can significantly impact radiative relaxations. For instance, when an excited molecule collides with a heavy atom, such as a halogen atom, the excess energy is converted into heat to relax the molecule back to its ground state, instead of being released through fluorescence emission. Other intermolecular processes, such as electron or proton transfer, excimer or exciplex formation, and energy transfer (discussed in section 1.3) can also quench fluorescence emission.<sup>16</sup>

### 1.1.3. The Stokes Shift

As mentioned above, Stokes' law states that the fluorescence energy is always lower than the absorbed energy, resulting in a fluorescence emission at a longer wavelength than the excitation wavelength.<sup>7</sup> Stokes Shift is defined as the energy gap between the first maximal absorption peak and the maximal emission peak in a fluorescence spectrum.<sup>13</sup> This energy gap between excitation and fluorescence emission is attributed to the rapid decay from IC to the  $S_1$  state, followed by subsequent fluorescence emission to higher energy levels in the  $S_0$  state. This is followed by the thermalization of the excess energy to the lowest energy level in  $S_0$ . Additionally, other factors such as solvent interaction, complex formation, or additional energy transfer can contribute to a larger Stokes Shift.<sup>17</sup>

### 1.1.4. Fluorescence Lifetime and Quantum Yield

Fluorescence lifetime and quantum yield are important parameters for characterizing fluorescent molecules. Fluorescence lifetime is defined as the average time an electron stays in the excited state before photoemission.<sup>17</sup> A typical fluorescence lifetime ranges from  $10^{-10}$  to  $10^{-7}$  seconds.<sup>13</sup> The excited molecule can return to the ground state  $S_0$  through either radiative or nonradiative processes. Hence, the fluorescence lifetime  $\tau_S$  of excited state  $S_1$  is given by equation 1.3.1:<sup>13</sup>

$$\tau_S = \frac{1}{k_r^S + k_{nr}^S} \quad (1.3.1)$$

Where  $k_r^S$  is the rate constant for radiative deactivation from  $S_1$  to  $S_0$  with fluorescence emission and  $k_{nr}^S$  refers to the overall nonradiative rate constant from  $S_1$ , involving IC to  $S_0$  and ISC.

Quantum yield, often denoted as  $\Phi_F$ , is defined as the ratio of emitted photon numbers to the absorbed photon numbers, in other words, fluorescence quantum yield is the fraction of

excited molecules that return to the  $S_0$  with the emission of fluorescence and is given in equation 1.3.2:<sup>13</sup>

$$\Phi_F = \frac{\kappa_r^S}{\kappa_r^S + \kappa_{nr}^S} = \kappa_r^S \tau_S \quad (1.3.2)$$

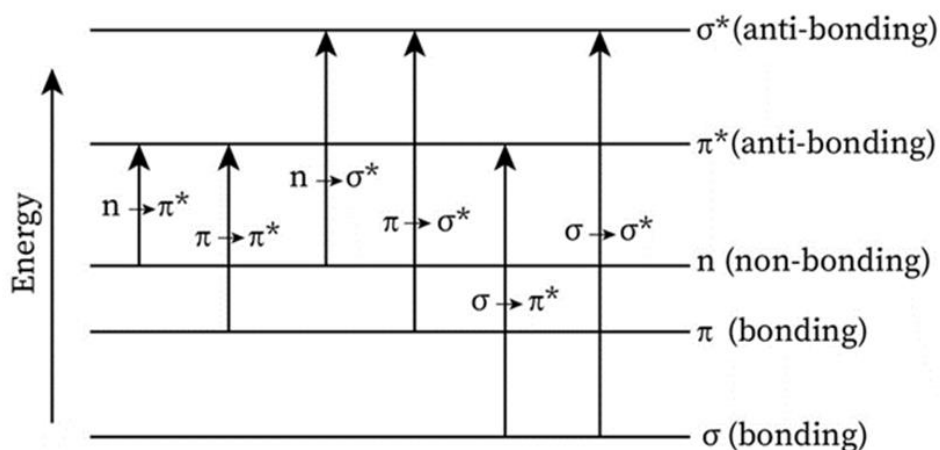
In equation 1.3.2, the fluorescence quantum yield  $\Phi_F$  is proportional to the fluorescence lifetime  $\tau_S$  under conditions where there is no external perturbation. For instance, intermolecular interaction can introduce additional relaxation pathways beyond the intramolecular processes discussed above. Consequently, the proportional relationship between  $\Phi_F$  and  $\tau_S$  can be disrupted, leading to deviation in the expected change between the fluorescence lifetime and quantum yield.<sup>13</sup>

## 1.2. Organic Chromophores

A chromophore is an organic molecule capable of absorbing light.<sup>18</sup> This section introduces molecular orbital transitions, followed by a discussion on the rylene diimide family, particularly naphthalene diimide and perylene diimide derivatives, which are the primary chromophores investigated in this dissertation.

### 1.2.1. Molecular Orbital Transitions

There are various molecular orbitals, such as the  $\sigma$  orbital, which can be formed from two  $s$ -atomic orbitals, or the overlap of an  $s$ - and a  $p$ -atomic orbital. Two  $p$ -atomic orbitals overlapping laterally form a  $\pi$  molecular orbital. Another type of molecular orbital is the  $n$  orbital, which arises from nonbonding electrons located on heteroatoms, such as oxygen and nitrogen. Electronic transitions occur when electrons in these orbitals absorb sufficient energy.<sup>19</sup> Different types of electronic transition are listed below in order of increasing energy gap  $\Delta E$ , where \* denotes the antibonding molecular orbitals (Figure 2.1.1):



$$\Delta E: n \rightarrow \pi^* < \pi \rightarrow \pi^* < n \rightarrow \sigma^* < \pi \rightarrow \sigma^* < \sigma \rightarrow \pi^* < \sigma \rightarrow \sigma^*$$

Figure 2.1.1: Energy level diagram of different electronic transitions.<sup>15,20</sup>

Planck's relation (Eq. 2.1.1) describes the energy of a virtual photon in terms of its wavelength.

$$E = h\nu = \frac{hc}{\lambda} \quad (2.1.1)$$

Where  $E$  (J) refers to the photon energy,  $h$  is the Planck constant ( $6.62 \times 10^{-34}$  J·s),  $\nu$  is the photon's frequency (Hz),  $c$  is the speed of light in vacuum ( $3.0 \times 10^8$  m·s<sup>-1</sup>), and  $\lambda$  (nm) is the wavelength of the photon.

According to Planck's relation, a photon with a higher energy has a shorter wavelength. A system of connected  $p$ -orbitals with delocalized electrons in a molecule, known as a conjugated system, decreases the  $\pi \rightarrow \pi^*$  transition energy gap, enabling the absorption of photons with longer wavelengths. 1,3-butadiene, which exhibits a conjugated system of two double bonds, has a maximal absorption band around 217 nm, while 1,3,5,7,9,11-dodecahexaene, which exhibits a conjugated system of six double bonds, has a maximal absorption band around 364 nm.<sup>21</sup> Organic aromatic compounds exhibit aromaticity, which describes a system in which a conjugated ring of unsaturated bonds, lone pairs, or empty orbitals exhibits stabilization due to delocalization and resonance. This stabilization is stronger than that would be expected from the stabilization of conjugation alone, leading to a lower energy gap in the  $\pi \rightarrow \pi^*$  transition. As a result, fluorescent molecules often have aromatic structures.<sup>21,22</sup> For instance, benzene has a maximal absorption band of around 255 nm. Naphthalene, consisting of a fused pair of benzene rings, has a maximal absorption band of around 360 nm.<sup>23-25</sup> Other factors aside from the conjugation of double bonds and aromatic structures can also strongly influence the optical properties of chromophores. Involving a heavy atom as a substituent in a chromophore, such as Br or I, can lead to fluorescence quenching. This occurs due to the heavy atom favoring spin-orbit coupling, which increases the efficiency

of ISC. Electron-donating substituents, like OH-, or NH<sub>2</sub>, as well as electron-withdrawing substituents, such as C=O, also affect their optical properties.<sup>15</sup> Additionally, chromophores containing heterocyclic atoms or metal complexes exhibit significant changes in their optical properties compared to their parent chromophores.<sup>19,21</sup>

## 1.2.2. Rylene Diimides

Rylene diimides are a class of compounds based on naphthalene units linked at the *peri*-position with terminal imide groups (Figure 2.2.1).<sup>26</sup> In contrast to other organic chromophores, rylene diimides exhibit not only a broad range of colors but also remarkable chemical, thermal, and photophysical stability.<sup>27,28</sup> The synthesis and functionalization of rylene-based organic chromophores have been widely investigated over several decades due to their potential applications in energy storage,<sup>29–32</sup> biological sensors,<sup>33–35</sup> and energy transfer.<sup>36–38</sup> Based on the number of naphthalene units, rylene diimides can be specifically classified as naphthalene diimide ( $n = 1$ ), perylene diimide ( $n = 2$ ), terylene diimide ( $n = 3$ ), and so forth.<sup>39</sup> As illustrated in Figure 2.2.1, the energy gap between the lowest unoccupied molecular orbital (LUMO) and highest occupied molecular orbital (HOMO) decreases with an increasing number of naphthalene units. This decrease in the energy gap results in the optical band shifting to a longer wavelength.<sup>39</sup>

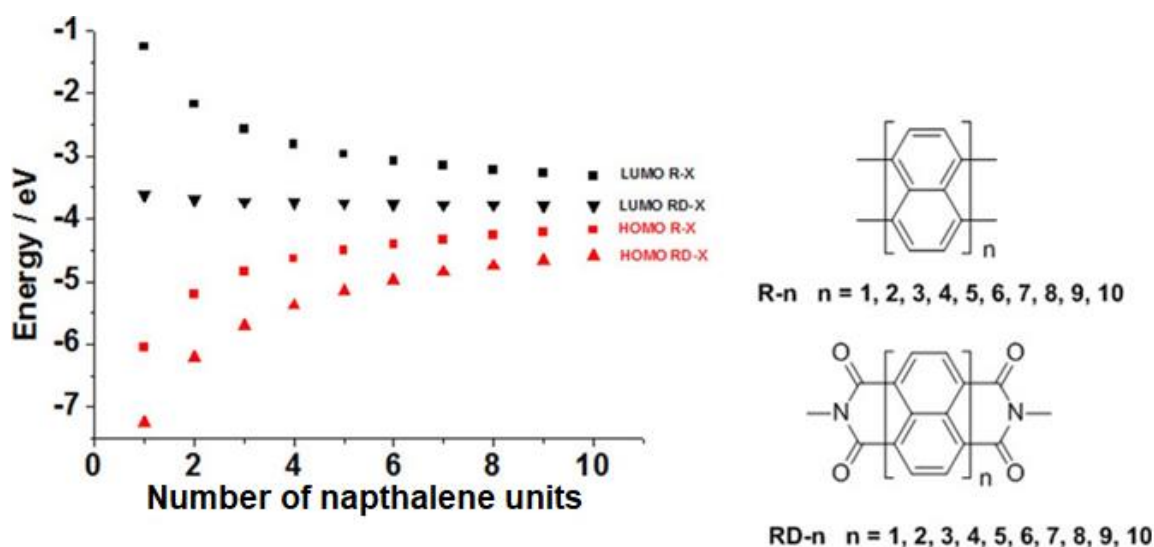
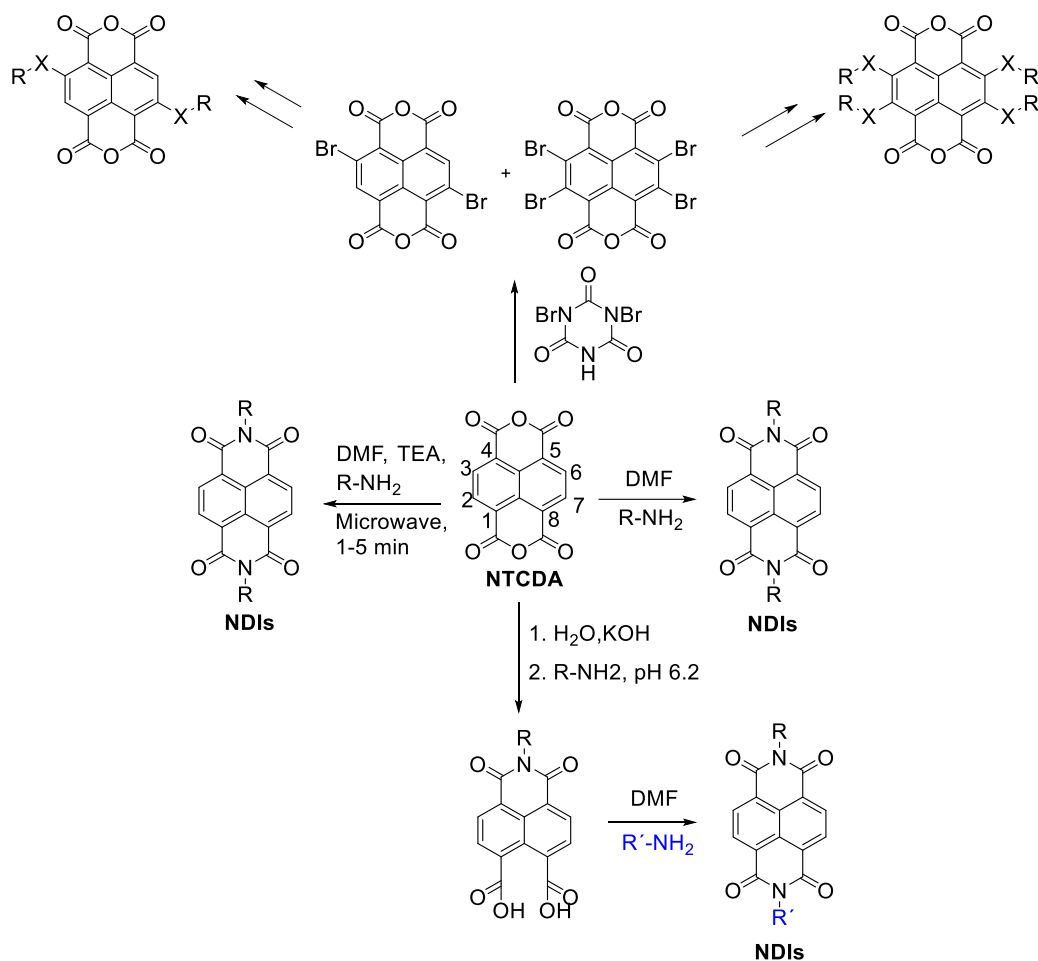


Figure 2.2.1: Theoretical LUMO and HOMO energy levels and the structures of rylene (R) and rylene diimide (RD).<sup>26,39</sup>

### 1.2.2.1. Naphthalene Diimides

Naphthalene diimides (NDIs), also known as 1,4,5,8-naphthalene diimides, are generally synthesized from the precursor 1,4,5,8-naphthalene tetracarboxylic dianhydride (NTCDA). NDIs are planar, neutral, chemically stable compounds<sup>40</sup> and they are the most basic

chromophores in the rylene diimides family.<sup>26</sup> The synthesis of NDIs is illustrated in Scheme 2.2.1.1.



Scheme 2.2.1.1: Brief synthesis routes of symmetrical NDIs, asymmetrical NDIs, and NDIs with core substitutions.<sup>40–43</sup>

Starting with commercially available precursor NTCDA, related symmetrical NDIs can be obtained with high yield through a one-pot condensation reaction with an appropriate amine in a high-boiling solvent, such as dimethylformamide (DMF).<sup>40,44</sup> Jeremy Sanders' group developed an alternative, straightforward synthesis procedure for symmetrical NDIs using a microwave reactor (Scheme 2.2.1.1).<sup>45</sup> The employment of a microwave reactor shortens the reaction time to 5 minutes and overcomes the limitation of pH-dependent amine choices.<sup>45</sup> On the other hand, asymmetrical NDIs composed of two different imide substituents can be synthesized via the formation of a pH-controlled monoimide intermediate, followed by the addition of a second primary amine.<sup>46</sup> Furthermore, substituents involving heteroatoms such as N, O, or S, at the core position 2,3,6,7 of NDIs result in tunable optical properties, first reported by Würthner et al. in 2002.<sup>41</sup> A summary of synthetic routes of core-substituted NDIs is given in Scheme 2.2.1.1 as well. Following the method developed by Vollmann et al., NDIs with halogen atoms at the core positions can be obtained, allowing further functionalization, which can result in a broad range of colors.<sup>42,43</sup>

NDIs without core substitutions are normally obtained as colorless compounds and exhibit three structured absorption bands at 340nm, 360nm, and 380 nm, corresponding to 0-2, 0-1, and 0-0 transitions, respectively. The corresponding emission peaks of these transitions are located at 400, 430 nm, and 460nm.<sup>47,48</sup> Studies have reported that the relative intensity ratio of absorption bands for 0-1 and 0-0 transitions provides aggregation information for NDIs.<sup>47</sup> Furthermore, modifications at core positions can tune the optical properties of NDIs, resulting in a wide range of colors and fluorescence emission wavelengths. Examples of core-substituted NDIs are shown in Figure 2.2.1.1.<sup>49</sup>

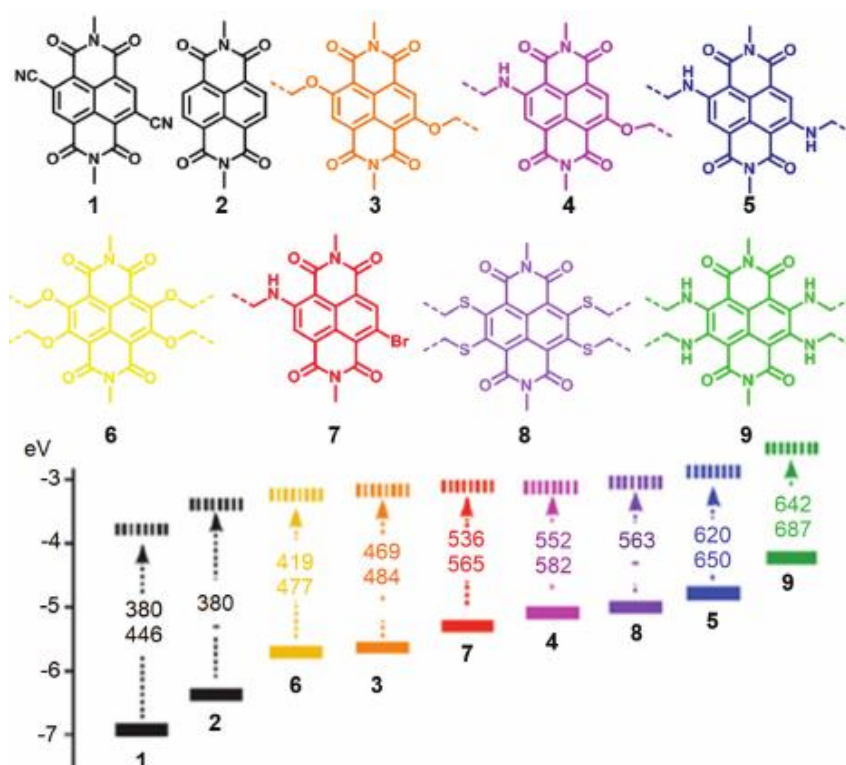


Figure 2.2.1.1: HOMO (bold) and LUMO (dashed) energy levels (eV) of NDIs and core-substituted NDIs, along with molecular structures corresponding to maximal absorption (top, nm) and emission band (bottom, nm).<sup>49</sup>

### 1.2.2.2. Perylene Diimides

Perylene diimides (PDIs) belong to the rylene family, composing two naphthalene units ( $n=2$ , Figure 2.2.1).<sup>39</sup> Discovered by Kardos in 1913, PDIs exhibit a high degree of conjugation, and significant chemical, thermal, and photophysical stability.<sup>50-52</sup> They also display a wide range of colors, including red, violet, and black.<sup>53</sup> Due to their excellent photophysical properties, PDIs have been applied in various fields such as dye-sensitized solar cells,<sup>54-56</sup> organic photovoltaics,<sup>57-59</sup> and organic transistors.<sup>60,61</sup>

Similar to NDIs, the synthesis of PDIs starts from commercially available precursor 3,4,9,10-perylene tetracarboxylic dianhydride (PTCDA).<sup>51</sup> Another approach to synthesizing PDIs is from acenaphthene, however, this method requires several reaction steps (Scheme 2.2.2.1).<sup>50</sup> Symmetrical PDIs can be obtained in a single-step reaction between PTCDA and an amine, with reaction conditions varying depending on the amine used.<sup>51,62</sup> The synthesis of asymmetrical PDIs involves the intermediate perylene monoimide (PMI). As illustrated in Scheme 2.2.2.1, starting from PTCDA, one approach involves the synthesis of symmetrical PDIs followed by partial hydrolysis to obtain PMI. The subsequent step involves attaching a second amine to the PMI to yield asymmetrical PDIs. An alternative method involves the partial hydrolysis of PTCDA followed by attachment of the first amine to achieve PMI, after which a second amine is attached, resulting in asymmetrical PDIs.<sup>63-65</sup>

Imide substituents have a minor impact on the electronic and optical properties of PDIs but strongly influence their solubility and aggregation behavior.<sup>50</sup> PDIs exhibit characteristic absorption peaks with high absorptive coefficients ( $\epsilon \approx 10^5$ ) at 458 nm, 490 nm, and 526 nm, correlating to the 0-2, 0-1, and 0-0 electronic transitions, respectively.<sup>66,67</sup> The corresponding emission peaks of these transitions are located at 540 nm, 576 nm, and 624nm.<sup>50,68</sup> Bay-substituted PDIs have been introduced to tune the optical properties of PDIs. Halogen functionalization enables the attachment of various aryl and aryloxy groups to 1, 6, 7, and 12 positions, resulting in a wide range of colors. Furthermore, bay substituents containing heteroatoms such as N, O, and S also influence the optical properties of PDIs, as shown in Figure 2.2.2.1.<sup>50,67</sup>





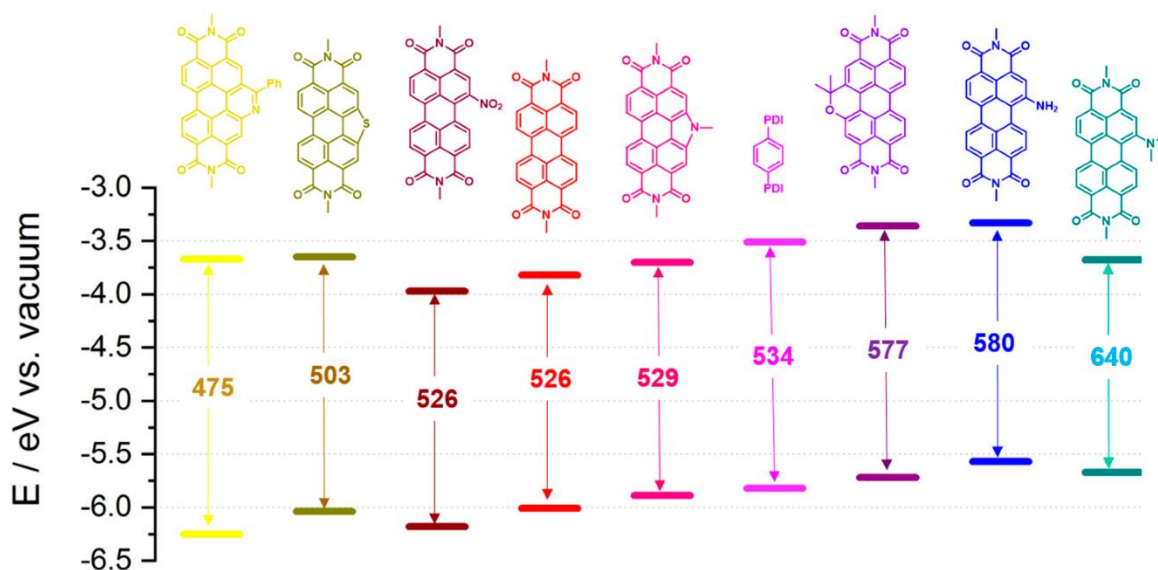


Figure 2.2.2.1: HOMO (bottom) and LUMO (top) energy levels (eV) of PDIs and bay substituted-PDIs, along with molecular structures and the wavelength of maximum absorption in nm.<sup>67,69–72</sup>

### 1.2.2.3. Molecular Self-Assembly

Molecular self-assembly is crucial for constructing thermodynamically stable supramolecular systems, spanning from the molecular scale up to millimeter dimensions, through noncovalent interactions. Both NDIs and PDIs tend to aggregate in an aqueous solution due to their  $\pi$ - $\pi$  interaction from the aromatic core. Various factors, including solvent polarity, substituents, and non-covalent interactions, strongly influence their assembly behavior, leading to the formation of diverse building blocks.<sup>29</sup>

Aggregations of chromophores in solution cause distinct changes in the absorption bands as compared to the monomeric species. H-type aggregation, where H stands for hypsochromic, is characterized by face-to-face stacking of planar molecules, leading to a blue-shifted absorption band and fluorescence emission quenching.<sup>73–75</sup> Conversely, J-type aggregation, discovered by Jelley and Scheibe independently in the 1930s, is characterized by head-to-tail arrangement of molecules in a concentrated solution.<sup>76–79</sup> This type of aggregation results in a red-shifted, sharper absorption band and no fluorescence quenching.<sup>75,78</sup> Normally, aggregation of chromophores in solution leads to emission intensity quenching, this phenomenon is defined as aggregation-caused quenching (ACQ). ACQ limits practical applications of chromophores in designing materials that require high-intensity fluorescence, such as in the fabrication of organic light-emitting diodes. In 2001, a new phenomenon, opposite to ACQ, known as aggregation-induced emission (AIE) was discovered, which describes the observation of much stronger emission of chromophores in an aggregate state than in a monomeric state.<sup>80</sup> AIE is the consequence of two factors. One factor is the fast energy

dissipation by crossing a conical intersection in the monomeric state but not in the aggregate state, which results in low emission in the monomeric state of chromophores. The second factor is the weak intermolecular coupling, which leads to slow energy/charge transfers in the aggregate state, preventing ACQ and resulting in strong emission intensity.<sup>81</sup> Moreover, the formation of excimer can lead to the observation of AIE of chromophores.<sup>82</sup> An excimer is a short-lived complex formed from one excited molecule and one molecule at the ground state and is characterized by a red-shifted broader emission band compared to its monomer.<sup>83</sup>

NDIs can form J-type aggregates in water but different substituents or solvent mixtures can lead to other types of aggregation of NDIs.<sup>84</sup> Study has reported phosphonic acid-terminated NDI exhibits strong H-bonding with melamine. The H-bonding disrupts the formation of J-type aggregation of NDIs, leading to a decrease in absorption band intensity and blue-shifted emission band.<sup>85</sup> Moreover, it has been reported that NDIs with short alkyl-chain (C3) imide substituents favor the formation of H-type aggregation and with long alkyl-chain (C8) imide substituents favor the formation of J-type aggregation in the same solvent.<sup>86</sup> Another optical property exhibited by NDIs is AIE. The AIE effect of NDIs can be observed upon the formation of an excimer, which results in a broad emission peak with high intensity at 510 nm.<sup>16,38,87,88</sup>

Due to the larger planar and aromatic core in PDIs compared with NDIs, PDIs exhibit stronger  $\pi$ - $\pi$  interactions compared to NDIs and typically tend to form H-type aggregates. However, several factors, such as solvent polarity, the introduction of substituents, temperature, external stimuli, and intermolecular interactions, can strongly influence their aggregation behavior.<sup>73</sup> Study has reported a PDI with a boronic acid imide substituent exhibits H-type aggregation in water. However, upon the addition of a chiral anticancer drug, this PDI exhibits J-type aggregation in water, due to the formation of a dynamic covalent bond between boronic acid and hydrogen groups of the chiral anticancer drug molecule.<sup>89</sup> As the aggregation behavior of NDIs and PDIs can be easily adjusted through changing solvents, substituents, and the addition of extra molecules, they are great candidates for developing energy transfer systems that require dynamic adjustments.

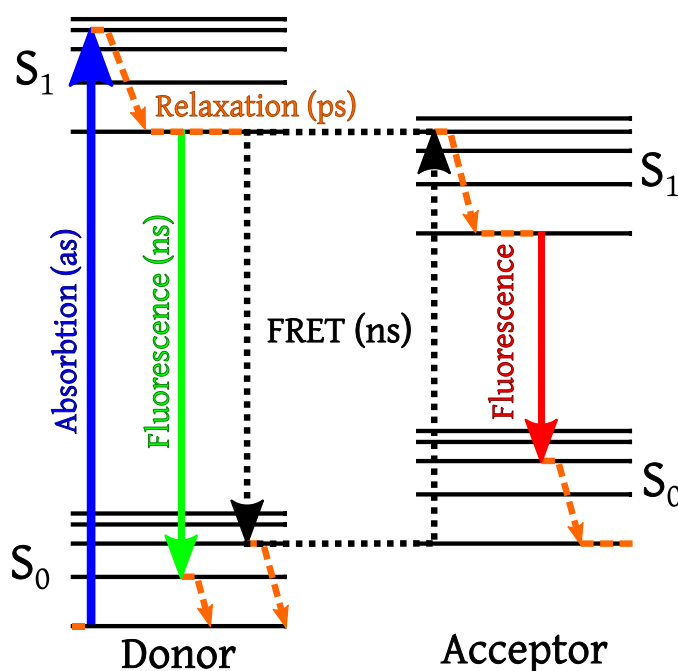
### 1.3. Electronic Energy Transfer

Electronic energy transfer refers to the transfer of energy from an excited donor molecule to an acceptor molecule. If the donor and acceptor are identical, the process is termed homotransfer, whereas the transfer between different molecules is termed heterotransfer.<sup>90</sup> Electronic energy transfer processes are classified into radiative and nonradiative, depending on whether a photon is involved. In classical terms, nonradiative energy transfer between two molecules is described as the interaction of two oscillating electric dipoles.<sup>91</sup> Through resonance, the excited energy from the oscillating donor dipole is transferred to the initially resting acceptor dipole. Hence nonradiative energy transfer is also known as resonance energy transfer or Förster resonance energy transfer (FRET), named after Theodor Förster, who developed the theoretical

framework of resonance energy transfer between molecules.<sup>91,92</sup> Unlike radiative energy transfer, nonradiative energy transfer is limited to a dipole-dipole interaction distance of up to approximately 10 nm. The overlap of the donor emission spectrum with the acceptor absorption spectrum is crucial for the occurrence of nonradiative energy transfer. However, the degree of optical spectral overlap is more critical for radiative energy transfer compared to nonradiative transfer.<sup>90,93</sup>

### 1.2.1. Förster Resonance Energy Transfer

FRET can be explained using the Perri-Jablonski diagram, as illustrated in Scheme 3.1.1. Initially, a donor molecule is excited from its ground state  $S_0$  to an excited singlet state  $S_1$  through the absorption of light.<sup>13,90</sup> IC leads to a rapid relaxation to the lowest energy level within  $S_1$ .<sup>13</sup> The excess energy of the excited donor can be transferred to a nearby acceptor molecule through nonradiative dipole-dipole interaction, in addition to other relaxation processes, such as donor fluorescence emission.<sup>16</sup> The energy transferred to the acceptor results in its excitation from ground state  $S_0$  to an excited singlet state  $S_1$ , followed by possible relaxation processes, including acceptor fluorescence emission.<sup>3,13,90</sup>



Scheme 3.1.1: The Perri-Jablonski diagram of FRET.

The efficiency of FRET, denoted as  $E$ , is influenced by several factors: spectral overlap between donor emission and acceptor absorption, intermolecular distance, and relative orientations, between donor and acceptor.<sup>90,91</sup> The Förster critical distance  $R_0$  (nm) describes the interaction distance between donor and acceptor at which the energy transfer efficiency is 50%, and it is described by the following equation 3.1.1, derived by Förster:

$$R_0^6 = \frac{9000(\ln 10)k^2\Phi_D^0}{128\pi^5 N_a n^4} J \quad (3.1.1)$$

Where  $k^2$  refers to the orientation factor,  $\Phi_D^0$  is the fluorescence quantum yield of the donor in the absence of the acceptor,  $n$  refers to the refractive index of the medium,  $N_a$  ( $\text{mol}^{-1}$ ) is the Avogadro constant,  $J$  ( $\text{nm}^4 \cdot \text{M}^{-1} \cdot \text{cm}^{-1}$ ) is the spectral overlap integral of donor emission and acceptor absorption, and is determined in equation 3.1.2:

$$J = \int_0^\infty F_D(\lambda)\varepsilon_A(\lambda)\lambda^4 d\lambda \quad (3.1.2)$$

Where  $F_D$  refers to the normalized emission spectrum of the excited donor, and  $\varepsilon_A$  ( $\text{m}^2 \cdot \text{mol}^{-1}$ ) is the absorption coefficient of the acceptor.<sup>90,93</sup>

The relationship between FRET efficiency  $E$  and donor-acceptor distance  $r$  (nm) can be described in equation 3.1.3:

$$E = \frac{1}{1 + \left(r/R_0\right)^6} \quad (3.1.3)$$

Hence, the donor-acceptor distance  $r$  can be calculated with equation 3.1.4:

$$r = \left(\frac{1}{E} - 1\right)^{1/6} R_0 \quad (3.1.4)$$

Through observation of donor fluorescence quenching in the presence and absence of the acceptor and enhancement of acceptor fluorescence upon the addition of donor in the steady-state fluorescence spectrum, FRET efficiency can be determined using the Förster equation 3.1.5:

$$E = 1 - \frac{I}{I_0} = 1 - \frac{\tau_D}{\tau_D^0} \quad (3.1.5)$$

Where  $I$  and  $I_0$  represent donor fluorescence intensity in the presence and absence of the acceptor, respectively. Additionally, FRET efficiency  $E$  can also be determined through the comparison of donor fluorescence lifetime in the absence  $\tau_D^0$  (s) and the presence  $\tau_D$  (s) of the acceptor, as shown in equation 3.1.5.<sup>90,94</sup>

## 1.2.2. Förster Resonance Energy Transfer in Supramolecular Systems

As FRET arises from the interaction between molecules and is dependent on distance and orientation between the donor and acceptor, it serves as a powerful tool in analyzing the dynamic formation of macromolecules and their interactions. Precise control over the donor-acceptor distance and orientation is crucial for achieving efficient FRET. There are various strategies to control the distance and orientation between donor and acceptor molecules for efficient FRET. MOFs are hybrid materials composed of chemically coordinated metal ions self-assembly and organic bridge ligands. On the one hand, MOFs can serve as a host for chromophores and provide a rigid matrix to achieve efficient FRET. For instance, a study reported the utilization of MOFs that entrap donors and acceptors in close proximity to develop FRET systems.<sup>95-97</sup> On the other hand, a MOF self can serve as a donor or an acceptor to develop a FRET system within MOF assemblies.<sup>98-100</sup> As MOFs contain metal ions, which can be harmful to the environment, covalent organic frameworks (COFs) have been used in the construction of donor-acceptor pairs with well-defined distances and angles to achieve efficient FRET. COFs are porous crystalline polymers with ordered structures through covalently bonded organic repeating units and were invented by Yaghi et al. in 2005.<sup>101</sup> Similar to MOFs, COFs can serve as a host for chromophores and bring them in close proximity to develop FRET systems.<sup>102,103</sup> COFs can also serve as a donor and/or an acceptor for FRET, as COFs often exhibit large conjugated systems, leading to efficient fluorescence emission.<sup>104,105</sup>

An important branch of supramolecular systems is macrocycle-based host-guest chemistry. A host-guest system is generally composed of a guest molecule coordinated with a macrocyclic host and forming an inclusive complex through weak intermolecular interactions such as H-bonding, electrostatic interaction, Van der Waals forces, etc.<sup>106,107</sup> Typical macrocyclic hosts such as cyclodextrins,<sup>108</sup> calixarenes,<sup>109</sup> cucurbiturils,<sup>110</sup> and pillararenes<sup>111</sup> have been developed and widely studied in host-guest chemistry. As the host-guest system is driven by non-covalent forces, it is sensitive to external stimuli, such as pH, light, and temperature. This provides the potential of dynamic adjustments for FRET within a host-guest system compared to MOFs or COFs-based FRET process. Studies have reported diverse FRET systems within host-guest systems.<sup>106</sup> For instance, a donor (perylene) and an acceptor (pyrene) were immobilized on the host (wheel) and guest (axis) of rotaxane, respectively, resulting in FRET due to the close proximity of the interlocked rotaxane.<sup>112</sup> Moreover, a host-guest system in which donor-acceptor pairs are covalently linked with each other as a guest can exhibit fluorescence switching on/off based on the interaction between host and guest, leading to the presence and absence of FRET process.<sup>113</sup>

Supramolecular polymers containing repeating units are connected via non-covalent interactions, similar to the driving forces in host-guest systems. As non-covalent interactions are weak compared to covalent bonds, supramolecular polymers exhibit flexibility and adaptivity upon external stimuli, making them advantageous platforms for developing FRET systems.<sup>114</sup> Donors and acceptors can be covalently and non-covalently attached to polymer chains for the FRET process.<sup>115,116</sup> As the conformation of chromophore-labeled polymer chains changes, the distance and orientations between donor and acceptor will be affected,

resulting in changes in FRET efficiency.<sup>117,118</sup> Conversely, FRET has been applied as a tool to understand the assembly mechanism and kinetics of aggregates in supramolecular polymer systems.<sup>119,120</sup>

Supramolecular system-based FRET, such as in MOFs and COFs, exhibits an advantage in the formation of donor-acceptor pairs with well-defined distances and orientations. Moreover, FRET in host-guest systems and supramolecular polymers demonstrates high flexibility, allowing for dynamic adjustments. However, such supramolecular systems also display a few limitations, such as the requirement of multiple synthesis steps, a high ratio of chromophores, and a lack of physical and chemical stability for FRET. The employment of inorganic nanoparticles for FRET provides an alternative strategy for achieving efficient FRET and will be discussed in the following section.

### 1.2.3. Förster Resonance Energy Transfer in Organic-Inorganic Hybrids

Introducing an inorganic nanoparticle template to the FRET system is a strategy that has been developed over the past decades to optimize energy transfer.<sup>121</sup> Hybrid systems, comprising inorganic nanoparticles and organic chromophores, offer several advantages, including optimal protection and stabilization of chromophores, the ability to control the ratio of various chromophores with different optical properties, and the potential for developing new types of devices such as light-harvesting devices, and light-emitting diodes.<sup>122,123</sup> Furthermore, organic chromophores can be linked to nanoparticles both covalently and noncovalently, enabling versatile synthesis at low cost while achieving efficient FRET and expanding the potential for customizing hybrid systems for various applications.

Various inorganic nanoparticles, such as metal nanoparticles, quantum dots, and clay minerals can be introduced in developing FRET. Inorganic nanoparticles such as quantum dots (QDs), which exhibit photoluminescence, are tiny semiconductor crystals with a size of 1-10 nm and normally have core/shell and core/double-shell structures such as ZnSe/ZnS, ZnSe/CdS, and CdSe/ZnSe/ZnS.<sup>124,125</sup> When a quantum dot is illuminated by light, electrons in the QD can be excited to a higher energy state and drop back to the ground state through fluorescence emission. The optical properties of QDs are dependent on their composition, structure, and size, demonstrating potential for serving as donors and/or acceptors for FRET. Studies have reported diverse QDs-based FRET systems, in which QDs serve as donors<sup>126,127</sup> or acceptors<sup>128</sup>, while organic chromophores labeled ligands on the surface of QDs serve as acceptors or donors, leading to the FRET process between QDs and organic chromophores. The linkers' length between QDs and chromophores can strongly affect FRET efficiency besides other factors such as surfactant, chromophore aggregation, chromophore concentration on the surfaces of QDs, etc.<sup>129-131</sup>

Inorganic nanoparticles which do not exhibit photoluminescence, such as clay minerals, can serve as a template to immobilize chromophores for FRET and provide precise control over donor-acceptor distances and orientations based on surface chemistry. In a clay mineral-

based FRET system, donor and acceptor molecules can be attached to either the same surface or different surfaces via surface chemistry, enabling the FRET process. Studies reported FRET systems building on layered silicate clays involving immobilization of donor and acceptor on the basal surface,<sup>132–134</sup> covalent linkages of donor on the edge surface, while the acceptor was attached to the basal surface via ion exchange.<sup>122</sup> Clay mineral-based FRET systems exhibit an advantage in the optimization of FRET by changing either the chromophores or the layered silicate clay aggregations, which can be achieved by varying solvent compositions and concentrations of chromophores, and the introduction of extra surfactants. Moreover, due to the large surface areas and anisotropic surface chemistry of clay minerals, efficient FRET can be achieved at relatively low chromophore concentrations.

## **1.4. Laponite**

This section provides an introduction to clay minerals, followed by an overview of Smectite clays, to which Lap belongs. It then presents a discussion about Lap, including its physical properties and potential for organic modification.

### **1.4.1. Clay Minerals**

Georgius Agricola first formalized a definition of clay in 1546, which has been revised many times since then. Nearly five centuries later, the term “clay” was defined by the Joint Nomenclature Committees of the Association Internationale pour l’Etude des Argiles and the Clay Minerals Society as naturally occurring material composed of fine-grained minerals, which is generally plastic at an appropriate water content and will harden when dried or fired.<sup>135</sup> Clay has been used since antiquity and has become indispensable in modern living. It is the primary material for many types of ceramics, such as porcelain, brick, tiles, and sanitary ware. Additionally, clay is an essential component in industries such as plastic, paint, paper, rubber, and cosmetics.<sup>136</sup> The term “clay mineral” refers to phyllosilicate minerals, and non-phyllosilicate minerals that impart plasticity to clay and harden upon drying or firing.<sup>135</sup> It is important to note that “clay” is distinct from clay mineral as it should not be used as a mineral term. Furthermore, clay minerals could include non-phyllosilicates, while phyllosilicates are the principal constituents of clay.<sup>136</sup>

Based on the ratio of tetrahedral to octahedral sheets, clay minerals are classified into 1:1 and 2:1 types. The 1:1 classification signifies a structure with one tetrahedral sheet paired with one octahedral sheet, while the 2:1 type indicates two tetrahedral sheets for one octahedral sheet.<sup>136</sup> For instance, the kaolin group, which includes kaolinite, dickite, halloysite, hisingerite, and nacrite, belongs to the 1:1 clay category.<sup>137</sup> The smectite group, which includes montmorillonite, beidellite, nontronite, saponite, and Lap, falls into the 2:1 group.<sup>138</sup> Clay minerals have garnered significant interest in material science due to their excellent

biocompatibility, affordability, natural abundance, and diverse morphologies, leading to widespread exploration of their potential applications.<sup>139</sup>

### 1.4.2. Smectites

Smectites are a group of swelling clay minerals characterized by a layered structure, composed of various silicate sheets, including dioctahedral minerals such as montmorillonite, beidellite, nontronite, and trioctahedral minerals such as hectorite, sauconite, and saponite.<sup>140</sup> As mentioned above, smectites belong to the 2:1 clay mineral group, involving two tetrahedral sheets for one octahedral sheet.<sup>141</sup> The different types of smectite vary in chemical composition, involving substitutions of Al for Si in tetrahedral cation sites and the substitution of Al, Fe, Mg, and Li in octahedral cation sites. Additionally, cations such as H, Na, Ca, or Mg adsorb externally on the interlamellar surface to balance the negative charge of the basal surfaces.<sup>141</sup> Smectites exhibit several unique properties, such as a large chemically active surface area through interlayer expansion, a constant cation exchange capacity (CEC) resulting from the isomorphic substitution in both the octahedral and tetrahedral sheets, and a relatively small crystal size (<2  $\mu\text{m}$ ).<sup>142</sup> Moreover, smectites demonstrate notable shrink-swell behavior, as they can absorb many times their weight in water, and drying cycles can lead to shrinkage in volume due to the removal of water trapped in the interlayer space. These properties have made smectites widely used in industrial applications such as ceramic, detergents, adhesives, medical formulations, etc.<sup>141</sup>

The interaction of water with clay minerals is complex and is influenced by various factors, such as the nature of clay mineral surface, extent and location of isomorphous substitution, types of exchangeable cations, pH, ionic compositions of the aqueous phase, the overall pore size distribution, and particle size and shape.<sup>143</sup> For instance, in  $\text{Na}^+$  exchanged smectites, there are five water molecules surrounding each  $\text{Na}^+$  ion while its position is dependent on the negative charge presented within silicate layers.<sup>144</sup> CEC describes the propensity of smectite for sorbing cationic species from solution and the value of CEC can be expressed in milliequivalents per g clay (meq/g).<sup>145</sup> Metal alkoxides and cationic organic molecules can intercalate into smectites via ion exchange. This leads to induced interlayer porosity and the formation of ordered vertical stacks of layered clays, which are referred to as pillared clays. The introduction of inorganic ions to interlayers leads to the pillaring of clays through the formation of solids within the interlayer via condensation. Studies have reported the growth of diverse metal oxides, such as  $\text{ZrO}_2$ ,<sup>146,147</sup>  $\text{TiO}_2$ ,<sup>148,149</sup> and  $\text{Al}_2\text{O}_3$ ,<sup>150,151</sup> in the interlayer space of layered clays, which induced the growth of Y-Zeolites in the interlayer, resulting in the development of porous materials applied in catalysis.<sup>152</sup> In contrast, cationic organic molecules such as alkylammonium-based surfactants, intercalate to the interlayers without forming solid phases, demonstrating a simpler formation of pillared clay and an increase in hydrophobicity.<sup>145,153</sup> The formation of pillared smectites through intercalations of various species provides the potential for developing materials with tailored properties for specific applications in material science.



Natural smectites are formed from the weathering of basalt, gabbro, and silica-rich volcanic glass.<sup>154</sup> A typical natural smectite is the Montmorillonite (MMT) with the chemical formula  $(\text{Na}, \text{Ca})_{0.3}(\text{Al}, \text{Mg})_2\text{Si}_4\text{O}_{10}(\text{OH})_2 \cdot n(\text{H}_2\text{O})$ , which was first discovered in 1847, in Montmorillon in the region of Vienne, France.<sup>155</sup> Each MMT layer is around 1 nm thick and composed of one O-Al(Mg)-O octahedral sheet, sandwiched between two O-Si-O tetrahedral sheets.<sup>156</sup> As mentioned above, smectites have been applied in many industrial applications. MMT is often preferred for these applications due to its specific properties, such as high surface area, good plasticity and viscosity, and high purity compared to other natural smectites. For instance, MMT is utilized in the oil drilling industry as a component of drilling mud, in order to keep the mud slurry viscous,<sup>157,158</sup> Moreover, MMT serves as an effective sorbent for heavy metals when added to water, attracting small particles and settling to the bottom.<sup>159</sup> While natural smectites such as MMT exhibit advantages in low cost and high swelling capacity, synthetic smectites such as Lap, which contain no mineral impurities and possess uniform compositions and structures, are more suitable for research purposes.

### 1.4.3. Physical Properties of Laponite

Lap is a synthetic smectite layered silicate with the chemical formula  $\text{Na}^{+0.7}[(\text{Si}_8\text{Mg}_{5.5}\text{Li}_{0.3})\text{O}_{20}(\text{OH})_4]^{-0.7}$ . Each layer is composed of one octahedral sheet containing a magnesium ion at its center and bounded by O and OH groups, sandwiched between two tetrahedral silicate sheets (Figure 4.3.1). Isomorphic substitution of some octahedral Mg atoms with Li results in an intrinsic negative charge, which is balanced by sodium ions associated with the basal surfaces.<sup>160</sup> Disc-shaped Lap particles have an average diameter of approximately 25 nm and a thickness of 0.92 nm. The molecular weight of Lap falls within the range of  $7.1 \times 10^5$  to  $9.3 \times 10^5$  g/mol, indicating an average number of  $1100 \pm 100$  unit cells within a single Lap particle.<sup>161-165</sup> When Lap is dispersed in an aqueous medium, some of the sodium ions in the interlayers diffuse, corresponding to the exchangeable sodium ions of Lap, which is the basis of its CEC. The CEC of Lap has been reported to be in the range of 0.55-0.8 mequiv/g, this value corresponds to around 450 exchangeable sodium ions per Lap particle. Furthermore, dispersion of Lap in water, with a pH in the range between 3 to 10, will increase to a pH of 10.4. This increase in pH is due to the dissociation of  $\text{OH}^-$  ions at the edge surface of Lap.<sup>164</sup>

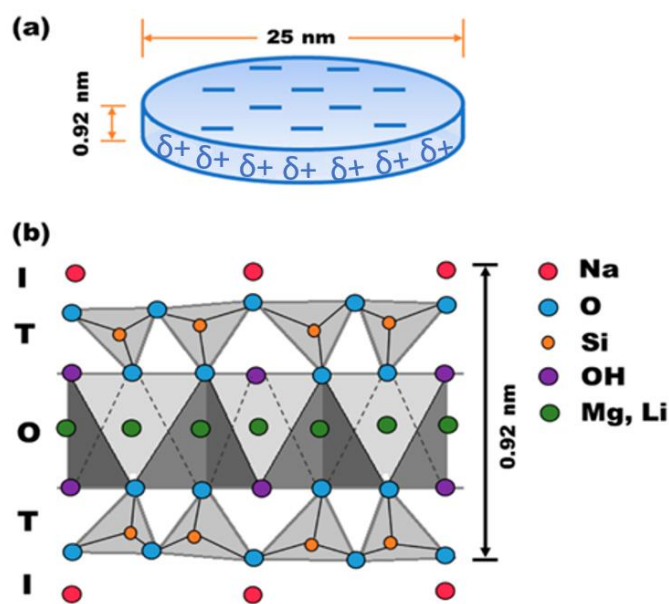


Figure 4.3.1: (a) Schematic of a single Lap particle in an aqueous medium. (b) Atomic arrangement in the unit cell of Lap: octahedral sheet (O) between two tetrahedral sheets (T) coordinated with interlayer sodium atoms (I).<sup>164</sup>

Lap particles are stacked parallel to each other in a dry state and undergo swelling and exfoliation when introduced in an aqueous medium. At concentrations below 2% (w/w), Lap dispersions exhibit aging times spanning months to years, eventually manifesting in two distinct physical states. These states comprise a gel mixed with clay-poor and clay-rich domains ( $C_{LAP} \leq 1\%$  w/w) and an equilibrium gel state characterized by a “house of cards” structure ( $1\% \text{ w/w} < C_{LAP} < 2\% \text{ w/w}$ ).<sup>166,167</sup> The aggregation behavior of Lap platelets in a dispersion can be finely adjusted by varying pH and temperature, and implementing various modifications of surfaces. Studies have reported that Lap platelets carry an overall negative charge in dispersion at pH 3 and above. Lower pH levels ( $< 3$ ) lead to the formation of a 'house of cards' structure resulting from the negatively charged basal surface and partially positively charged edge surfaces. In contrast, at higher pH levels ( $> 11$ ), the prevailing repulsive interaction between negatively charged basal surfaces resulted in more fluid Lap dispersion.<sup>168,169</sup>

#### 1.4.4. Organic Modification of Laponite

As mentioned above, Lap acquires negative charges on its basal surface when dispersed in an aqueous medium and it has been reported that there are around 450 exchangeable sodium ions on each Lap particle. Therefore, cationic molecules can adsorb on the Lap basal surface through ion exchange, enabling organic modifications on the basal surface and achieving a more hydrophobic basal surface. Moreover, the Lap edge surface is positively charged at a low pH ( $< 3$ ), allowing for the adsorption of ionic molecules at the edge surface. Such different modifications on Lap surfaces via non-covalent interactions can benefit the formation of high-

strength hydrogel. Studies have reported the formation of hydrogel based on Lap with great mechanical strength,<sup>170,171</sup> which also demonstrates self-healing properties after damage, resulting from the reversibility of non-covalent interactions.<sup>172</sup> Moreover, the intercalations of excess cationic surfactants, such as cetyltrimethylammonium bromide (CTAB),<sup>173</sup> cetylpyridinium chloride,<sup>174</sup> to the Lap interlayers, leading to the expansion of interlayer space.

The free silanol groups present on the edge surface enable covalent modification through the formation of Si-O-Si bonds. As there are no silanol groups at the basal surface, such organic modification on the edge surface occurs independently from the basal surface. Studies have reported the covalent linkages of diverse alkoxy silanes, such as dimetyloctylmethoxysilane, 3-azidopropyltrimethoxysilane, aminopropyl dimethylethoxysilane (APES), and 3-aminopropyltrimethoxy silane (APTES), to the edge surface through silanol coupling. Their results also revealed that trialkoxysilane such as APTES can link multiple Lap sheets together, including pillaring, whereas monoalkoxysilane such as APES does not exhibit this behavior.<sup>174-176</sup> Furthermore, such covalent modification at the edge surface enables further functionalizations with targeted functional groups. For instance, various organic chromophores have been covalently linked to the Lap edge surface through reaction with an amine-terminated alkoxy silane<sup>177</sup> or click chemistry with an azido-terminated alkoxy silane,<sup>176</sup> resulting in fluorescent Lap particles. Moreover, such modifications can induce additional non-covalent interactions, such as  $\pi$ - $\pi$  stacking between molecules, which may disrupt the typical 'house of cards' structure of Lap.<sup>176</sup>

Due to Lap's uniform structure, high surface area, colloidal stability, and tunable chemical and physical properties through modification, Lap finds widespread application across various industries including biomedical, cosmetics, personal care products, and food packing.<sup>167</sup> Organic modification on Lap surfaces can increase the hydrophobicity of Lap, enable encapsulation of targeted drug molecules in drug delivery, and protect drugs against degradation in the physiological environment. For instance, studies have reported successful encapsulations of the anticancer drug doxorubicin (DOX) in Lap through associations of pH-sensitive polymers<sup>178,179</sup> or cross-linked alginate hydrogel.<sup>180</sup> The incorporation of Lap in cosmetic formulation enables the delivery of incompatible ingredients within a single formulation due to the ability to exchange cations.<sup>181,182</sup> Additionally, Lap can provide an advantage in the solubilization of hydrophobic chromophores in water, and serve as a vehicle for a large number and wide range of chromophores, making Lap a great candidate for bioimaging.<sup>183</sup> Studies have reported that the interactions of chromophores with Lap always led to spectral and intensity changes in both absorption and emission. For instance, when neutral Nile red is adsorbed to Lap in water, it exhibits fluorescence, whereas neutral Nile red is reported to be almost non-emissive in water.<sup>184</sup> Similarly, the non-emissive crystal violet exhibits fluorescence upon interaction with Lap.<sup>185</sup>

## 1.5. Motivation

The motivation for this dissertation lies in developing hybrid materials that combine the unique photophysical properties of organic chromophores with structural advances of layered silicate clays. Layered silicate clays, specifically Lap, possess basal and edge surfaces with different chemical properties, allowing for independent modifications on their basal surface and edge surface. This unique feature facilitates precise and targeted functionalization strategies. As discussed above, the free silanol groups on the Lap edge surface are accessible for covalent linkages of chromophores at the edge surface, and the Lap basal surface is capable of immobilizing chromophores via ion exchange on the Lap basal surface. The first aim of this dissertation is the linkages of diverse chromophores to the Lap anisotropic chemical surfaces to achieve organic-inorganic hybrid materials with targeted optical properties.

Building upon chromophore-modified Lap, the second aim is to establish FRET systems by immobilizing donor and acceptor molecules either on the basal surface via ion exchange and/or on the edge surface via covalent bonds. Such FRET systems involving Lap as a template, provide a well-defined framework, allowing for precise control over the distances and orientations of donor and acceptor molecules. The third aim is to optimize FRET efficiency by dynamically adjusting the aggregation state of either Lap or the bound chromophores. NDIs and PDIs are good candidates as donors and acceptors in such FRET systems, as their aggregation states can be easily manipulated by varying solvent compositions, in addition to their diverse optical properties and physicochemical stability. The aggregation state of Lap can also be adjusted through the introduction of surfactants to form pillared Lap particles.

Developing these new hybrid materials with tailored optical properties could offer enhanced performance in various applications, including environmental monitoring, medical diagnostics, and the development of new sensors. Moreover, the ability to control and modify anisotropic surfaces of layered silicate clays also opens up possibilities for creating multifunctional materials with applications beyond FRET, such as in catalysis and semiconductor technologies.

## 2. Layered silicate edge-linked perylene diimides: Synthesis, self-assembly and energy transfer

This Chapter has been published as:

Xiang, H., Valandro, S. R., & Hill, E. H. (2023). Layered silicate edge-linked perylene diimides: Synthesis, self-assembly and energy transfer. *Journal of Colloid and Interface Science*, 629, 300-306.

In this research work, two PDIs featuring distinct ending groups were linked to the edge surface of Lap through a condensation reaction involving an amine group. Upon characterizations, two resulting hybrids exhibited dissimilar dispersibilities under identical water content conditions. Owing to  $\pi$ - $\pi$  stacking of the perylene core, both hybrids displayed the formation of H-aggregation with increasing water content. Additionally, a cationic donor was introduced to the basal surface of PDIs-modified Lap via ion exchange, leading to the observation of FRET from the basal surface located donor to the edge surface bound donor.

This study represents a pioneering effort in synthesizing PDIs-modified Lap and introducing a new model of FRET on Lap, thus encouraging further exploration of utilizing Lap as a scaffold for constructing FRET systems.



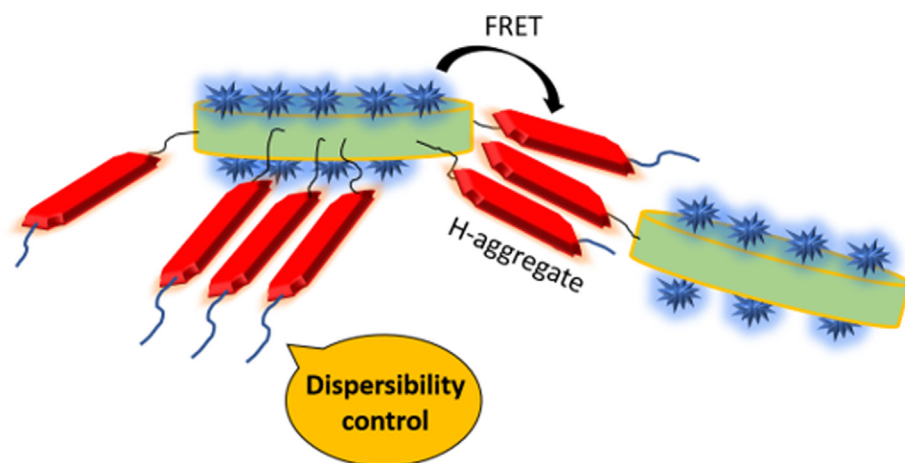
# Layered silicate edge-linked perylene diimides: Synthesis, self-assembly and energy transfer

Hongxiao Xiang<sup>a</sup>, Silvano R. Valandro<sup>a,b</sup>, Eric H. Hill<sup>a,b,\*</sup>

<sup>a</sup>Institute of Physical Chemistry, University of Hamburg, Grindelallee 117, 20146 Hamburg, Germany

<sup>b</sup>The Hamburg Center for Ultrafast Imaging (CUI), Luruper Chausee 149, 22761 Hamburg, Germany

## GRAPHICAL ABSTRACT



## ARTICLE INFO

### Article history:

Received 26 May 2022

Revised 2 September 2022

Accepted 11 September 2022

Available online 15 September 2022

### Keywords:

Nanoclays

Nanohybrids

H-Aggregates

FRET

Solvent-induced Aggregation

Laponite

## ABSTRACT

The control over intermolecular interactions between chromophores at nanomaterial interfaces is important for sensing and light-harvesting applications. To that aim, inorganic nanoparticles with anisotropic shape and surface chemistry can serve as useful supports for organic modification. Herein, novel asymmetric perylene diimides with aspartic acid and oleyl terminal groups were grafted to the edges of the layered silicate clay Laponite, a water-dispersible discoidal nanoparticle. The photophysical properties and solvent-dependent self-assembly of the nanoclay-grafted perylenes were investigated, revealing that the polarity of the terminating ligand dictates the aggregation behavior in aqueous solution, where increased water content generally led to the formation of perylene H-aggregates. The anionic basal surface of the nanoclay provided a binding site for a cationic fluorophore, leading to energy transfer from the face-bound donor to the edge-bound perylene acceptor. This study encourages further research on the use of functional ligands for the formation of organic–inorganic hybrids, particularly where inorganic template particles with specific surface chemistry can be exploited to study intermolecular interactions. Overall, these findings should advance further design and implementation of novel semiconducting ligands towards inorganic–organic hybrids, with potential applications in sensing and energy harvesting.

© 2022 Elsevier Inc. All rights reserved.

\* Corresponding author at: Institute of Physical Chemistry, University of Hamburg, Grindelallee 117, 20146 Hamburg, Germany.

E-mail address: [eric.hill@chemie.uni-hamburg.de](mailto:eric.hill@chemie.uni-hamburg.de) (E.H. Hill).

## 1. Introduction

The functionalization of nanomaterial interfaces with spatially-separated regions of different surface chemistry can provide avenues to functionalize these regions with specific molecules as a means to study their interactions. In particular, charge- and energy-transfer processes at interfaces can be understood by utilizing such strategies with different organic ligands [1–3]. This strategy can allow the investigation of charge and energy transfer between conjugated organic molecules, which is of particular interest for developing sensors and light-harvesting devices [4–7]. While such studies have traditionally been carried out using organic linkers of different sizes, the increasing use of inorganic–organic hybrid nanomaterials toward energy and sensing applications calls for further investigation of energy transfer between organic molecules bound to inorganic nanomaterial interfaces [8–11].

Among conjugated organic molecules, perylene-3,4,9,10-tetra carboxylic acid diimide derivatives (PDI) have been the focus of recent studies, due to their excellent chemical and physical properties, such as thermal, photo, and weather stability, near-unity fluorescence quantum yields, and strong electron-accepting character [12–15]. Such properties lead to wide applications such as organic solar cells, chemo-sensor, organic photovoltaic devices, and dye lasers [16–18]. The properties of PDI derivatives can be modified by different functional groups. Imide substituents can change the solubility of the PDI, and substituents on the 'bay'-site can modify their electronic and optical properties [12]. Furthermore, the self-assembly of PDIs can be influenced by solvents and functional groups, and the fluorescent properties and tunable modes of self-assembly also make PDIs attractive for energy transfer and polarized emission strategies [19–20].

Laponite (Lap) is a synthetic disc-like layered magnesiosilicate clay with a diameter of 25 nm, a thickness of 0.92 nm, and a chemical formula of  $\text{Na}_{0.7}(\text{H}_2\text{O})_n\{(\text{Li}_{0.3}\text{Mg}_{5.5})[\text{Si}_8\text{O}_{20}(\text{OH})_4]\}$  [21]. When Lap is dispersed in an aqueous medium, it is negatively charged on the basal surface, with partially-positively charged edges at neutral pH. This anisotropic surface chemistry allows the Lap basal surface and edge sites to be independently functionalized. The basal surface can be functionalized by cationic organic molecules via ion exchange [22–25]. On the other hand, the Si-OH edge sites can be covalently functionalized via silanol chemistry [6,26–28]. Felbeck et al. reported the covalent modification of Lap with different fluorophores, such as neutral dansyl derivative and fluorescamine [29]. Nakayama et al. also grafted pyrene (donor) to the edges of a  $\sim 50$  nm dia. layered silicate, and adsorbed a cationic porphyrin (acceptor) on the surface, establishing that energy transfer between could be used as spectroscopic molecular ruler [6]. However, neither the functionalization of Lap with PDIs, nor energy transfer with an edge-bound acceptor, have been reported.

Herein, the synthesis and characterization of two novel organic–inorganic hybrids based on perylene-diimide covalently linked onto the Lap edge are reported. Two different asymmetric PDIs were synthesized with one end functionalized with a mono alkoxysilane, and the other imide end terminated with either an N-linked aspartic acid (Lap-PDIa) or an oleyl ( $\text{C}_{18}\text{H}_{35}$ ) chain (Lap-PDIo). The use of an amine-terminated silane allowed covalent linkage of these PDIs to the Lap edge via silanol chemistry. The photophysical properties of both Lap-PDI hybrids were investigated, and the influence of the terminating ligand on the solvent-induced self-assembly revealed water-induced H-aggregation due to strong hydrophobic interactions, which was more severe in the case of the oleyl-terminated PDI. Furthermore, the cationic fluorophore 4',6'-diamidino-2-phenylindole (DAPI) was adsorbed on the surface of Lap, and the fluorescence resonance energy transfer (FRET) between DAPI and PDI was studied.

## 2. Results and discussion

The synthesis of the asymmetric PDIs and their clay-bound hybrids Lap-PDIo and Lap-PDIa is summarized in Scheme 1. Detailed synthetic methods for Lap-PDIo and Lap-PDIa are given in the Supporting Information. Briefly, in the synthesis of Lap-PDIo, the key intermediate perylene monoimide terminated with an oleyl chain (PMIo) was prepared according to the following method: perylene-3,4,9,10-tetracarboxylic acid monoanhydride monopotassium carboxylate was reacted with oleylamine to produce PMIo [30]. PMIo was reacted with Lap-APES to produce the target compound Lap-PDIo [31]. The attempted preparation of the perylene monoimide containing aspartic acid as a ligand (PMIa) by the same method as PMIo did not yield the PMIa product, instead mostly the dianhydride was formed. In order to obtain the target compound Lap-PDIa, an intermediate PDIa was synthesized, followed by partial hydrolysis with KOH to produce the PMIa [32]. Reaction of PMIa with Lap-APES yielded Lap-PDIa [31].

Fourier-transformed Infrared Spectroscopy (FT-IR) was used to characterize the functionalization of Lap with APES and PDIs (Fig. 1a). All samples show peaks at  $963\text{ cm}^{-1}$  and  $648\text{ cm}^{-1}$ , attributed to the Si-O stretching and OH bending vibrations, respectively, which are characteristic of layered silicates such as Lap [33]. By the modification of Lap with APES, a new peak can be observed at  $1255\text{ cm}^{-1}$  due to the C-N stretching vibration. The FT-IR spectrum for Lap-PDIo display new peaks at  $2848\text{ cm}^{-1}$  and  $2918\text{ cm}^{-1}$  which correspond to the C-H stretching vibration of alkanes. Lap-PDIo also shows peaks at  $1687$ ,  $1641$ , and  $1595\text{ cm}^{-1}$  which can be attributed to different modes of the N-C=O vibration [34]. Lap-PDIa shows similar peaks for the N-C=O modes as Lap-PDIo, in addition to a broad peak around  $3300\text{ cm}^{-1}$  due to the O-H stretch. While FT-IR suggests functionalization of Lap with PDIs was successful, further characterization by Thermogravimetric Analysis (TGA) was carried out to further establish the degree of functionalization (Fig. 1b). Solid state Cross-polarization/magic angle spinning (CP/MAS)  $^{29}\text{Si}$  and  $^{13}\text{C}$  NMR were carried out to characterize Lap-APES, Lap-PDIo and Lap-PDIa. In the  $^{29}\text{Si}$  ssNMR spectra of Lap-APES, Lap-PDIo and Lap-PDIa (Figure S1-S3), peaks at 10–20 ppm indicate the successful linkage of APES to the Lap edge, whereas the peaks at  $-95$  ppm and at  $-85$  ppm indicate condensed and incompletely condensed Si in laponite, respectively [27]. In the  $^{13}\text{C}$  ssNMR spectrum of Lap-APES, four peaks for carbon are shown, corresponding to the carbons in the APES chain (Figure S4).  $^{13}\text{C}$  ssNMR shows a single peak at  $165.5$  ppm and  $162.1$  ppm in Lap-PDIo (Figure S5) and Lap-PDIa (Figure S6), respectively, corresponding to C=O carbons adjacent to diimide N.

TGA results show that Lap by itself has a mass loss below  $150\text{ }^\circ\text{C}$  due to physisorbed water, and a second mass loss which starts at  $150\text{ }^\circ\text{C}$  and goes beyond  $700\text{ }^\circ\text{C}$ , due to interlayer water molecules in Lap particles [28,35]. For Lap-APES, two main weight losses are observed: (i) at low temperatures ( $<150\text{ }^\circ\text{C}$ ) attributed to adsorbed water, and (ii) in the range of  $\sim 150$  to  $\sim 500\text{ }^\circ\text{C}$  attributed to ethoxysilane decomposition [27]. For Lap-PDIo and Lap-PDIa, a main mass loss between  $\sim 200\text{ }^\circ\text{C}$ – $700\text{ }^\circ\text{C}$  was observed. This loss is assigned to the decomposition of PDI linked to Lap. The mass loss of the total organic content on Lap-PDIa and Lap-PDIo was 12.37% and 9.38%, respectively. Felbeck et al. have reported that the maximum number of reactive Si-OH groups is around 420 per particle [29]. As the final product was obtained by stepwise functionalization the degree of functionalization cannot be accurately determined by elemental analysis, thus TGA was used to estimate the degree of functionalization as previously reported by Wheeler et al. [27] The organic content of Lap-PDIo and Lap-PDIa estimated by TGA revealed that approximately 90 units of PDIo and 270 units

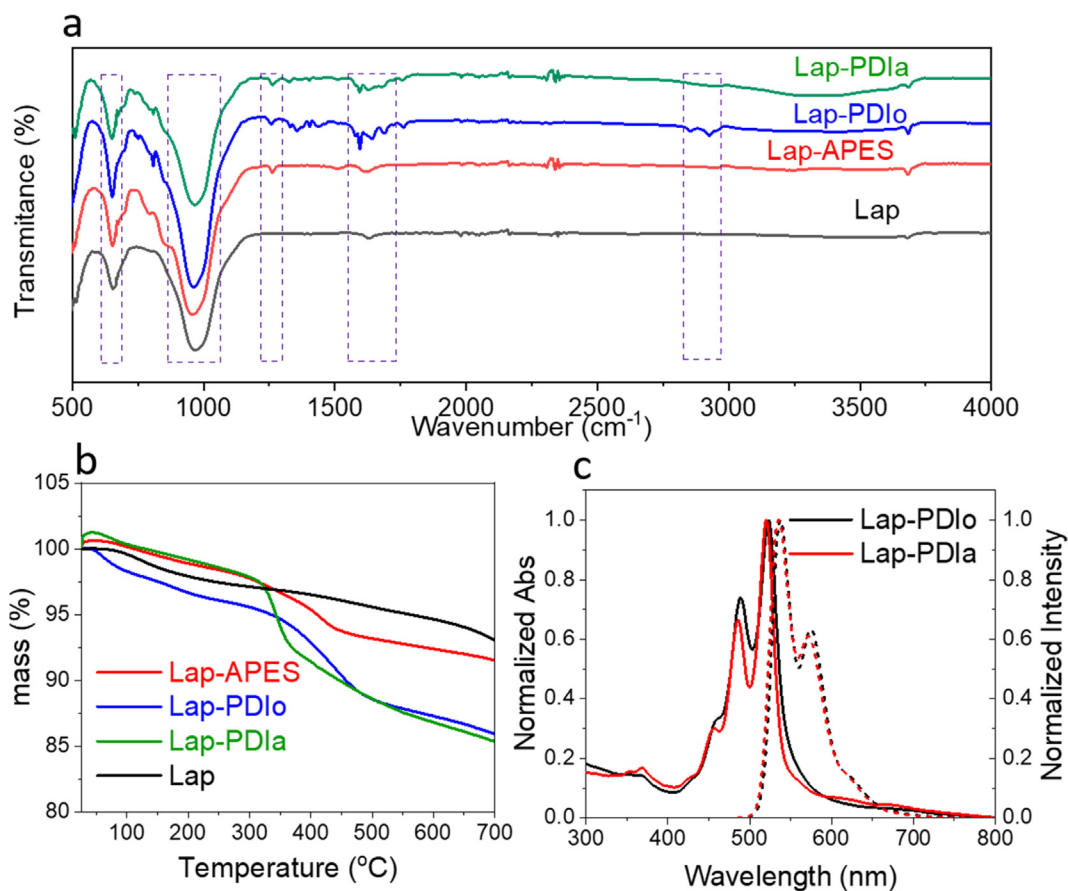
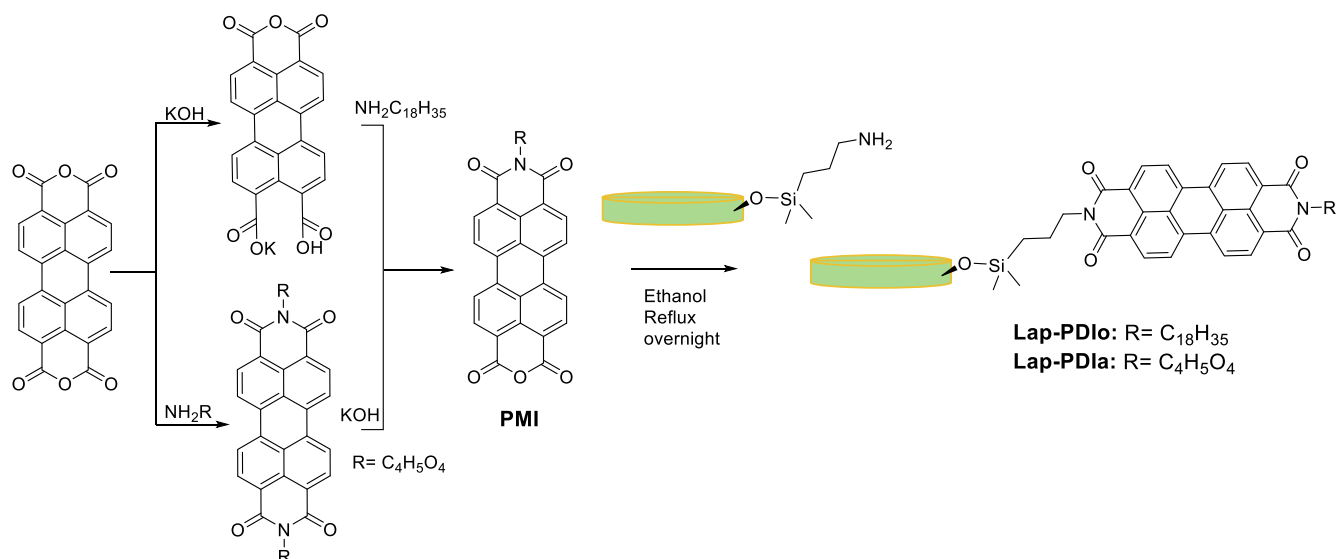


**Fig. 1.** (a) FT-IR spectra and (b) TGA curves of Laponite, Lap-APES, Lap-PDIo and Lap-PDIa. (c) Normalized UV-Vis absorption and fluorescence emission spectra of Lap-PDIo and Lap-PDIa (0.01 mg ml<sup>-1</sup>) in DMF.

PDIa were linked per particle of Lap, in agreement with previous reports. The lower number of PDI units in Lap-PDIo could be due to steric hindrance during grafting caused by the size and steric hindrance of the oleyl chain. The relatively low organic content compared to Lap in the hybrids can also be observed by FT-IR,

where the characteristic peaks of Lap are significantly stronger in intensity than those of the attached perylenes.

The ground-state electronic properties of Lap-PDIo and Lap-PDIa were explored by UV-vis absorption spectroscopy in DMF at room temperature (Fig. 1c). The UV-vis spectra show similar spec-



tral characteristics between Lap-PDlo and Lap-PDIa, with the  $S_0-S_1$  electronic transition at  $\sim 520$  nm ( $\sim 19230$   $\text{cm}^{-1}$ ) and strong vibronic progressions at  $\sim 485$  nm ( $20618$   $\text{cm}^{-1}$ ) and  $\sim 458$  nm ( $21834$   $\text{cm}^{-1}$ ). The vibronic progression has been ascribed to the vinyl stretching mode ( $\nu_{C=C} \sim 1400$   $\text{cm}^{-1}$ ) [36]. In order to rule out the adsorption of PMI precursors, as opposed to silanol linkage on the Lap edge, UV-Vis was used to study the adsorption of PMIo on Lap and Lap-APES (Figure S8) compared to Lap-PDlo. The concentration of PMIo that was added is the same as PDlo in the hybrid Lap-PDlo (0.01 mg/mL). PMIo is not soluble in DMF, and the observed absorption of PMIo in presence of Lap and Lap-APES is insignificant. On the other hand, the hybrid Lap-PDlo showed a strong absorption band from the PDI moiety. Fluorescence emission spectra (Fig. 1c) of Lap-PDlo and Lap-PDIa show the characteristic emission ( $\lambda_{\text{max}} = 535$  nm) and well-resolved vibronic fine structure of PDI. Relative fluorescence quantum yields were determined (using Rhodamine B (0.31) [37] as reference) as 0.52 for Lap-PDlo and 0.58 for Lap-PDIa, which is reduced from the near-unity quantum yield of PDI, possibly due to the presence of aggregates which could decrease the radiative decay rate. Time-resolved single-photon counting was used to determine the singlet excited state lifetimes of Lap-PDlo and Lap-PDIa. With excitation at 470 nm and emission monitored at 535 nm, Lap-PDlo and Lap-PDIa decay monoexponentially in 4.1 and 4.2 ns, respectively.

Self-assembly of Lap-PDlo and Lap-PDIa were investigated by UV-Vis and fluorescence spectroscopy (Fig. 2). The UV-Vis spectra of Lap-PDlo at low content of water (0–10% v/v) show the sharp absorption bands of PDI chromophores, suggesting little aggregation of Lap-PDlo (Fig. 2a). On the other hand, at water content

25% and above, a slightly blueshifted absorption concomitant with reduction in absorption and loss of definition of the peaks at 520 and 485 nm is observed. This behavior is typical of aggregation of PDI, where the chromophores are in a sandwich-type packing, known as H-aggregation [38–39]. Fluorescence spectroscopy corroborates this observation, where fluorescence quenching and loss of the fluorescence band attributed to monomeric PDI is observed with water contents at 25% and above (Fig. 2b). The UV-Vis (Fig. 2c) and fluorescence spectra (Fig. 2d) for Lap-PDIa at different percentages of water in DMF show similar behavior as Lap-PDlo, where at low water content PDI is mostly monomeric and at increased water content aggregation takes place. However, in the case of Lap-PDIa, at 25% water content the fluorescence still indicates monomeric PDI, whereas Lap-PDlo is already highly aggregated. This behavior can be attributed to the oleyl chain of Lap-PDlo favoring aggregation due to its hydrophobicity compared to the N-linked aspartic acid, which is more hydrophilic. The absorbance spectrum of Lap-PDIa in 25% water already shows significant broadening and reduction in peak intensity induced by aggregation, albeit not completely. While there is possibly some interparticle aggregation, the relatively high density of PDI grafted along the Lap edge suggests that intraparticle aggregation is largely responsible for the observed solvent-induced photophysical changes.

In order to investigate the reversibility of the aggregation, stock dispersions of Lap-PDlo and Lap-PDIa were prepared in 1:9 DMF/water. In this condition, both Lap-PDlo and Lap-PDIa are completely aggregated. The dispersions were then diluted to result in different DMF:water ratios. As shown in Figure S9, the deaggrega-

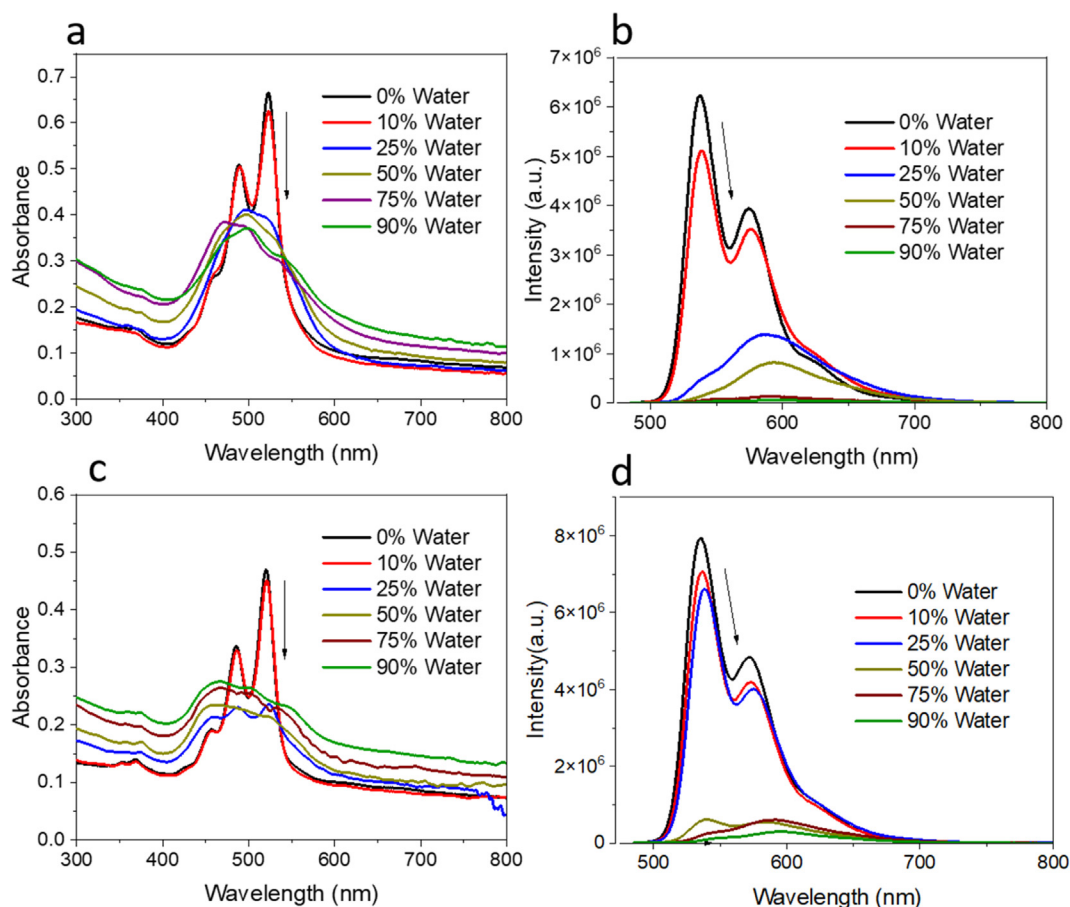


**Fig. 2.** (a) UV-Vis absorption and (b) fluorescence emission spectra Lap-PDlo ( $0.01$   $\text{mg ml}^{-1}$ ) ( $\lambda_{\text{exc}} = 470$  nm) in different DMF/water mixtures, and (c) UV-Vis absorption and (d) fluorescence emission spectra of Lap-PDIa ( $0.01$   $\text{mg ml}^{-1}$ ), ( $\lambda_{\text{exc}} = 470$  nm) in different DMF/water mixtures. Arrow indicates increasing water content.

tion of Lap-PDlo is partially reversible, whereas the deaggregation of Lap-PDla appears completely reversible. This difference in behavior is reasonable, due to the hydrophobicity of the oleyl terminal group compared to the succinic acid group.

The anisotropic surface chemistry of Lap platelets allows the investigation of intermolecular interactions that take place between the edge- and face-bound molecules. To that effect, DAPI was adsorbed to the surface of Lap-PDlo and the energy transfer between DAPI and PDI was evaluated. Fluorescence spectra of DAPI in 9:1 DMF/water dispersion with excitation at 345 nm were recorded as a function of the added Lap-PDlo (Fig. 3a). The emission band centered at 465 nm is attributed to the fluorescence of DAPI. A decrease in DAPI fluorescence intensity with an increase in the concentration of Lap-PDlo is observed. Moreover, the fluorescence bands of Lap-PDlo are clearly observed increasing concomitant with the amount added ( $\lambda \sim 535$  nm). There are two possible explanations for this decrease in fluorescence intensity: (i) energy transfer between DAPI and Lap-PDlo and (ii) aggregation of DAPI molecules on the surface of Lap nanoparticles. Despite many literature reports on the aggregation of cationic dyes on layered silicate clays, no extant studies have reported the aggregation of DAPI. Furthermore, at a high concentration of Lap-PDI, a blue shift in the emission band of DAPI is observed. This shift may arise from the interaction between DAPI molecules and the PDI moieties (potentially  $\pi$ - $\pi$  interactions between the indole and perylene), as similar behavior has been reported for interactions of DAPI and nucleic acids [40].

To disentangle the influence of possible aggregation of DAPI on Lap from the loss of DAPI fluorescence due to FRET, control experiments with DAPI and pure Lap were carried out (Figure S10). Fig. 3b shows  $F/F_0$  as a function of the concentration of Lap-PDlo and pure Lap, in different solvent compositions. Here,  $F$  refers to the fluorescence intensity of DAPI in the presence of Lap-PDlo or Lap, and  $F_0$  is that of DAPI alone. A small decrease in the DAPI fluorescence intensity was also observed when Lap was added, suggesting H-type aggregation of DAPI on the Lap basal surface. However, the decrease in fluorescence intensity is more prominent when Lap-PDlo is added, indicating that the main deactivation path for the DAPI fluorescence quenching is energy transfer to the Lap-PDlo (Fig. 3b). The energy transfer was also evaluated in 1:1 DMF/water, as this represents a state where Lap-PDlo is more aggregated (Figure S11 and S12). A similar decrease in DAPI fluorescence can be seen, however, the band for Lap-PDlo is not observed due to the low fluorescence quantum yield in 1:1 DMF/water dispersion.

The energy transfer efficiencies for DAPI  $\rightarrow$  Lap-PDlo ( $[Lap-PDI] = 0.091$  mg/mL) were calculated from the data shown in Fig. 3 using the equation  $E = [1 - (F_{da}/F_d)] - F_{Control}$ , where  $F_{da}$  and  $F_d$  are the fluorescence (area under the curve at 465 nm) of donor (DAPI) in the presence and absence of acceptor (Lap-PDlo), respectively.  $F_{Control}$  is the contribution of the DAPI aggregation from the control experiments using Lap.  $F_{Control} = 1 - (F_{Lap}/F_d)$ , where  $F_{Lap}$  and  $F_d$  are the fluorescence (area under the curve at 465 nm) of DAPI in the presence and absence of pure Lap, respectively. The calculated

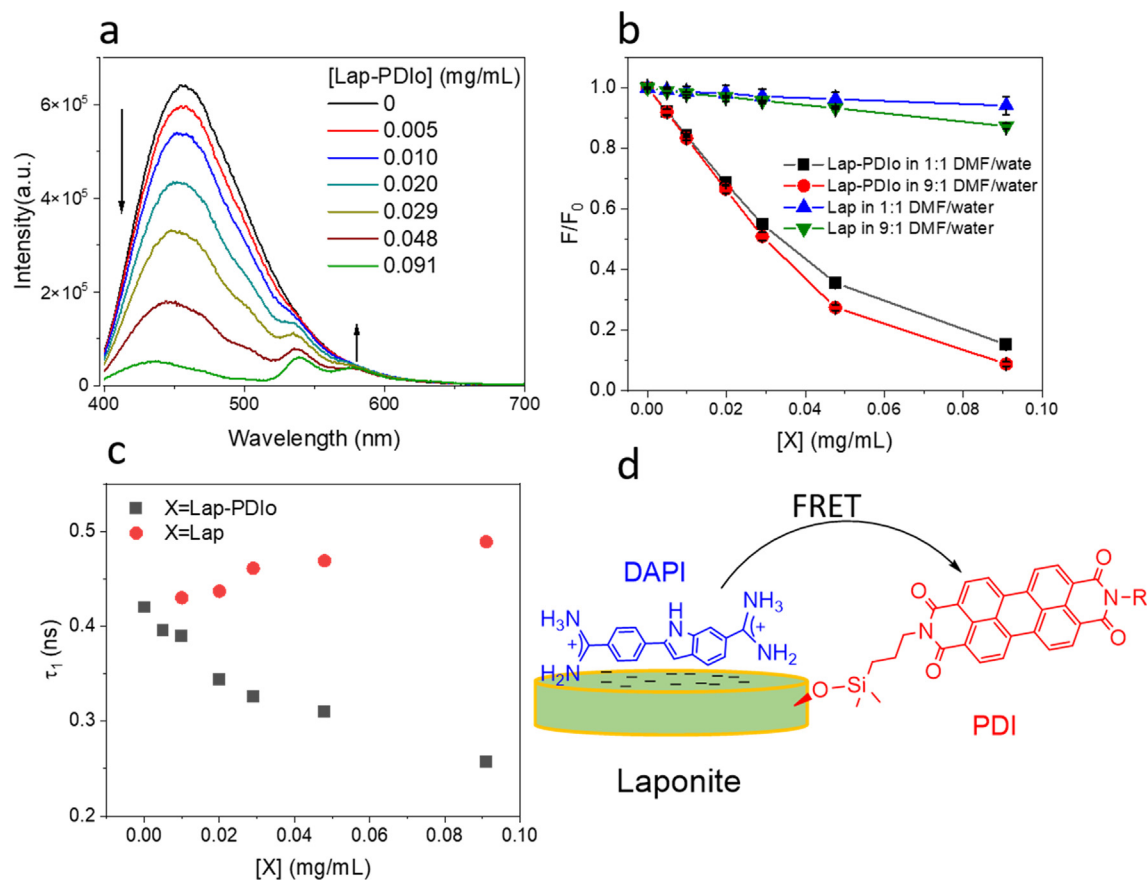


**Fig. 3.** (a) Fluorescence emission of mixture containing 10  $\mu$ M of DAPI with different concentrations of Lap-PDlo in 9:1 DMF/water, (b)  $F/F_0$  as function of concentration of Lap-PDlo and Lap in 9:1 DMF/water and 1:1 DMF/water dispersions, (c)  $\tau_1$  as a function of concentration of Lap-PDlo and Lap in 9:1 DMF/water dispersions, and (d) representative scheme of the energy transfer from the DAPI adsorbed on the Lap surface to the PDI linked on edge-surface. Image is not drawn to scale.

energy transfer efficiency  $E$  for the Lap-PDlo mixtures are 78% in 9:1 DMF/water and 79% in 1:1 DMF/water. These results indicate that the degree of aggregation does not affect the energy transfer efficiency, suggesting that energy transfer occurs mainly from DAPI to PDI on the same Lap particle.

Fluorescence lifetime measurements support the DAPI → Lap-PDlo energy transfer mechanism (Table S1). DAPI decays biexponentially, where the two components are attributed to different conformers [41–42]. Comparing  $\tau_1$  as a function of the added amount of Lap-PDlo and pure Lap, it is clear that the DAPI lifetimes components get shorter as Lap-PDlo is added (Fig. 3c). Although only  $\tau_1$  is shown in Fig. 3c, both  $\tau_1$  and  $\tau_2$  decrease as Lap-PDlo is added (Table S1). This indicates a new path of excited state deactivation, such as energy transfer. On the other hand, control experiments where pure Lap was added instead of Lap-PDlo show a small increase in the lifetime components, which is likely associated with the aggregation of DAPI on the surface of Lap (Table S2) [43]. The scheme in Fig. 3d illustrates the likely energy transfer process, where the energy transfer occurs from the DAPI adsorbed on the surface to the PDI chromophores grafted on the edge surface of Lap nanoparticles.

### 3. Conclusions

In summary, the synthesis of two organic–inorganic hybrids based on PDI derivatives covalently linked to the edge sites of Lap has been achieved. The hybrids Lap-PDlo and Lap-PDIa maintain the photophysical characteristics of the PDI chromophore, while being granted partial water dispersibility due to Lap. While in aqueous media the Lap-PDI hybrids aggregated due to hydrophobic interactions between PDIs, the polarity of the terminal group could alter the water dispersibility by a significant degree, with Lap-PDIa fully dispersed and Lap-PDlo aggregated at 25% water. Moreover, energy transfer from DAPI (donor) to Lap-PDlo (acceptor) was observed, promoted by the close proximity of the edge-bound PDI to the face-bound DAPI.

The control over intermolecular interactions at nanomaterial interfaces is highly relevant for future advances in organic–inorganic hybrid materials. Layered silicate nanomaterials are highly attractive due to their distinct surface chemistry, which allow two different moieties to be placed within 10–20 nm. Collectively, the study reported herein may enlighten research towards synthesis of organic–inorganic hybrids based on organic chromophores and layered silicates or even other layered materials, such as 2D heterostructured semiconductors based on layered silicates [44–46]. Although this work is primarily aimed towards perylene diimide-based hybrids, this synthetic approach can be generalized to other diimides such as larger rylenes and naphthalenes. Furthermore, strategies involving tuning of colloidal interactions between the clay surface independently of those of the attached ligand may yield interesting colloidal assemblies. Overall, this work opens a new direction to future studies of inorganic–organic hybrids based on perylene diimide derivatives with enhanced water dispersibility and easily modified electronic properties. This work will advance further design and implementation of novel semiconducting ligands towards inorganic–organic hybrids, with potential applications in sensing and energy harvesting.

### CRediT authorship contribution statement

**Hongxiao Xiang:** Investigation, Writing – original draft, Writing – review & editing. **Silvano R. Valandro:** Investigation, Writing – original draft, Writing – review & editing. **Eric H. Hill:** Conceptualization, Supervision, Writing – review & editing.

### Declaration of Competing Interest

The authors declare that they have no known competing financial interests or personal relationships that could have appeared to influence the work reported in this paper.

### Acknowledgements

This research was funded by the Deutsche Forschungsgemeinschaft (DFG) – project ID 447787198. E.H.H. and S.V. are supported by the Cluster of Excellence “Advanced Imaging of Matter” of the DFG–EXC 2056—project ID 390715994. This research was funded in part by the DAAD from the funds of German Federal Ministry of Education and Research (BMBF), under the MOPGA-GRI program (57565165). We gratefully acknowledge the central measurement facilities of the Chemistry Department of the University of Hamburg for providing elemental analysis and access to NMR equipment. We also gratefully acknowledge Dr. Jan Dirk Epping (Institute of Chemistry, TU Berlin) for providing solid state NMR characterization.

### Appendix A. Supplementary data

Detailed synthetic methods, Additional fluorescence spectra and tabulated fluorescence lifetimes from FRET experiments. Supplementary data to this article can be found online at <https://doi.org/10.1016/j.jcis.2022.09.055>.

### References

- [1] T. Shichi, K. Takagi, *Clay Minerals as Photochemical Reaction Fields*, *J. Photochem. Photobiol. C. J. Photochem. Photobiol. C Photochem. Rev.* 1 (September) (2000) 113–130.
- [2] D. Dey, D. Bhattacharjee, S. Chakraborty, S.A. Hussain, Effect of Nanoclay Laponite and PH on the Energy Transfer between Fluorescent Dyes, *J. Photochem. Photobiol. A Chem.* 252 (2013) 174–182, <https://doi.org/10.1016/j.jphotochem.2012.12.003>.
- [3] N. Epelde-Elezcano, E. Duque-Redondo, V. Martínez-Martínez, H. Manzano, I. López-Arbeloá, Preparation, Photophysical Characterization, and Modeling of LDS722/Laponite 2D-Ordered Hybrid Films, *Langmuir* 30 (33) (2014) 10112–10117, <https://doi.org/10.1021/ja502081c>.
- [4] L. Wu, C. Huang, B.P. Emery, A.C. Sedgwick, S.D. Bull, X.P. He, H. Tian, J. Yoon, J. L. Sessler, T.D. James, Förster Resonance Energy Transfer (FRET)-Based Small-Molecule Sensors and Imaging Agents, *Chem. Soc. Rev.* 49 (15) (2020) 5110–5139, <https://doi.org/10.1039/c9cs00318e>.
- [5] P.M. Neema, A.M. Tomy, J. Cyriac, Chemical Sensor Platforms Based on Fluorescence Resonance Energy Transfer (FRET) and 2D Materials, *TrAC - Trends Anal. Chem.* 124 (2020), <https://doi.org/10.1016/j.trac.2019.115797>.
- [6] A. Nakayama, J. Mizuno, Y. Ohtani, T. Shimada, S. Takagi, Elucidation of the Adsorption Distribution of Cationic Porphyrin on the Inorganic Surface by Energy Transfer as a Molecular Ruler, *J. Phys. Chem. C* 122 (8) (2018) 4365–4371, <https://doi.org/10.1021/acs.jpcc.7b12104>.
- [7] Y. Ishida, T. Shimada, D. Masui, H. Tachibana, H. Inoue, S. Takagi, Efficient Excited Energy Transfer Reaction in Clay/Porphyrin Complex toward an Artificial Light-Harvesting System, *J. Am. Chem. Soc.* 133 (36) (2011) 14280–14286, <https://doi.org/10.1021/ja204425u>.
- [8] L. De Luca, G. Giacomelli, A. Porcheddu, Beckmann Rearrangement of Oximes under Very Mild Conditions, *J. Org. Chem.* 67 (17) (2002) 6272–6274, <https://doi.org/10.1021/jo025960d>.
- [9] H.E. Song, M. Taniguchi, J.R. Diers, C. Kirmaier, D.F. Bocian, J.S. Lindsey, D. Holten, Linker Dependence of Energy and Hole Transfer in Neutral and Oxidized Multiporphyrin Arrays, *J. Phys. Chem. B* 113 (52) (2009) 16483–16493, <https://doi.org/10.1021/jp9072558>.
- [10] T.H. Evers, E.M.W.M. van Dongen, A.C. Faesen, E.W. Meijer, M. Merkx, Quantitative Understanding of the Energy Transfer between Fluorescent Proteins Connected via Flexible Peptide Linkers, *Biochemistry* 45 (44) (2006) 13183–13192, <https://doi.org/10.1021/bi061288t>.
- [11] M. Gilbert, B. Albinsson, Photoinduced Charge and Energy Transfer in Molecular Wires, *Chem. Soc. Rev.* 44 (4) (2015) 845–862, <https://doi.org/10.1039/c4cs00221k>.
- [12] C. Huang, S. Barlow, S.R. Marder, Perylene-3,4,9,10-Tetracarboxylic Acid Diimides: Synthesis, Physical Properties, and Use in Organic Electronics, *J. Org. Chem.* 76 (8) (2011) 2386–2407, <https://doi.org/10.1021/jo2001963>.

- [13] F. Würthner, Perylene Bisimide Dyes as Versatile Building Blocks for Functional Supramolecular Architectures, *Chem. Commun.* 4 (14) (2004) 1564–1579, <https://doi.org/10.1039/b401630k>.
- [14] R. Gronheid, J. Hofkens, F. Köhn, T. Weil, E. Reuther, K. Müllen, F.C. De Schryver, Intramolecular Förster Energy Transfer in a Dendritic System at the Single Molecule Level, *J. Am. Chem. Soc.* 124 (11) (2002) 2418–2419, <https://doi.org/10.1021/ja017442a>.
- [15] S. Tiwari, N.C. Greenham, Charge Mobility Measurement Techniques in Organic Semiconductors, *Opt. Quantum Electron.* 41 (2) (2009) 69–89, <https://doi.org/10.1007/s11082-009-9323-0>.
- [16] E. Kozma, M. Catellani, Perylene Diimides Based Materials for Organic Solar Cells, *Dye. Pigment.* 98 (1) (2013) 160–179, <https://doi.org/10.1016/j.dyepig.2013.01.020>.
- [17] P. Singh, A. Hirsch, S. Kumar, Perylene Diimide-Based Chemosensors Emerging in Recent Years: From Design to Sensing, *TrAC - Trends Anal. Chem.* 138 (2021), <https://doi.org/10.1016/j.trac.2021.116237> 116237.
- [18] W.S. Shin, H.H. Jeong, M.K. Kim, S.H. Jin, M.R. Kim, J.K. Lee, J.W. Lee, Y.S. Gal, Effects of Functional Groups at Perylene Diimide Derivatives on Organic Photovoltaic Device Application, *J. Mater. Chem.* 16 (4) (2006) 384–390, <https://doi.org/10.1039/b512983d>.
- [19] M. Hecht, P. Leowanawat, T. Gerlach, V. Stepanenko, M. Stolte, M. Lehmann, F. Würthner, Self-Sorting Supramolecular Polymerization: Helical and Lamellar Aggregates of Tetra-Bay-Acyloxy Perylene Bisimide, *Angew. Chem.* 132 (39) (2020) 17232–17238, <https://doi.org/10.1002/ange.202006744>.
- [20] S. Ogi, V. Stepanenko, K. Sugiyasu, M. Takeuchi, F. Würthner, Mechanism of Self-Assembly Process and Seeded Supramolecular Polymerization of Perylene Bisimide Organogelator, *J. Am. Chem. Soc.* 137 (9) (2015) 3300–3307, <https://doi.org/10.1021/ja511952c>.
- [21] K. Suman, Y.M. Joshi, Microstructure and Soft Glassy Dynamics of an Aqueous Laponite Dispersion, *Langmuir* 34 (44) (2018) 13079–13103, <https://doi.org/10.1021/acs.langmuir.8b01830>.
- [22] S.R. Valandro, A.L. Poli, T.F.A. Correia, P.C. Lombardo, C.C. Schmitt, Photophysical Behavior of Isocyanine/Clay Hybrids in the Solid State, *Langmuir* 33 (4) (2017) 891–899, <https://doi.org/10.1021/acs.langmuir.6b03898>.
- [23] M. Grabolle, M. Starke, U. Resch-Genger, Highly Fluorescent Dye-Nanoclay Hybrid Materials Made from Different Dye Classes, *Langmuir* 32 (14) (2016) 3506–3513, <https://doi.org/10.1021/acs.langmuir.5b04297>.
- [24] R.A. Schoonheydt, L. Heughebaert, Clay Adsorbed Dyes: Methylene Blue on Laponite, *Clay Miner.* 27 (1) (1992) 91–100, <https://doi.org/10.1180/claymin.1992.027.1.09>.
- [25] E.H. Hill, Y. Zhang, D.G. Whitten, Aggregation of Cationic P-Phenylene Ethynyls on Laponite Clay in Aqueous Dispersions and Solid Films, *J. Colloid Interface Sci.* 449 (2015) 347–356, <https://doi.org/10.1016/j.jcis.2014.12.006>.
- [26] N.N. Herrera, J.M. Letoffe, J.L. Putaux, L. David, E. Bourgeat-Lami, Aqueous Dispersions of Silane-Functionalized Laponite Clay Platelets. A First Step toward the Elaboration of Water-Based Polymer/Clay Nanocomposites, *Langmuir* 20 (5) (2004) 1564–1571, <https://doi.org/10.1021/la0349267>.
- [27] P.A. Wheeler, J. Wang, J. Baker, L.J. Mathias, Synthesis and Characterization of Covalently Functionalized Laponite Clay, *Chem. Mater.* 17 (11) (2005) 3012–3018, <https://doi.org/10.1021/cm050306a>.
- [28] M. Park, I.K. Shim, E.Y. Jung, J.H. Choy, Modification of External Surface of Laponite by Silane Grafting, *J. Phys. Chem. Solids* 65 (2–3) (2004) 499–501, <https://doi.org/10.1016/j.jpcs.2003.10.031>.
- [29] T. Felbeck, K. Hoffmann, M.M. Lezhnina, U.H. Kynast, U. Resch-Genger, Fluorescent Nanoclays: Covalent Functionalization with Amine Reactive Dyes from Different Fluorophore Classes and Surface Group Quantification, *J. Phys. Chem. C* 119 (23) (2015) 12978–12987, <https://doi.org/10.1021/acs.jpcc.5b01482>.
- [30] H. Tröster, Untersuchungen Zur Protonierung von Perylen-3,4,9,10-Tetracarbonsäurealkalisalzen, *Dye. Pigment.* 4 (3) (1983) 171–177, [https://doi.org/10.1016/0143-7208\(83\)80015-1](https://doi.org/10.1016/0143-7208(83)80015-1).
- [31] L. Xu, V.R. Manda, L.E. McNamara, M.P. Jahan, H. Rathnayake, N.I. Hammer, Covalent Synthesis of Perylenediimide-Bridged Silsesquioxane Nanoribbons and Their Electronic Properties, *RSC Adv.* 4 (57) (2014) 30172–30179, <https://doi.org/10.1039/c4ra03260h>.
- [32] Y. Nagao, Synthesis and Properties of Perylene Pigments, *Prog. Org. Coatings* 31 (1–2) (1997) 43–49, [https://doi.org/10.1016/S0300-9440\(97\)00017-9](https://doi.org/10.1016/S0300-9440(97)00017-9).
- [33] H. Pálková, J. Madejová, M. Zimowska, E.M. Serwicka, Laponite-Derived Porous Clay Heterostructures: II. FTIR Study of the Structure Evolution, Microporous Mesoporous Mater. 127 (3) (2010) 237–244, <https://doi.org/10.1016/j.micromeso.2009.07.012>.
- [34] H.R. Cheng, Y. Qian, Intramolecular Fluorescence Resonance Energy Transfer in a Novel PDI-BODIPY Dendritic Structure: Synthesis, Hg<sup>2+</sup> Sensor and Living Cell Imaging, *Sens. Actuators, B Chem.* 219 (2015) 57–64, <https://doi.org/10.1016/j.snb.2015.04.086>.
- [35] P.A. Wheeler, J. Wang, L.J. Mathias, Poly(Methyl Methacrylate)/Laponite Nanocomposites: Exploring Covalent and Ionic Clay Modifications, *Chem. Mater.* 18 (17) (2006) 3937–3945, <https://doi.org/10.1021/cm0526361>.
- [36] E. Sebastian, M. Hariharan, Null Exciton-Coupled Chromophoric Dimer Exhibits Symmetry-Breaking Charge Separation, *J. Am. Chem. Soc.* 143 (34) (2021) 13769–13781, <https://doi.org/10.1021/jacs.1c05793>.
- [37] D. Magde, G.E. Rojas, P.G. Seybold, Solvent Dependence of the Fluorescence Lifetimes of Xanthene Dyes, *Photochem. Photobiol.* 70 (5) (1999) 737–744, <https://doi.org/10.1111/j.1751-1097.1999.tb08277.x>.
- [38] E. Krieg, E. Shirman, H. Weissman, E. Shimoni, S.G. Wolf, I. Pinkas, B. Rybtchinski, Supramolecular Gel Based on a Perylene Diimide Dye: Multiple Stimuli Responsiveness, Robustness, and Photofunction, *J. Am. Chem. Soc.* 131 (40) (2009) 14365–14373, <https://doi.org/10.1021/ja903938g>.
- [39] S. Samanta, D. Chaudhuri, Suppressing Excimers in H-Aggregates of Perylene Bisimide Folda-Dimer: Role of Dimer Conformation and Competing Assembly Pathways, *J. Phys. Chem. Lett.* 8 (14) (2017) 3427–3432, <https://doi.org/10.1021/acs.jpcclett.7b01338>.
- [40] J. Kapuscinski, DAPI: A DMA-Specific Fluorescent Probe, *Biotech. Histochem.* 70 (5) (1995) 220–233, <https://doi.org/10.3109/10520299509108199>.
- [41] M.L. Barcellona, G. Cardiel, E. Gratton, Time-Resolved Fluorescence of DAPI in Solution and Bound to Polydeoxynucleotides, *Biochem. Biophys. Res. Commun.* 170 (1) (1990) 270–280, [https://doi.org/10.1016/0006-291X\(90\)91270-3](https://doi.org/10.1016/0006-291X(90)91270-3).
- [42] Y. Imai, H. Abe, T. Goto, Y. Yoshimura, S. Kushiyama, H. Matsumoto, Orientational Ordering of Crystal Domains in Ionic Liquid Based Mixtures, *J. Phys. Chem. B* 112 (32) (2008) 9841–9846, <https://doi.org/10.1021/jp8014194>.
- [43] D. Chaudhuri, D. Li, Y. Che, E. Shafran, J.M. Gerton, L. Zang, J.M. Lupton, Enhancing Long-Range Exciton Guiding in Molecular Nanowires by H-Aggregation Lifetime Engineering, *Nano Lett.* 11 (2) (2011) 488–492, <https://doi.org/10.1021/nl1033039>.
- [44] S. Jatav, K.P. Furlan, J. Liu, E.H. Hill, Heterostructured Monolayer MoS<sub>2</sub> Nanoparticles toward Water-Dispersible Catalysts, *ACS Appl. Mater. Interfaces* 12 (17) (2020) 19813–19822, <https://doi.org/10.1021/acsaami.0c02246>.
- [45] J. Liu, S. Jatav, E.H. Hill, Few-Layer In<sub>2</sub>S<sub>3</sub> in Laponite Interlayers: A Colloidal Route Toward Heterostructured Nanohybrids with Enhanced Photocatalysis, *Chem. Mater.* 32 (23) (2020) 10015–10024, <https://doi.org/10.1021/acs.chemmater.0c03207>.
- [46] J. Liu, S. Jatav, P. Wessel, E.H. Hill, Templating Unidirectional Bismuth Oxide Crystal Growth with Layered Silicates for Enhanced Photocatalysis, *J. Phys. Chem. C* 126 (10) (2022) 4975–4983, <https://doi.org/10.1021/acs.jpcc.1c10853>.

### **3. 2D Nanomaterial-Directed Molecular Aggregation and Energy Transfer between Edge-Bound Donor-Acceptor pairs**

This Chapter has been published as:

Xiang, H., Valandro, S. R., & Hill, E. H. (2023). 2D Nanomaterial-Directed Molecular Aggregation and Energy Transfer between Edge-Bound Donor–Acceptor Pairs. *The Journal of Physical Chemistry C*, 127(31), 15416-15422.

Following previous published work. A PDI featuring a glycol terminal group was successfully covalently linked to the Lap edge surface. This hybrid formed H-aggregate with increasing water content as well, exhibiting enhanced aqueous dispersibility compared to the two hybrids obtained in the previous study. Subsequently, a NDI with a glycol terminal group was synthesized and linked to the Lap edge surface. This NDI-based hybrid formed excimers with increasing water content and exhibited AIE. The emission spectrum of the NDI-based hybrid overlapped effectively with the absorption spectrum of the PDI-based hybrid, resulting in FRET from the edge-bound donor of one Lap to the edge-bound acceptor of another upon their mixing.

Additionally, a cationic surfactant was introduced onto the basal surface of the hybrid, leading to the formation of pillared Lap discs. This structural modification resulted in enhanced FRET, likely due to the optimization of donor-acceptor distance and orientation. This work demonstrated the pioneering work of tethering NDI to Lap and developing a new PDI-based Lap with improved water dispersibility. FRET from the edge surface bound donor to the edge surface bound acceptor of Lap was observed. Furthermore, the incorporation of a cationic surfactant led to enhanced FRET, introducing a novel approach for optimizing FRET in a fixed system.



# 2D Nanomaterial-Directed Molecular Aggregation and Energy Transfer between Edge-Bound Donor–Acceptor Pairs

Hongxiao Xiang, Silvano R. Valandro, and Eric H. Hill\*



Cite This: *J. Phys. Chem. C* 2023, 127, 15416–15422



Read Online

ACCESS |



Metrics & More

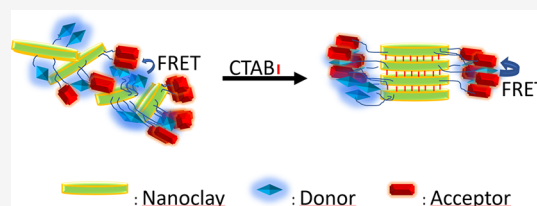


Article Recommendations



Supporting Information

**ABSTRACT:** Förster resonance energy transfer (FRET) is a phenomenon that is observed between an excited energy donor and ground-state acceptor in close proximity. The efficiency of FRET varies with the distance and orientation of the donor–acceptor pair, solvent, and other competing processes. Layered silicates, with their ability to stack in “pillars” with a certain interlayer spacing, present a useful platform to influence the interactions of edge-bound groups. In this study, asymmetric perylene and naphthalene diimides were grafted to the edge of the layered silicate Laponite, and their photophysical properties and aggregation behavior were studied in different compositions of water and dimethylformamide. FRET was observed from naphthalene diimide- to perylene diimide-functionalized Laponite, and pillaring of Laponite with a cationic surfactant led to significantly enhanced FRET, which was attributed to the reorientation of chromophores due to the organized stacking of pillared particles. This study reports how ordering of the discoidal layered silicate nanoparticles into organized stacks can tune the aggregation of edge-bound FRET pairs. This can aid in understanding donor–acceptor interactions at the interface of anisotropic nanomaterials and improve control over the distance and orientation of donor–acceptor pairs and resulting energy transfer processes. Furthermore, this is the first example of the attachment of naphthalene diimides to layered silicate edge sites. This study opens the door to further studies of geometry-dependent energy flows in inorganic–organic hybrid materials and will advance applications in sensing, energy, and molecular electronics.



FRET was observed from naphthalene diimide- to perylene diimide-functionalized Laponite, and pillaring of Laponite with a cationic surfactant led to significantly enhanced FRET, which was attributed to the reorientation of chromophores due to the organized stacking of pillared particles. This study reports how ordering of the discoidal layered silicate nanoparticles into organized stacks can tune the aggregation of edge-bound FRET pairs. This can aid in understanding donor–acceptor interactions at the interface of anisotropic nanomaterials and improve control over the distance and orientation of donor–acceptor pairs and resulting energy transfer processes. Furthermore, this is the first example of the attachment of naphthalene diimides to layered silicate edge sites. This study opens the door to further studies of geometry-dependent energy flows in inorganic–organic hybrid materials and will advance applications in sensing, energy, and molecular electronics.

## INTRODUCTION

Förster resonance energy transfer (FRET) is a phenomenon that occurs when a donor molecule, in an excited state, transfers its energy to an acceptor molecule that is in close proximity, typically within 10 nm.<sup>1,2</sup> To observe FRET, light emitted by the excited donor molecule must be absorbed by the acceptor molecule, and the orientation and relative position of the two molecules is also critical.<sup>1,3,4</sup> Other aspects, such as the lifetime of the excited state, competing processes involving intermolecular quenching, electron transfer reactions, intersystem crossing, and solvent composition will also affect the efficiency of the energy transfer rate.<sup>5,6</sup> Therefore, improving the FRET efficiency of donor–acceptor systems is crucial to expand applications, which include monitoring protein–protein interactions,<sup>7,8</sup> photovoltaics,<sup>9</sup> specifically dye-sensitized solar cells,<sup>10</sup> and organic light-emitting devices,<sup>11</sup> among others. Previous studies have primarily focused on donor–acceptor systems in which donor and acceptor molecules are linked via organic linkers. For example, Jia et al. used mixed organic linkers to control the distance and orientations of donor–acceptors pairs.<sup>12</sup> However, when the donor–acceptor molecules are connected via organic linkers, it is difficult to enhance the efficiency of FRET once the distance between the donor and acceptor is fixed, thereby limiting the possibilities for enhancement of FRET in such systems.<sup>12,13</sup>

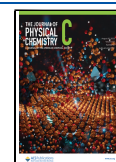
As hybrid systems offer various avenues to regulate the interactions between donor and acceptor molecules, layered

silicate-based hybrids represent an interesting system for studies of FRET at solid interfaces.<sup>14–16</sup> Nakayama et al. investigated energy transfer from an edge-bound pyrene to a cationic porphyrin on the basal surface of saponite, a discoidal layered silicate with a diameter of 50 nm, which led to some control over the aggregate structure, resulting in enhancement of FRET.<sup>17</sup> We recently used a layered silicate with half the edge length of saponite, Laponite (Lap), as a template for studying FRET between chromophores on its basal surface and edges. Lap is a synthetic layered silicate with an anionic basal surface and Si–OH groups on the edges.<sup>18,19</sup> Asymmetric perylene diimide (PDI) acceptors with different terminal groups were covalently attached via silanol coupling at the edges, and a cationic fluorophore was bound to the basal surface via ionic interactions, leading to FRET from the face-bound donor to the edge-bound acceptors.<sup>20</sup> However, the study of donor–acceptor interactions between molecules bound to the edges of adjacent layered silicate platelets had not been carried out. Furthermore, cationic surfactants can be

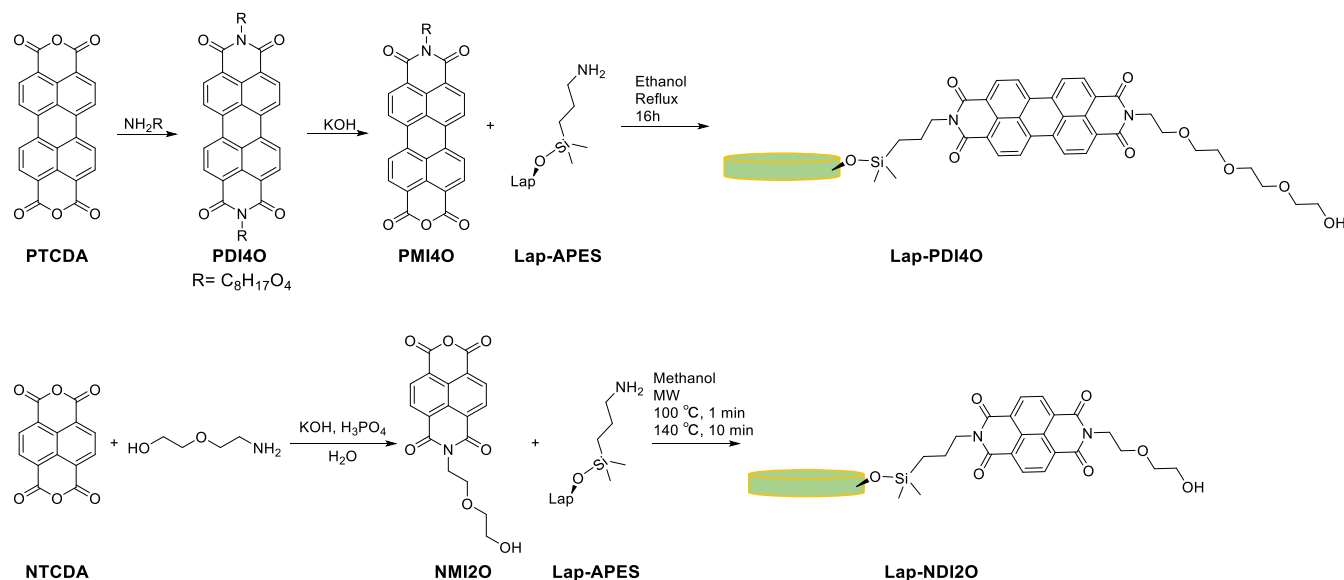
Received: July 6, 2023

Revised: July 19, 2023

Published: August 1, 2023



Scheme 1. Synthetic Routes for Lap-PDI4O and Lap-NDI2O



used to organize layered silicates into ordered “pillars” composed of vertically stacked particles resulting from the binding of the cationic surfactant to adjacent basal surfaces within the interlayer space and stabilized by the van der Waals interactions of the surfactant backbone.<sup>21–23</sup> Surfactant pillaring has previously been used as a strategy to improve molecular adsorption in the interlayer space,<sup>24,25</sup> for the growth of photocatalytic oxides, and more recently to direct the confined growth of semiconductors within the interlayer space.<sup>26–29</sup>

In this study, two different organic–inorganic hybrids were prepared by covalently attaching perylene diimide tetraethylene glycol (Lap-PDI4O) and naphthalene diimide diglycol (Lap-NDI2O) to the Lap edge (Scheme 1). Their optical properties and aggregation behavior were studied in solvents with varying water and DMF content. The addition of the Lap-PDI4O acceptor to the Lap-NDI2O donor resulted in the energy transfer between the two hybrids. Interestingly, significant enhancement of FRET was achieved by pillaring Lap with the cationic surfactant cetyltrimethylammonium bromide (CTAB), which is likely due to the ordered pillared structure improving overlap between adjacent NDI and PDI-modified Lap platelets. Interestingly, a DMF-rich solvent composition was found to lead to more efficient FRET without pillaring, whereas a water-rich solvent led to greater enhancement when pillaring, likely due to altered surfactant phase behavior in the presence of DMF. This study reports a method to extend control over donor–acceptor distance and orientation by alteration of the aggregation state of the inorganic component of the hybrid separately from that of the donor or acceptor. This suggests that control over interlayer spacing can serve as a sort of “molecular ruler” to study FRET processes between adjacent layered materials in a vertical stack. This not only improved energy transfer, but such an approach has the potential for broad applications in sensing, polarized emission, and photovoltaics.

## METHODS

The synthesis of two organic–inorganic hybrids, Lap-NDI2O and Lap-PDI4O, is summarized in Scheme 1.

Briefly, to synthesize Lap-PDI4O, a symmetric tetraethylene-glycol-substituted perylene diimide (PDI4O) was first synthesized according to the method described by Traeger et al.<sup>30</sup> Perylene-3,4,9,10-tetracarboxylic acid dianhydride was reacted with tetraethyleneglycol monoamine in dry DMF. In the next step, tetraethyleneglycol perylene monoimide (PMI4O) was synthesized through partial hydrolysis of tetraethyleneglycol perylene diimide (PDI4O) with potassium hydroxide.<sup>31,32</sup> Finally, PMI4O was reacted with amino-propyldimethylethoxysilane-modified Lap (Lap-APES), yielding the hybrid Lap-PDI4O.<sup>19,33</sup> To synthesize Lap-NDI2O, naphthalene diglycol monoimide (NMI2O) was first synthesized from naphthalene tetracarboxylic acid dianhydride according to the method described by Imato et al.<sup>34</sup> In the next step, NMI2O was reacted with Lap-APES to form Lap-NDI2O following a modification of the method by Prentice et al.<sup>35</sup> Detailed synthetic methods and characterization details are given in the Supporting Information.

## RESULTS AND DISCUSSION

Following the synthesis and purification of the hybrids Lap-NDI2O and Lap-PDI4O, Fourier-transformed infrared spectroscopy (FT-IR) was used to analyze the functional groups present (Figure 1). The peaks observed at 960 and 648 cm<sup>−1</sup> (Figure 1a) for both Lap-PDI4O and Lap-NDI2O were attributed to the Si–O stretching of the tetrahedral layers and O–Si–O bending modes of Lap.<sup>36</sup> The peaks at 3683 and 3679 cm<sup>−1</sup> were assigned to the stretching vibrations of hydroxyl groups in Si–OH and Mg–OH, respectively. After grafting organic molecules on the edge, a shift from 3679 to 3683 cm<sup>−1</sup> was observed (Figure S1a), due to the formation of Si–O–Si–C bonds on the edge surface of Lap.<sup>37</sup> Furthermore, the peaks at 2958 and 2929 cm<sup>−1</sup> (Figure S1b), which correspond to the methyl C–H stretching mode, indicated successful coupling to the Lap edge.<sup>36,37</sup> Additionally, a relatively weak peak at 1350 cm<sup>−1</sup> can be observed due to the C–N stretching mode of imides. The peaks at 1626 and 1657 cm<sup>−1</sup> in Lap-NDI2O (Figures 1b and S2a) and 1639 and 1689 cm<sup>−1</sup> in Lap-PDI4O (Figures 1b and S2b) correspond to N–C=O vibrations of rylene diimide,<sup>38,39</sup> further indicating

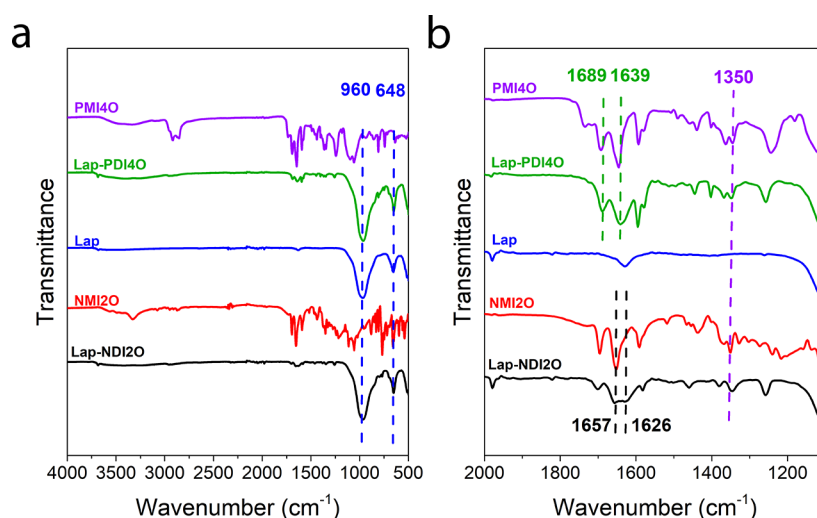


**Figure 1.** FT-IR spectra of pristine Laponite (Lap), perylene monoimide (PMI4O), perylene diimide-modified Laponite (Lap-PDI4O), naphthalene monoimide (NDI2O), and naphthalene diimide-modified Laponite (Lap-NDI2O).

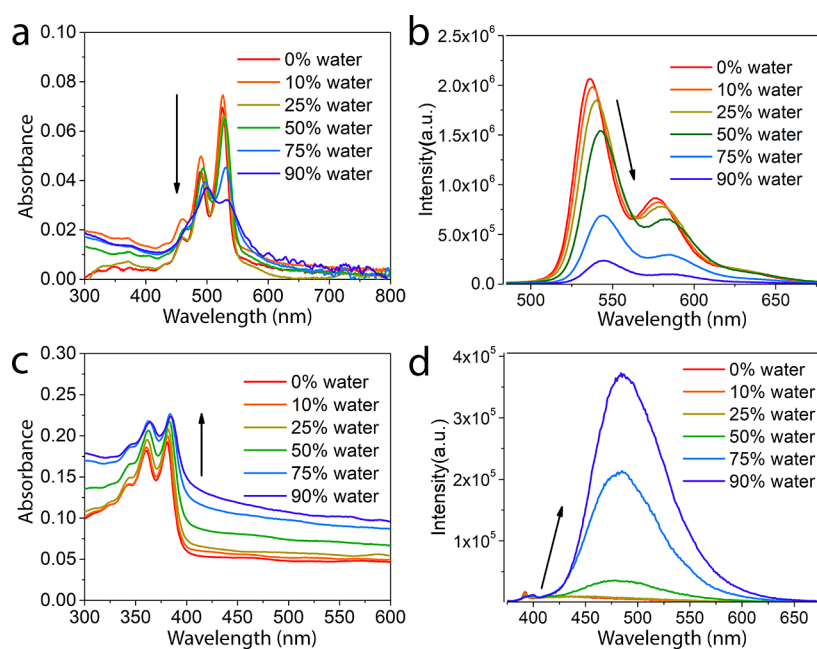


**Figure 2.** (a) UV-vis absorption and (b) fluorescence emission spectra of perylene-modified Laponite (Lap-PDI4O, 0.01 mg/mL,  $\lambda_{\text{exc}} = 470$  nm) in different DMF/water mixtures, and (c) UV-vis absorption and (d) fluorescence emission spectra of naphthalene-modified Laponite (Lap-NDI2O, 0.1 mg/mL,  $\lambda_{\text{exc}} = 350$  nm) in different DMF/water mixtures. Arrow indicates increasing water content.

successful linkage to the Lap edge. X-ray diffraction (XRD) measurements were carried out to determine the interlayer spacing of the hybrids (Figure S3). In comparison to APES-modified Lap, functionalization caused a slight increase of  $d_{001}$ , which corresponds to the basal spacing of Lap,<sup>40</sup> by 0.6 and 0.9 Å for NDI2O and PDI4O, respectively. This slight increase in interlayer spacing may result from the organic molecules on the edge bending toward the basal surface and causing steric hindrance.

Thermogravimetric analysis (TGA) was carried out to establish the degree of organic functionalization on Lap (Figure S4). TGA results showed a 2.47% mass loss for grafted perylene monoimide moieties in Lap-PDI4O from 150 to 600 °C compared to Lap-APES. Following the estimation by Wheeler et al.,<sup>19</sup> an estimated single Lap sheet mass of  $3.2 \times 10^{-18}$  g was used and each perylene monoimide residue (at

551.5 g/mol) corresponds to  $9.1 \times 10^{-22}$  g after reaction with APES, which are linked on the edge of Lap. Each Lap particle has gained  $8.1 \times 10^{-20}$  g organic content, indicating that approximately 88 perylenes are linked on the edge of Lap. Following the same calculation with Lap-NDI2O, a mass loss of 1.77% corresponds to approximately 102 naphthalenes on the edge of Lap. Felbeck et al. reported that the maximum number of reactive Si-OH groups is around 420 per particle.<sup>41</sup> The degree of functionalization below this maximum is likely due to the steric obstruction caused by bound perylene/naphthalenes.

The ground-state electronic properties of Lap-PDI4O and Lap-NDI2O were first studied via UV-vis absorption spectroscopy in DMF at room temperature (Figures 2a,c). Absorption spectra of Lap-PDI4O exhibited similar spectral characteristics compared to previous Lap-PDI hybrids,<sup>20</sup> with



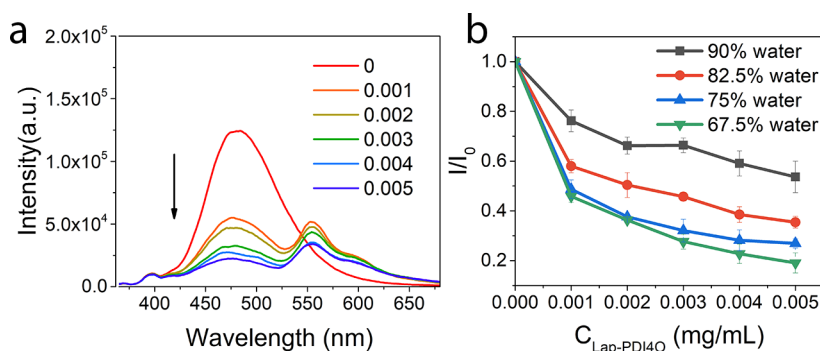


**Figure 3.** (a) Fluorescence emission spectra ( $\lambda_{\text{exc}} = 350$ ) of the donor Lap-NDI2O (0.1 mg/mL) with increasing concentration of the acceptor Lap-PDI4O in 67.5% water. Arrow indicates increasing acceptor concentration; (b)  $I/I_0$  at 485 nm as a function of the concentration of Lap-PDI4O in different DMF/water mixtures.

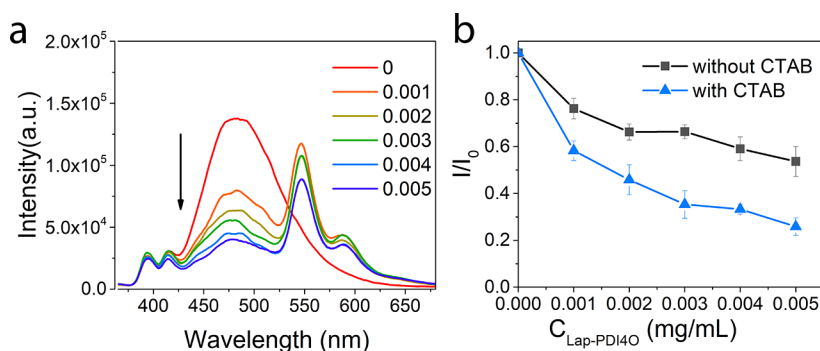


**Figure 4.** (a) Fluorescence emission spectra ( $\lambda_{\text{exc}} = 350$  nm) of donor Lap-NDI2O (0.1 mg/mL) with increasing concentrations of acceptor Lap-PDI4O (mg/mL) in 90% water following 24 h pillaring with 0.778  $\mu\text{mol}$  CTAB; arrow indicates increasing Lap-PDI4O concentration; (b)  $I/I_0$  at 485 nm as a function of the concentration of Lap-PDI4O in 90% water with CTAB pillaring (blue) and without (black).

the absorbance at 523 nm corresponding to  $S_0-S_1$  electronic transition and peaks at 459 and 488 nm corresponding to the vibronic progression of vinyl stretching in perylene.<sup>42</sup> For Lap-NDI2O in DMF, absorption bands at 342, 361, and 382 nm of monomeric naphthalene diimide molecules in solution were observed, which corresponded to 0–2, 0–1, and 0–0 transitions, respectively.<sup>43</sup> A typical emission spectrum was observed for Lap-PDI4O, featuring a band at 535 nm and a vibronic progression at 577 nm (Figure 2b).<sup>20</sup> The relative fluorescence quantum yield of Lap-PDI4O was determined to be 0.73, utilizing rhodamine B in ethanol as a standard (0.70).<sup>44</sup> A weak emission signal was observed for Lap-NDI2O in DMF, with maximum emission intensity at 392 nm, which could be attributed to the low quantum yield of Lap-NDI2O in DMF (Figure 2d).<sup>43,45</sup> Quinine sulfate in 0.5 M sulfuric acid was used as a standard (0.54) to determine the relative fluorescence quantum yield of Lap-NDI2O, which is 0.001. This low quantum efficiency of Lap-NDI2O in DMF is in agreement with previously reported values for non-core-substituted naphthalene diimides.<sup>46</sup>

UV–visible spectroscopy of Lap-PDI4O and Lap-NDI2O dispersions at different DMF/water ratios was performed. Lap-PDI4O (Figure 2a) exhibited a decrease in the intensity of the absorption bands accompanied by a hypsochromic shift of the  $\lambda_{\text{max}}$  of 26 nm as the water content increased. This blue shift is characteristic of bay-unsubstituted perylene diimides, which indicates a predominant H-type excitonic coupling.<sup>47</sup> The H-type excitonic coupling is more pronounced above 75% water content. The previous study with Lap-PDI hybrids terminated with oleyl and aspartic acid residues showed relatively high

degrees of aggregation with 25 and 50% water content, respectively.<sup>20</sup> The enhancement of PDI water dispersibility in the present study is due to the tetraethyleneglycol end-groups of Lap-PDI4O.<sup>32</sup> A decrease in fluorescence intensity was observed as the water content increased (Figure 2b), which was attributed to  $\pi-\pi$  stacking of perylene structures in an H-type aggregate.<sup>48–50</sup> The UV–vis spectra of Lap-NDI2O (Figure 2c) showed slightly redshifted absorption bands and an increase in the baseline absorbance due to scattering as the water content increased, indicating aggregation. As the water content increased, a new and intense band ( $\lambda_{\text{max}} = 485$  nm) appeared in the fluorescence spectra (Figure 2d), which was attributed to the formation of NDI excimers.<sup>43,51</sup> Such aggregation-induced emission is favorable for energy transfer applications in high water content systems.<sup>52</sup> These findings show that the aggregation behavior of Lap-NDI2O and Lap-PDI4O can be tuned by varying solvent compositions, which can be utilized in applications involving energy transfer mechanisms such as FRET.

The significant overlap between the excimer emission of Lap-NDI2O and the absorption of Lap-PDI4O indicates that the two hybrids are good candidates for studying energy transfer in water-rich solvents (Figure S8). Therefore, to study FRET between the two hybrids, Lap-NDI2O was employed as the donor and Lap-PDI4O as the acceptor. As Lap-PDI4O was added, a decrease in the intensity of the 485 nm excimer emission band of Lap-NDI2O, and emission at 550 nm, typical of Lap-PDI4O emission, was observed at solvent compositions above 67.5% water (Figures 3a and S9). These observations suggest energy transfer from the excimers of Lap-NDI2O to

Lap-PDI4O. Energy transfer efficiencies from Lap-NDI2O to Lap-PDI4O were calculated from the data shown in Figure 3b using the equation  $E = [1 - (F_{da}/F_d)]$ , where  $F_{da}$  and  $F_d$  represent the fluorescence intensities at 485 nm of the donor (Lap-NDI2O) in the presence and absence of the acceptor (Lap-PDI4O), respectively. An enhanced FRET efficiency was observed at increased DMF concentrations, ranging from 0.47 in 90% water to 0.81 in 67.5% water content with the presence of 5  $\mu\text{g/mL}$  Lap-PDI4O. While high DMF content led to the lower fluorescence intensity of Lap-NDI2O in the absence of the acceptor due to reduced excimer formation, increased FRET efficiency may result from reduced self-aggregation of edge-bound ligands of the same platelet. Simulations have shown that previously-studied hybrids can result in aggregate numbers above 5 at high water contents.<sup>53</sup>

To study the effect of Lap pillaring on FRET between edge-bound donors–acceptors, CTAB was added (0.778  $\mu\text{mol}$ ), corresponding to 1.2 times the cation exchange capacity of Lap, which was previously estimated to be 0.55–0.8 mequiv/g.<sup>18</sup> XRD showed that pillaring with CTAB shifted the  $d_{001}$  reflection to lower angles, indicating an expansion of the interlayer to a range of spacings up to  $\sim 2.3$  nm (Figure S3). In 90% water (Figure 4b), the efficiency of FRET from Lap-NDI2O to Lap-PDI4O is greatly enhanced after pillaring of the hybrids with CTAB, compared with non-pillared hybrids. Specifically, the FRET efficiency of pillared hybrids in the presence of 5  $\mu\text{g/mL}$  Lap-PDI4O in 90% water increased by 60% (Figure 4b). This is attributed to the ordered stacking of Lap attached to NDI2O and PDI4O, which leads to a more favorable spatial orientation of NDI2O with PDI4O molecules at the edge of Lap, thereby enhancing FRET. Furthermore, fluorescence lifetime measurements revealed a decrease from an average lifetime of 9.6 ns without added Lap-PDI4O, to 7 ns with 1  $\mu\text{g/mL}$  Lap-PDI4O, steadily decreasing to 3.5 ns with 5  $\mu\text{g/mL}$  Lap-PDI4O (Table S1), supporting increased energy transfer in the pillared system.

Pillaring with CTAB appears to result in reduced “random” aggregation of bound PDI and NDI, as indicated by the observation of emission peaks at 394 and 415 nm, corresponding to the NDI2O monomer,<sup>51</sup> and at 550 and 590 nm, which correspond to the PDI4O monomer (Figure 4a).<sup>32</sup> On the other hand, dispersions containing 67.5, 75, and 82.5% water showed an insignificant change in the FRET efficiency comparing pillared and non-pillared systems (Figure S10). The lack of a change of FRET efficiency upon pillaring in a solvent with increased DMF is attributed to an increased critical micelle concentration of the surfactant, which results in a lower degree of CTAB adsorption on the basal surfaces of Lap. del Mar Graciani et al. reported the critical micelle concentration of CTAB increased from 0.925 to 3.74  $\mu\text{mol/mL}$ , as DMF content increased from 0 to 20 wt %.<sup>54</sup> This, in turn, would reduce the effectiveness of pillaring and thus the influence on FRET efficiency.

## CONCLUSIONS

In this study, hybrids composed of perylene diimide- or naphthalene diimide-functionalized Laponite (Lap-PDI4O and Lap-NDI2O, respectively) were synthesized via silanol coupling of asymmetric diimides to the layered silicate edge. The optical properties and aggregation behavior of the hybrids in different compositions of a DMF/water mixed solvent were investigated with absorption and fluorescence spectroscopy, and aggregation of both hybrids was found to be affected by

the solvent composition. With increasing water content, PDIs of Lap-PDI4O formed H-aggregates, whereas NDIs of Lap-NDI2O formed excimers with typical aggregation-enhanced emission from NDIs. The tetraethylene glycol terminal group on the PDI of Lap-PDI4O improved the water dispersibility compared to succinate or oleyl-terminated PDI-modified Lap reported previously.<sup>20</sup> Subsequently, FRET from Lap-NDI2O to Lap-PDI4O was investigated by adding small amounts (1 to 5%) of the acceptor-bound Lap-PDI4O to a dispersion containing a greater amount of donor-bound Lap. In order to study the influence of modification of the Lap aggregation mode on the aggregation of the edge-bound ligands, the FRET efficiency upon pillaring of Lap by the cationic surfactant CTAB was studied. Enhanced FRET was observed from pillared Lap-NDI2O to Lap-PDI4O in a water-rich solvent compared to non-pillared hybrids, which suggests that the reorganization of the Lap aggregate structure via pillaring leads to better overlap between the edge-bound donor and acceptor molecules. This is likely due to the reduced formation of “random” aggregates and the stacked nature of the pillared Lap lending itself to interactions between adjacent donor- and acceptor-bound Lap discs. Interestingly, when pillaring was carried out in solvent compositions with DMF greater than 17.5%, there was no significant FRET enhancement from pillaring due to the increased critical micelle concentration of CTAB under these conditions.

In summary, this study establishes two organic–inorganic hybrids composed of perylene and naphthalene diimides bound to the edge sites of layered silicates and represents the first example of the attachment of naphthalene diimides to layered silicate edges. The use of ethylene glycol terminations also provided improved aqueous dispersibility compared to previous study. Furthermore, the capability for independent modification of the layered silicate edges and faces provided the means to study how pillaring of the layered silicate template with a cationic surfactant influenced donor–acceptor interactions via FRET. These results suggest that modification of the interlayer spacing between the basal surfaces of pillared layered silicates by changing surfactant or ionic strength may provide a sort of “molecular ruler” to study how interlayer spacing distances influence the energy transfer in such edge-bound donor–acceptor systems.<sup>55–57</sup> This effect may also have potential use in highly aggregated systems to achieve efficient FRET, which could be of particular use in applications in photovoltaics, organic light emitting devices, and sensors.<sup>9,11,58</sup> Future investigations should focus on designing different organic–inorganic donor–acceptor pairs with different tendencies toward aggregation and various solvent dispersibilities, and exploring the effect of interlayer spacing on the donor–acceptor coupling of edge-bound moieties.

## ASSOCIATED CONTENT

### Supporting Information

The Supporting Information is available free of charge at <https://pubs.acs.org/doi/10.1021/acs.jpcc.3c04555>.

Detailed synthetic methods, additional fluorescence spectra, FT-IR spectra, XRD spectra, <sup>1</sup>H NMR spectra, TGA curves, and tabulated fluorescence lifetimes (PDF)

## AUTHOR INFORMATION

### Corresponding Author

Eric H. Hill — Institute of Physical Chemistry, University of Hamburg, 20146 Hamburg, Germany; The Hamburg Center for Ultrafast Imaging (CUI), 22761 Hamburg, Germany; [orcid.org/0000-0003-3063-1447](https://orcid.org/0000-0003-3063-1447); Email: [eric.hill@chemie.uni-hamburg.de](mailto:eric.hill@chemie.uni-hamburg.de)

### Authors

Hongxiao Xiang — Institute of Physical Chemistry, University of Hamburg, 20146 Hamburg, Germany

Silvano R. Valandro — Institute of Physical Chemistry, University of Hamburg, 20146 Hamburg, Germany; The Hamburg Center for Ultrafast Imaging (CUI), 22761 Hamburg, Germany; [orcid.org/0000-0002-4652-768X](https://orcid.org/0000-0002-4652-768X)

Complete contact information is available at:  
<https://pubs.acs.org/10.1021/acs.jpcc.3c04555>

### Notes

The authors declare no competing financial interest.

## ACKNOWLEDGMENTS

This research was funded by the Deutsche Forschungsgemeinschaft (DFG)—project ID 447787198. E.H.H. and S.R.V. are supported by the Cluster of Excellence “Advanced Imaging of Matter” of the DFG—EXC 2056—project ID 390715994. This research was funded in part by the DAAD from the funds of the German Federal Ministry of Education and Research (BMBF), under the MOPGA-GRI program (57565165). We gratefully acknowledge the central measurement facilities of the Chemistry Department of the University of Hamburg for providing elemental analysis, mass spectrometry measurements, and access to NMR equipment.

## REFERENCES

- (1) Kaur, A.; Kaur, P.; Ahuja, S. Förster Resonance Energy Transfer (FRET) and Applications Thereof. *Anal. Methods* **2020**, *12*, 5532–5550.
- (2) Förster, T. Zwischenmolekulare Energiewanderung Und Fluoreszenz. *Ann. Phys.* **1948**, *437*, 55–75.
- (3) Sahoo, H. Förster Resonance Energy Transfer—A Spectroscopic Nanoruler: Principle and Applications. *J. Photochem. Photobiol., C* **2011**, *12*, 20–30.
- (4) Saini, S.; Srinivas, G.; Bagchi, B. Distance and Orientation Dependence of Excitation Energy Transfer: From Molecular Systems to Metal Nanoparticles. *J. Phys. Chem. B* **2009**, *113*, 1817–1832.
- (5) Wu, J.; Liu, F.; Ma, J.; Silbey, R. J.; Cao, J. Efficient Energy Transfer in Light-Harvesting Systems: Quantum-Classical Comparison, Flux Network, and Robustness Analysis. *J. Chem. Phys.* **2012**, *137*, 174111.
- (6) Dietrich, A.; Buschmann, V.; Müller, C.; Sauer, M. Fluorescence Resonance Energy Transfer FRET and Competing Processes in Donor-acceptor Substituted DNA Strands: A Comparative Study of Ensemble and Single-Molecule Data. *Rev. Mol. Biotechnol.* **2002**, *82*, 211–231.
- (7) Miyawaki, A.; Niino, Y. Molecular Spies for Bioimaging-Fluorescent Protein-Based Probes. *Mol. Cell* **2015**, *58*, 632–643.
- (8) Evers, T. H.; Van Dongen, E. M. W. M.; Faesen, A. C.; Meijer, E. W.; Merkx, M. Quantitative Understanding of the Energy Transfer between Fluorescent Proteins Connected via Flexible Peptide Linkers. *Biochemistry* **2006**, *45*, 13183–13192.
- (9) Hedley, G. J.; Ruseckas, A.; Samuel, I. D. W. Light Harvesting for Organic Photovoltaics. *Chem. Rev.* **2017**, *117*, 796–837.
- (10) Basham, J. I.; Mor, G. K.; Grimes, C. A. Förster Resonance Energy Transfer in Dye-Sensitized Solar Cells. *ACS Nano* **2010**, *4*, 1253–1258.
- (11) Hong, G.; Gan, X.; Leonhardt, C.; Zhang, Z.; Seibert, J.; Busch, J. M.; Bräse, S. A Brief History of OLEDs—Emitter Development and Industry Milestones. *Adv. Mater.* **2021**, *33*, 2005630.
- (12) Jia, J.; Gutiérrez-Arzaluz, L.; Shekhah, O.; Alsadun, N.; Czaban-Jóźwiak, J.; Zhou, S.; Bakr, O. M.; Mohammed, O. F.; Eddaoudi, M. Access to Highly Efficient Energy Transfer in Metal-Organic Frameworks via Mixed Linkers Approach. *J. Am. Chem. Soc.* **2020**, *142*, 8580–8584.
- (13) Adhikari, S.; Mandal, S.; Ghosh, A.; Guria, S.; Das, D. Tuning of Donor-Acceptor Linker in Rhodamine-Coumarin Conjugates Leads Remarkable Solvent Dependent FRET Efficiency for Al<sup>3+</sup> Imaging in HeLa Cells. *Sens. Actuators, B* **2016**, *234*, 222–230.
- (14) Bujdák, J. Hybrid Systems Based on Organic Dyes and Clay Minerals: Fundamentals and Potential Applications. *Clay Miner.* **2015**, *50*, 549–571.
- (15) Bujdák, J. The Effects of Layered Nanoparticles and Their Properties on the Molecular Aggregation of Organic Dyes. *J. Photochem. Photobiol., C* **2018**, *35*, 108–133.
- (16) Bujdák, J. Resonance Energy Transfer in Hybrid Systems of Photoactive Dye Molecules and Layered Inorganics. *Struct. Bonding* **2020**, *183*, 205–250.
- (17) Nakayama, A.; Mizuno, J.; Ohtani, Y.; Shimada, T.; Takagi, S. Elucidation of the Adsorption Distribution of Cationic Porphyrin on the Inorganic Surface by Energy Transfer as a Molecular Ruler. *J. Phys. Chem. C* **2018**, *122*, 4365–4371.
- (18) Suman, K.; Joshi, Y. M. Microstructure and Soft Glassy Dynamics of an Aqueous Laponite Dispersion. *Langmuir* **2018**, *34*, 13079–13103.
- (19) Wheeler, P. A.; Wang, J.; Baker, J.; Mathias, L. J. Synthesis and Characterization of Covalently Functionalized Laponite Clay. *Chem. Mater.* **2005**, *17*, 3012–3018.
- (20) Xiang, H.; Valandro, S. R.; Hill, E. H. Layered Silicate Edge-Linked Perylene Diimides: Synthesis, Self-Assembly and Energy Transfer. *J. Colloid Interface Sci.* **2023**, *629*, 300–306.
- (21) Najafi, H.; Farajfaed, S.; Zolgharnian, S.; Mosavi Mirak, S. H.; Asasian-Kolur, N.; Sharifian, S. A Comprehensive Study on Modified-Pillared Clays as an Adsorbent in Wastewater Treatment Processes. *Process Saf. Environ. Prot.* **2021**, *147*, 8–36.
- (22) Karaca, S.; Gürses, A.; Korucu, M. E. Investigation of the Orientation of CTA + Ions in the Interlayer of CTAB Pillared Montmorillonite. *J. Chem.* **2013**, *2013*, 274838.
- (23) Yang, R. T.; Baksh, M. S. A. Pillared Clays as a New Class of Sorbents for Gas Separation. *AIChE J.* **1991**, *37*, 679–686.
- (24) Michot, L. J.; Pinnavaia, T. J. Adsorption of Chlorinated Phenols from Aqueous Solution by Surfactant-Modified Pillared Clays. *Clays Clay Miner.* **1991**, *39*, 634–641.
- (25) Bouras, O.; Bollinger, J. C.; Baudu, M.; Khalaf, H. Adsorption of Diuron and Its Degradation Products from Aqueous Solution by Surfactant-Modified Pillared Clays. *Appl. Clay Sci.* **2007**, *37*, 240–250.
- (26) Gil, A.; Gandía, L. M.; Vicente, M. A. Recent Advances in the Synthesis and Catalytic Applications of Pillared Clays. *Catal. Rev.—Sci. Eng.* **2000**, *42*, 145–212.
- (27) Liu, J.; Jatav, S.; Hill, E. H. Few-Layer In<sub>2</sub>S<sub>3</sub> in Laponite Interlayers: A Colloidal Route Toward Heterostructured Nanohybrids with Enhanced Photocatalysis. *Chem. Mater.* **2020**, *32*, 10015–10024.
- (28) Jatav, S.; Furlan, K. P.; Liu, J.; Hill, E. H. Heterostructured Monolayer MoS<sub>2</sub> Nanoparticles toward Water-Dispersible Catalysts. *ACS Appl. Mater. Interfaces* **2020**, *12*, 19813–19822.
- (29) Jatav, S.; Liu, J.; Herber, M.; Hill, E. H. Facet Engineering of Bismuth Molybdate via Confined Growth in a Nanoscale Template toward Water Remediation. *ACS Appl. Mater. Interfaces* **2021**, *13*, 18713–18723.
- (30) Traeger, H.; Sagara, Y.; Kiebal, D. J.; Schrettl, S.; Weder, C. Folded Perylene Diimide Loops as Mechanoresponsive Motifs. *Angew. Chem., Int. Ed.* **2021**, *60*, 16191–16199.



- (31) Nagao, Y. Synthesis and Properties of Perylene Pigments. *Prog. Org. Coat.* **1997**, *31*, 43–49.
- (32) Huang, C.; Barlow, S.; Marder, S. R. Perylene-3,4,9,10-Tetracarboxylic Acid Diimides: Synthesis, Physical Properties, and Use in Organic Electronics. *J. Org. Chem.* **2011**, *76*, 2386–2407.
- (33) Xu, L.; Manda, V. R.; McNamara, L. E.; Jahan, M. P.; Rathnayake, H.; Hammer, N. I. Covalent Synthesis of Perylene-diimide-Bridged Silsesquioxane Nanoribbons and Their Electronic Properties. *RSC Adv.* **2014**, *4*, 30172–30179.
- (34) Imato, K.; Yamanaka, R.; Nakajima, H.; Takeda, N. Fluorescent Supramolecular Mechanophores Based on Charge-Transfer Interactions. *Chem. Commun.* **2020**, *56*, 7937–7940.
- (35) Prentice, G. M.; Emmett, L. M.; Zhu, H.; Kociok-Köhn, G.; Pantos, G. D. Thermally Stable Recyclable Naphthalenediimide-Siloxane Polymers. *Supramol. Chem.* **2016**, *28*, 161–167.
- (36) Pálková, H.; Madejová, J.; Zimowska, M.; Serwicka, E. M. Laponite-Derived Porous Clay Heterostructures: II. FTIR Study of the Structure Evolution. *Microporous Mesoporous Mater.* **2010**, *127*, 237–244.
- (37) Herrera, N. N.; Letoffe, J. M.; Reymond, J. P.; Bourgeat-Lami, E. Silylation of Laponite Clay Particles with Monofunctional and Trifunctional Vinyl Alkoxysilanes. *J. Mater. Chem.* **2005**, *15*, 863–871.
- (38) Cheng, H. R.; Qian, Y. Intramolecular Fluorescence Resonance Energy Transfer in a Novel PDI-BODIPY Dendritic Structure: Synthesis, Hg<sup>2+</sup> Sensor and Living Cell Imaging. *Sens. Actuators, B* **2015**, *219*, 57–64.
- (39) Kar, H.; Molla, M. R.; Ghosh, S. Two-Component Gelation and Morphology-Dependent Conductivity of a Naphthalene-Diimide (NDI)  $\pi$ -System by Orthogonal Hydrogen Bonding. *Chem. Commun.* **2013**, *49*, 4220–4222.
- (40) Daniel, L. M.; Frost, R. L.; Zhu, H. Y. Edge-Modification of Laponite with Dimethyl-Octylmethoxysilane. *J. Colloid Interface Sci.* **2008**, *321*, 302–309.
- (41) Felbeck, T.; Hoffmann, K.; Lezhnina, M. M.; Kynast, U. H.; Resch-Genger, U. Fluorescent Nanoclays: Covalent Functionalization with Amine Reactive Dyes from Different Fluorophore Classes and Surface Group Quantification. *J. Phys. Chem. C* **2015**, *119*, 12978–12987.
- (42) Sebastian, E.; Hariharan, M. Null Exciton-Coupled Chromophoric Dimer Exhibits Symmetry-Breaking Charge Separation. *J. Am. Chem. Soc.* **2021**, *143*, 13769–13781.
- (43) Kumari, N.; Naqvi, S.; Ahuja, M.; Bhardwaj, K.; Kumar, R. Facile Synthesis of Naphthalene Diimide (NDI) Derivatives: Aggregation-Induced Emission, Photophysical and Transport Properties. *J. Mater. Sci.: Mater. Electron.* **2020**, *31*, 4310–4322.
- (44) Divya, K. P.; Savithri, S.; Ajayaghosh, A. A Fluorescent Molecular Probe for the Identification of Zinc and Cadmium Salts by Excited State Charge Transfer Modulation. *Chem. Commun.* **2014**, *50*, 6020–6022.
- (45) Ozser, M. E.; Uzun, D.; Elci, I.; Icil, H.; Demuth, M. Novel Naphthalene Diimides and a Cyclophane Thereof: Synthesis, Characterization, Photophysical and Electrochemical Properties. *Photochem. Photobiol. Sci.* **2003**, *2*, 218–223.
- (46) Maniam, S.; Higginbotham, H. F.; Bell, T. D. M.; Langford, S. J. Harnessing Brightness in Naphthalene Diimides. *Chem.—Eur. J.* **2019**, *25*, 7044–7057.
- (47) Gershberg, J.; Fennel, F.; Rehm, T. H.; Lochbrunner, S.; Würthner, F. Anti-Cooperative Supramolecular Polymerization: A New K2-K Model Applied to the Self-Assembly of Perylene Bisimide Dye Proceeding via Well-Defined Hydrogen-Bonded Dimers. *Chem. Sci.* **2016**, *7*, 1729–1737.
- (48) Seo, J.; Khazi, M. I.; Bae, K.; Kim, J.-M.; Seo, J.; Khazi, M. I.; Bae, K.; Kim, J.-M. Temperature-Controlled Pathway Complexity in Self-Assembly of Perylene Diimide-Polydiacetylene Supramolecule. *Small* **2023**, *19*, 2206428.
- (49) Samanta, S.; Chaudhuri, D. Suppressing Excimers in H-Aggregates of Perylene Bisimide Folda-Dimer: Role of Dimer Conformation and Competing Assembly Pathways. *J. Phys. Chem. Lett.* **2017**, *8*, 3427–3432.
- (50) Würthner, F.; Saha-Möller, C. R.; Fimmel, B.; Ogi, S.; Leowanawat, P.; Schmidt, D. Perylene Bisimide Dye Assemblies as Archetype Functional Supramolecular Materials. *Chem. Rev.* **2016**, *116*, 962–1052.
- (51) Boer, S. A.; Cox, R. P.; Beards, M. J.; Wang, H.; Donald, W. A.; Bell, T. D. M.; Turner, D. R. Elucidation of Naphthalene Diimide Metallomacrocycles and Catenanes by Solvent Dependent Excimer and Exciplex Emission. *Chem. Commun.* **2019**, *55*, 663–666.
- (52) De, S.; Das, G. Exploring the Aggregation and Light-Harvesting Aptitude of Naphthalimide-Based Amphiphile and Non-Amphiphile AIEgen. *Langmuir* **2022**, *38*, 6158–6163.
- (53) Hill, E. Investigating Solvent-Induced Aggregation in Edge-Functionalized Layered Silicate Clays via All-Atom Molecular Dynamics Simulations. *ChemRxiv* **2022**, DOI: 10.26434/chemrxiv-2022-2spqk.
- (54) del Mar Graciani, M.; Muñoz, M.; Rodríguez, A.; Moyá, M. L. Water-N,N-Dimethylformamide Alkyltrimethylammonium Bromide Micellar Solutions: Thermodynamic, Structural, and Kinetic Studies. *Langmuir* **2005**, *21*, 3303–3310.
- (55) Osman, M. A.; Ploetze, M.; Skrabal, P. Structure and Properties of Alkylammonium Monolayers Self-Assembled on Montmorillonite Platelets. *J. Phys. Chem. B* **2004**, *108*, 2580–2588.
- (56) Sun, J.; Zhuang, G.; Wu, S.; Zhang, Z. Structure and Performance of Anionic-Cationic-Organic-Montmorillonite in Different Organic Solvents. *RSC Adv.* **2016**, *6*, 54747–54753.
- (57) Liao, L.; Lv, G.; Cai, D.; Wu, L. The Sequential Intercalation of Three Types of Surfactants into Sodium Montmorillonite. *Appl. Clay Sci.* **2016**, *119*, 82–86.
- (58) Wu, L.; Huang, C.; Emery, B. P.; Sedgwick, A. C.; Bull, S. D.; He, X. P.; Tian, H.; Yoon, J.; Sessler, J. L.; James, T. D. Förster Resonance Energy Transfer (FRET)-Based Small-Molecule Sensors and Imaging Agents. *Chem. Soc. Rev.* **2020**, *49*, 5110–5139.

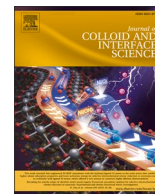
## 4. Cascade Förster resonance energy transfer between layered silicate edge-linked chromophores

This Chapter has been published as:

Xiang, H., Hill, E. H. (2024). Cascade Förster Resonance Energy Transfer Between Layered Silicate Edge-linked Chromophores. *Journal of Colloid and Interface Science*, 676, 543-550.

In the previous study, NDI-modified Lap displayed AIE and served as a donor for the FRET process. Building on this, we utilized the NDI-modified Lap as a donor and introduced cationic R6G on the Lap basal surface via ion exchange as an acceptor. Moreover, a Nile red derivative was successfully covalently linked to the Lap edge surface, exhibiting solvatochromism upon the characterization, indicating solvent-tunable optical properties.

Upon combining the hybrids containing NDIs, R6G, and Nile red derivative, a two-step FRET cascade from the edge surface bound NDIs to the basal surface located R6G and then to another edge surface bound Nile red was observed. Varying solvent composition led to enhanced cascade FRET. This research achieved a two-step FRET cascade system between modified anisotropic surfaces of Lap and introduced a novel model for Lap-based cascade FRET systems for future investigation.



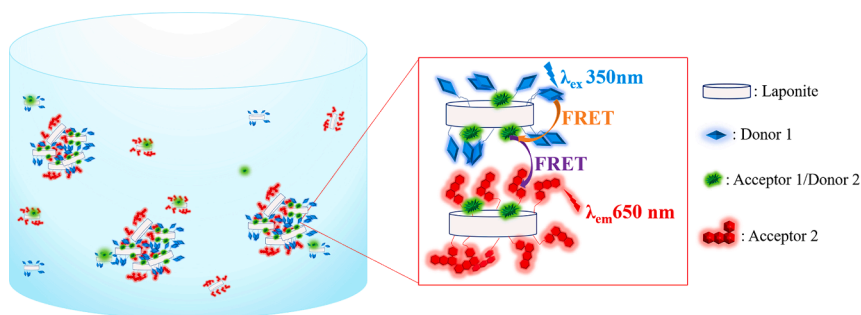
## Cascade Förster resonance energy transfer between layered silicate edge-linked chromophores

Hongxiao Xiang<sup>a</sup>, Eric H. Hill<sup>a,b,\*</sup>

<sup>a</sup> Institute of Physical Chemistry, University of Hamburg, Grindelallee 117, 20146 Hamburg, Germany

<sup>b</sup> The Hamburg Center for Ultrafast Imaging (CUI), Luruper Chausee 149, 22761 Hamburg, Germany

### GRAPHICAL ABSTRACT



### ARTICLE INFO

#### Keywords:

Förster resonance energy transfer cascade  
Inorganic/Organic Nanohybrid  
Laponite  
Layered silicate clay  
2D Materials

### ABSTRACT

Förster resonance energy transfer (FRET) serves as a critical mechanism to study intermolecular interactions and the formation of macromolecular assemblies. Cascade FRET is a multi-step FRET process which can overcome limitations associated with traditional single-step FRET. Herein, a novel organic–inorganic hybrid composed of a Nile red derivative attached to the edge of the layered silicate clay Laponite (Lap-NR) was used to facilitate cascade FRET between Laponite sheets. Utilizing naphthalene-diimide edge-modified Laponite (Lap-NDI) as the initial donor, Rhodamine 6G on the basal surface of Laponite as the first acceptor, and Lap-NR as the second acceptor, cascade FRET was achieved. The influence of solvent composition in a DMF/water mixture on cascade FRET was investigated, revealing that a higher water content led to an enhancement of the cascade FRET process, which is attributed to increased aggregation-induced emission of Lap-NDI and the enhanced quantum yield of R6G in water. This study provides a unique approach to achieve cascade FRET by taking advantage of the anisotropic surface chemistry of a two-dimensional nanomaterial, providing a colloiddally-driven alternative with improved tunability compared to macromolecular routes. The flexibility and simplicity of this approach will advance the state of the art of organic–inorganic hybrids for applications in optoelectronics, sensors, and hybrid photovoltaics.

\* Corresponding author at: Institute of Physical Chemistry, University of Hamburg, Grindelallee 117, 20146 Hamburg, Germany.

E-mail address: [eric.hill@uni-hamburg.de](mailto:eric.hill@uni-hamburg.de) (E.H. Hill).

<https://doi.org/10.1016/j.jcis.2024.07.106>

Received 24 May 2024; Received in revised form 3 July 2024; Accepted 12 July 2024

Available online 15 July 2024

0021-9797/© 2024 The Authors. Published by Elsevier Inc. This is an open access article under the CC BY-NC license (<http://creativecommons.org/licenses/by-nc/4.0/>).

## 1. Introduction

Förster resonance energy transfer (FRET) is a distance-dependent physical optical phenomenon, that describes the energy transferred from an excited molecule (donor) to another molecule (acceptor) through non-radiative dipole–dipole coupling [1–4]. Unlike Dexter-type energy transfer, which describes direct electron exchange within a sub-nanometric distance between molecules, FRET is applied to study longer-range molecular energy transfer, typically between 1 nm to 10 nm [5,6]. FRET serves as a powerful tool for analyzing macromolecular interactions in diverse fields, such as biological sensors, light harvesting in dye-sensitized solar cells, and metallic nanomaterial-involved quantum information storage devices [7–13]. However, FRET efficiency is limited when the molecule's interaction distance exceeds 10 nm. The molecular orientation of donor and acceptor, and aspects such as the overlap of donor emission and acceptor absorption, and the donor emission lifetime, also significantly impact the efficiency of FRET [4,14]. Researchers have employed various strategies to address the challenges inherent in FRET studies [15,16]. Supramolecular strategies such as fluorescent amphiphile-based nanoparticles [17], macrocyclic host–guest systems [18], and the utilization of metal coordinated scaffolds [19], and biomolecular scaffolds [20], have shown the potential to address these challenges by controlling the relative distance and orientation between donors and acceptors, to enhance FRET. On the other hand, the control over donor–acceptor overlap within the backbone structure of individual polymer chains containing both donors and acceptors has also shown promise as a method to improve FRET [21]. However, these strategies suffer from several limitations. For example, environmental variations, such as fluctuations in pH values, changes in salt concentrations, and mechanical stress can significantly impact the structural stability of systems based on non-covalent interactions, such as micellar systems [22]. On the other hand, macromolecular systems based on covalent interactions, such as those composed of scaffolds and polymer chains, face challenges with poor dynamic tunability of chromophore interactions, complicated multi-step synthesis, which potentially results in correspondingly high material costs [23,24].

The implementation of two-dimensional (2D) nanoparticle templates to mediate donor–acceptor interactions is a promising strategy for enhancing FRET efficiency. For instance, the immobilization of dyes on Laponite basal surfaces through ion exchange led to an enhancement in FRET between the two dyes [25], whereas FRET from dye-modified Saponite sheet edges to porphyrins bound to the basal surface has been reported [26]. The aggregation of clay nanosheets can be adjusted to tune the energy transfer efficiency, and chromophores can be independently attached to the anisotropic surfaces of smectite clays in the layered silicate family [26–29]. Laponite, a disc-like silica clay with a diameter of 25 nm and approximately 1 nm thickness, exhibits negative charges on its basal surface and neutral or partially positive charges on its edges when dispersed in an aqueous medium [28,30,31]. Recently, we achieved FRET from 4',6-Diamidino-2-phenylindole (DAPI) bound to the basal surface to an edge-bound perylene diimide acceptor [27]. Furthermore, efficient FRET from a Laponite edge-linked naphthalene donor to a Laponite edge-linked perylene acceptor as achieved, and the significant role of the aggregation state of the clay sheets on FRET from adjacent edge-bound chromophores was uncovered via the ordered stacking of Laponite sheets due to “pillaring” with alkylammonium surfactant [29]. However, both studies were limited to single-step FRET, where the donor emission was limited to 600 nm or below, restricting the range of viable donor–acceptor pairs.

Multi-step FRET, or cascade FRET, has emerged as an effective strategy to overcome the limitations associated with intermolecular distance and insufficient spectral overlap between two chromophores in conventional FRET [14,32–35]. In a cascade FRET, multiple acceptors are employed, allowing the initial excess energy from the donor to be transferred across a broader spectral window in comparison to conventional single-step FRET. By offering a greater selection of

donor–acceptor pairs and extending the permissible distances, cascade FRET significantly broadens the applicability of FRET. Chen et al. conducted a comprehensive review of cascade FRET within supramolecular systems [16]. Various systems have been explored, with examples including the facilitation of cascade FRET processes in supramolecular systems through non-covalent molecular interactions. For instance, flexible dendrimer structures have been found to promote cascade FRET processes by preventing aggregation-induced self-quenching [36]. Conversely, the utilization of dye aggregation has been demonstrated to create a cascade FRET system, resulting in a remarkable 200 nm shift between the excitation and emission wavelengths [33].

Herein, we describe a two-step cascade FRET system that takes advantage of Laponite's anisotropic surface chemistry. A naphthalene diimide-based chromophore bound to the Laponite edge (Lap-NDI) was employed as the initial donor. Rhodamine 6G (R6G) was non-covalently bound to the Laponite basal surface through ion exchange, acting as the first acceptor. Then, a novel hybrid material composed of a Nile red derivative linked to the Laponite edge (Lap-NR) was synthesized, which serves as the second acceptor in the FRET cascade. Single-step FRET between individual donor–acceptor pairs in this system was investigated, followed by the investigation of the FRET cascade in the complete three-component system. Furthermore, the influence of solvent composition on cascade FRET efficiency was examined by varying the proportions of DMF and water. This study shows that 2D nanomaterial templates with anisotropic surface chemistry can be utilized to achieve cascade FRET, extending the Stokes shift to near-infrared wavelengths. The capability to independently modify the basal surface and edge of Laponite particles with viable donor–acceptor pairs, can potentially achieve further extension to multi-step cascade FRET. Overall, this approach can simplify the design of energy transfer-based devices, and advance the state of the art of organic–inorganic hybrids for sensors, optoelectronics, and photovoltaic applications.

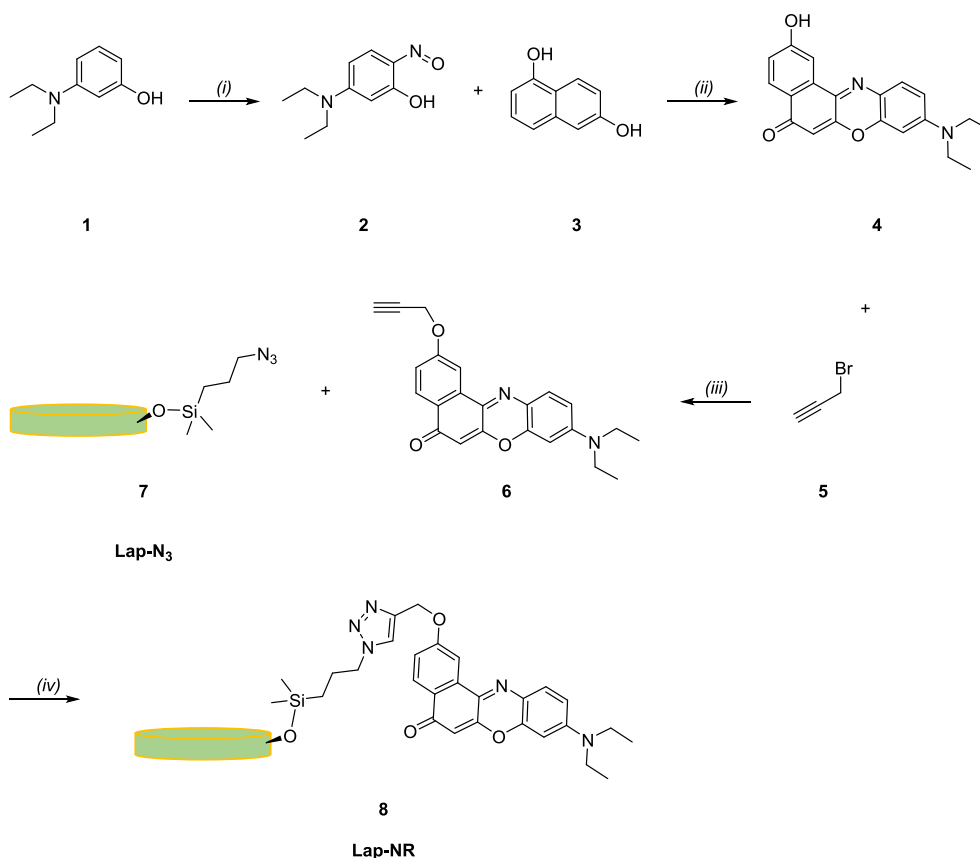
## 2. Materials and methods

**Materials.** Compounds were used as received without extra purification. 3-(Diethylamino) phenol (compound 1) and rhodamine 6G (R6G) were purchased from Sigma-Aldrich (Germany). 1,6-Dihydroxynaphthalene (compound 3) was purchased from ChemPUR (Germany). Propargyl bromide (compound 5, 80 % in toluene) was purchased from Alfa Aesar (Massachusetts, USA). Laponite-RD was obtained from BYK Additives (Germany). Other chemicals and solvents used for synthesis and purification are given in the [Supporting Information](#).

**Abbreviated Synthesis of Lap-NR.** Lap-NDI was synthesized as reported in our previous work, and was used as the first donor in the FRET cascade herein [29]. R6G is commercially available and was directly employed in this study without additional modification. The synthetic route for the second acceptor Lap-NR is illustrated in [Scheme 1](#).

In the synthesis of Lap-NR, the first step involved modifying the Laponite edge through silane chemistry so that Si-OH groups on the Laponite edges are modified with azide functional groups [37,38]. Nile red derivative 6, featuring a triple bond end group, was synthesized using commercially available compound 1 as the starting material. Click chemistry was employed to covalently attach compound 6 onto the Laponite edge through the formation of a triazole group [39–42]. The comprehensive synthetic procedures and characterization of precursors, intermediates, and products are provided in the [Supporting Information](#).

**Characterization.** Fourier-transform infrared spectroscopy (FT-IR) spectra were collected (Invenio®, Bruker, Massachusetts, USA) using a “Golden Gate” single reflection attenuated total reflection system with 128 scans and a resolution of 4 cm<sup>-1</sup>. Thermogravimetric analysis (TGA) measurements were carried out from 25 °C to 1000 °C with 10 K/min heating rate under N<sub>2</sub> flow (20 mL/min) (TG 209F1 Libra, NETZSCH, Bayern, Germany). <sup>1</sup>H NMR spectroscopy was carried out using either a Fourier HD 300 MHz NMR or an Avance I 400 MHz NMR (Bruker, Massachusetts, USA). A Fluorescence Spectrophotometer (Cary Eclipse,



**Scheme 1.** Synthetic route for Lap-NR. (i)  $\text{NaNO}_2$ , 37% HCl,  $0^\circ\text{C} - 5^\circ\text{C}$ , 4 h; (ii) DMF,  $155^\circ\text{C}$ , 4 h; (iii) anhydrous DMF,  $\text{K}_2\text{CO}_3$ ,  $70^\circ\text{C}$ , 3 h; (iv)  $\text{CuSO}_4$ , Sodium ascorbate,  $\text{H}_2\text{O}/\text{tert-BuOH}$  (1:1), 10 min,  $100^\circ\text{C}$  in MW.

Agilent, Santa Clara, CA, USA) was used for collecting steady-state fluorescence spectra. UV-Vis spectra were collected on a UV – Vis spectrometer (Cary 60, Agilent, Santa Clara, CA, USA). Time-resolved photoluminescence measurements were performed on a FluoTime 300 fluorescence spectrometer (Picoquant, Berlin, Germany), in which the light source was a supercontinuum laser (SuperK Fianum, NKT Photonics, Copenhagen, Denmark) which passed through a deep UV supercontinuum extension unit (SuperK Extend-UV (DUV), NKT Photonics). Average fluorescence lifetimes were averaged over amplitudes. Quantum yields were measured using a fluorescence spectrometer equipped with an integrating sphere and Fluorescence V3.9 software (Fluorolog 3, Horiba, Kyoto, Japan).

**FRET experiments.** Lap-NDI was dispersed in DMF and sonicated for 15 min to prepare stock solutions at a concentration of 1 mg/mL. A stock solution of R6G at 1 mM was dissolved in water. For the FRET study from Lap-NDI to R6G, Lap-NDI was diluted to a concentration of 0.1 mg/mL in a solvent mixture composed of water and DMF, with varying water content from 37.5 % to 62.5 %. R6G (10  $\mu\text{M}$ ) was then prepared in a solvent with an identical composition. The R6G solution was then added in 0.016  $\mu\text{M}$  increments to the diluted Lap-NDI dispersion, until reaching a final concentration of 0.133  $\mu\text{M}$  R6G. Fluorescence spectra were collected with and without R6G at varying concentrations. The second acceptor, Lap-NR, was prepared at 1 mg/mL in a similar water/DMF mixture and sonicated for 15 min. To investigate cascade FRET, Lap-NR was introduced in 3.3  $\mu\text{g}/\text{mL}$  increments to the mixture of Lap-NDI and R6G, until reaching a final concentration of 0.05 mg/mL Lap-NR. Fluorescence spectra were collected with and without Lap-NR at varying concentrations, and furthermore, control experiments where unmodified Laponite was added in lieu of Lap-NR or Lap-NDI were carried out.

### 3. Results and discussion

Lap-NR was characterized by Fourier-transform infrared spectroscopy (FT-IR) following its synthesis and purification. The results are given in Fig. 1. Significantly intense peaks identified at  $651\text{ cm}^{-1}$  and  $960\text{ cm}^{-1}$  correspond to the Si-O-Si bending and Si-O stretching modes in Laponite. These characteristics are observed in pristine Laponite, Lap- $\text{N}_3$ , and Lap-NR, in contrast to Nile red precursor 6 (Fig. 1a) [43]. The moderate peak observed at  $1660\text{ cm}^{-1}$  in Lap-NR signifies an overlap of C=C stretching vibrations in conjugated, cyclic alkenes, and the triazole N=N stretch [44,45]. The distinct peaks at  $2106\text{ cm}^{-1}$  and  $3190\text{ cm}^{-1}$  in compound 6 (Fig. 2b) are attributed to the  $\text{C}\equiv\text{C}$  stretching and C–H stretching modes of alkynes, respectively [39]. Notably, in Lap- $\text{N}_3$ , there is a peak centered around  $2106\text{ cm}^{-1}$  (Fig. 2b), attributed to azide  $\text{N}=\text{N}=\text{N}$  stretching vibration [38]. In summary, the absence of alkyne and azide stretching vibrations, and the presence of triazole stretching in Lap-NR compared to Lap- $\text{N}_3$  and compound 6, indicate the successful click chemistry reaction and the attachment of the Nile red derivative to Laponite. Furthermore, the identification of C–H stretching at  $2940\text{ cm}^{-1}$  and  $3190\text{ cm}^{-1}$ , attributed to alkane and alkene, respectively, supports the effective attachment of organic compounds onto the inorganic material Laponite (Fig. 1b) [43]. Moreover, the observed peaks at  $3685\text{ cm}^{-1}$  and  $3679\text{ cm}^{-1}$  correspond to O–H stretching vibrations of Mg-OH and Si-OH in Laponite, respectively (Figure S1). Compared to pristine Laponite, the center of these two peaks has shifted to  $3687\text{ cm}^{-1}$  in Lap-NR, and to  $3685\text{ cm}^{-1}$  in Lap- $\text{N}_3$ . This shift is a consequence of Si-O-Si-C formation through organic modification at the edge via silanol condensation [46].

The organic content in the hybrid materials Lap- $\text{N}_3$  and Lap-NR was determined by TGA following the approach by Wheeler et al. [28] A weight loss of 3.67 % in the temperature range of  $150^\circ\text{C}$  to  $600^\circ\text{C}$  in the



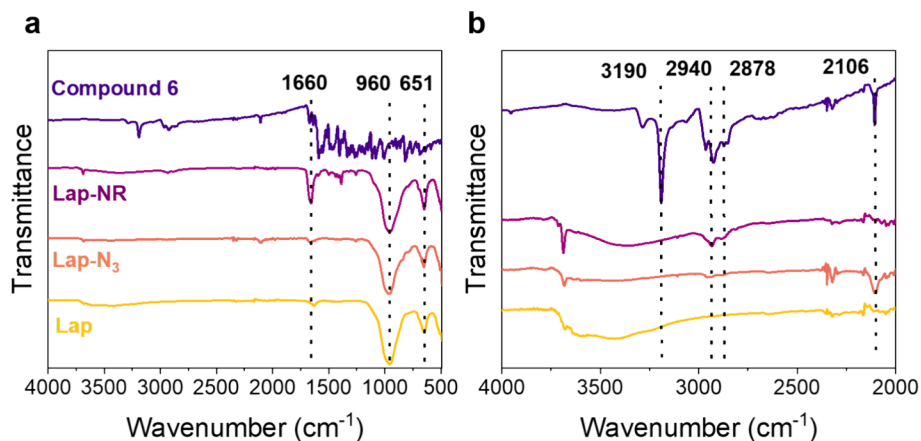


**Fig. 1.** (a) Full FT-IR spectra and (b) Zoom into the region from 2000–4000 cm<sup>-1</sup> of compound 6 (purple), Nile red derivative modified Laponite (Lap-NR, purple-red), azide end group modified Laponite (Lap-N<sub>3</sub>, orange), and the pristine Laponite (Lap, yellow).

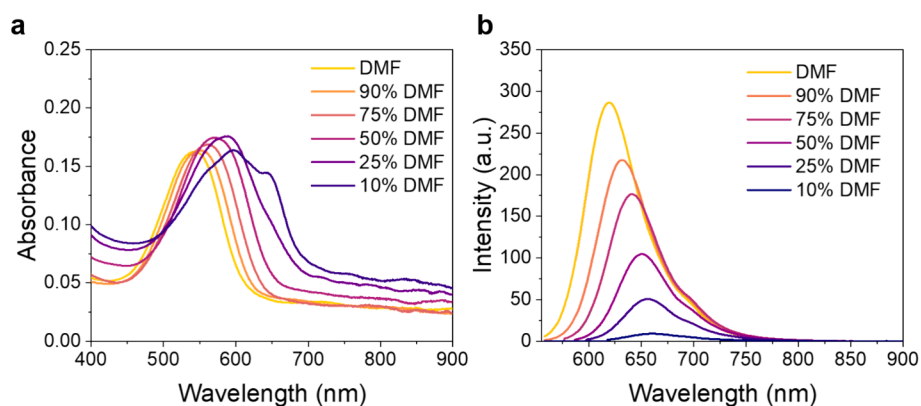


**Fig. 2.** (a) UV-Vis absorbance and (b) Fluorescence spectra of Nile red derivative modified Laponite Lap-NR in various water/DMF composites, 0.1 mg/mL,  $\lambda_{\text{ex}} = 540$  nm.

TGA curve of Lap-N<sub>3</sub>, in comparison to pristine Laponite, indicated an average presence of 278 azide residues on a single Laponite particle, calculated with an estimated individual Laponite mass of  $3.2 \times 10^{-18}$  g (Figure S2). In the Lap-NR TGA curve, a 6.81 % decrease in mass relative to Lap-N<sub>3</sub>, corresponds to 226 Nile red triazole residues on each Laponite sheet. Considering that Felbeck et al report  $\sim 420$  modifiable silanol groups per Laponite particle, these TGA results suggest a reasonably effective modification [28,47].

The optical properties of the synthesized acceptor Lap-NR (Fig. 2) were characterized by UV-Vis absorption and fluorescence spectroscopy in various compositions of water and dimethylformamide (DMF). The  $\lambda_{\text{max}}$  of the absorption band of Lap-NR shifted from 540 nm to 595 nm as the solvent polarity increased from pure DMF to 10 % DMF (90 % water) (Fig. 2a), which is attributed to the well-characterized solvatochromic behavior of monomeric Nile red derivatives [39,48–52]. The shoulder at 645 nm apparent in 10 % DMF is likely due to the formation of a J-type aggregate of edge-bound Nile red molecules [53,54]. The fluorescence spectra of Lap-NR (Fig. 2b) also displayed a bathochromic shift from 618 nm to 680 nm in maximum emission as solvent polarity increased. Additionally, the intensity of maximum emission decreased by 97 % in 10 % DMF compared to the maximum emission intensity in pure DMF, likely due to the combined influence of solvent polarity and aggregation-induced quenching [31,51,52].

The absorption spectrum of R6G in water exhibits a primary band at 525 nm and a weak shoulder at 493 nm, attributed to the 0–0 and 0–1 vibronic transitions of monomeric R6G, respectively (Fig. S3a). A monomeric emission band at 550 nm was observed in the fluorescence

spectrum of R6G in water (Fig. S3b) [55,56]. As the water content decreases to 10 %, a slight bathochromic shift to 534 nm in the absorption spectrum, and 558 nm in the fluorescence spectrum, was observed. This is a result of varied solvent parameters such as polarity and refractive index [57]. The adsorption of R6G on the basal surface of Laponite led to a 2 nm bathochromic shift compared to pure R6G in an identical solvent composition, which indicates the monomeric organization of R6G on Laponite (Fig. S4a–b) [58,59]. The excimer emission of the naphthalene, with the emission  $\lambda_{\text{max}}$  at 485 nm in Lap-NDI overlaps significantly with the  $\lambda_{\text{max}}$  of absorption at 535 nm of R6G in 50 % water. Furthermore, the  $\lambda_{\text{max}}$  of emission of R6G monomer at 558 nm also overlaps with the absorption  $\lambda_{\text{max}}$  at 569 nm of Lap-NR (Figure S5a). The significant overlap between absorbance and emission bands indicates that Lap-NDI, R6G, and Lap-NR are good candidates for designing a FRET cascade. Furthermore, an energy level diagram of the designed cascade FRET system is illustrated in Figure S5b. In the first step of the FRET cascade, Lap-NDI is excited from the  $S_0$  ground state to the  $S_1$  excited state through absorption of light, and the excess energy at the  $S_1$  state is non-radiatively transferred to a nearby R6G acceptor, leading to the quenching of the donor emission and excitation of the acceptor to the  $S_1$  excited state. In the second step, non-radiative energy transfer from the  $S_1$  excited state of R6G to a nearby Lap-NR acceptor leads to a similar excitation of Lap-NR to the  $S_1$  excited state and corresponding quenching of the R6G emission.

Single-step FRET of the separate donor–acceptor pairs were individually studied (Fig. 3a–c). As the concentration of R6G increases, the excimer emission of Lap-NDI with the maximum band at 485 nm

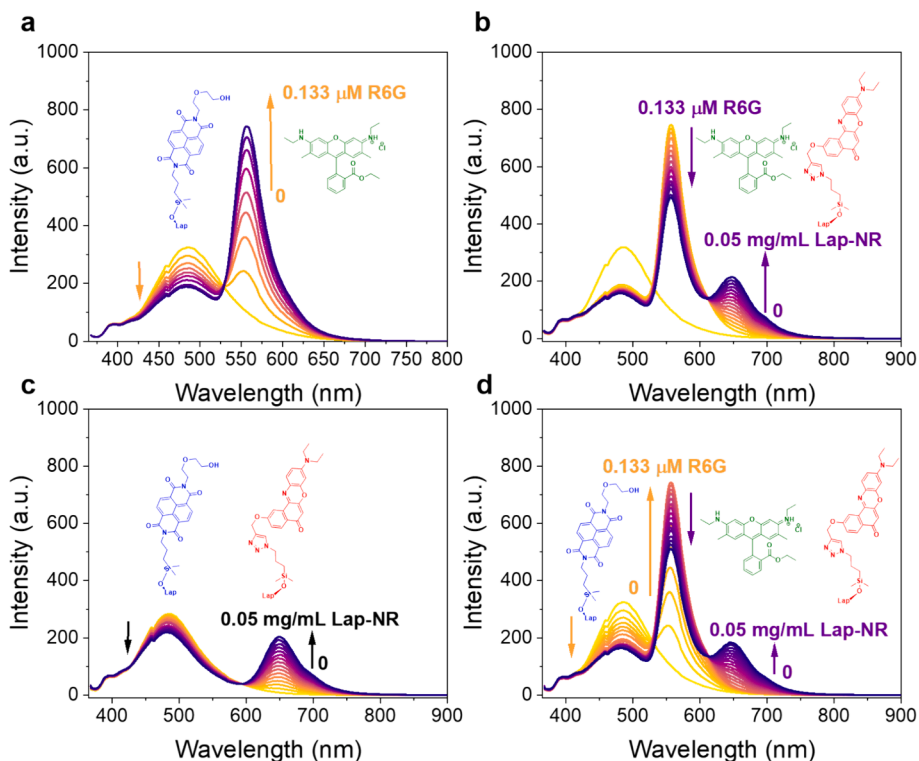


**Fig. 3.** (a) Single-step FRET from Lap-NDI to R6G in a 1:1 water/DMF mixture; (b) from R6G to Lap-NR; (c) from Lap-NDI to Lap-NR; (d) Two-step cascade FRET from Lap-NDI to Lap-NR;  $\lambda_{ex} = 350$  nm, arrows indicate the emission intensity change in the process of FRET.

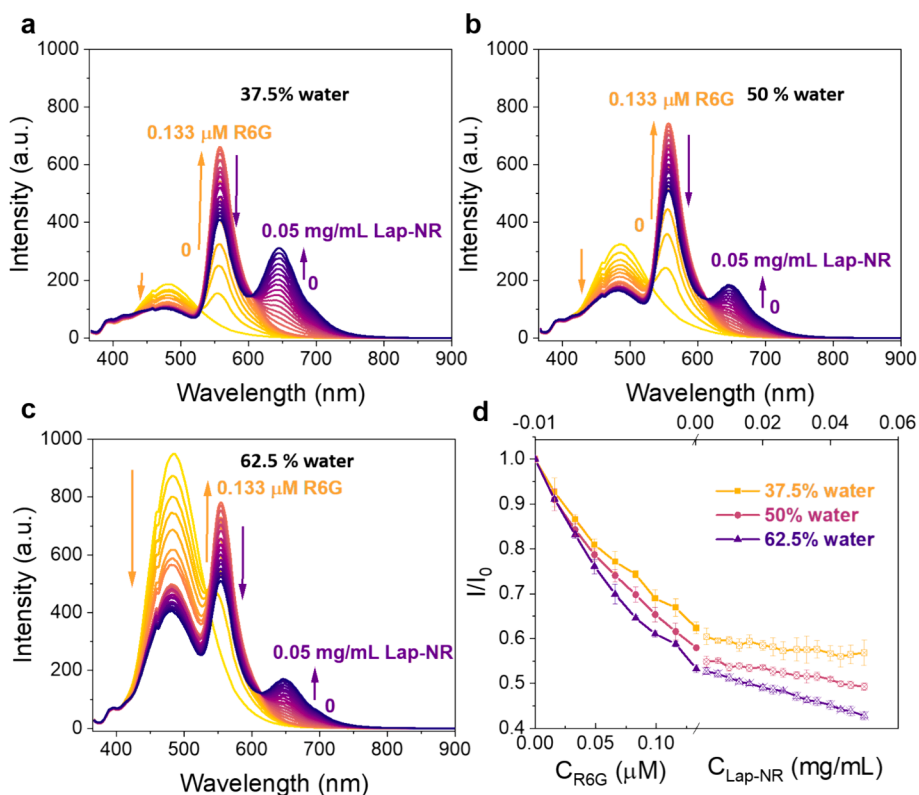


**Fig. 4.** Cascade FRET in (a) 37.5 % water; (b) 50 % water; (c) 62.5 % water; (d)  $I/I_0$  at 485 nm at increasing concentrations of R6G (solid symbol) and Lap-NR (crossed symbol) – 37.5 % water: orange square; 50 % water: red circle; 62.5 % water: purple triangle;  $\lambda_{ex} = 350$  nm, arrows indicate the emission intensity change in the cascade FRET.

gradually decreases. The presence and enhancement of the R6G emission band at 560 nm indicates energy transfer from the Lap-NDI excimer to R6G (Fig. 3a). The efficiency of FRET from Lap-NDI to R6G is calculated to be 42 % following the equation  $E = [1 - I_{DA}/I_D]$ , in which  $I_{DA}$  and  $I_D$  refer to the emission intensity of donor in the presence and the absence of acceptor, respectively [4,6]. The final concentration of R6G is 0.133  $\mu\text{M}$ , which is below 0.1 % of the cation exchange capacity (CEC) of Laponite (0.55 – 0.8 mequiv/g) [60]. Martínez et al reported that R6G adsorbs onto the Laponite basal surface in a monomeric state when its concentration is below 0.1 % of the CEC [61]. The reported radius of Laponite is approximately 12.5 nm, within which R6G likely can be found on the basal surface. Thus, it is highly likely that an R6G molecule is bound to the basal surface within the 1–10 nm distance necessary for FRET [6,60]. Furthermore, the low concentration of R6G restricts the occurrence of sub-nanometric Dexter-type energy transfer [5]. Thus, the quenching of Lap-NDI emission is then predominantly attributed to Förster-type energy transfer (FRET). As the concentration of the second acceptor Lap-NR was increased to 0.05 mg/mL, a reduction in the emission intensity of R6G was observed, with an average efficiency of 34 % (Fig. 3b). Moreover, upon the addition of Lap-NR to Lap-NDI without the addition of R6G, minor quenching of the excimer emission of Lap-NDI was noted (24 %, Fig. 3c), as there is minor spectral overlap between Lap-NDI emission and Lap-NR absorption (Figure S5a). The two-step cascade FRET process first showed emission quenching of Lap-NDI excimer and enhancement of R6G emission upon the addition of the first acceptor (R6G), followed by quenching of R6G emission upon addition of the second acceptor Lap-NR (Fig. 3d).

Fluorescence lifetimes were measured for Lap-NDI and R6G to substantiate the cascade FRET process (Tables S1 and S2). The initial average lifetime for Lap-NDI of 4.46 ns at 480 nm in the absence of R6G progressively decreased, resulting in a lifetime of 2.77 ns after the addition of 0.133  $\mu\text{M}$  R6G. This trend supports the occurrence of FRET from Lap-NDI excimer to R6G monomer on the Laponite surface (Table S1). As the concentration of Lap-NR was increased from 0 to 0.05 mg/mL in the presence of Lap-NDI (Table S2), the fluorescence lifetime of R6G decreased from 8.0 ns to 7.17 ns for  $\tau_1$  and from 3.22 to 2.89 ns for  $\tau_2$ , confirming FRET from R6G on Laponite to Lap-NR. Furthermore, the contribution from  $\tau_1$  increased from 10 % to 17 % as Lap-NR concentration was increased from 0 to 0.05 mg/mL (Table S2). In order to disentangle the contributions of quenching due to interactions with Laponite, several control experiments were carried out. The addition of unmodified Laponite to the dispersion of Lap-NDI resulted in a 10 % average reduction in emission at 485 nm, likely due to the presence of unmodified Laponite sheets intercalating between Lap-NDI, inducing deaggregation of the NDI chromophore (Figure S6a). Furthermore, the addition of unmodified Laponite to the dispersion of Laponite and R6G led to only a 4 % emission reduction at 550 nm, supporting a negligible contribution to the quenching of R6G from Laponite alone (Figure S6b). These control experiments further corroborated a cascade FRET process.

The influence of solvent composition on cascade FRET was investigated by using water/DMF mixtures containing 37.5 % water and 62.5 % water (Fig. 4). The interactions observed in all three solvent compositions show R6G quenching of Lap-NDI excimer emission at 485 nm, and Lap-NR induced quenching of R6G emission at 550 nm, confirming the integrity of the cascade FRET. With an increase in water content from 37.5 % to 62.5 %, Lap-NDI exhibited the most intense initial excimer emission at 485 nm, attributed to the aggregation-induced emission of naphthalene diimide (Fig. 4a-c) [29]. Additionally, the quantum yield of pure R6G was noted as 0.95 in water and 0.75 in DMF, leading to an enhancement of R6G emission at 585 nm in 62.5 % water, compared to the R6G emission intensity in 37.5 % water and 50 % water (Fig. 4a-c) [62]. The combination of these two effects contributed to an enhanced FRET efficiency from Lap-NDI to R6G on Laponite in 62.5 % water (Fig. 4d). Furthermore, the quantum yields of Lap-NR were determined to be 0.46 in DMF, 0.19 in 37.5 % water, 0.14 in 50 % water,

and 0.12 in 62.5 % water, leading to a more pronounced emission enhancement of Lap-NR in 37.5 % water compared with the dispersions containing 50 % and 67.5 % water (Fig. 4a-c). In 62.5 % water, Lap-NR appears to quench the emission of the Lap-NDI excimer more efficiently, likely due to increased deaggregation of the NDI chromophore induced by the intercalation of Lap-NR between Lap-NDI sheets (Fig. 4d).

#### 4. Conclusions

In summary, this study reports the synthesis of a new organic–inorganic hybrid Lap-NR, consisting of a Nile red derivative covalently attached to the Laponite edge via silanol coupling. Lap-NR exhibited a pronounced absorption band at 540 nm in pure DMF, and the addition of water led to a strong solvatochromic shift to 595 nm. The emission peak of Lap-NR also shifted from 618 nm to 680 nm when the water content was changed from 0 % to 90 %, accompanied by a decrease in quantum yield. Building upon previous work, a cascade FRET system was designed utilizing Lap-NDI, consisting of a naphthalene diimide chromophore bound to the Laponite edge, as the initial donor. This system incorporated R6G adsorbed on Laponite as the first acceptor, and the synthesized Lap-NR as the subsequent acceptor.

Upon the addition of R6G to a dispersion containing Lap-NDI and Lap-NR, cascade FRET from the NDI-modified Laponite edge to the R6G-modified Laponite basal surface, then to the Nile red derivative-modified Laponite edge, was observed. The single-step FRET processes between Lap-NDI / R6G, R6G / Lap-NR, and Lap-NDI / Lap-NR revealed FRET efficiencies of 42 % from Lap-NDI to R6G, 34 % from R6G to Lap-NR, and 24 % from Lap-NDI to Lap-NR in 50 % water. The overall two-step energy transfer efficiency was determined to be 43 %, 51 %, and 57 % in 37.5 %, 50 %, and 67.5 % water, respectively. These observations, coupled with control experiments and fluorescence lifetime measurements, confirmed that the ability to control the modification of Laponite with chromophores at the edge or basal surfaces allowed the design of a two-step cascade FRET process. Moreover, the influence of solvent composition on the FRET cascade revealed that cascade FRET in this system is most efficient in a 62.5 % water dispersion, which is attributed to increased aggregation-induced emission of Lap-NDI and the enhanced quantum yield of R6G in water.

Modification of 2D nanomaterial edge and basal surfaces with different chromophores is a versatile route to achieve cascade FRET with dynamic tunability of the distances and orientations of chromophores. Cascade FRET within supramolecular systems can be achieved through a diverse range of non-covalent scaffolds, such as the formation of micellar and host–guest complexes [16,18]. These systems are advantageous in bringing chromophores into proximity and avoiding the tedious synthesis of covalent systems. However, these approaches limit the selections of donor–acceptor pairs, the dynamic adjustment in a fixed system, and stabilities [16]. Herein, we reported a novel approach to design a FRET cascade which utilized the unique surface chemistry anisotropy of Laponite to attach energy donors and acceptors in a logical manner. This shows the potential for such layered materials to serve as templates for energy transfer from single-step FRET to multi-step cascade FRET, extending the energy window to result in a Stokes shift of 300 nm.

In contrast to strategies which control donor–acceptor interactions via supramolecular strategies and intra-chain interactions within polymers, and donor–acceptor pairs [15,21], organic–inorganic hybrids based on colloidal templates with anisotropic surface chemistry provide the flexibility to tune FRET through factors such as pH, solvent, degree of functionalization, and aggregation state of the template [63]. This approach provides a wider selection of dyes, including neutral and charged molecules, and supports the application in other phases than colloids such as solids, gels, and thin films. Furthermore, the versatile functionalization, enhanced stability, and low cost of 2D nanomaterials are advantageous for the scalability of FRET applications in industrial settings. The diversity of 2D nanomaterial-based cascade FRET systems,

available in forms such as colloid, solid materials, and films, enables various fabrication methods for applications in biosensing, drug delivery, and energy storage devices. However, fine control of dye distribution and degree of modification on 2D nanomaterials requires further investigation. Moreover, a deeper understanding of the interactions between various colloidal species such as surfactants, polymers, and dye molecules would be beneficial for optimizing FRET. In this respect, computational approaches such as molecular dynamics and Monte-Carlo simulations of such inorganic–organic hybrid systems can provide a molecular-level understanding of dynamic processes such as intermolecular interactions, solvent effects, and adsorption at the nanomaterial surfaces [64,65]. In summary, this study paves the way for future research on 2D nanomaterial-based inorganic–organic hybrids for the design of dynamic, tunable sensors and optoelectronic devices.

### CRedit authorship contribution statement

**Hongxiao Xiang:** Writing – review & editing, Writing – original draft, Investigation, Conceptualization. **Eric H. Hill:** .

### Declaration of competing interest

The authors declare that they have no known competing financial interests or personal relationships that could have appeared to influence the work reported in this paper.

### Data availability

Data will be made available on request.

### Acknowledgments

This research was supported by the Deutsche Forschungsgemeinschaft (DFG), Germany, project ID 447787198. E.H.H. is supported by the Cluster of Excellence “Advanced Imaging of Matter” of the DFG - EXC 2056, project ID 390715994. Financial support was also provided by the German Federal Ministry of Education and Research (BMBF), Germany, through the MOPGA-GRI program (57565165). We gratefully acknowledge the central measurement facilities of the Chemistry Department of the University of Hamburg for their assistance with mass spectrometry and for providing access to NMR equipment. We also sincerely acknowledge Öznur Tokmak (Fraunhofer Institute for Applied Polymer Research) for advice regarding the Integrating Sphere Fluorimeter.

### Appendix A. Supplementary material

Supplementary data to this article can be found online at <https://doi.org/10.1016/j.jcis.2024.07.106>.

### References

- [1] P.G. Wu, L. Brand, Resonance energy transfer: Methods and applications, *Anal. Biochem.* 218 (1994) 1–13, <https://doi.org/10.1006/abio.1994.1134>.
- [2] G.A. Jones, D.S. Bradshaw, Resonance energy transfer: from fundamental theory to recent applications, *Front. Phys.* 7 (2019) 1–19, <https://doi.org/10.3389/fphy.2019.00100>.
- [3] T. Ha, J. Fei, S. Schmid, N.K. Lee, R.L. Gonzalez, S. Paul, S. Yeou, Fluorescence resonance energy transfer at the single-molecule level, *Nat. Rev. Methods Prim.* 4 (2024) 21, <https://doi.org/10.1038/s43586-024-00298-3>.
- [4] T. Förster, Zwischenmolekulare Energiewanderung und Fluoreszenz, *Ann. Phys.* 437 (1948) 55–75, <https://doi.org/10.1002/andp.19484370105>.
- [5] D.L. Dexter, A theory of sensitized luminescence in solids, *J. Chem. Phys.* 21 (1953) 836–850, <https://doi.org/10.1063/1.1699044>.
- [6] J.R. Lakowicz, *Energy Transfer*, in: *Princ. Fluoresc. Spectrosc.*, Second Ed., Springer US, Boston, MA, 1999: pp. 367–394. Doi: 10.1007/978-1-4757-3061-6\_13.
- [7] M.T. Efa, J.C. Huang, T. Imae, Cascade Förster Resonance Energy Transfer Studies for Enhancement of Light Harvesting on Dye-Sensitized Solar Cells, *Nanomaterials* 12 (2022) 1–17, <https://doi.org/10.3390/nano12224085>.
- [8] K.E. Sapsford, L. Berti, I.L. Medintz, Materials for fluorescence resonance energy transfer analysis: Beyond traditional donor-acceptor combinations, *Angew. Chemie - Int. Ed.* 45 (2006) 4562–4589, <https://doi.org/10.1002/anie.200503873>.
- [9] K. Aoki, Y. Kamioka, M. Matsuda, Fluorescence resonance energy transfer imaging of cell signaling from in vitro to in vivo: Basis of biosensor construction, live imaging, and image processing, *Dev. Growth Differ.* 55 (2013) 515–522, <https://doi.org/10.1111/dgd.12039>.
- [10] Z. He, F. Li, P. Zuo, H. Tian, Principles and Applications of Resonance Energy Transfer Involving Noble Metallic Nanoparticles, *Materials (basel)*. 16 (2023) 3083, <https://doi.org/10.3390/ma16083083>.
- [11] A. Dietrich, V. Buschmann, C. Müller, M. Sauer, Fluorescence resonance energy transfer (FRET) and competing processes in donor-acceptor substituted DNA strands: a comparative study of ensemble and single-molecule data, *Rev. Mol. Biotechnol.* 82 (2002) 211–231, [https://doi.org/10.1016/S1389-0352\(01\)00039-3](https://doi.org/10.1016/S1389-0352(01)00039-3).
- [12] J.I. Basham, G.K. Mor, C.A. Grimes, Förster resonance energy transfer in dye-sensitized solar cells, *ACS Nano* 4 (2010) 1253–1258, <https://doi.org/10.1021/nn100422a>.
- [13] A.C.S. Samia, S. Dayal, C. Burda, Invited Review Quantum Dot-based Energy Transfer: Perspectives and Potential for Applications in Photodynamic Therapy, *Photochem. Photobiol.* 82 (2006) 61–68, <https://doi.org/10.1562/2005-05-11-1R3-525>.
- [14] G.D. Scholes, Long-Range Resonance Energy Transfer in Molecular Systems, *Annu. Rev. Phys. Chem.* 54 (2003) 57–87, <https://doi.org/10.1146/annurev.physchem.54.011002.103746>.
- [15] X.Y. Dai, M. Huo, Y. Liu, Phosphorescence resonance energy transfer from purely organic supramolecular assembly, *Nat. Rev. Chem.* 7 (2023) 854–874, <https://doi.org/10.1038/s41570-023-00555-1>.
- [16] D. Chen, T. Xiao, É. Monflier, L. Wang, Multi-step FRET systems based on discrete supramolecular assemblies, *Commun. Chem.* 7 (2024) 1–10, <https://doi.org/10.1038/s42004-024-01175-6>.
- [17] H.A. Behanna, K. Rajangam, S.I. Stupp, Modulation of Fluorescence through Coassembly of Molecules in Organic Nanostructures, *J. Am. Chem. Soc.* 129 (2007) 321–327, <https://doi.org/10.1021/ja062415b>.
- [18] Z.-Y. Gu, D.-S. Guo, M. Sun, Y. Liu, Effective Enlargement of Fluorescence Resonance Energy Transfer of Poly-Porphyrin Mediated by  $\beta$ -Cyclodextrin Dimers, *J. Org. Chem.* 75 (2010) 3600–3607, <https://doi.org/10.1021/jo100351f>.
- [19] Y. Li, S.S. Rajasree, G.Y. Lee, J. Yu, J.-H. Tang, R. Ni, G. Li, K.N. Houk, P. Deria, P. J. Stang, Anthracene–Triphenylamine-Based Platinum(II) Metallocages as Synthetic Light-Harvesting Assembly, *J. Am. Chem. Soc.* 143 (2021) 2908–2919, <https://doi.org/10.1021/jacs.0c12853>.
- [20] P.K. Dutta, R. Varghese, J. Nangreave, S. Lin, H. Yan, Y. Liu, DNA-Directed Artificial Light-Harvesting Antenna, *J. Am. Chem. Soc.* 133 (2011) 11985–11993, <https://doi.org/10.1021/ja1115138>.
- [21] S. Valdez, M. Robertson, Z. Qiang, Fluorescence Resonance Energy Transfer Measurements in Polymer Science: A Review, *Macromol. Rapid Commun.* 43 (2022) 1–19, <https://doi.org/10.1002/marc.202200421>.
- [22] S.C. Owen, D.P.Y. Chan, M.S. Shoichet, Polymeric micelle stability, *Nano Today* 7 (2012) 53–65, <https://doi.org/10.1016/j.nantod.2012.01.002>.
- [23] C. Hippus, I.H.M. Van Stokkum, M. Gsänger, M.M. Groeneveld, R.M. Williams, F. Wüthner, Sequential FRET processes in calix[4]arene-linked orange-red-green perylene bisimide dye zigzag arrays, *J. Phys. Chem. C* 112 (2008) 2476–2486, <https://doi.org/10.1021/jp711120v>.
- [24] H. Najafi, S. Farajfaed, S. Zolgharnian, S.H. Mosavi Mirak, N. Asasian-Kolur, S. Sharifian, A comprehensive study on modified-pillared clays as an adsorbent in wastewater treatment processes, *Process Saf. Environ. Prot.* 147 (2021) 8–36, <https://doi.org/10.1016/j.psep.2020.09.028>.
- [25] D. Dey, D. Bhattacharjee, S. Chakraborty, S.A. Hussain, Effect of nanoclay laponite and pH on the energy transfer between fluorescent dyes, *J. Photochem. Photobiol. A Chem.* 252 (2013) 174–182, <https://doi.org/10.1016/j.jphotochem.2012.12.003>.
- [26] A. Nakayama, J. Mizuno, Y. Ohtani, T. Shimada, S. Takagi, Elucidation of the Adsorption Distribution of Cationic Porphyrin on the Inorganic Surface by Energy Transfer as a Molecular Ruler, *J. Phys. Chem. C* 122 (2018) 4365–4371, <https://doi.org/10.1021/acs.jpcc.7b12104>.
- [27] H. Xiang, S.R. Valandro, E.H. Hill, Layered silicate edge-linked perylene diimides: Synthesis, self-assembly and energy transfer, *J. Colloid Interface Sci.* 629 (2023) 300–306, <https://doi.org/10.1016/j.jcis.2022.09.055>.
- [28] P.A. Wheeler, J. Wang, J. Baker, L.J. Mathias, Synthesis and characterization of covalently functionalized laponite clay, *Chem. Mater.* 17 (2005) 3012–3018, <https://doi.org/10.1021/cm050306a>.
- [29] H. Xiang, S.R. Valandro, E.H. Hill, 2D Nanomaterial-Directed Molecular Aggregation and Energy Transfer between Edge-Bound Donor-Acceptor Pairs, *J. Phys. Chem. C* 127 (2023) 15416–15422, <https://doi.org/10.1021/acs.jpcc.3c04555>.
- [30] J.A. Broussard, K.J. Green, Research Techniques Made Simple: Methodology and Applications of Förster Resonance Energy Transfer (FRET) Microscopy, *J. Invest. Dermatol.* 137 (2017) 185–191, <https://doi.org/10.1016/j.jid.2017.09.006>.
- [31] J. Bujdák, The effects of layered nanoparticles and their properties on the molecular aggregation of organic dyes, *J. Photochem. Photobiol. C Photochem. Rev.* 35 (2018) 108–133, <https://doi.org/10.1016/j.jphotochemrev.2018.03.001>.
- [32] C.E. Rowland, J.B. Delehanty, C.L. Dwyer, I.L. Medintz, Growing applications for bioassembled Förster resonance energy transfer cascades, *Mater. Today* 20 (2017) 131–141, <https://doi.org/10.1016/j.mattod.2016.09.013>.
- [33] K. Parafiniuk, L. Sznitko, M. Zelechowska, J. Mysliwiec, Near-infrared distributed feedback laser emission based on cascade Förster resonance energy transfer to Nile



- Blue aggregates, *Org. Electron.* 33 (2016) 121–127, <https://doi.org/10.1016/j.orgel.2016.03.007>.
- [34] E. Haustein, M. Jahnz, P. Schwille, Triple FRET: A tool for Studying Long-Range Molecular Interactions, *ChemPhysChem* 4 (2003) 745–748, <https://doi.org/10.1002/cphc.200200634>.
- [35] J. Ruan, F. Li, H. Tian, J. Yu, H. Deng, S. Ge, K.W. Leong, A cascade FRET photosensitizer that enhances photodynamic therapy for ocular melanoma, *Nano Today* 47 (2022) 101684, <https://doi.org/10.1016/j.nantod.2022.101684>.
- [36] J.M. Serin, D.W. Brousmiche, J.M.J. Fréchet, Cascade energy transfer in a conformationally mobile multichromophoric dendrimer, *Chem. Commun.* 2 (2002) 2605–2607, <https://doi.org/10.1039/b207905d>.
- [37] P. Paoprasert, J.W. Spalenka, D.L. Peterson, R.E. Ruther, R.J. Hamers, P.G. Evans, P. Gopalan, Grafting of poly(3-hexylthiophene) brushes on oxides using click chemistry, *J. Mater. Chem.* 20 (2010) 2651–2658, <https://doi.org/10.1039/b920233a>.
- [38] C.G. Colletti, M. Massaro, G. Lazzara, G. Cavallaro, S. Milioto, I. Pibiri, R. Noto, S. RIELA, Synthesis, characterization and study of covalently modified triazole LAPONITE® edges, *Appl. Clay Sci.* 187 (2020) 105489, <https://doi.org/10.1016/j.clay.2020.105489>.
- [39] M. Börgardt, K. Verlinden, M. Neidhardt, T. Wöhrle, A. Herbst, S. Laschat, C. Janiak, T.J.J. Müller, Synthesis and optical properties of covalently bound Nile Red in mesoporous silica hybrids-comparison of dye distribution of materials prepared by facile grafting and by co-condensation routes, *RSC Adv.* 6 (2016) 6209–6222, <https://doi.org/10.1039/c5ra22736d>.
- [40] A. Ionescu, N. Godbert, A. Crispini, R. Termine, A. Golemme, M. Ghedini, Photoconductive Nile red cyclopalladated metallomesogens, *J. Mater. Chem.* 22 (2012) 23617–23626, <https://doi.org/10.1039/c2jm34946a>.
- [41] S.-Y. Park, Y. Kubota, K. Funabiki, M. Shiro, M. Matsui, Near-infrared solid-state fluorescent naphthooxazine dyes attached with bulky dibutylamino and perfluoroalkenyl groups at 6- and 9-positions, *Tetrahedron Lett.* 50 (2009) 1131–1135, <https://doi.org/10.1016/j.tetlet.2008.12.081>.
- [42] N. Yotapan, C. Charoenpakdee, P. Wathanathavorn, B. Ditmangklo, H. A. Wagenknecht, T. Vilaivan, Synthesis and optical properties of pyrrolidinyl peptide nucleic acid carrying a clicked Nile red label, *Beilstein J. Org. Chem.* 10 (2014) 2166–2174, <https://doi.org/10.3762/bjoc.10.224>.
- [43] H. Pálková, J. Madejová, M. Zimowska, E.M. Serwicka, Laponite-derived porous clay heterostructures: II, FTIR Study of the Structure Evolution, *Microporous Mesoporous Mater.* 127 (2010) 237–244, <https://doi.org/10.1016/j.micromeso.2009.07.012>.
- [44] I.I. Sahay, P.S. Ghalsasi, Synthesis of new 1,2,3-triazole linked benzimidazole molecules as anti-proliferative agents, *Synth. Commun.* 47 (2017) 825–834, <https://doi.org/10.1080/00397911.2017.1289412>.
- [45] M.K. Trivedi, R.M. Tallapragada, Characterization of Physical, Spectral and Thermal Properties of Biofield Treated 1,2,4-Triazole, *J. Mol. Pharm. Org. Process Res.* 03 (2015) 2–7, <https://doi.org/10.4172/2329-9053.1000128>.
- [46] N.N. Herrera, J.M. Letoffe, J.P. Raymond, E. Bourgeat-Lami, Silylation of laponite clay particles with monofunctional and trifunctional vinyl alkoxy silanes, *J. Mater. Chem.* 15 (2005) 863–871, <https://doi.org/10.1039/b415618h>.
- [47] T. Felbeck, K. Hoffmann, M.M. Lezhnina, U.H. Kynast, U. Resch-Genger, Fluorescent nanoclays: Covalent functionalization with amine reactive dyes from different fluorophore classes and surface group quantification, *J. Phys. Chem. C* 119 (2015) 12978–12987, <https://doi.org/10.1021/acs.jpcc.5b01482>.
- [48] J.R. Korber, C.W. Barth, S.L. Gibbs, Nile Red derivatives enable improved ratiometric imaging for nerve-specific contrast, *J. Biomed. Opt.* 23 (2018) 1, <https://doi.org/10.1117/1.jbo.23.7.076002>.
- [49] V.V. Kostjukov, Excitation of neutral red dye in aqueous media: comparative theoretical analysis of neutral and cationic forms, *J. Mol. Model.* 28 (2022) 1–9, <https://doi.org/10.1007/s00894-022-05098-8>.
- [50] A. Ghanadzadeh Gilani, M. Moghadam, M.S. Zakerhamidi, Solvatochromism of Nile red in anisotropic media, *Dye. Pigment.* 92 (2012) 1052–1057, <https://doi.org/10.1016/j.dyepig.2011.07.018>.
- [51] L. Sessa, S. Concilio, M. Di Martino, A.M. Nardiello, Y. Miele, F. Rossi, J. Brunetti, B. Panunzi, S. Pioletto, A selective Nile Red based solvatochromic probe: A study of fluorescence in LUVs and GUVs model membranes, *Dye. Pigment.* 196 (2021) 109759, <https://doi.org/10.1016/j.dyepig.2021.109759>.
- [52] T.J. Zuehlsdorff, P.D. Haynes, M.C. Payne, N.D.M. Hine, Predicting solvatochromic shifts and colours of a solvated organic dye: The example of Nile red, *J. Chem. Phys.* 146 (2017), <https://doi.org/10.1063/1.4979196>.
- [53] A. Ray, S. Das, N. Chattopadhyay, Aggregation of Nile Red in Water: Prevention through Encapsulation in  $\beta$ -Cyclodextrin, *ACS Omega* 4 (2019) 15–24, <https://doi.org/10.1021/acsomega.8b02503>.
- [54] T. Felbeck, T. Behnke, K. Hoffmann, M. Grabolle, M.M. Lezhnina, U.H. Kynast, U. Resch-Genger, Nile-red-nanoclay hybrids: Red emissive optical probes for use in aqueous dispersion, *Langmuir* 29 (2013) 11489–11497, <https://doi.org/10.1021/la402165q>.
- [55] J. Saha, A. Datta Roy, D. Dey, S. Chakraborty, D. Bhattacharjee, P.K. Paul, S. A. Hussain, Investigation of fluorescence resonance energy transfer between fluorescein and rhodamine 6G, *Spectrochim. Acta - Part A Mol. Biomol. Spectrosc.* 149 (2015) 143–149, <https://doi.org/10.1016/j.saa.2015.04.027>.
- [56] M. Fischer, J. Georges, Use of thermal lens spectrometry for the investigation of dimerization equilibria of rhodamine 6G in water and aqueous micellar solutions, *Spectrochim. Acta - Part A Mol. Biomol. Spectrosc.* 53 (1997) 1419–1430, [https://doi.org/10.1016/S0584-8539\(97\)00027-5](https://doi.org/10.1016/S0584-8539(97)00027-5).
- [57] A. Ogunsipe, Solvent Effects on the Spectral Properties of Rhodamine 6G: Estimation of Ground and Excited State Dipole Moments, *J. Solution Chem.* 47 (2018) 203–219, <https://doi.org/10.1007/s10953-017-0706-8>.
- [58] F. López Arbeloa, T. López Arbeloa, E. Gil Lage, I. López Arbeloa, F.C. De Schryver, Photophysical properties of rhodamines with monoethylamino groups R19 and R6G in water-ethanol mixtures, *J. Photochem. Photobiol. A Chem.* 56 (1991) 313–321, [https://doi.org/10.1016/1010-6030\(91\)80031-C](https://doi.org/10.1016/1010-6030(91)80031-C).
- [59] S. Salleres, F.L. Arbeloa, V. Martínez, T. Arbeloa, I.L. Arbeloa, Adsorption of fluorescent R6G dye into organophilic C12TMA laponite films, *J. Colloid Interface Sci.* 321 (2008) 212–219, <https://doi.org/10.1016/j.jcis.2007.12.049>.
- [60] K. Suman, Y.M. Joshi, Microstructure and Soft Glassy Dynamics of an Aqueous Laponite Dispersion, *Langmuir* 34 (2018) 13079–13103, <https://doi.org/10.1021/acs.langmuir.8b01830>.
- [61] V.M. Martínez, F.L. Arbeloa, J.B. Prieto, I.L. Arbeloa, Characterization of rhodamine 6G aggregates intercalated in solid thin films of laponite clay. 2 fluorescence spectroscopy, *J. Phys. Chem. B* 109 (2005) 7443–7450, <https://doi.org/10.1021/jp050440i>.
- [62] X.F. Zhang, Y. Zhang, L. Liu, Fluorescence lifetimes and quantum yields of ten rhodamine derivatives: Structural effect on emission mechanism in different solvents, *J. Lumin.* 145 (2014) 448–453, <https://doi.org/10.1016/j.jlumin.2013.07.066>.
- [63] J. Bujdák, Resonance Energy Transfer in Hybrid Systems of Photoactive Dye Molecules and Layered Inorganics, in: V. Martínez-Martínez, L. Arbeloa (Eds.), *Dye. Photoactive Mol. Microporous Syst*, Springer, Cham, 2020, pp. 205–250, [https://doi.org/10.1007/430\\_2020\\_55](https://doi.org/10.1007/430_2020_55).
- [64] O.F. Zaidan, J.A. Greathouse, R.T. Pabalan, Monte Carlo and Molecular Dynamics Simulation of Uranyl Adsorption on Montmorillonite Clay, *Clays Clay Miner.* 51 (2003) 372–381, <https://doi.org/10.1346/CCMN.2003.0510402>.
- [65] E.H. Hill, Investigating Solvent-Induced Aggregation in Edge-Functionalized Layered Silicates via All-Atom Molecular Dynamics Simulations, *J. Phys. Chem. B* 127 (2023) 8066–8073, <https://doi.org/10.1021/acs.jpcc.3c04432>.

## 5. Discussion and Outlook

### 5.1. Discussion

The Lap anisotropic chemical surfaces facilitate independent and targeted modification on each surface. Based on this property, several organic chromophores were covalently bonded or ion-exchanged to the Lap edge surface via covalent bonds or basal surface via ion exchange, respectively, leading to the establishment of three distinct FRET systems between chromophore-modified Lap surfaces. In the first part of this dissertation,<sup>37</sup> two organic-inorganic hybrids were synthesized through covalent linkage of two PDIs—with oleyl-chain or succinic acid as a terminal group, respectively, to the Lap edge surfaces. These hybrids exhibit the photophysical characteristics of PDIs. In aqueous media, the PDI groups of the hybrids formed H-aggregate through  $\pi$ - $\pi$  stacking of perylene cores, with the succinic acid terminal group conferring better water dispersibility compared to the oleyl-chain. Furthermore, FRET from 4',6-diamidino-2-phenylindole (DAPI), which is attached to the Lap basal surface via ion exchange, to covalently bound PDIs on the Lap edge surface was observed. This FRET system achieved efficiencies of 78% in 90% and 79% in 50% water, facilitated by the spatial proximity between edge surface-bound PDIs and basal surface immobilized DAPI.

The second part of this dissertation achieved the synthesis of hybrids where PDIs or NDIs, incorporating tetraethylene glycol or diethylene glycol terminal group, respectively, are covalently linked to the Lap edge surface via silanol coupling.<sup>38</sup> Optical properties and aggregation behavior of synthesized hybrids were investigated in varied DMF/water solvent compositions. The tetraethylene glycol terminal group on PDIs enhanced water dispersibility compared to previously reported PDIs-modified Lap, while NDIs with diethylene glycol terminal group exhibited the formation of excimer associated with AIE. Upon mixing these hybrids' dispersions, FRET from the NDIs excimer at the Lap edge surface to the PDIs at another Lap edge surface was observed, achieving an efficiency of 47% in 90% water. This efficiency was enhanced up to 74% when Lap was pillared with cationic surfactant CTAB. The CTAB intercalated into interlayers of Lap, resulting in an interlayer spacing expansion to approximately 2.3 nm and an ordered stacking of Lap. The ordered stacking of Lap improved donor-acceptor overlap and resulted in such enhancement of FRET.

In the final part of this dissertation, a new organic-inorganic hybrid composed of Nile red derivative, which was linked to the Lap edge surface via silanol coupling, was synthesized.<sup>186</sup> This hybrid exhibited Nile red optical properties, characterized by a pronounced absorption band and a solvatochromic shift in response to varying solvent compositions. Expanding on previous research discussed in the first two chapters, a cascade FRET system was established involving Lap edge covalently bound NDIs as the first donor, and through ion exchanged R6G on the Lap basal surface, and Nile red derivative covalently modified Lap as sequential acceptors. Cascade FRET occurs from Lap edge bound NDIs to Lap basal surface located R6G, and subsequently to Lap edge bound Nile red derivative and an overall highest efficiency of 57% in 67.5% water was achieved.

In summary, this dissertation developed several new organic-inorganic hybrid materials involving modification to the Lap edge surface by covalently linking NDIs, PDIs, and Nile red derivative, and ion-exchanged cationic molecules to its basal surface. Following these modifications, the optical properties of resulting hybrids were investigated, revealing a variety of aggregate behavior: the formation of excimer with AIE in NDIs-modified Lap, H-aggregate formation in PDIs-modified Lap, and solvatochromic property in Nile red derivative-modified Lap. Building on these obtained fluorescent hybrids, FRET investigations were carried out across various configurations: from Lap basal surface immobilized donor to Lap edge surface-bound acceptor, from Lap edge surface-bound donor to Lap edge surface-bound acceptor, and from Lap edge surface bound donor to Lap basal surface located acceptor (also served as a donor for the next step), extending to another Lap edge surface-bound acceptor. These studies demonstrated efficient FRET at relatively low chromophore concentrations. Furthermore, this dissertation uncovered that variations in solvent compositions and aggregation behavior of Lap achieved through the introduction of surfactant, can significantly enhance FRET. These findings presented the potential for advances enabled by the synthesis of hybrids combining two-dimensional nanoparticles and organic chromophores and also provided an expansion of potential applications of nanoparticles in photophysical-based devices, such as light-emitting diodes, biosensors, and photovoltaics.

## 5.2. Outlook

The research results discussed in this dissertation raise various potential future research interests of organic-inorganic hybrids. This section discusses two specific directions of interest that build on the achieved results as examples.

### 5.2.1. Modifications on One-Dimensional Clay

Lap exhibits free silanol groups at the edge surface and negative charges on the basal surface when dispersed in an aqueous medium. This property is fundamental to the research presented in this dissertation. Other clay mineral, such as halloysite, also features anisotropic surfaces and offer the potential for similar modifications. Halloysite is a dioctahedral 1:1 tubular clay from the kaolin group, composed of one  $\text{SiO}_4$  tetrahedral sheet and one  $\text{AlO}_2(\text{OH})_4$  octahedral sheet.<sup>187</sup> The length of a halloysite tube ranges from 0.02 to over 30 micrometers. The internal lumen surface consists of hydrophilic Al-OH groups, resulting in a positively charged surface.<sup>188</sup> This allows for the attachment of anionic chromophores via ion exchange, and the chemically active Al-OH groups enable covalent modification with organic chromophores as well. Conversely, the external surface of the halloysite is composed of hydrophobic Si-O-Si groups, giving it a negatively charged surface, which facilitates the attachment of cationic chromophores through ion exchange.<sup>189</sup> A FRET system could be formed by immobilizing donor and acceptor molecules on the internal lumen surface. Furthermore, donor and acceptor

molecules can also be attached separately to the external surface and the internal lumen surface of halloysite, FRET in such system would likely be less efficient compared to that of a system where both the donor and acceptor molecules are immobilized on the internal lumen surface. The expected different FRET efficiency could be primarily due to spatial separation caused by anisotropic surfaces of halloysite tube.

### **5.2.2. Development of Chromophore-Modified Laponite Thin Films**

This dissertation primarily focused on dispersions, yet the fabrication of modified Lap thin films presents significant potential for the versatile development of Lap-based devices. Techniques such as the evaporation method and spin-coating can be employed to finely tune the morphology of these thin films.<sup>18</sup> The first approach, building on previously reported work, involves the fabrication of thin films using synthesized hybrids. Due to the distinct water dispersibility of all the synthesized hybrids, the formation of thin films could vary in terms of time, solvent polarity, thickness, and mechanical strength. These variables offer insights for optimizing the modification of Lap thin films for targeted applications, such as packing material, drug delivery, and personal care products.<sup>190</sup>

Moreover, the optical properties of Lap thin films also represent a significant area for future research. Investigations into aspects such as chromophore aggregation, polarized fluorescence emission, and energy transfer processes could not only deepen our understanding of the fundamental properties of modified-Lap thin films but also encourage the development of advanced photo-functional materials for a wide range of applications, including optical glasses, biosensors, energy storage devices, and solid-state tunable lasers.<sup>18,191</sup>



## Bibliography

- (1) Braslavsky, S. E. Glossary of Terms Used in Photochemistry, 3rd Edition (IUPAC Recommendations 2006). *Pure Appl. Chem.* **2007**, *79* (3), 293–465. <https://doi.org/10.1351/pac200779030293>.
- (2) Kulmala, S.; Suomi, J. Current Status of Modern Analytical Luminescence Methods. *Anal. Chim. Acta* **2003**, *500* (1–2), 21–69. <https://doi.org/10.1016/j.aca.2003.09.004>.
- (3) Valeur, B.; Berberan-Santos, M. N. Introduction. In *Molecular Fluorescence*; Wiley: Weinheim, Germany, 2012; pp 1–30. <https://doi.org/10.1002/9783527650002.ch1>.
- (4) Saffold, W. E. Lignum Nephriticum. *Annu. Rep. Board Regents Smithsonian Institution.* **1915**, 271–298.
- (5) He, B.; Zhang, J.; Zhang, J.; Zhang, H.; Wu, X.; Chen, X.; Kei, K. H. S.; Qin, A.; Sung, H. H. Y.; Lam, J. W. Y.; Tang, B. Z. Clusteroluminescence from Cluster Excitons in Small Heterocyclics Free of Aromatic Rings. *Adv. Sci.* **2021**, *8* (7). <https://doi.org/10.1002/advs.202004299>.
- (6) Acuña, A. U.; Amat-Guerri, F.; Morcillo, P.; Liras, M.; Rodríguez, B. Structure and Formation of the Fluorescent Compound of Lignum Nephriticum. *Org. Lett.* **2009**, *11* (14), 3020–3023. <https://doi.org/10.1021/ol901022g>.
- (7) Stokes, G. G. On the Change of Refrangibility of Light. *Philos. Trans. R. Soc. London* **1852**, *142*, 463–562. <https://doi.org/10.1098/rstl.1852.0022>.
- (8) Stokes, G. G. On the Change of Refrangibility of Light.—No. II. *Philos. Trans. R. Soc. London* **1853**, *143*, 385–396. <https://doi.org/10.1098/rstl.1853.0016>.
- (9) Bill, H.; Sierro, J.; Lacroix, R. Origin of Coloration in Some Fluorites. *Am. Mineral.* **1967**, *52* No.7-8, 1003–1008.
- (10) Becquerel, E. *La Lumi è Re. Ses Causes et Ses Effets*; Firmin Didot frères, fils et cie: Paris, 1867.
- (11) Perrin, F. La Fluorescence Des Solutions. *Ann. Phys. (Paris).* **1929**, *10* (12), 169–275. <https://doi.org/10.1051/anphys/192910120169>.
- (12) Jabłoński, A. Über Den Mechanismus Der Photolumineszenz von Farbstoffphosphoren. *Zeitschrift für Phys.* **1935**, *94* (1–2), 38–46. <https://doi.org/10.1007/BF01330795>.
- (13) Valeur, B.; Berberan-Santos, M. N. Characteristics of Fluorescence Emission. In *Molecular Fluorescence*; Wiley: Weinheim, Germany, 2012; pp 53–74. <https://doi.org/10.1002/9783527650002.ch3>.
- (14) Marian, C. M. Spin-Orbit Coupling in Molecules. In *Reviews in Computational Chemistry*; Lipkowitz, K. B., Boyd, D. B., Eds.; John Wiley & Sons, Inc., 2001; pp 99–204. <https://doi.org/10.1002/0471224413.ch3>.
- (15) Valeur, B.; Berberan-Santos, M. N. Absorption of Ultraviolet, Visible, and Near-Infrared Radiation. In *Molecular Fluorescence*; Wiley: Weinheim, Germany, 2012; pp 31–51. <https://doi.org/10.1002/9783527650002.ch2>.
- (16) Valeur, B.; Berberan-Santos, M. N. Effects of Intermolecular Photophysical Processes

- on Fluorescence Emission. In *Molecular Fluorescence*; Wiley: Weinheim, Germany, 2012; pp 141–179. <https://doi.org/10.1002/9783527650002.ch6>.
- (17) Lakowicz, J. R. Introduction to Fluorescence. In *Principles of Fluorescence Spectroscopy*; Springer US: Boston, MA, 2006; pp 1–26. [https://doi.org/10.1007/978-0-387-46312-4\\_1](https://doi.org/10.1007/978-0-387-46312-4_1).
- (18) Martínez Martínez, V.; López Arbeloa, F.; Bañuelos Prieto, J.; Arbeloa López, T.; López Arbeloa, I. Characterization of Supported Solid Thin Films of Laponite Clay. Intercalation of Rhodamine 6G Laser Dye. *Langmuir* **2004**, *20* (14), 5709–5717. <https://doi.org/10.1021/la049675w>.
- (19) Birks, J. B. Photophysics of Aromatic Molecules. *Berichte der Bunsengesellschaft für Phys. Chemie* **1970**, *74* (12), 1294–1295. <https://doi.org/10.1002/bbpc.19700741223>.
- (20) Karuppaiah, S.; Krishnan, M. UV-Visible Spectroscopy for Colorimetric Applications. In *Colorimetry*; IntechOpen, 2022. <https://doi.org/10.5772/intechopen.101165>.
- (21) Klessinger, M.; Michl, J. Excited States in Photochemistry of Organic Molecules. *J. Am. Chem. Soc.* **1996**, *118* (7), 1815–1816. <https://doi.org/10.1021/ja955368o>.
- (22) Schleyer, P. von R. Introduction: Aromaticity. *Chem. Rev.* **2001**, *101* (5), 1115–1118. <https://doi.org/10.1021/cr0103221>.
- (23) Jones, R. N. Some Factors Influencing the Ultraviolet Absorption Spectra of Polynuclear Aromatic Compounds. II. The Spectra of Aryl Carbinols and Polybenzfluorenes. *J. Am. Chem. Soc.* **1945**, *67* (11), 2021–2027. <https://doi.org/10.1021/ja01227a047>.
- (24) Clar, E. Absorption Spectra of Aromatic Hydrocarbons at Low Temperatures. LV-Aromatic Hydrocarbons. *Spectrochim. Acta* **1950**, *4* (2), 116–121. [https://doi.org/10.1016/S0371-1951\(50\)80005-X](https://doi.org/10.1016/S0371-1951(50)80005-X).
- (25) Jin, H.; Giri, B. R.; Liu, D.; Farooq, A. A High Temperature Shock Tube Study of Phenyl Recombination Reaction Using Laser Absorption Spectroscopy. *Proc. Combust. Inst.* **2021**, *38* (1), 919–927. <https://doi.org/10.1016/j.proci.2020.06.164>.
- (26) Zhao, X.; Xiong, Y.; Ma, J.; Yuan, Z. Rylene and Rylene Diimides: Comparison of Theoretical and Experimental Results and Prediction for High-Rylene Derivatives. *J. Phys. Chem. A* **2016**, *120* (38), 7554–7560. <https://doi.org/10.1021/acs.jpca.6b07552>.
- (27) Weil, T.; Vosch, T.; Hofkens, J.; Peneva, K.; Müllen, K. The Rylene Colorant Family—Tailored Nanoemitters for Photonics Research and Applications. *Angew. Chemie Int. Ed.* **2010**, *49* (48), 9068–9093. <https://doi.org/10.1002/anie.200902532>.
- (28) Chen, L.; Li, C.; Müllen, K. Beyond Perylene Diimides: Synthesis, Assembly and Function of Higher Rylene Chromophores. *J. Mater. Chem. C* **2014**, *2* (11), 1938–1956. <https://doi.org/10.1039/C3TC32315C>.
- (29) Liang, N.; Meng, D.; Wang, Z. Giant Rylene Imide-Based Electron Acceptors for Organic Photovoltaics. *Acc. Chem. Res.* **2021**, *54* (4), 961–975. <https://doi.org/10.1021/acs.accounts.0c00677>.
- (30) Yan, C.; Barlow, S.; Wang, Z.; Yan, H.; Jen, A. K.-Y.; Marder, S. R.; Zhan, X. Non-Fullerene Acceptors for Organic Solar Cells. *Nat. Rev. Mater.* **2018**, *3* (3), 18003. <https://doi.org/10.1038/natrevmats.2018.3>.

- (31) Liang, N.; Jiang, W.; Hou, J.; Wang, Z. New Developments in Non-Fullerene Small Molecule Acceptors for Polymer Solar Cells. *Mater. Chem. Front.* **2017**, *1* (7), 1291–1303. <https://doi.org/10.1039/C6QM00247A>.
- (32) Biradar, M. R.; Bhosale, S. V.; Morajakar, P. P.; Bhosale, S. V. A Review on Energy Storage Devices Based on Rylene Imide Dyes: Synthesis, Applications and Challenges. *Fuel* **2022**, *310*, 122487. <https://doi.org/10.1016/j.fuel.2021.122487>.
- (33) Karmakar, P.; Manna, S.; Maiti, K.; Ali, S. S.; Guria, U. N.; Sarkar, R.; Datta, P.; Mandal, D.; Mahapatra, A. K. A Perylene Diimide Based Fluorescent Probe for Caffeine in Aqueous Medium. *Supramol. Chem.* **2019**, *31* (1), 28–35. <https://doi.org/10.1080/10610278.2018.1530352>.
- (34) Kumar, K.; Kaur, S.; Kaur, S.; Bhargava, G.; Kumar, S.; Singh, P. Self-Assembled Nanofibers of Perylene Diimide for the Detection of Hypochlorite in Water, Bio-Fluids and Solid-State: Exogenous and Endogenous Bioimaging of Hypochlorite in Cells. *J. Mater. Chem. B* **2020**, *8* (1), 125–135. <https://doi.org/10.1039/C9TB01902B>.
- (35) Schill, J.; van Dun, S.; Pouderoijen, M. J.; Janssen, H. M.; Milroy, L.; Schenning, A. P. H. J.; Brunsveld, L. Synthesis and Self-Assembly of Bay-Substituted Perylene Diimide Gemini-Type Surfactants as Off-On Fluorescent Probes for Lipid Bilayers. *Chem. – A Eur. J.* **2018**, *24* (30), 7734–7741. <https://doi.org/10.1002/chem.201801022>.
- (36) Yuan, L.; Lin, W.; Zheng, K.; Zhu, S. FRET-Based Small-Molecule Fluorescent Probes: Rational Design and Bioimaging Applications. *Acc. Chem. Res.* **2013**, *46* (7), 1462–1473. <https://doi.org/10.1021/ar300273v>.
- (37) Xiang, H.; Valandro, S. R.; Hill, E. H. Layered Silicate Edge-Linked Perylene Diimides: Synthesis, Self-Assembly and Energy Transfer. *J. Colloid Interface Sci.* **2023**, *629*, 300–306. <https://doi.org/10.1016/j.jcis.2022.09.055>.
- (38) Xiang, H.; Valandro, S. R.; Hill, E. H. 2D Nanomaterial-Directed Molecular Aggregation and Energy Transfer between Edge-Bound Donor-Acceptor Pairs. *J. Phys. Chem. C* **2023**, *127* (31), 15416–15422. <https://doi.org/10.1021/acs.jpcc.3c04555>.
- (39) Lee, S. K.; Zu, Y.; Herrmann, A.; Geerts, Y.; Müllen, K.; Bard, A. J. Electrochemistry, Spectroscopy and Electrogenenerated Chemiluminescence of Perylene, Terrylene, and Quaterylene Diimides in Aprotic Solution. *J. Am. Chem. Soc.* **1999**, *121* (14), 3513–3520. <https://doi.org/10.1021/ja984188m>.
- (40) Bhosale, S. V.; Jani, C. H.; Langford, S. J. Chemistry of Naphthalene Diimides. *Chem. Soc. Rev.* **2008**, *37* (2), 331–342. <https://doi.org/10.1039/B615857A>.
- (41) Würthner, F.; Ahmed, S.; Thalacker, C.; Debaerdemaeker, T. Core-Substituted Naphthalene Bisimides: New Fluorophors with Tunable Emission Wavelength for FRET Studies. *Chem. - A Eur. J.* **2002**, *8* (20), 4742–4750. [https://doi.org/10.1002/1521-3765\(20021018\)8:20<4742::AID-CHEM4742>3.0.CO;2-L](https://doi.org/10.1002/1521-3765(20021018)8:20<4742::AID-CHEM4742>3.0.CO;2-L).
- (42) Vollmann, H.; Becker, H.; Corell, M.; Streeck, H. Beiträge Zur Kenntnis Des Pyrens Und Seiner Derivate. *Justus Liebigs Ann. Chem.* **1937**, *531* (1), 1–159. <https://doi.org/10.1002/jlac.19375310102>.
- (43) Sasikumar, M.; Suseela, Y. V.; Govindaraju, T. Dibromohydantoin: A Convenient Brominating Reagent for 1,4,5,8-Naphthalenetetracarboxylic Dianhydride. *Asian J. Org. Chem.* **2013**, *2* (9), 779–785. <https://doi.org/10.1002/ajoc.201300088>.

- (44) Sessler, J. L.; Brown, C. T.; O'Connor, D.; Springs, S. L.; Wang, R.; Sathiosatham, M.; Hirose, T. A Rigid Chlorin–Naphthalene Diimide Conjugate. A Possible New Noncovalent Electron Transfer Model System. *J. Org. Chem.* **1998**, *63* (21), 7370–7374. <https://doi.org/10.1021/jo9810112>.
- (45) Pengo, P.; Pantoş, G. D.; Otto, S.; Sanders, J. K. M. Efficient and Mild Microwave-Assisted Stepwise Functionalization of Naphthalenediimide with  $\alpha$ -Amino Acids. *J. Org. Chem.* **2006**, *71* (18), 7063–7066. <https://doi.org/10.1021/jo061195h>.
- (46) Imato, K.; Yamanaka, R.; Nakajima, H.; Takeda, N. Fluorescent Supramolecular Mechanophores Based on Charge-Transfer Interactions. *Chem. Commun.* **2020**, *56* (57), 7937–7940. <https://doi.org/10.1039/d0cc03126g>.
- (47) Kumari, N.; Naqvi, S.; Ahuja, M.; Bhardwaj, K.; Kumar, R. Facile Synthesis of Naphthalene Diimide (NDI) Derivatives: Aggregation-Induced Emission, Photophysical and Transport Properties. *J. Mater. Sci. Mater. Electron.* **2020**, *31* (5), 4310–4322. <https://doi.org/10.1007/s10854-020-02986-8>.
- (48) Maniam, S.; Higginbotham, H. F.; Bell, T. D. M.; Langford, S. J. Harnessing Brightness in Naphthalene Diimides. *Chem. - A Eur. J.* **2019**, *25* (29), 7044–7057. <https://doi.org/10.1002/chem.201806008>.
- (49) Sakai, N.; Mareda, J.; Vauthey, E.; Matile, S. Core-Substituted Naphthalenediimides. *Chem. Commun.* **2010**, *46* (24), 4225. <https://doi.org/10.1039/c0cc00078g>.
- (50) Huang, C.; Barlow, S.; Marder, S. R. Perylene-3,4,9,10-Tetracarboxylic Acid Diimides: Synthesis, Physical Properties, and Use in Organic Electronics. *J. Org. Chem.* **2011**, *76* (8), 2386–2407. <https://doi.org/10.1021/jo2001963>.
- (51) Würthner, F. Perylene Bisimide Dyes as Versatile Building Blocks for Functional Supramolecular Architectures. *Chem. Commun.* **2004**, *4* (14), 1564–1579. <https://doi.org/10.1039/b401630k>.
- (52) Kardos, M. Über Einige Aceanthrenchinon- Und 1.9-Anthracen-Derivate. *Berichte der Dtsch. Chem. Gesellschaft* **1913**, *46* (2), 2086–2091. <https://doi.org/10.1002/cber.191304602126>.
- (53) Wonneberger, H.; Ma, C.-Q.; Gatys, M. A.; Li, C.; Bäuerle, P.; Müllen, K. Terthiophene–Perylene Diimides: Color Tuning via Architecture Variation. *J. Phys. Chem. B* **2010**, *114* (45), 14343–14347. <https://doi.org/10.1021/jp911800q>.
- (54) Giri, D.; Raut, S. K.; Patra, S. K. Diketopyrrolopyrrole/Perylene-Diimide and Thiophene Based D- $\pi$ -A Low Bandgap Polymer Sensitizers for Application in Dye Sensitized Solar Cells. *Dye. Pigment.* **2020**, *174*, 108032. <https://doi.org/10.1016/j.dyepig.2019.108032>.
- (55) Zafer, C.; Kus, M.; Turkmen, G.; Dincalp, H.; Demic, S.; Kuban, B.; Teoman, Y.; Icli, S. New Perylene Derivative Dyes for Dye-Sensitized Solar Cells. *Sol. Energy Mater. Sol. Cells* **2007**, *91* (5), 427–431. <https://doi.org/10.1016/j.solmat.2006.10.004>.
- (56) Kozma, E.; Catellani, M. Perylene Diimides Based Materials for Organic Solar Cells. *Dye. Pigment.* **2013**, *98* (1), 160–179. <https://doi.org/10.1016/j.dyepig.2013.01.020>.
- (57) Li, C.; Wonneberger, H. Perylene Imides for Organic Photovoltaics: Yesterday, Today, and Tomorrow. *Adv. Mater.* **2012**, *24* (5), 613–636. <https://doi.org/10.1002/adma.201104447>.

- (58) Mohapatra, A. A.; Pranav, M.; Yadav, S.; Gangadharappa, C.; Wu, J.; Labanti, C.; Wolansky, J.; Benduhn, J.; Kim, J.-S.; Durrant, J.; Patil, S. Interface Engineering in Perylene Diimide-Based Organic Photovoltaics with Enhanced Photovoltage. *ACS Appl. Mater. Interfaces* **2023**, *15* (21), 25224–25231. <https://doi.org/10.1021/acsami.3c02003>.
- (59) Farahat, M. E.; Welch, G. C. N-Annulated Perylene Diimide Non-Fullerene Acceptors for Organic Photovoltaics. *Colorants* **2023**, *2* (1), 151–178. <https://doi.org/10.3390/colorants2010011>.
- (60) Würthner, F.; Stolte, M. Naphthalene and Perylene Diimides for Organic Transistors. *Chem. Commun.* **2011**, *47* (18), 5109. <https://doi.org/10.1039/c1cc10321k>.
- (61) Yuen, J. D.; Pozdin, V. A.; Young, A. T.; Turner, B. L.; Giles, I. D.; Naciri, J.; Trammell, S. A.; Charles, P. T.; Stenger, D. A.; Daniele, M. A. Perylene-Diimide-Based n-Type Semiconductors with Enhanced Air and Temperature Stable Photoconductor and Transistor Properties. *Dye. Pigment.* **2020**, *174*, 108014. <https://doi.org/10.1016/j.dyepig.2019.108014>.
- (62) Nagao, Y. Synthesis and Properties of Perylene Pigments. *Prog. Org. Coatings* **1997**, *31* (1–2), 43–49. [https://doi.org/10.1016/S0300-9440\(97\)00017-9](https://doi.org/10.1016/S0300-9440(97)00017-9).
- (63) Huang, H.; Che, Y.; Zang, L. Direct Synthesis of Highly Pure Perylene Tetracarboxylic Monoimide. *Tetrahedron Lett.* **2010**, *51* (50), 6651–6653. <https://doi.org/10.1016/j.tetlet.2010.10.071>.
- (64) Nagao, Y.; Abe, Y.; Misono, T. Synthesis and Properties of N,N'-Unsymmetrical Dialkyl-3,4,9,10-Perylenebis(Dicarboximide)s. *Dye. Pigment.* **1985**, *6* (4), 303–311. [https://doi.org/10.1016/0143-7208\(85\)87006-6](https://doi.org/10.1016/0143-7208(85)87006-6).
- (65) Pasaogullari, N.; Icil, H.; Demuth, M. Symmetrical and Unsymmetrical Perylene Diimides: Their Synthesis, Photophysical and Electrochemical Properties. *Dye. Pigment.* **2006**, *69* (3), 118–127. <https://doi.org/10.1016/j.dyepig.2005.03.001>.
- (66) Sebastian, E.; Hariharan, M. Null Exciton-Coupled Chromophoric Dimer Exhibits Symmetry-Breaking Charge Separation. *J. Am. Chem. Soc.* **2021**, *143* (34). <https://doi.org/10.1021/jacs.1c05793>.
- (67) Rocard, L.; Goujon, A.; Hudhomme, P. Nitro-Perylenediimide: An Emerging Building Block for the Synthesis of Functional Organic Materials. *Molecules* **2020**, *25* (6), 1402. <https://doi.org/10.3390/molecules25061402>.
- (68) Asir, S.; Demir, A. S.; Icil, H. The Synthesis of Novel, Unsymmetrically Substituted, Chiral Naphthalene and Perylene Diimides: Photophysical, Electrochemical, Chiroptical and Intramolecular Charge Transfer Properties. *Dye. Pigment.* **2010**, *84* (1), 1–13. <https://doi.org/10.1016/j.dyepig.2009.04.014>.
- (69) Chen, K.-Y.; Chang, C.-W. Highly Soluble Monoamino-Substituted Perylene Tetracarboxylic Dianhydrides: Synthesis, Optical and Electrochemical Properties. *Int. J. Mol. Sci.* **2014**, *15* (12), 22642–22660. <https://doi.org/10.3390/ijms151222642>.
- (70) Tsai, H.-Y.; Chang, C.-W.; Chen, K.-Y. 1,6- and 1,7-Regioisomers of Dinitro- and Diamino-Substituted Perylene Bisimides: Synthesis, Photophysical and Electrochemical Properties. *Tetrahedron Lett.* **2014**, *55* (4), 884–888. <https://doi.org/10.1016/j.tetlet.2013.12.041>.
- (71) Rocard, L.; Hatych, D.; Chartier, T.; Cauchy, T.; Hudhomme, P. Original Suzuki–

- Miyaura Coupling Using Nitro Derivatives for the Synthesis of Perylene diimide-Based Multimers. *European J. Org. Chem.* **2019**, 2019 (47), 7635–7643. <https://doi.org/10.1002/ejoc.201901319>.
- (72) Gupta, R. K.; Shankar Rao, D. S.; Prasad, S. K.; Achalkumar, A. S. Columnar Self-Assembly of Electron-Deficient Dendronized Bay -Annulated Perylene Bisimides. *Chem. – A Eur. J.* **2018**, 24 (14), 3566–3575. <https://doi.org/10.1002/chem.201705290>.
- (73) Wu, J.; Peng, M.; Mu, M.; Li, J.; Yin, M. Perylene Diimide Supramolecular Aggregates: Constructions and Sensing Applications. *Supramol. Mater.* **2023**, 2, 100031. <https://doi.org/10.1016/j.supmat.2023.100031>.
- (74) Stepanenko, V.; Li, X. Q.; Gershberg, J.; Würthner, F. Evidence for Kinetic Nucleation in Helical Nanofiber Formation Directed by Chiral Solvent for a Perylene Bisimide Organogelator. *Chem. - A Eur. J.* **2013**, 19 (13), 4176–4183. <https://doi.org/10.1002/chem.201204146>.
- (75) Spano, F. C.; Silva, C. H- and J-Aggregate Behavior in Polymeric Semiconductors. *Annu. Rev. Phys. Chem.* **2014**, 65 (1), 477–500. <https://doi.org/10.1146/annurev-physchem-040513-103639>.
- (76) JELLEY, E. E. Spectral Absorption and Fluorescence of Dyes in the Molecular State. *Nature* **1936**, 138 (3502), 1009–1010. <https://doi.org/10.1038/1381009a0>.
- (77) Shao, H.; Parquette, J. R. A  $\pi$ -Conjugated Hydrogel Based on an Fmoc-Dipeptide Naphthalene Diimide Semiconductor. *Chem. Commun.* **2010**, 46 (24), 4285. <https://doi.org/10.1039/c0cc00701c>.
- (78) Kar, H.; Gehrig, D. W.; Laquai, F.; Ghosh, S. J-Aggregation, Its Impact on Excited State Dynamics and Unique Solvent Effects on Macroscopic Assembly of a Core-Substituted Naphthalenediimide. *Nanoscale* **2015**, 7 (15), 6729–6736. <https://doi.org/10.1039/C5NR00483G>.
- (79) Hestand, N. J.; Spano, F. C. Expanded Theory of H- and J-Molecular Aggregates: The Effects of Vibronic Coupling and Intermolecular Charge Transfer. *Chem. Rev.* **2018**, 118 (15), 7069–7163. <https://doi.org/10.1021/acs.chemrev.7b00581>.
- (80) Luo, J.; Xie, Z.; Lam, J. W. Y.; Cheng, L.; Tang, B. Z.; Chen, H.; Qiu, C.; Kwok, H. S.; Zhan, X.; Liu, Y.; Zhu, D. Aggregation-Induced Emission of 1-Methyl-1,2,3,4,5-Pentaphenylsilole. *Chem. Commun.* **2001**, No. 18, 1740–1741. <https://doi.org/10.1039/b105159h>.
- (81) Guan, J.; Shen, C.; Peng, J.; Zheng, J. What Leads to Aggregation-Induced Emission? *J. Phys. Chem. Lett.* **2021**, 12 (17), 4218–4226. <https://doi.org/10.1021/acs.jpcllett.0c03861>.
- (82) Tong, D.; Duan, H.; Wang, J.; Yang, Z.; Lin, Y. Aggregation-Enhanced Excimer Emission (AEEE) Based on Pyrenylchalcone and 2-to-4 Molecular Decoder by Biothiols and Polyanions in Aqueous Media. *Sensors Actuators B Chem.* **2014**, 195, 80–84. <https://doi.org/10.1016/j.snb.2014.01.003>.
- (83) Kaur, A.; Lim, Z.; Yang, K.; New, E. J. Fluorescent Sensors for Biological Metal Ions. In *Comprehensive Supramolecular Chemistry II*; Elsevier, 2017; pp 295–317. <https://doi.org/10.1016/B978-0-12-409547-2.12612-5>.
- (84) Das, A.; Ghosh, S. H-Bonding Directed Programmed Supramolecular Assembly of

- Naphthalene-Diimide (NDI) Derivatives. *Chem. Commun.* **2016**, 52 (42), 6860–6872. <https://doi.org/10.1039/C6CC01983H>.
- (85) Bhosale, R. S.; Al Kobaisi, M.; Bhosale, S. V.; Bhargava, S.; Bhosale, S. V. Flower-like Supramolecular Self-Assembly of Phosphonic Acid Appended Naphthalene Diimide and Melamine. *Sci. Rep.* **2015**, 5 (1), 14609. <https://doi.org/10.1038/srep14609>.
- (86) Insuasty, A.; Carrara, S.; Xuechen, J.; McNeill, C. R.; Hogan, C.; Langford, S. J. Aggregation-Induced Emission of Naphthalene Diimides: Effect of Chain Length on Liquid and Solid-Phase Emissive Properties. *Chem. – An Asian J.* **2024**, 19 (9). <https://doi.org/10.1002/asia.202400152>.
- (87) Kobaisi, M. Al; Bhosale, S. V.; Latham, K.; Raynor, A. M.; Bhosale, S. V. Functional Naphthalene Diimides: Synthesis, Properties, and Applications. *Chem. Rev.* **2016**, 116 (19), 11685–11796. <https://doi.org/10.1021/acs.chemrev.6b00160>.
- (88) Pervin, R.; Manian, A.; Chen, Z.; Christofferson, A. J.; Owyong, T. C.; Bradley, S. J.; White, J. M.; Ghiggino, K. P.; Russo, S. P.; Wong, W. W. H. Medium Effects on the Fluorescence of Imide-Substituted Naphthalene Diimides. *J. Photochem. Photobiol. A Chem.* **2023**, 436, 114364. <https://doi.org/10.1016/j.jphotochem.2022.114364>.
- (89) Zhao, H.; Hussain, S.; Liu, X.; Li, S.; Lv, F.; Liu, L.; Wang, S. Design of an Amphiphilic Perylene Diimide for Optical Recognition of Anticancer Drug through a Chirality-Induced Helical Structure. *Chem. – A Eur. J.* **2019**, 25 (42), 9834–9839. <https://doi.org/10.1002/chem.201901948>.
- (90) Valeur, B.; Berberan-Santos, M. N. Excitation Energy Transfer. In *Molecular Fluorescence*; Wiley: Weinheim, Germany, 2012; pp 213–261. <https://doi.org/10.1002/9783527650002.ch8>.
- (91) Förster, T. Zwischenmolekulare Energiewanderung Und Fluoreszenz. *Ann. Phys.* **1948**, 437 (1–2), 55–75. <https://doi.org/10.1002/andp.19484370105>.
- (92) Scholes, G. D. Long-Range Resonance Energy Transfer in Molecular Systems. *Annu. Rev. Phys. Chem.* **2003**, 54 (1), 57–87. <https://doi.org/10.1146/annurev.physchem.54.011002.103746>.
- (93) Sahoo, H. Förster Resonance Energy Transfer - A Spectroscopic Nanoruler: Principle and Applications. *J. Photochem. Photobiol. C Photochem. Rev.* **2011**, 12 (1), 20–30. <https://doi.org/10.1016/j.jphotochemrev.2011.05.001>.
- (94) Lakowicz, J. R. Energy Transfer. In *Principles of Fluorescence Spectroscopy*; Springer US: Boston, MA, 1999; pp 367–394. [https://doi.org/10.1007/978-1-4757-3061-6\\_13](https://doi.org/10.1007/978-1-4757-3061-6_13).
- (95) Tan, H.; Wu, X.; Weng, Y.; Lu, Y.; Huang, Z.-Z. Self-Assembled FRET Nanoprobe with Metal–Organic Framework As a Scaffold for Ratiometric Detection of Hypochlorous Acid. *Anal. Chem.* **2020**, 92 (4), 3447–3454. <https://doi.org/10.1021/acs.analchem.9b05565>.
- (96) Wang, J.; Chen, H.; Ru, F.; Zhang, Z.; Mao, X.; Shan, D.; Chen, J.; Lu, X. Encapsulation of Dual-Emitting Fluorescent Magnetic Nanoprobe in Metal-Organic Frameworks for Ultrasensitive Ratiometric Detection of Cu 2+. *Chem. – A Eur. J.* **2018**, 24 (14), 3499–3505. <https://doi.org/10.1002/chem.201704557>.
- (97) Wang, Z.; Chen, R.; Xiong, Y.; Cepe, K.; Schneider, J.; Zboril, R.; Lee, C.; Rogach, A. L. Incorporating Copper Nanoclusters into Metal-Organic Frameworks: Confinement-

- Assisted Emission Enhancement and Application for Trinitrotoluene Detection. *Part. Part. Syst. Charact.* **2017**, *34* (6). <https://doi.org/10.1002/ppsc.201700029>.
- (98) Jia, J.; Gutiérrez-Arzaluz, L.; Shekhah, O.; Alsadun, N.; Czaban-Jóźwiak, J.; Zhou, S.; Bakr, O. M.; Mohammed, O. F.; Eddaoudi, M. Access to Highly Efficient Energy Transfer in Metal–Organic Frameworks via Mixed Linkers Approach. *J. Am. Chem. Soc.* **2020**, *142* (19), 8580–8584. <https://doi.org/10.1021/jacs.0c02007>.
- (99) Cao, L.-H.; Li, H.-Y.; Xu, H.; Wei, Y.-L.; Zang, S.-Q. Diverse Dissolution–Recrystallization Structural Transformations and Sequential Förster Resonance Energy Transfer Behavior of a Luminescent Porous Cd-MOF. *Dalt. Trans.* **2017**, *46* (35), 11656–11663. <https://doi.org/10.1039/C7DT02697H>.
- (100) Yang, W.; Zhang, G.; Weng, W.; Qiu, B.; Guo, L.; Lin, Z.; Chen, G. Signal on Fluorescence Biosensor for MMP-2 Based on FRET between Semiconducting Polymer Dots and a Metal Organic Framework. *RSC Adv.* **2014**, *4* (102), 58852–58857. <https://doi.org/10.1039/C4RA12478B>.
- (101) Côté, A. P.; Benin, A. I.; Ockwig, N. W.; O’Keeffe, M.; Matzger, A. J.; Yaghi, O. M. Porous, Crystalline, Covalent Organic Frameworks. *Science (80-. )*. **2005**, *310* (5751), 1166–1170. <https://doi.org/10.1126/science.1120411>.
- (102) Bao, B.; Ma, M.; Zai, H.; Zhang, L.; Fu, N.; Huang, W.; Wang, L. Conjugated Polymer Nanoparticles for Label-Free and Bioconjugate-Recognized DNA Sensing in Serum. *Adv. Sci.* **2015**, *2* (3). <https://doi.org/10.1002/advs.201400009>.
- (103) Liu, W.; Cao, Y.; Wang, W.; Gong, D.; Cao, T.; Qian, J.; Iqbal, K.; Qin, W.; Guo, H. Mechanochromic Luminescent Covalent Organic Frameworks for Highly Selective Hydroxyl Radical Detection. *Chem. Commun.* **2019**, *55* (2), 167–170. <https://doi.org/10.1039/C8CC07783E>.
- (104) Wessig, P.; Behrends, N.; Kumke, M. U.; Eisold, U. FRET Pairs with Fixed Relative Orientation of Chromophores. *European J. Org. Chem.* **2016**, *2016* (26), 4476–4486. <https://doi.org/10.1002/ejoc.201600489>.
- (105) Albers, A. E.; Okreglak, V. S.; Chang, C. J. A FRET-Based Approach to Ratiometric Fluorescence Detection of Hydrogen Peroxide. *J. Am. Chem. Soc.* **2006**, *128* (30), 9640–9641. <https://doi.org/10.1021/ja063308k>.
- (106) Lou, X.-Y.; Song, N.; Yang, Y.-W. Fluorescence Resonance Energy Transfer Systems in Supramolecular Macrocyclic Chemistry. *Molecules* **2017**, *22* (10), 1640. <https://doi.org/10.3390/molecules22101640>.
- (107) Wright, D. S.; Niu, H.-C. Supramolecular Chemistry of P-Block Elements. In *Comprehensive Inorganic Chemistry III*; Elsevier, 2023; pp 652–664. <https://doi.org/10.1016/B978-0-12-823144-9.00004-2>.
- (108) Del Valle, E. M. M. Cyclodextrins and Their Uses: A Review. *Process Biochem.* **2004**, *39* (9), 1033–1046. [https://doi.org/10.1016/S0032-9592\(03\)00258-9](https://doi.org/10.1016/S0032-9592(03)00258-9).
- (109) Guo, D.-S.; Liu, Y. Calixarene-Based Supramolecular Polymerization in Solution. *Chem. Soc. Rev.* **2012**, *41* (18), 5907. <https://doi.org/10.1039/c2cs35075k>.
- (110) Lee, J. W.; Samal, S.; Selvapalam, N.; Kim, H.-J.; Kim, K. Cucurbituril Homologues and Derivatives: New Opportunities in Supramolecular Chemistry. *Acc. Chem. Res.* **2003**, *36* (8), 621–630. <https://doi.org/10.1021/ar020254k>.



- (111) Sathiyajith, C.; Shaikh, R. R.; Han, Q.; Zhang, Y.; Meguellati, K.; Yang, Y.-W. Biological and Related Applications of Pillar[n]Arenes. *Chem. Commun.* **2017**, 53 (4), 677–696. <https://doi.org/10.1039/C6CC08967D>.
- (112) Ogoshi, T.; Yamafuji, D.; Yamagishi, T.; Brouwer, A. M. Förster Resonance Energy Transfer by Formation of a Mechanically Interlocked [2]Rotaxane. *Chem. Commun.* **2013**, 49 (48), 5468. <https://doi.org/10.1039/c3cc42612b>.
- (113) Bojtár, M.; Szakács, Z.; Hessz, D.; Bazsó, F. L.; Kállay, M.; Kubinyi, M.; Bitter, I. Supramolecular FRET Modulation by Pseudorotaxane Formation of a Ditopic Stilbazolium Dye and Carboxylato-Pillar[5]Arene. *Dye. Pigment.* **2016**, 133, 415–423. <https://doi.org/10.1016/j.dyepig.2016.06.030>.
- (114) Valdez, S.; Robertson, M.; Qiang, Z. Fluorescence Resonance Energy Transfer Measurements in Polymer Science: A Review. *Macromol. Rapid Commun.* **2022**, 43 (24), 1–19. <https://doi.org/10.1002/marc.202200421>.
- (115) Sethy, R.; Kumar, J.; Métivier, R.; Louis, M.; Nakatani, K.; Mecheri, N. M. T.; Subhakumari, A.; Thomas, K. G.; Kawai, T.; Nakashima, T. Enantioselective Light Harvesting with Perylenediimide Guests on Self-Assembled Chiral Naphthalenediimide Nanofibers. *Angew. Chemie Int. Ed.* **2017**, 56 (47), 15053–15057. <https://doi.org/10.1002/anie.201707160>.
- (116) Xu, L.; Chen, D.; Zhang, Q.; He, T.; Lu, C.; Shen, X.; Tang, D.; Qiu, H.; Zhang, M.; Yin, S. A Fluorescent Cross-Linked Supramolecular Network Formed by Orthogonal Metal-Coordination and Host–Guest Interactions for Multiple Ratiometric Sensing. *Polym. Chem.* **2018**, 9 (4), 399–403. <https://doi.org/10.1039/C7PY01788J>.
- (117) Gao, Z.; Han, Y.; Wang, F. Cooperative Supramolecular Polymers with Anthracene–endoperoxide Photo-Switching for Fluorescent Anti-Counterfeiting. *Nat. Commun.* **2018**, 9 (1), 3977. <https://doi.org/10.1038/s41467-018-06392-x>.
- (118) Baker, M. B.; Albertazzi, L.; Voets, I. K.; Leenders, C. M. A.; Palmans, A. R. A.; Pavan, G. M.; Meijer, E. W. Consequences of Chirality on the Dynamics of a Water-Soluble Supramolecular Polymer. *Nat. Commun.* **2015**, 6 (1), 6234. <https://doi.org/10.1038/ncomms7234>.
- (119) Huang, C.-B.; Xu, L.; Zhu, J.-L.; Wang, Y.-X.; Sun, B.; Li, X.; Yang, H.-B. Real-Time Monitoring the Dynamics of Coordination-Driven Self-Assembly by Fluorescence-Resonance Energy Transfer. *J. Am. Chem. Soc.* **2017**, 139 (28), 9459–9462. <https://doi.org/10.1021/jacs.7b04659>.
- (120) Leenders, C. M. A.; Baker, M. B.; Pijpers, I. A. B.; Lafleur, R. P. M.; Albertazzi, L.; Palmans, A. R. A.; Meijer, E. W. Supramolecular Polymerisation in Water; Elucidating the Role of Hydrophobic and Hydrogen-Bond Interactions. *Soft Matter* **2016**, 12 (11), 2887–2893. <https://doi.org/10.1039/C5SM02843D>.
- (121) Bujdák, J. Hybrid Systems Based on Organic Dyes and Clay Minerals: Fundamentals and Potential Applications. *Clay Miner.* **2015**, 50 (5), 549–571. <https://doi.org/10.1180/claymin.2015.050.5.01>.
- (122) Nakayama, A.; Mizuno, J.; Ohtani, Y.; Shimada, T.; Takagi, S. Elucidation of the Adsorption Distribution of Cationic Porphyrin on the Inorganic Surface by Energy Transfer as a Molecular Ruler. *J. Phys. Chem. C* **2018**, 122 (8), 4365–4371. <https://doi.org/10.1021/acs.jpcc.7b12104>.

- (123) Ishida, Y.; Takagi, S. Tuning Emission Properties by Dye Encapsulation into Layered Silicates. In *Dyes and Photoactive Molecules in Microporous Systems*; 2020; pp 185–204. [https://doi.org/10.1007/430\\_2020\\_58](https://doi.org/10.1007/430_2020_58).
- (124) Kesrevani, R. K.; Sharma, A. K. Nanoarchitected Biomaterials: Present Status and Future Prospects in Drug Delivery. In *Nanoarchitectonics for Smart Delivery and Drug Targeting*; Elsevier, 2016; pp 35–66. <https://doi.org/10.1016/B978-0-323-47347-7.00002-1>.
- (125) Verma, A. K.; Noumani, A.; Yadav, A. K.; Solanki, P. R. FRET Based Biosensor: Principle Applications Recent Advances and Challenges. *Diagnostics* **2023**, *13* (8), 1375. <https://doi.org/10.3390/diagnostics13081375>.
- (126) Shi, L.; Rosenzweig, N.; Rosenzweig, Z. Luminescent Quantum Dots Fluorescence Resonance Energy Transfer-Based Probes for Enzymatic Activity and Enzyme Inhibitors. *Anal. Chem.* **2007**, *79* (1), 208–214. <https://doi.org/10.1021/ac0614644>.
- (127) Li, L.; Liu, J.; Yang, X.; Peng, Z.; Liu, W.; Xu, J.; Tang, J.; He, X.; Wang, K. Quantum Dot/Methylene Blue FRET Mediated NIR Fluorescent Nanomicelles with Large Stokes Shift for Bioimaging. *Chem. Commun.* **2015**, *51* (76), 14357–14360. <https://doi.org/10.1039/C5CC06258F>.
- (128) Clapp, A. R.; Medintz, I. L.; Fisher, B. R.; Anderson, G. P.; Mattoussi, H. Can Luminescent Quantum Dots Be Efficient Energy Acceptors with Organic Dye Donors? *J. Am. Chem. Soc.* **2005**, *127* (4), 1242–1250. <https://doi.org/10.1021/ja045676z>.
- (129) Wu, N.; Kirkwood, N.; Neto, N. S.; Pervin, R.; Mulvaney, P.; Wong, W. W. H. Energy Transfer between CdZnS Quantum Dots and Perylene Diimide Dyes. *J. Phys. Chem. C* **2023**, *127* (4), 2116–2126. <https://doi.org/10.1021/acs.jpcc.3c00053>.
- (130) Dworak, L.; Matylitsky, V. V.; Ren, T.; Basché, T.; Wachtveitl, J. Acceptor Concentration Dependence of Förster Resonance Energy Transfer Dynamics in Dye–Quantum Dot Complexes. *J. Phys. Chem. C* **2014**, *118* (8), 4396–4402. <https://doi.org/10.1021/jp409807x>.
- (131) Chou, K.; Dennis, A. Förster Resonance Energy Transfer between Quantum Dot Donors and Quantum Dot Acceptors. *Sensors* **2015**, *15* (6), 13288–13325. <https://doi.org/10.3390/s150613288>.
- (132) Belušáková, S.; Martínez-Martínez, V.; Arbeloa, I. L.; Bujdák, J. Resonance Energy Transfer between Dye Molecules in Colloids of a Layered Silicate. The Effect of Dye Surface Concentration. *J. Phys. Chem. C* **2017**, *121* (15), 8300–8309. <https://doi.org/10.1021/acs.jpcc.7b00947>.
- (133) Hussain, S. A.; Chakraborty, S.; Bhattacharjee, D.; Schoonheydt, R. A. Fluorescence Resonance Energy Transfer between Organic Dyes Adsorbed onto Nano-Clay and Langmuir–Blodgett (LB) Films. *Spectrochim. Acta Part A Mol. Biomol. Spectrosc.* **2010**, *75* (2), 664–670. <https://doi.org/10.1016/j.saa.2009.11.037>.
- (134) Dey, D.; Bhattacharjee, D.; Chakraborty, S.; Hussain, S. A. Effect of Nanoclay Laponite and PH on the Energy Transfer between Fluorescent Dyes. *J. Photochem. Photobiol. A Chem.* **2013**, *252*, 174–182. <https://doi.org/10.1016/j.jphotochem.2012.12.003>.
- (135) Guggenheim, S.; Martin, R. T. Definition of Clay and Clay Mineral: Joint Report of the Aipea Nomenclature and CMS Nomenclature Committees. *Clays Clay Miner.* **1995**, *43*

- (2), 255–256. <https://doi.org/10.1346/CCMN.1995.0430213>.
- (136) Bergaya, F.; Lagaly, G. Clays, Clay Minerals, and Clay Science. In *Handbook of Clay Science*; Elsevier Ltd.: London, UK, 2006; pp 1–18. [https://doi.org/10.1016/S1572-4352\(05\)01001-9](https://doi.org/10.1016/S1572-4352(05)01001-9).
- (137) Brindley, G. W.; Keith Robinson. The Structure of Kaolinite. *Mineral. Mag. J. Mineral. Soc.* **1946**, 27 (194), 242–253. <https://doi.org/10.1180/minmag.1946.027.194.04>.
- (138) Emmerich, K.; Wolters, F.; Kahr, G.; Lagaly, G. Clay Profiling: The Classification of Montmorillonites. *Clays Clay Miner.* **2009**, 57 (1), 104–114. <https://doi.org/10.1346/CCMN.2009.0570110>.
- (139) Kalendova, A.; Kupkova, J.; Urbaskova, M.; Merinska, D. Applications of Clays in Nanocomposites and Ceramics. *Minerals* **2024**, 14 (1), 93. <https://doi.org/10.3390/min14010093>.
- (140) Nawaz, S.; Ahmad, M.; Asif, S.; Klemeš, J. J.; Mubashir, M.; Munir, M.; Zafar, M.; Bokhari, A.; Mukhtar, A.; Saqib, S.; Khoo, K. S.; Show, P. L. Phyllosilicate Derived Catalysts for Efficient Conversion of Lignocellulosic Derived Biomass to Biodiesel: A Review. *Bioresour. Technol.* **2022**, 343, 126068. <https://doi.org/10.1016/j.biortech.2021.126068>.
- (141) Odom, I. E. Smectite Clay Minerals: Properties and Uses. *Philos. Trans. R. Soc. London. Ser. A, Math. Phys. Sci.* **1984**, 311 (1517), 391–409. <https://doi.org/10.1098/rsta.1984.0036>.
- (142) Borchardt, G. Smectites. In *Minerals in Soil Environments*; Dixon, B., Weed, S. B., Eds.; Soil Science Society of America, Inc., 2018; pp 675–727. <https://doi.org/10.2136/sssabookser1.2ed.c14>.
- (143) Johnston, C. T. Clay Mineral–Water Interactions. In *Developments in Clay Science*; 2018; pp 89–124. <https://doi.org/10.1016/B978-0-08-102432-4.00004-4>.
- (144) Boek, E. S.; Sprik, M. Ab Initio Molecular Dynamics Study of the Hydration of a Sodium Smectite Clay. *J. Phys. Chem. B* **2003**, 107 (14), 3251–3256. <https://doi.org/10.1021/jp0262564>.
- (145) Brigatti, M. F.; Galan, E.; Theng, B. K. G. Structures and Mineralogy of Clay Minerals. In *Handbook of Clay Science*; Elsevier Ltd.: Oxford, UK, 2006; pp 19–86. [https://doi.org/10.1016/S1572-4352\(05\)01002-0](https://doi.org/10.1016/S1572-4352(05)01002-0).
- (146) Matthes, W.; Madsen, F. T.; Kahr, G. Sorption of Heavy-Metal Cations by Al and Zr-Hydroxy-Intercalated and Pillared Bentonite. *Clays Clay Miner.* **1999**, 47 (5), 617–629. <https://doi.org/10.1346/CCMN.1999.0470508>.
- (147) BURCH, R. Zr-Containing Pillared Interlayer Clays I. Preparation and Structural Characterisation. *J. Catal.* **1986**, 97 (2), 503–510. [https://doi.org/10.1016/0021-9517\(86\)90021-7](https://doi.org/10.1016/0021-9517(86)90021-7).
- (148) Yamanaka, S.; Nishihara, T.; Hattori, M.; Suzuki, Y. Preparation and Properties of Titania Pillared Clay. *Mater. Chem. Phys.* **1987**, 17 (1–2), 87–101. [https://doi.org/10.1016/0254-0584\(87\)90050-2](https://doi.org/10.1016/0254-0584(87)90050-2).
- (149) Sterte, J. Synthesis and Properties of Titanium Oxide Cross-Linked Montmorillonite. *Clays Clay Miner.* **1986**, 34 (6), 658–664.

<https://doi.org/10.1346/CCMN.1986.0340606>.

- (150) Hutson, N. D.; Hoekstra, M. J.; Yang, R. T. Control of Microporosity of Al<sub>2</sub>O<sub>3</sub>-Pillared Clays: Effect of PH, Calcination Temperature and Clay Cation Exchange Capacity. *Microporous Mesoporous Mater.* **1999**, *28* (3), 447–459. [https://doi.org/10.1016/S1387-1811\(98\)00334-5](https://doi.org/10.1016/S1387-1811(98)00334-5).
- (151) Occelli, M. L.; Tindwa, R. M. Physicochemical Properties of Montmorillonite Interlayered with Cationic Oxyaluminum Pillars. *Clays Clay Miner.* **1983**, *31* (1), 22–28. <https://doi.org/10.1346/CCMN.1983.0310104>.
- (152) Figueras, F. Pillared Clays as Catalysts. *Catal. Rev.* **1988**, *30* (3), 457–499. <https://doi.org/10.1080/01614948808080811>.
- (153) Hill, E. H. Layered 2D Material Heterostructures – a Colloidal Perspective. *J. Mater. Chem. C* **2024**, *12* (30), 11285–11318. <https://doi.org/10.1039/D4TC01102C>.
- (154) Gindy, N. N. Comprehensive Geological Study on Recent Surface Sediments of a Small North African Reservoir, Egypt. *Egypt. J. Aquat. Res.* **2018**, *44* (3), 213–218. <https://doi.org/10.1016/j.ejar.2018.07.002>.
- (155) Yaghmaeiyan, N.; Mirzaei, M.; Delghavi, R. Montmorillonite Clay: Introduction and Evaluation of Its Applications in Different Organic Syntheses as Catalyst: A Review. *Results Chem.* **2022**, *4*, 100549. <https://doi.org/10.1016/j.rechem.2022.100549>.
- (156) Diañez, I.; Martínez, I.; Partal, P. Synergistic Effect of Combined Nanoparticles to Elaborate Exfoliated Egg-White Protein-Based Nanobiocomposites. *Compos. Part B Eng.* **2016**, *88*, 36–43. <https://doi.org/10.1016/j.compositesb.2015.10.034>.
- (157) Zhuang, G.; Gao, J.; Peng, S.; Zhang, Z. Synergistically Using Layered and Fibrous Organoclays to Enhance the Rheological Properties of Oil-Based Drilling Fluids. *Appl. Clay Sci.* **2019**, *172*, 40–48. <https://doi.org/10.1016/j.clay.2019.02.014>.
- (158) Zhuang, G.; Zhang, H.; Wu, H.; Zhang, Z.; Liao, L. Influence of the Surfactants' Nature on the Structure and Rheology of Organo-Montmorillonite in Oil-Based Drilling Fluids. *Appl. Clay Sci.* **2017**, *135*, 244–252. <https://doi.org/10.1016/j.clay.2016.09.033>.
- (159) Bhattacharyya, K. G.; Gupta, S. Sen. Adsorption of a Few Heavy Metals on Natural and Modified Kaolinite and Montmorillonite: A Review. *Adv. Colloid Interface Sci.* **2008**, *140* (2), 114–131. <https://doi.org/10.1016/j.cis.2007.12.008>.
- (160) Ferreira, C. M.; da Silva, G. J.; Santos, M. B. L. Structure Investigation of a Laponite-NaCl Dispersion Induced by Desiccation in a Confined Geometry Using SAXS. *Appl. Clay Sci.* **2023**, *245*, 107119. <https://doi.org/10.1016/j.clay.2023.107119>.
- (161) Qi, Y.; Al-Mukhtar, M.; Alcover, J.-F.; Bergaya, F. Coupling Analysis of Macroscopic and Microscopic Behaviour in Highly Consolidated Na-Laponite Clays. *Appl. Clay Sci.* **1996**, *11* (2–4), 185–197. [https://doi.org/10.1016/S0169-1317\(96\)00016-6](https://doi.org/10.1016/S0169-1317(96)00016-6).
- (162) Li, L.; Harnau, L.; Rosenfeldt, S.; Ballauff, M. Effective Interaction of Charged Platelets in Aqueous Solution: Investigations of Colloid Laponite Suspensions by Static Light Scattering and Small-Angle x-Ray Scattering. *Phys. Rev. E* **2005**, *72* (5), 051504. <https://doi.org/10.1103/PhysRevE.72.051504>.
- (163) Avery, R. .; Ramsay, J. D. . Colloidal Properties of Synthetic Hectorite Clay Dispersions. *J. Colloid Interface Sci.* **1986**, *109* (2), 448–454. [63](https://doi.org/10.1016/0021-</a></p></div><div data-bbox=)

9797(86)90322-X.











- (164) Suman, K.; Joshi, Y. M. Microstructure and Soft Glassy Dynamics of an Aqueous Laponite Dispersion. *Langmuir* **2018**, *34* (44), 13079–13103. <https://doi.org/10.1021/acs.langmuir.8b01830>.
- (165) Shafran, K.; Jeans, C. V.; Kemp, S. J.; Murphy, K. Dr Barbara S. Neumann: Clay Scientist, Industrial Pioneer, Creator of Laponite®. *Elements* **2021**, *17* (1), 69–70. <https://doi.org/10.2138/gselements.17.1.69>.
- (166) Tanaka, H.; Meunier, J.; Bonn, D. Nonergodic States of Charged Colloidal Suspensions: Repulsive and Attractive Glasses and Gels. *Phys. Rev. E* **2004**, *69* (3), 031404. <https://doi.org/10.1103/PhysRevE.69.031404>.
- (167) Brunchi, C.-E.; Morariu, S. Laponite®—From Dispersion to Gel—Structure, Properties, and Applications. *Molecules* **2024**, *29* (12), 2823. <https://doi.org/10.3390/molecules29122823>.
- (168) Pek-Ing, A.; Yee-Kwong, L. Surface Chemistry and Rheology of Laponite Dispersions — Zeta Potential, Yield Stress, Ageing, Fractal Dimension and Pyrophosphate. *Appl. Clay Sci.* **2015**, *107*, 36–45. <https://doi.org/10.1016/j.clay.2015.01.033>.
- (169) Au, P.-I.; Hassan, S.; Liu, J.; Leong, Y.-K. Behaviour of LAPONITE® Gels: Rheology, Ageing, PH Effect and Phase State in the Presence of Dispersant. *Chem. Eng. Res. Des.* **2015**, *101*, 65–73. <https://doi.org/10.1016/j.cherd.2015.07.023>.
- (170) Raquez, J.-M.; Habibi, Y.; Murariu, M.; Dubois, P. Polylactide (PLA)-Based Nanocomposites. *Prog. Polym. Sci.* **2013**, *38* (10–11), 1504–1542. <https://doi.org/10.1016/j.progpolymsci.2013.05.014>.
- (171) Babu Valapa, R.; Loganathan, S.; Pugazhenthii, G.; Thomas, S.; Varghese, T. O. An Overview of Polymer–Clay Nanocomposites. In *Clay-Polymer Nanocomposites*; Elsevier, 2017; pp 29–81. <https://doi.org/10.1016/B978-0-323-46153-5.00002-1>.
- (172) Wang, Q.; Mynar, J. L.; Yoshida, M.; Lee, E.; Lee, M.; Okuro, K.; Kinbara, K.; Aida, T. High-Water-Content Mouldable Hydrogels by Mixing Clay and a Dendritic Molecular Binder. *Nature* **2010**, *463* (7279), 339–343. <https://doi.org/10.1038/nature08693>.
- (173) Hanley, H. J. M.; Muzny, C. D.; Butler, B. D. Surfactant Adsorption on a Clay Mineral: Application of Radiation Scattering. *Langmuir* **1997**, *13* (20), 5276–5282. <https://doi.org/10.1021/la962048p>.
- (174) Li, Y.; Du, N.; Song, S.; Hou, W. Adsorption of Cetylpyridinium Chloride at Silica Nanoparticle/Water Interfaces (I): Dependence of Adsorption Equilibrium on Particle Size. *Langmuir* **2021**, *37* (26), 7966–7974. <https://doi.org/10.1021/acs.langmuir.1c00681>.
- (175) Wheeler, P. A.; Wang, J.; Baker, J.; Mathias, L. J. Synthesis and Characterization of Covalently Functionalized Laponite Clay. *Chem. Mater.* **2005**, *17* (11), 3012–3018. <https://doi.org/10.1021/cm050306a>.
- (176) Colletti, C. G.; Massaro, M.; Lazzara, G.; Cavallaro, G.; Milioto, S.; Pibiri, I.; Noto, R.; Riela, S. Synthesis, Characterization and Study of Covalently Modified Triazole LAPONITE® Edges. *Appl. Clay Sci.* **2020**, *187* (January), 105489. <https://doi.org/10.1016/j.clay.2020.105489>.

- (177) Felbeck, T.; Hoffmann, K.; Lezhnina, M. M.; Kynast, U. H.; Resch-Genger, U. Fluorescent Nanoclays: Covalent Functionalization with Amine Reactive Dyes from Different Fluorophore Classes and Surface Group Quantification. *J. Phys. Chem. C* **2015**, *119* (23), 12978–12987. <https://doi.org/10.1021/acs.jpcc.5b01482>.
- (178) Wang, J.; Wang, G.; Sun, Y.; Wang, Y.; Yang, Y.; Yuan, Y.; Li, Y.; Liu, C. In Situ Formation of PH-/Thermo-Sensitive Nanohybrids via Friendly-Assembly of Poly(N-Vinylpyrrolidone) onto LAPONITE®. *RSC Adv.* **2016**, *6* (38), 31816–31823. <https://doi.org/10.1039/C5RA25628C>.
- (179) Wang, S.; Wu, Y.; Guo, R.; Huang, Y.; Wen, S.; Shen, M.; Wang, J.; Shi, X. Laponite Nanodisks as an Efficient Platform for Doxorubicin Delivery to Cancer Cells. *Langmuir* **2013**, *29* (16), 5030–5036. <https://doi.org/10.1021/la4001363>.
- (180) Gonçalves, M.; Figueira, P.; Maciel, D.; Rodrigues, J.; Shi, X.; Tomás, H.; Li, Y. Antitumor Efficacy of Doxorubicin-Loaded Laponite/Alginate Hybrid Hydrogels. *Macromol. Biosci.* **2014**, *14* (1), 110–120. <https://doi.org/10.1002/mabi.201300241>.
- (181) Carretero, M. I.; Pozo, M. Clay and Non-Clay Minerals in the Pharmaceutical and Cosmetic Industries Part II. Active Ingredients. *Appl. Clay Sci.* **2010**, *47* (3–4), 171–181. <https://doi.org/10.1016/j.clay.2009.10.016>.
- (182) Viseras, C.; Sánchez-Espejo, R.; Palumbo, R.; Liccardi, N.; García-Villén, F.; Borrego-Sánchez, A.; Massaro, M.; Riela, S.; López-Galindo, A. Clays in Cosmetics and Personal-Care Products. *Clays Clay Miner.* **2021**, *69* (5), 561–575. <https://doi.org/10.1007/s42860-021-00154-5>.
- (183) Tomás, H.; Alves, C. S.; Rodrigues, J. Laponite®: A Key Nanoplatform for Biomedical Applications? *Nanomedicine Nanotechnology, Biol. Med.* **2018**, *14* (7), 2407–2420. <https://doi.org/10.1016/j.nano.2017.04.016>.
- (184) Felbeck, T.; Behnke, T.; Hoffmann, K.; Grabolle, M.; Lezhnina, M. M.; Kynast, U. H.; Resch-Genger, U. Nile-Red–Nanoclay Hybrids: Red Emissive Optical Probes for Use in Aqueous Dispersion. *Langmuir* **2013**, *29* (36), 11489–11497. <https://doi.org/10.1021/la402165q>.
- (185) Ley, C.; Brendlé, J.; Walter, A.; Jacques, P.; Ibrahim, A.; Allonas, X. On the Interaction of Triarylmethane Dye Crystal Violet with LAPONITE® Clay: Using Mineral Nanoparticles to Control the Dye Photophysics. *Phys. Chem. Chem. Phys.* **2015**, *17* (26), 16677–16681. <https://doi.org/10.1039/C5CP02370J>.
- (186) Xiang, H.; Hill, E. H. Cascade Förster Resonance Energy Transfer between Layered Silicate Edge-Linked Chromophores. *J. Colloid Interface Sci.* **2024**, *676*, 543–550. <https://doi.org/10.1016/j.jcis.2024.07.106>.
- (187) Massaro, M.; Cavallaro, G.; Colletti, C. G.; Lazzara, G.; Milioto, S.; Noto, R.; Riela, S. Chemical Modification of Halloysite Nanotubes for Controlled Loading and Release. *J. Mater. Chem. B* **2018**, *6* (21), 3415–3433. <https://doi.org/10.1039/C8TB00543E>.
- (188) Joussein, E.; Petit, S.; Churchman, J.; Theng, B.; Righi, D.; Delvaux, B. Halloysite Clay Minerals — a Review. *Clay Miner.* **2005**, *40* (4), 383–426. <https://doi.org/10.1180/0009855054040180>.
- (189) Tan, D.; Yuan, P.; Liu, D.; Du, P. Surface Modifications of Halloysite; 2016; pp 167–201. <https://doi.org/10.1016/B978-0-08-100293-3.00008-X>.

- (190) Li, X.; Liu, A.; Ye, R.; Wang, Y.; Wang, W. Fabrication of Gelatin–Laponite Composite Films: Effect of the Concentration of Laponite on Physical Properties and the Freshness of Meat during Storage. *Food Hydrocoll.* **2015**, *44*, 390–398. <https://doi.org/10.1016/j.foodhyd.2014.10.014>.
- (191) Fatnassi, M.; Es-Souni, M. Nanoscale Phase Separation in Laponite–Polypyrrole Nanocomposites. Application to Electrodes for Energy Storage. *RSC Adv.* **2015**, *5* (28), 21550–21557. <https://doi.org/10.1039/C4RA16540C>.













# Appendix I

## Chemicals









Name	CAS Number	Pictograms	Hazard Statements	Precautionary Statements
potassium hydroxide	1310-58-3		H290, H302, H314	P280, P305+P351+P338, P310
hydrochloric acid	7647-01-0		H290, H314, H335	P260, P280, P303+P361+P353, P305+P351+P338
phosphoric acid	7664-38-2		H290, H314	P280, P305+P351+P338, P310
<i>tert</i> -butanol	75-65-0		H225, H319, H332, H335	P210, P261, P305+P351+P338
potassium carbonate	584-08-7		H302, H315, H319, H335	P261, P305+P351+P338
2-propanol	67-63-0		H225, H302, H319, H336	P210, P261, P305+P351+P338
chloroform	67-66-3		H302, H315, H319, H331, H336, H351, H361d, H372	P201, P202, P235, P260, P264, P270, P271, P280, P281, P301+P330+P331, P302+P352, P304+P340, P305+P351+P338, P308+P313, P310, P311, P314, P332+P313, P337+P313, P362, P403+P233, P405, P501
deuteriochloroform	865-49-6		H302, H315, H319, H331, H336, H351, H361, H372, H373	P201, P202, P260, P261, P264, P270, P271, P280, P281, P301+P312, P302+P352, P304+P340, P305+P351+P338, P308+P313, P311, P312, P314, P321, P330, P332+P313, P337+P313, P362, P403+P233, P405, P501
methanol	67-56-1		H225, H301, H302, H305, H311, H331, H370	P210, P233, P235, P240, P241, P242, P243, P260, P264, P270, P271, P280, P301+P330+P331, P302+P352, P303+P361+P353, P304+P340, P305+P351+P338, P307+P311, P310, P311, P312, P337+P313, P361, P363, P370+P378, P403+P233, P405, P501
absolute ethanol	64-17-5		H225, H319, H360D	P210, P233, P240, P241, P242, P305+P351+P338



<i>N, N</i> -dimethylformamide	68-12-2		H226, H312, H319, H332, H360	P280, P305+P351+P338, P308+P313
4',6-diamidino-2-phenyl-indol-dihydrochloride imidazole	28718-90-3		H315, H317, H335	P261, P264, P271, P272, P280, P302+P352
	288-32-4		H302, H314, H360D	P263, P270, P280, P301+P310, P305+P351+P338, P308+P313
1,4,5,8-naphthalenetetracarboxylic dianhydride	81-30-1		H315, H317, H335, H319	P261, P264, P271, P280, P302+P352, P305+P351+P338
dichloromethane	75-09-2		H315, H319, H335, H336, H351, H373	P261, P281, P305+P351+P338
2-(2-Aminoethoxy) ethanol	929-06-6		H314, H318	P280, P301+P330+P331, P303+P361+P353, P305+P351+P338, P363
acetic acid	64-19-7		H226, H314	P280, P305+P351+P338, P310
sodium azide	26628-22-8		H300, H310, H410	P260, P280, P301+P310, P501
sodium nitrite	7632-00-0		H272, H301, H319, H400	P220, P273, P301+P310, P305+P351+P338
toluene	108-88-3		H225, H304, H315, H336, H361d, H373	P210, P240, P301+P310, P302+P352, P308+P313, P314, P403+P233
<i>n</i> -hexane	110-54-3		H225, H302, H305, H315, H336, H361fd, H373, H411	P201, P202, P210, P233, P235, P240, P241, P242, P243, P260, P264, P271, P273, P280, P281, P301+P330+P331, P302+P352, P303+P361+P353, P304+P340, P308+P313, P310, P312, P314, P332+P313, P363, P370+P378, P391, P403+P233, P405, P501
ethyl acetate	141-78-6		H225, H319, H336	P210, P233, P240, P305+P351+P338, P403+P235
copper(II) sulfate	7758-99-8		H302, H318, H410	P264, P273, P301+P312, P305+P351+P338, P391

(3-chloropropyl) methoxydimethylsilane	18171-14-7		H226	P210, P233, P240, P241, P242, P243, P280, P303+P361+P353, P370+P378, P403+P235, P501
3-(diethylamino) phenol	91-68-9	 	H301, H411	P264, P270, P273
rhodamine 6G	989-38-8	   	H301, H302, H318, H410, H411	P264, P270, P273, P280, P301+P310, P301+P312, P305+P351+P338, P310, P321, P330, P391, P405, P501
1,6-Dihydroxynaphthalene	575-44-0		H315, H319, H335	P261, P264, P271, P280, P302+P352, P305+P351+P338
propargyl bromide	106-96-7	   	H225, H301, H304, H314, H335, H336, H361d, H373	P210, P280, P301+P330+P331, P303+P361+P353, P305+P351+P338

## GHS hazard pictograms

 GHS01: explosive	 GHS02: flammable	 GHS03: oxidizing	 GHS05: corrosive
 GHS06: toxic	 GHS07: harmful	 GHS08: health hazard	 GHS09: environmental hazard

## Hazard statements

Code	Phrase
H225	Highly flammable liquid and vapour.
H226	Flammable liquid and vapour.
H272	May intensify fire: OXIDISER.
H290	May be corrosive to metals.
H300	Fatal if swallowed.
H301	Toxic if swallowed.
H302	Harmful if swallowed.
H304	May be fatal if swallowed and enters airways.
H305	May be harmful if swallowed and enters airways.
H310	Fatal in contact with skin.
H311	Toxic in contact with skin.
H312	Harmful in contact with skin.
H314	Causes severe skin burns and eye damage.
H315	Causes skin irritation.
H317	May cause an allergic skin reaction.
H318	Causes serious eye damage.
H319	Causes serious eye irritation.
H332	Harmful if inhaled.
H335	May cause respiratory irritation.
H336	May cause drowsiness or dizziness.
H331	Toxic if inhaled.
H351	Suspected of causing cancer.
H360	May damage fertility or the unborn child.
H360D	May damage the unborn child.
H361d	Suspected of damaging the unborn child.
H361fd	Suspected of damaging fertility. Suspected of damaging the unborn child.
H361	Suspected of damaging fertility or the unborn child.
H370	Causes damage to organs.
H372	Causes damage to organs through prolonged or repeated exposure.
H373	May cause damage to organs through prolonged or repeated exposure.
H400	Very toxic to aquatic life.
H410	Very toxic to aquatic life with long-lasting effects.
H411	Toxic to aquatic life with long-lasting effects.

## Precautionary statements

Code	Phrase
P201	Obtain special instructions before use.
P202	Do not handle until all safety precautions have been read and understood.
P210	Keep away from heat, hot surfaces, sparks, open flames and other ignition sources. No smoking.
P220	Keep/Store away from clothing/.../combustible materials.
P233	Keep container tightly closed.
P235	Keep cool.
P240	Ground and bond container and receiving equipment.
P241	Use explosion-proof electrical/ventilating/light/.../equipment.
P242	Use only non-sparking tools
P243	Take precautionary measures to prevent static discharges.
P260	Do not breathe dust/fume/gas/mist/vapours/spray.
P261	Avoid breathing dust/fume/gas/mist/vapours/spray.
P263	Avoid contact during pregnancy and while nursing.
P264	Wash ... thoroughly after handling.
P270	Do not eat, drink or smoke when using this product.
P271	Use only outdoors or in a well-ventilated area.
P272	Contaminated work clothing should not be allowed out of the workplace.
P273	Avoid release to the environment.
P280	Wear protective gloves/protective clothing/eye protection/face protection.
P281	Use personal protective equipment as required.
P310	Immediately call a POISON CENTER or doctor/physician.
P311	Call a POISON CENTER or doctor/physician.
P312	Call a POISON CENTER or doctor/physician if you feel unwell.
P314	Get Medical advice/attention if you feel unwell.
P321	Specific treatment (see ... on this label).
P330	Rinse mouth.
P361	Remove/Take off immediately all contaminated clothing.
P362	Take off contaminated clothing.
P363	Wash contaminated clothing before reuse.
P391	Collect spillage.
P405	Store locked up.
P501	Dispose of contents/container to ...
P301+P310	IF SWALLOWED: Immediately call a POISON CENTER or doctor/physician.
P301+P312	IF SWALLOWED: Call a POISON CENTER or doctor/physician if you feel unwell.
P301+P330+P331	IF SWALLOWED: Rinse mouth. Do NOT induce vomiting.
P302+P352	IF ON SKIN: Wash with soap and water.
P303+P361+P353	IF ON SKIN (or hair): Remove/Take off immediately all contaminated clothing. Rinse skin with water [or shower].
P304+P340	IF INHALED: Remove victim to fresh air and keep at rest in a position comfortable for breathing.
P305+P351+P338	IF IN EYES: Rinse continuously with water for several minutes. Remove contact lenses if present and easy to do. Continue rinsing.

P307+P311	IF exposed or concerned: Call a POISON CENTER or doctor/physician.
P308+P313	IF exposed or concerned: Get medical advice/attention.
P332+P313	If skin irritation occurs: Get medical advice/attention.
P337+P313	If eye irritation persists: Get medical advice/attention.
P370+P378	In case of fire: Use ... to extinguish.
P403+P233	Store in a well ventilated place. Keep container tightly closed.
P403+P235	Store in a well ventilated place. Keep cool.

Note: "... " = to be specified

## **Appendix II**

### **Supplementary Information for Chapter 2**

**Layered silicate edge-linked perylene diimides: Synthesis, self-assembly and energy transfer**

## Supporting Information:

### Layered Silicate Edge-Linked Perylene Diimides: Synthesis, Self-Assembly and Energy Transfer

Hongxiao Xiang<sup>1</sup>, Silvano R. Valandro<sup>1,2</sup>, Eric H. Hill<sup>1,2\*</sup>

<sup>1</sup>Institute of Physical Chemistry, University of Hamburg, Grindelallee 117, 20146 Hamburg, Germany

<sup>2</sup>The Hamburg Center for Ultrafast Imaging (CUI), Luruper Chausee 149, 22761 Hamburg, Germany

\*Corresponding author: [eric.hill@chemie.uni-hamburg.de](mailto:eric.hill@chemie.uni-hamburg.de)

#### Experimental Section

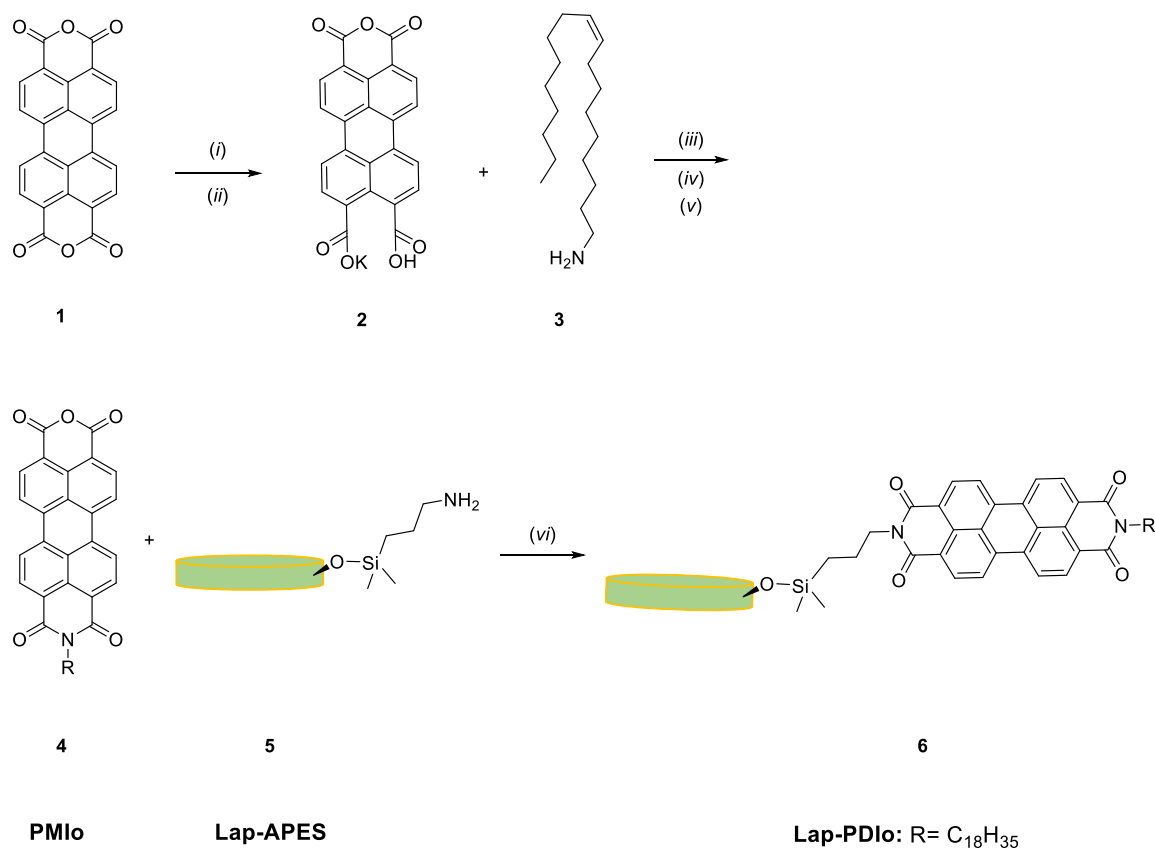
**Materials.** Perylene-3,4,9,10-tetracarboxylic acid dianhydride (PTCDA) and L-aspartic acid were purchased from Alfa Aesar. Potassium hydroxide (85%) and concentrated hydrochloric acid (37%) were purchased from ChemSolute. Phosphoric acid, *tert*-Butanol and potassium carbonate were purchased from Grüssing. Oleyl amine was purchased from ABCR. Laponite-RD was donated by BYK Additives (Germany). 2-propanol, chloroform was purchased from VWR Chemicals. Chloroform-d was purchased from Euriso-Top. Aminopropyltrimethoxysilane (APES) was purchased from Fluorochem. Methanol and Absolute ethanol were purchased from FisherScientific. *N,N*-Dimethylformamide was purchased from TCI (Germany). 4',6-Diamidino-2-phenyl-indol-dihydrochlorid (DAPI) was purchased from Serva. Imidazole was purchased from ChemPur. All the purchased chemicals were used as received, without further purification. Millipore-filtered water with a resistivity of 18.2 M $\Omega$ ·cm was used for all reactions and for preparation of dispersions.

**Characterization.** <sup>1</sup>H-NMR spectra were collected on a Bruker Fourier HD 300 MHz. (Massachusetts, USA). Solid state NMR spectra were recorded with a 400 MHz spectrometer operating at 79.44 MHz for <sup>29</sup>Si, 100.56 MHz for <sup>13</sup>C. (Bruker Avance, Massachusetts, USA). All experiments were carried out at a magic angle spinning (MAS) rate of 10 kHz using a 4 mm MAS HX double resonance probe. The <sup>1</sup>H  $\pi/2$  pulse length was 4.6  $\mu$ s. The <sup>13</sup>C{<sup>1</sup>H} and <sup>29</sup>Si{<sup>1</sup>H} cross-polarization (CP)/MAS spectra were measured using contact time of 2.0 ms and a recycle delay of 2s, with two pulse phase modulation (TPPM) heteronuclear dipolar

decoupling applied during acquisition. The  $^1\text{H}$ ,  $^{13}\text{C}$  and  $^{29}\text{Si}$  spectra are referenced to external TMS at 0 ppm using adamantane as a secondary reference for  $^1\text{H}$  and  $^{13}\text{C}$  and TKS (tetrakis(trimethylsilyl)silane) as a secondary reference for  $^{29}\text{Si}$ . Fourier-transform infrared spectroscopy (FT-IR) measurements were performed using a golden gate Attenuated Total Reflectance (ATR) setup, 128 scans were averaged and recorded at a resolution of  $4\text{ cm}^{-1}$  (Bruker Invenio®, Massachusetts, USA). Thermogravimetric analysis was carried out from  $25\text{ }^\circ\text{C}$  to  $700\text{ }^\circ\text{C}$  with a heating rate of  $10\text{ K/min}$  and nitrogen gas was purged at a rate of  $25\text{ mL/min}$ , all samples were dried at  $100\text{ }^\circ\text{C}$  overnight before TGA measurements (TG 209F1 Libra, NETZSCH, Bayern, Germany). UV–Vis absorbance spectra were collected on a Cary 60 UV–Vis spectrometer (Agilent, Santa Clara, CA, USA). Steady-State Fluorescence spectra were collected on a Fluoromax-4 spectrometer (HORIBA, Kyōto, Japan). Time-resolved photoluminescence measurements were carried out on a FluoTime 300 fluorescence spectrometer (Picoquant, Berlin, Germany). A supercontinuum laser (SuperK Fianum, NKT Photonics, Copenhagen, Denmark) was used as a light source. The laser beam passed through a deep UV supercontinuum extension unit (SuperK Extend-UV (DUV), NKT Photonics, Copenhagen, Denmark) and was then directed to the FluoTime 300.

**Synthesis.** The synthetic routes adopted for the preparation of Lap-PDIo and Lap-PDIa are shown in Scheme S1 and S2.





**Scheme S1:** Syntheses of designed compounds. (i) KOH (5%), 90 °C, 4 hours; (ii) H<sub>3</sub>PO<sub>4</sub> (10%), 90 °C, 1 hour, (iii) water/2-propanol (1:1), 0-5 °C, 4 hours; (iv) 90 °C, 2 hours; (v) 10% HCl, 1 hour; (vi) EtOH, reflux, overnight.

*Compound 2, Perylene-3,4,9,10-tetracarboxylic acid monoanhydride monopotassium carboxylate.*<sup>1</sup> PTCDA **1** (3 g, 7.6 mmol) was added into a 50 mL round bottom flask with 34 mL 5 % KOH solution and stirred at 90 °C for 4 hours. After cooling down to room temperature, 7 mL 10% H<sub>3</sub>PO<sub>4</sub> was added and stirred at 90 °C for one hour. After filtration the residue was washed with water followed by drying at 110°C and a bordeaux-red powder **2** was gained.

Yield: 91%, FT-IR (Golden gate ATR, 4 cm<sup>-1</sup>):  $\nu = 1760, 1722, 1591, 1508, 1406, 1375, 1342, 1228, 1211, 1180, 1147, 1002, 852, 800, 759, 738, 684, 648, 611, 553, 536$ . Anal. Calcd. for C<sub>24</sub>H<sub>9</sub>KO<sub>7</sub> (*M*<sub>w</sub>, 448.4 g/mol); C, 64.28; H, 2.02; K, 8.72. Found: C, 63.54; H, 2.06; K, 8.31.

*Compound 4, N-(9Z)-octadecen-3,4,9,10-peryene tetracarboxylic monoanhydride monoimide*<sup>1-4</sup> Oleylamine **3** (1.34 g, 1.6 mL, 5 mmol), a mixture of 15 mL water and 15 mL 2-

propanol were added into a 100 mL round bottom flask and cooled down to 0-5 °C in an ice bath. Perylene-3,4,9,10-tetracarboxylic acid monoanhydride monopotassium carboxylate **2** (0.5 g, 2.5 mmol) was added in the cooled flask. The reaction mixture was stirred at 0-5 °C for 4 hours. After stirring the mixture at 90 °C for 2 hours, 64 mL 10% HCl was added and stirred at 90 °C for another 2 hours followed by stirring at room temperature overnight. After filtration the residue was washed with water and dried in an oven at 110 °C. The crude product was suspended in 10% KOH solution and stirred at 90 °C until there is no more perylene dianhydride, which was controlled by observance of a complete yellowish outlet on filter paper from a cooled tip sample. After cooling down the mixture was filtered out and washed with warm 10% K<sub>2</sub>CO<sub>3</sub> until the filtrate was colorless. To remove the trace of diimide product, the product was washed with chloroform for several times. At the end, the purified product **4** was dried in an oven at 60°C overnight.

Yield: 75%, FT-IR (Golden gate ATR, 4 cm<sup>-1</sup>):  $\nu = 2921, 2852, 1689, 1650, 1591, 1564, 1508, 1456, 1419, 1373, 1350, 1301, 1247, 1218, 1188, 1166, 1083, 964, 848, 827, 806, 790, 769, 750, 605, 573, 538$ . Anal. Calcd. for C<sub>42</sub>H<sub>43</sub>NO<sub>5</sub> (*Mw*, 641.8 g/mol); C, 78.6; H, 6.75; N, 2.18; O, 12.46. Found: C, 76.91; H, 6.15; N, 2.01; O, 13.65.

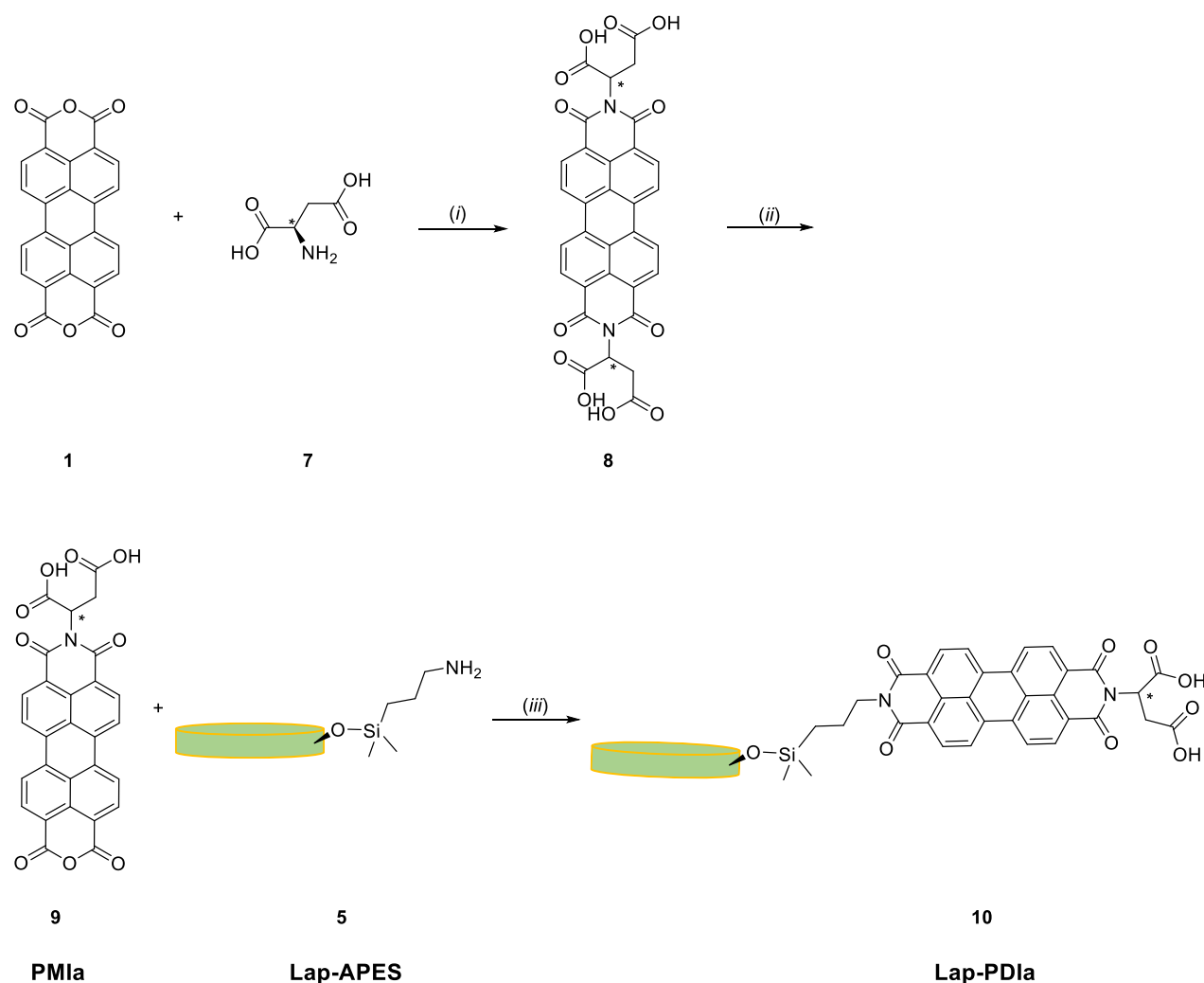
*Compound 5, APES functionalized laponite.*<sup>3</sup> Laponite-RD (5 g) was added in 200 mL deionized water and stirred at 50 °C for one hour. Aminopropyldimethylethoxysilane APES (2.0 mL, 12.4 mmol) was mixed with 50 mL deionized water under stirring for 30 minutes. The APES solution was poured slowly in the laponite dispersion under vigorous stirring. The mixture was stirred at 50 °C for 16 hours. After cooling down the crude product was collected via centrifugation under 7500 rpm for 15 minutes. The crude product was dried in an oven at 110°C overnight. After drying the crude product was dispersed in 200 mL 60% methanol/water and stirred at room temperature overnight. The crude product was collected via centrifugation (7500 rpm, 15 minutes) and washed five times with 60% methanol/water. The purified product **5** was dried at 110 °C and stored for further work.

Yield: 71%, FT-IR (Golden gate ATR, 4 cm<sup>-1</sup>):  $\nu = 1622, 1263, 962, 653$ . Elemental Analysis for compound 5, Found: C, 3.54; H, 2.06; N, 0.66. Solid state CP/MAS <sup>29</sup>Si NMR ( $\delta = 8-20$  ppm, C-Si(OSi);  $\delta = -86$  ppm, incompletely condensed Si in laponite;  $\delta = -95$  ppm, fully condensed Si in laponite).<sup>5</sup> Solid state CP/MAS <sup>13</sup>C NMR ( $\delta = -1.8$  ppm, 2CH<sub>3</sub>Si;  $\delta = 13.6$  ppm, CH<sub>2</sub>;  $\delta = 21.4$  ppm, CH<sub>2</sub>;  $\delta = 43.2$  ppm, CH<sub>2</sub>NH<sub>2</sub>).

*Compound 6, N, N'-(9Z)-octadecen-3,4,9,10-perylene tetracarboxylic diimide functionalized laponite.*<sup>6</sup> **4** (15.5 mg), **5** (91.6 mg) and 30 mL absolute ethanol were added into a 50 mL round bottom flask and the mixture was stirred under reflux overnight. After cooling down the crude

product was collected via centrifugation (7500 rpm, 15 minutes) and washed 3 times with chloroform and 3 times with water to remove unreacted reactant. The product **6** was dried in an oven at 60°C overnight and stored for further characterization and photophysical study.

Yield: 80%, FT-IR (Golden gate ATR, 4 cm<sup>-1</sup>):  $\nu = 2925, 2850, 1760, 1689, 1641, 1595, 1577, 1404, 1356, 1331, 1257, 964, 808, 652$ . Elemental Analysis for compound **6**, Found: C, 11.51; H, 2.26; N, 0.58. Solid state CP/MAS <sup>29</sup>Si NMR ( $\delta = 8-20$  ppm, C-Si(OSi);  $\delta = -86$  ppm, incompletely condensed Si in lapointe;  $\delta = -95$  ppm, fully condensed Si of laponite). Solid state CP/MAS <sup>13</sup>C NMR ( $\delta = -1.1$  ppm, 2CH<sub>3</sub>Si;  $\delta = 13.8$  ppm, CH<sub>3</sub>-oleyl;  $\delta = 21.8$  ppm, 2CH<sub>2</sub>;  $\delta = 29.4$  ppm, 14CH<sub>2</sub>;  $\delta = 43.3$  ppm, 2CH<sub>2</sub>N;  $\delta = 117.9$  ppm, 4C-perylene;  $\delta = 123.2$  ppm, 8CH-perylene,  $\delta = 130$  ppm, 4C-perylene, C=C-oleyl;  $\delta = 135.2$  ppm, 4C-perylene,  $\delta = 165.5$  ppm, 4C=O-imide).



**Scheme S2:** Syntheses of designed compounds. (i) imidazole, 130 °C, 6 hours; (ii) KOH, tert-Butanol, 20 minutes. (iii) EtOH, reflux, overnight,

*Compound 8. N,N'-Di(2-succinic acid)-perylene-3,4,9,10-tetracarboxylic Bisimide.*<sup>7,8</sup> L-aspartic acid **7** (0.7 g, 5 mmol), PTCDA **1** (1 g, 2.5 mmol) and 10 g imidazole were weighted in a 30 mL bottom flask under argon flow. The mixture was heated at 130 °C for 6 hours. After cooling the mixture down to 90 °C, 20 mL deionized water was poured into it. The mixture was filtered to remove unreacted reactants. For acidification, 2N HCl was added in the filtrate and stirred overnight to precipitate out. The solid was filtered out followed by washed with water and methanol. The product **8** was dried at 60 °C and a rose red powder was gained.

Yield: 96%, FT-IR (Golden gate ATR, 4 cm<sup>-1</sup>):  $\nu = 3101, 2943, 1659, 1637, 1589, 1574, 1506, 1433, 1400, 1360, 1340, 1251, 1169, 1130, 991, 958, 856, 808, 793, 744, 711, 627$ . <sup>1</sup>H (300 MHz, d<sub>6</sub>-DMSO,)  $\delta$ : 12.80 (s, 4H), 8.50 (t, 4H), 8.37 (d, 4H), 6.07 (m, 2H), 3.44 (m, 2H), 2.81 (m, 2H) Anal. Calcd. for C<sub>32</sub>H<sub>16</sub>N<sub>2</sub>O<sub>12</sub> (Mw, 622.498 g/mol); C, 61.74; H, 2.91; N, 4.5; O, 30.84. Found: C, 58.9; H, 3.84; N, 4.2, O, 31.67.

*Compound 9, N-(9)-succinic acid-3,4,9,10-perylene tetracarboxylic monoanhydride monoimide.*<sup>9</sup> Product **8** (113 mg, 0.18 mmol), 5 mL *tert*-Butanol and 110 mg potassium hydroxide were weight in a 25 mL bottom flask and heated to reflux. After 20 minutes there was no more reactant **8** by control with TLC (methanol: water = 1:1) and cooled the reaction mixture down to room temperature. 5 mL acetic acid and 5 mL 2N HCl were added and stirred overnight. The solid was filtered out followed by washing with water. For purification the crude product was dispersed in 20 mL 10% potassium carbonate solution and stirred under reflux until the mixture turned green. The mixture was filtered and washed with warm 10% potassium carbonate until the filtrate became colorless. After washing the solid with 50 mL 2N HCl and water, the purified product **9** was dried in an oven at 60 °C and stored for further characterization. Anal. Calcd. for C<sub>28</sub>H<sub>13</sub>NO<sub>9</sub> (Mw, 507.06 g/mol); C, 66.28; H, 2.58; N, 2.76; O, 28.38. Found: C, 58.37; H, 2.48; N, 2.87.

Yield: 11%, FT-IR (Golden gate ATR, 4 cm<sup>-1</sup>):  $\nu = 3078, 2875, 1761, 1724, 1693, 1661, 1591, 1506, 1431, 1404, 1369, 1319, 1296, 1267, 1234, 1180, 1147, 1120, 1120, 1012, 937, 858, 806, 793, 758, 730, 640, 602, 571$ .

*Compound 10, N, N'-(2,9)- butane dioic -3,4,9,10-perylene tetracarboxylic diimide functionalized laponite.*<sup>6</sup> **6** (15.5 mg), **3** (105 mg) and 30 mL absolute ethanol were added into a 50 mL round bottom flask and the mixture was stirred under reflux overnight. After cooling down the crude product was collected via centrifugation (7500 rpm, 15 minutes) and washed 3 times with ethanol and 3 times with water to remove unreacted reactant. The product was dried in an oven at 60°C overnight and stored for further characterization and photophysical study.

Yield: 96%, FT-IR (Golden gate ATR,  $4\text{ cm}^{-1}$ ):  $\nu = 3383, 1679, 1629, 1595, 1512, 1402, 1327, 1261, 962, 808, 741, 673, 650$ . Elemental Analysis for compound 10, Found: C, 7.29; H, 2.34; N, 0.84. Solid state CP/MAS  $^{29}\text{Si}$  NMR ( $\delta = 8\text{-}20\text{ ppm}$ , C-Si(OSi);  $\delta = -85\text{ ppm}$ , incompletely condensed Si in lapointe;  $\delta = -95\text{ ppm}$ , fully condensed Si of laponite). Solid state CP/MAS  $^{13}\text{C}$  NMR ( $\delta = -0.9\text{ ppm}$ ,  $2\text{CH}_3\text{Si}$ ;  $\delta = 14.2\text{ ppm}$ , OSiCH<sub>2</sub>;  $\delta = 21.5\text{ ppm}$ , SiCH<sub>2</sub>CH<sub>2</sub>;  $\delta = 30.3\text{ ppm}$ , CH<sub>2</sub>COOH;  $\delta = 43.2\text{ ppm}$ , CHN/CH<sub>2</sub>N;  $\delta = 105.9\text{ ppm}$ , 2C-perylene;  $\delta = 108.3\text{ ppm}$ , 2C-perylene,  $\delta = 123.5\text{ ppm}$ , 8CH-perylene;  $\delta = 132.7\text{ ppm}$ , 8C-perylene,  $\delta = 162.1\text{ ppm}$ , 6C=O).

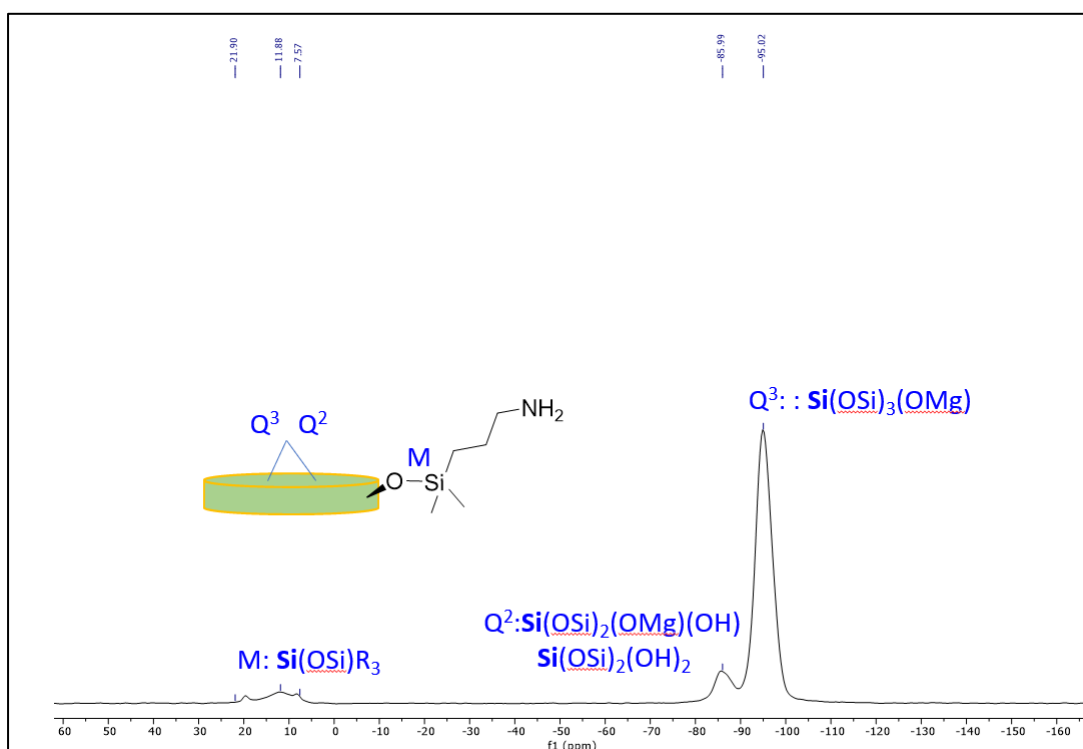


**Figure S1.** Solid state CP/MAS  $^{29}\text{Si}$  NMR spectrum of Lap-APES.

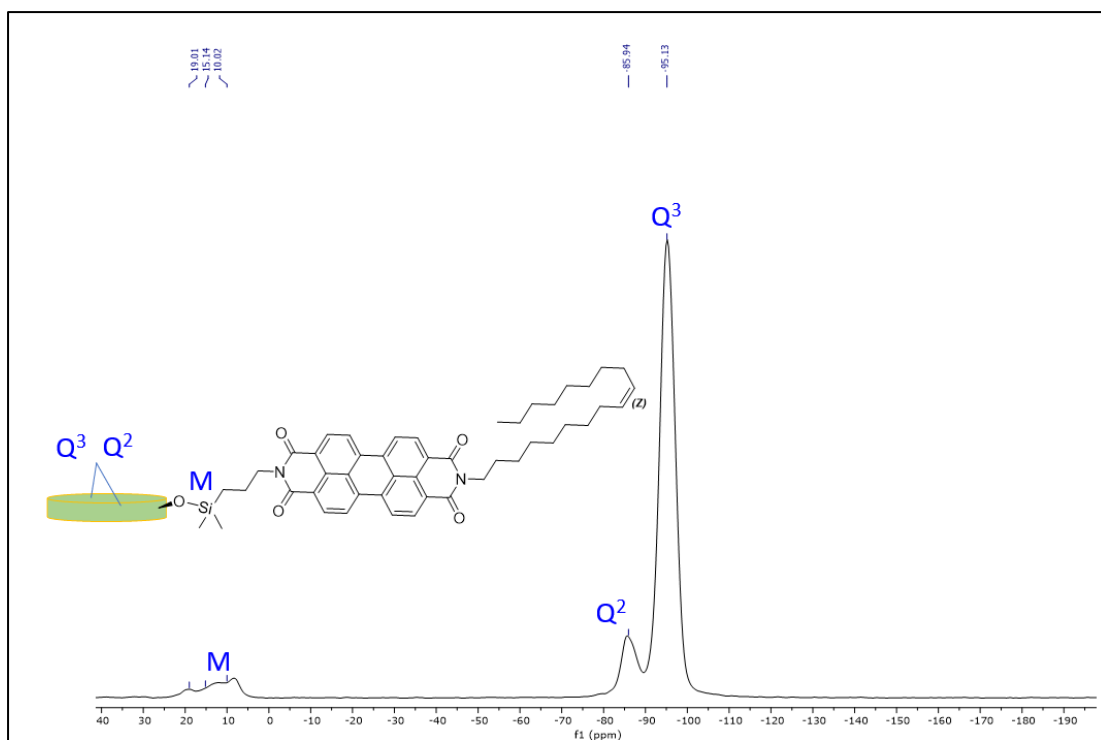


**Figure S2.** Solid state CP/MAS  $^{29}\text{Si}$  NMR of Lap-PDII.

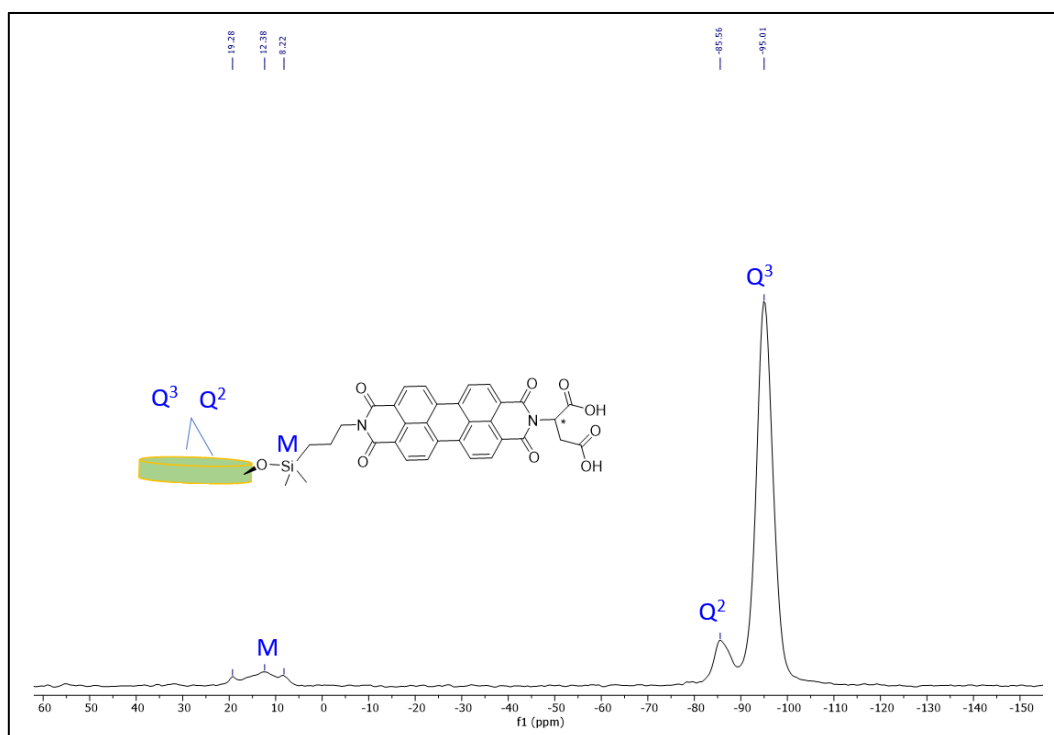


**Figure S3.** Solid state CP/MAS  $^{29}\text{Si}$  NMR of Lap-PDIa.

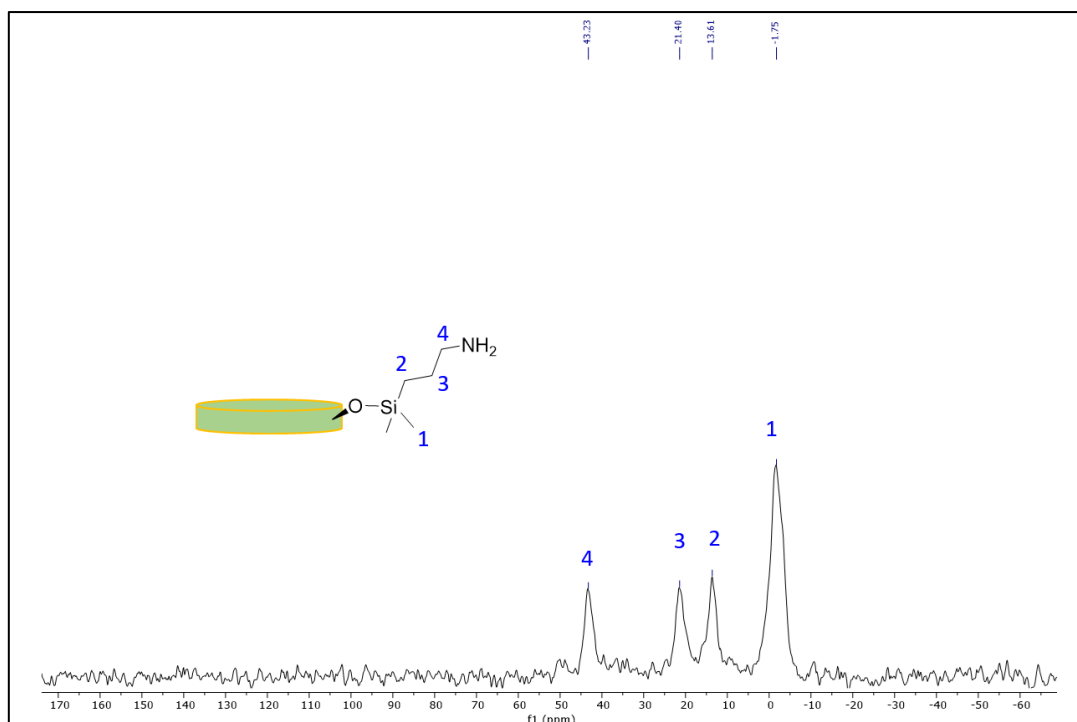


**Figure S4.** Solid state CP/MAS <sup>13</sup>C NMR spectrum of Lap-APES.

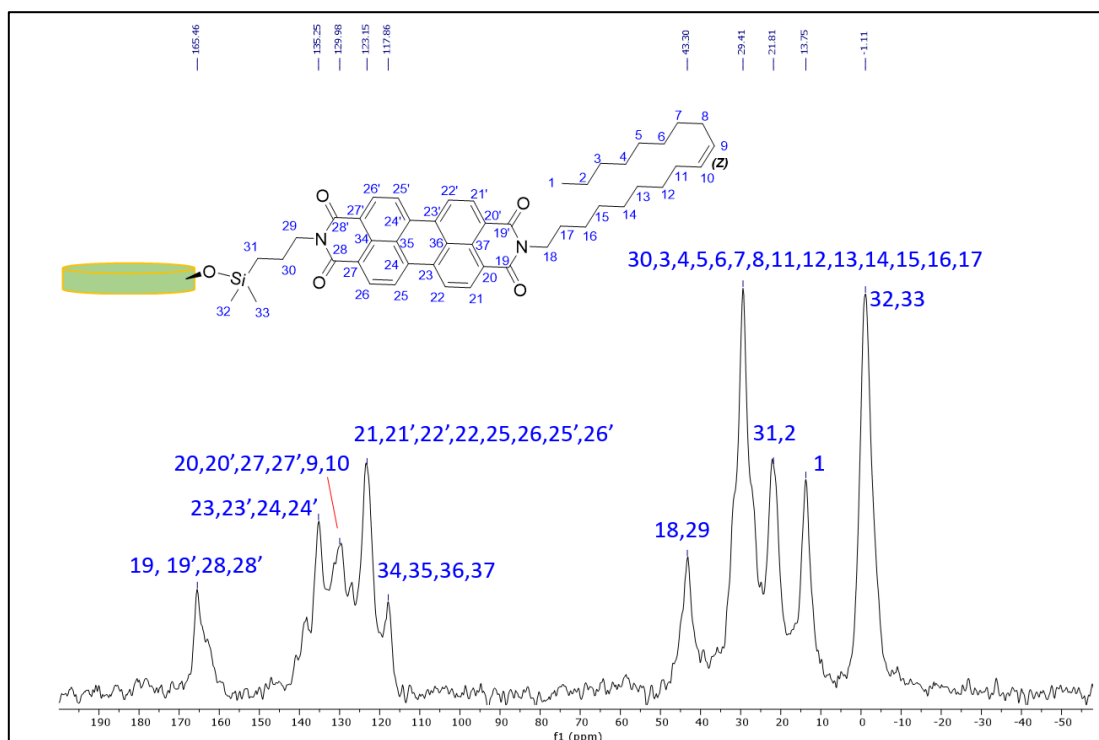


**Figure S5.** Solid state CP/MAS <sup>13</sup>C NMR of Lap-PDIO.

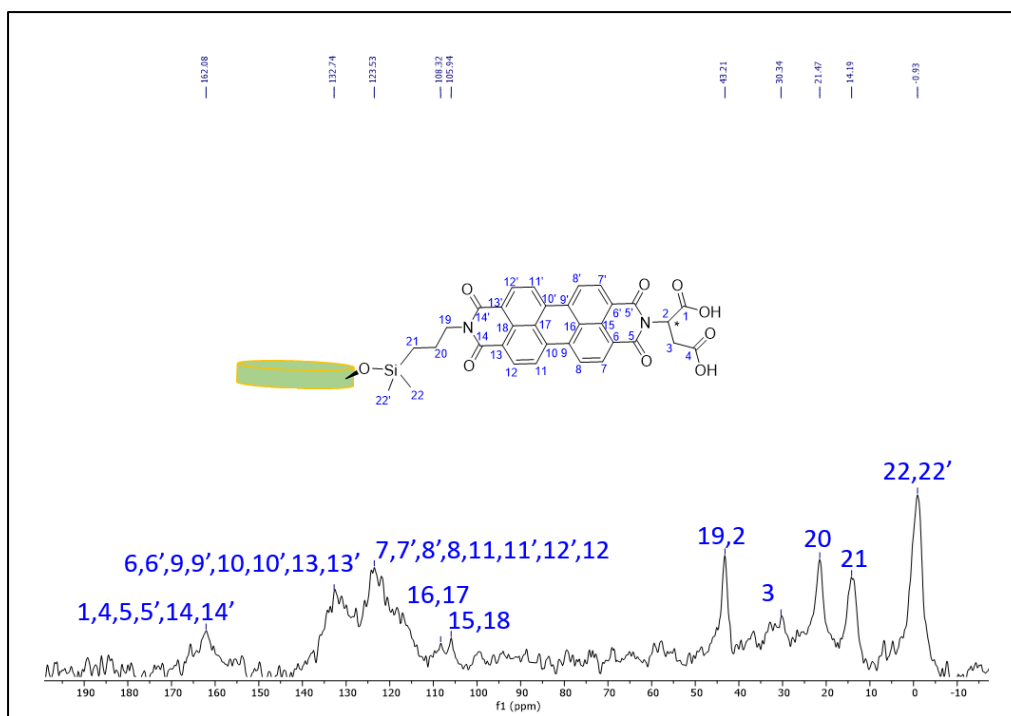


**Figure S6.** Solid state CP/MAS  $^{13}\text{C}$  NMR of Lap-PD1a.

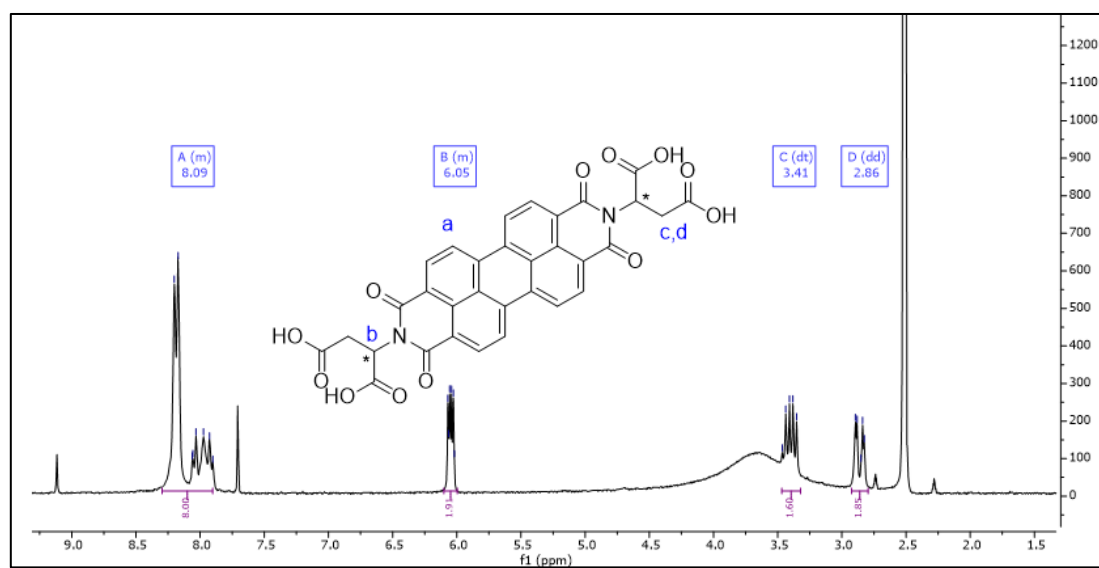


**Figure S7.**  $^1\text{H}$ -NMR spectrum of compound 8 in  $\text{d}_6\text{-DMSO}$ .



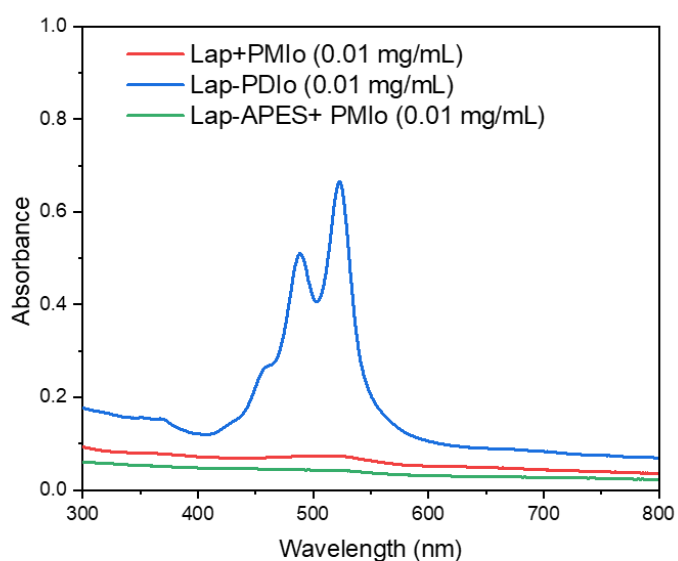


**Figure S8.** UV-Vis absorption of PMIo and Lap, PMIo and Lap-APES and Lap-PDIo in DMF.

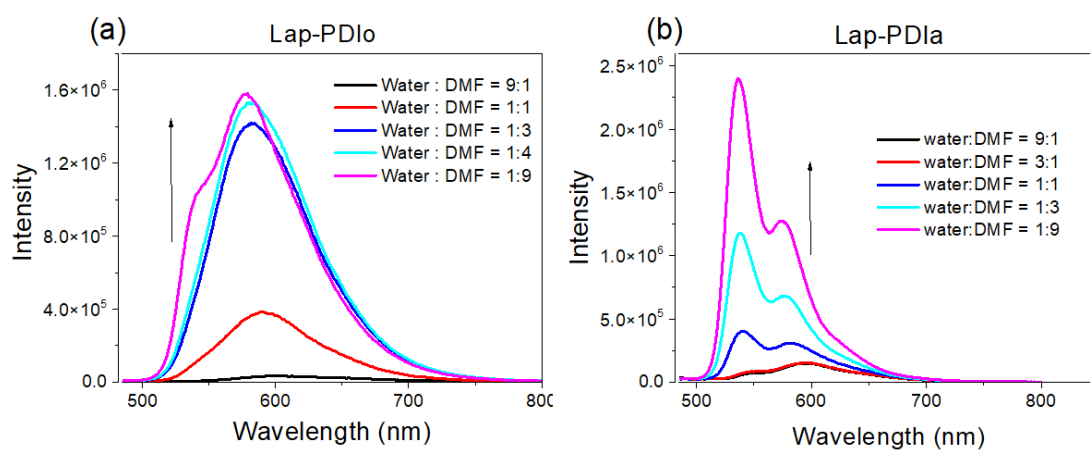


**Figure S9.** Fluorescence emission spectra (a) Lap-PDIo ( $0.01 \text{ mg ml}^{-1}$ ) and (b) Lap-PDIa ( $0.01 \text{ mg ml}^{-1}$ ) starting from a 1:9 DMF/water stock dispersion ( $\lambda_{\text{exc}} = 470 \text{ nm}$ ) in different water/DMF mixtures.

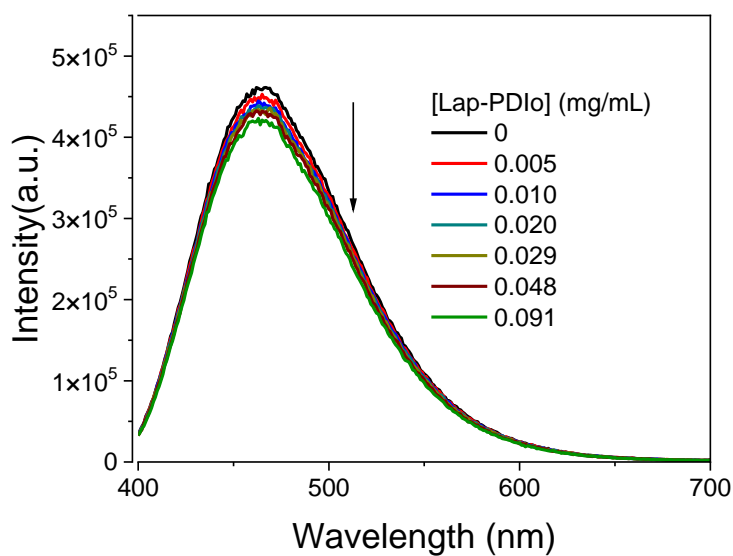


**Figure S10.** Fluorescence emission of mixture containing 10  $\mu\text{M}$  of DAPI with different concentrations of Lap in 1:1 DMF/water.

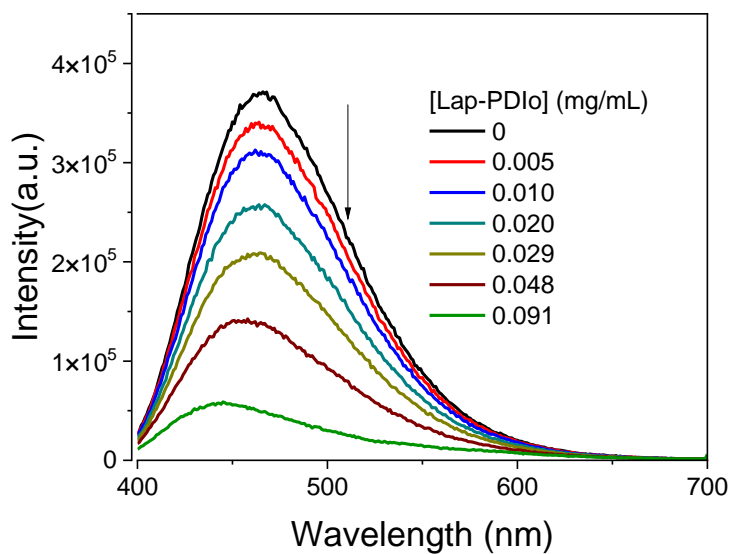


**Figure S11.** Fluorescence emission of mixture containing 10  $\mu\text{M}$  of DAPI with different concentrations of Lap-PDIo in 1:1 DMF/water.

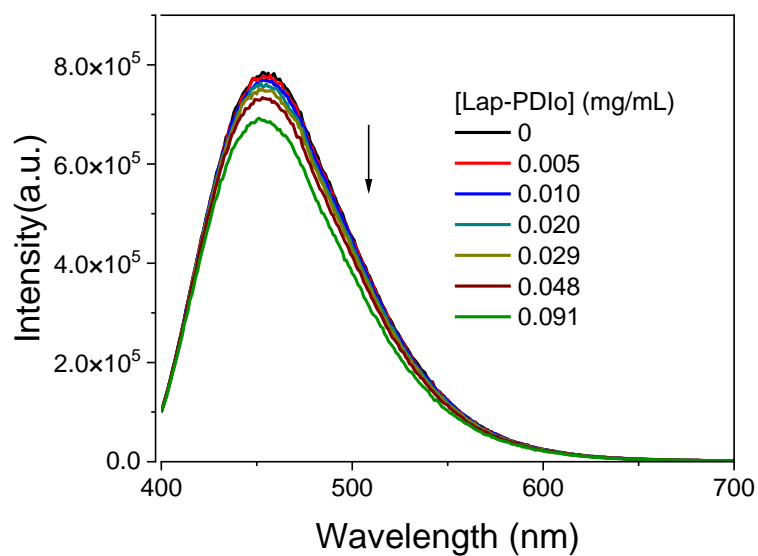


**Figure S12.** Fluorescence emission of mixture containing 10  $\mu\text{M}$  of DAPI with different concentrations of Lap in 9:1 DMF/water.

**Table S1.** Fluorescence Lifetimes of DAPI with different concentrations of Lap-PDIo measured at 467 nm.

[Lap-PDIo] (mg/mL)	90% DMF		50% DMF	
	$\tau_1$ (ns)	$\tau_2$ (ns)	$\tau_1$ (ns)	$\tau_2$ (ns)
0	0.42 (0.15)	2.80 (0.85)	0.34 (0.13)	2.11 (0.87)
0.005	0.40 (0.16)	2.80 (0.84)	0.32 (0.14)	2.14 (0.86)
0.010	0.39 (0.17)	2.80 (0.83)	0.32 (0.15)	2.16 (0.85)
0.020	0.34 (0.18)	2.78 (0.82)	0.29 (0.16)	2.16 (0.84)
0.029	0.33 (0.18)	2.77 (0.82)	0.32 (0.17)	2.19 (0.83)
0.048	0.31 (0.22)	2.75 (0.77)	0.33 (0.21)	2.23 (0.79)
0.091	0.26 (0.42)	2.67 (0.58)	0.30 (0.34)	2.28 (0.66)

**Table S2.** Fluorescence Lifetimes of DAPI with different concentrations of Lap measured at 467 nm.

[Lap] (mg/mL)	90% DMF		50% DMF	
	$\tau_1$ (ns)	$\tau_2$ (ns)	$\tau_1$ (ns)	$\tau_2$ (ns)
0				
0.005	0.43 (0.09)	2.75 (0.91)	0.34 (0.17)	2.11 (0.83)
0.010	0.43 (0.11)	2.75 (0.89)	0.35 (0.17)	2.12 (0.83)
0.020	0.44 (0.14)	2.74 (0.86)	0.36 (0.13)	2.14 (0.87)
0.029	0.46 (0.14)	2.75 (0.86)	0.39 (0.13)	2.17 (0.87)
0.048	0.47 (0.11)	2.73 (0.89)	0.35 (0.11)	2.18 (0.89)
0.091	0.49 (0.11)	2.70 (0.89)	0.41 (0.12)	2.25 (0.88) 0.

## References

- (1) Pasaogullari, N.; Icil, H.; Demuth, M. Symmetrical and Unsymmetrical Perylene Diimides: Their Synthesis, Photophysical and Electrochemical Properties. *Dye. Pigment.* **2006**, *69* (3), 118–127. <https://doi.org/10.1016/j.dyepig.2005.03.001>.
- (2) Nagao, Y.; Abe, Y.; Misono, T. Synthesis and Properties of N,N'-Unsymmetrical Dialkyl-3,4,9,10-Perylenebis(Dicarboximide)S. *Dye. Pigment.* **1985**, *6* (4), 303–311. [https://doi.org/10.1016/0143-7208\(85\)87006-6](https://doi.org/10.1016/0143-7208(85)87006-6).
- (3) Kaiser, H.; Lindner, J.; Langhals, H. Synthese von Nichtsymmetrisch Substituierten Perylen-Fluoreszenzfarbstoffen. *Chem. Ber.* **1991**, *124* (3), 529–535. <https://doi.org/10.1002/cber.19911240319>.
- (4) Tröster, H. Untersuchungen Zur Protonierung von Perylen-3,4,9,10-Tetracarbonsäurealkalisalzen. *Dye. Pigment.* **1983**, *4* (3), 171–177. [https://doi.org/10.1016/0143-7208\(83\)80015-1](https://doi.org/10.1016/0143-7208(83)80015-1).
- (5) Wheeler, P. A.; Wang, J.; Baker, J.; Mathias, L. J. Synthesis and Characterization of Covalently Functionalized Laponite Clay. *Chem. Mater.* **2005**, *17* (11), 3012–3018. <https://doi.org/10.1021/cm050306a>.
- (6) Xu, L.; Manda, V. R.; McNamara, L. E.; Jahan, M. P.; Rathnayake, H.; Hammer, N. I.

Covalent Synthesis of Perylenediimide-Bridged Silsesquioxane Nanoribbons and Their Electronic Properties. *RSC Adv.* **2014**, 4 (57), 30172–30179.

<https://doi.org/10.1039/c4ra03260h>.

- (7) Kozma, E.; Grisci, G.; Mróz, W.; Catellani, M.; Eckstein-Andicsovà, A.; Pagano, K.; Galeotti, F. Water-Soluble Aminoacid Functionalized Perylene Diimides: The Effect of Aggregation on the Optical Properties in Organic and Aqueous Media. *Dye. Pigment.* **2016**, 125, 201–209. <https://doi.org/10.1016/j.dyepig.2015.10.019>.
- (8) Zhong, L.; Xing, F.; Shi, W.; Yan, L.; Xie, L.; Zhu, S. Synthesis, Spectra, and Electron-Transfer Reaction of Aspartic Acid-Functionalized Water-Soluble Perylene Bisimide in Aqueous Solution. *ACS Appl. Mater. Interfaces* **2013**, 5 (8), 3401–3407. <https://doi.org/10.1021/am4004446>.
- (9) Nagao, Y. Synthesis and Properties of Perylene Pigments. *Prog. Org. Coatings* **1997**, 31 (1–2), 43–49. [https://doi.org/10.1016/S0300-9440\(97\)00017-9](https://doi.org/10.1016/S0300-9440(97)00017-9).

## **Appendix III**

### **Supplementary Information for Chapter 3**

#### **2D Nanomaterial-Directed Molecular Aggregation and Energy Transfer between Edge-Bound Donor-Acceptor pairs**

## **Supporting Information:**

### **2D Nanomaterial-Directed Molecular Aggregation and Energy Transfer between Edge-Bound Donor-Acceptor Pairs**

Hongxiao Xiang<sup>1</sup>, Silvano R. Valandro<sup>1,2</sup>, Eric H. Hill<sup>1,2\*</sup>

<sup>1</sup>Institute of Physical Chemistry, University of Hamburg, Grindelallee 117, 20146 Hamburg, Germany

<sup>2</sup>The Hamburg Center for Ultrafast Imaging (CUI), Luruper Chausee 149, 22761 Hamburg, Germany

\*E-mail: [eric.hill@chemie.uni-hamburg.de](mailto:eric.hill@chemie.uni-hamburg.de)

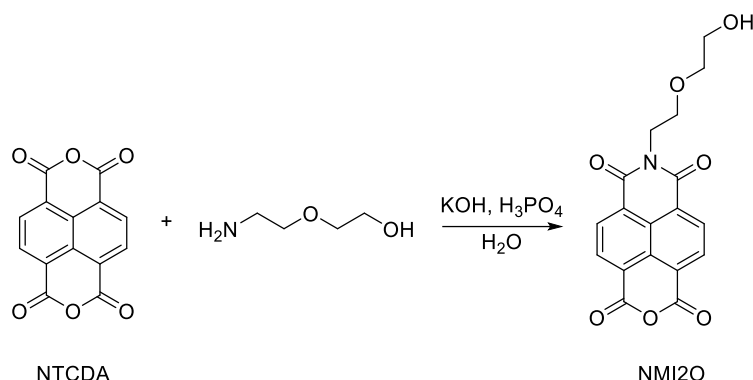
## Experimental Section

**Materials.** All chemicals were used as received without further purification. Millipore-filtered water with a resistivity of 18.2 M $\Omega$ ·cm was used for all reactions and preparation of dispersions. Laponite-RD was donated by BYK Additives (Germany). 1,4,5,8-Naphthalentetracarboxylic acid dianhydride (NTCDA) and tetraethylene glycol monoamine were purchased from ChemPUR. Perylene-3,4,9,10-tetracarboxylic acid dianhydride (PTCDA) was purchased from Alfa Aesar. Potassium hydroxide (85%) and concentrated hydrochloric acid (37%) were purchased from ChemSolute. Phosphoric acid, *tert*-Butanol, dichloromethane, and sea sand were purchased from Grüssing. Aminopropyltrimethoxysilane (APES) was purchased from Fluorochem. Methanol, absolute ethanol, and anhydrous *N,N*-Dimethylformamide (DMF) were purchased from FisherScientific. *N,N*-Dimethylformamide was purchased from TCI (Germany). 2-(2-Aminoethoxy)ethanol and TLC Silica gel 60 plates were purchased from Merck (Germany). Chloroform and acetic acid were purchased from VWR Chemicals. Chloroform-*d* and dimethylsulfoxide-*d*<sub>6</sub> were purchased from Euriso-Top. Silica gel for column chromatography was purchased from Macherey-Nagel.

**Characterization.** UV-Vis spectra were collected on a Cary 60 UV-Vis spectrometer (Agilent, Santa Clara, CA, USA). A Horiba Fluoromax-4 spectrometer (HORIBA, Kyōto, Japan) was used for collecting Steady-State Fluorescence spectra. Time-resolved photoluminescence measurements were performed on a FluoTime 300 fluorescence spectrometer (Picoquant, Berlin, Germany), in which the light source was a supercontinuum laser (SuperK Fianum, NKT Photonics, Copenhagen, Denmark) which passed through a deep UV supercontinuum extension unit (SuperK Extend-UV (DUV), NKT Photonics). Fourier-transform infrared spectroscopy (FT-IR) measurements were carried out on a Bruker Invenio® (Massachusetts, USA). FT-IR spectra were collected by using Golden Gate ATR, 128 scans were averaged and recorded at a resolution of 4 cm<sup>-1</sup>. A NETZSCH TG 209F1 Libra (NETZSCH, Bayern, Germany) was used for thermogravimetric analysis (TGA) from 25 °C to 700 °C with 10 K/min heating rate under 20 mL/min flow rate of nitrogen gas. All samples were dried at 100 °C in an oven overnight before TGA measurements. X-Ray diffractions were performed on a PANalytical X'PERT Pro diffractometer (Philips, Netherlands) with Cu K $\alpha$  radiation (wavelength: 1.54Å). Bruker Fourier HD 300 MHz and a Bruker Avance I 400MHz (Massachusetts, USA) were used for <sup>1</sup>H-NMR characterizations.



**Synthesis.** *Synthesis of Naphthene diglycol monoimide (NMI2O)*<sup>1</sup>

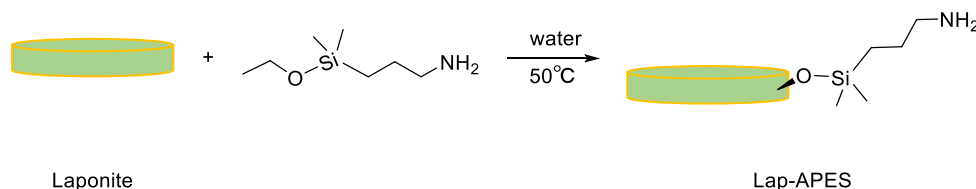


**Scheme S1.** synthesis route of NMI2O

Naphthalene-1,4,5,8-tetracarboxylic dianhydride (NTCDA, 1.62 mmol, 0.43 g) was dissolved in 59 ml water under stirring, and 165  $\mu$ L 2-(2-aminoethoxy) ethanol was added. In the next step, potassium hydroxide (KOH, 0.45 g, 8.02 mmol) was weighed and added to the mixture. The pH value was adjusted to 6.36 by adding 10% (w/w) phosphoric acid, followed by heating at 100 °C for 36 hours. After cooling to room temperature, the pH value of the reaction mixture was adjusted to 4.05 by adding acetic acid. In the next step, the mixture was concentrated to around 30 mL by rotary evaporation. The product was precipitated out when cooled down to 4 °C in an ice bath, followed by filtration and drying at 80°C in an oven.

Yield: 51%, <sup>1</sup>H NMR (400 MHz, DMSO-*d*<sub>6</sub>, 298.15 K, **Fig. S2**):  $\delta$  (ppm) = 8.48 (d, *J* = 7.6 Hz, 2H, aromatic), 7.96 (d, *J* = 7.6 Hz, 2H, aromatic), 4.24 (t, *J* = 6.4 Hz, 2H, CH<sub>2</sub>), 3.00–4.20 (br, 6H, CH<sub>2</sub>). FT-IR (Golden gate ATR, 4 cm<sup>-1</sup>):  $\nu$  = 1695, 1650, 1587, 1518, 1432, 1351, 1220, 1118, 1058, 951, 881, 830, 810, 770, 720, 663, 592, 557, 536. LC-MS (ESI): 355.063 [M]<sup>-</sup>, calculated for C<sub>18</sub>H<sub>13</sub>NO<sub>7</sub><sup>-</sup> [M]<sup>-</sup>: 355.068.

*Synthesis of APES functionalized Laponite (Lap-APES)*<sup>2</sup>

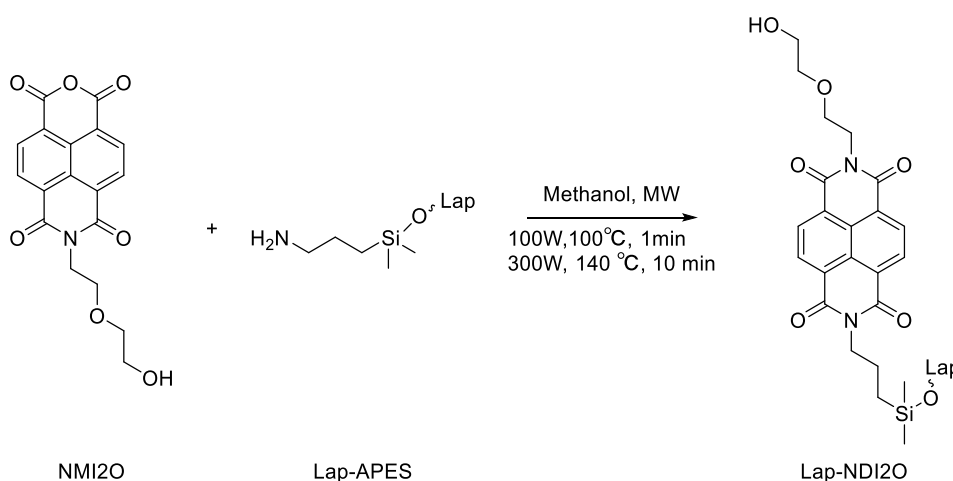


**Scheme S2.** synthesis route of Lap-APES

Laponite-RD (5 g) was weighed and added to 200 mL water at 50 °C and stirred for one hour. Aminopropyltrimethoxysilane (APES, 1.71 g, 2 mL, 10.62 mmol) was dissolved in 50 mL water and stirred for 30 min. The APES solution was added into the Laponite dispersion slowly and the reaction mixture was stirred at 50 °C for 16 hours. After cooling down, the clay was collected via centrifugation at 7500 rpm for 5 min, and washed with water three times. The resulting crude product was dispersed in 60% methanol/water and stirred for 24 hours. The clay was collected via centrifugation at 7500 rpm for 5 min followed by washing with 60% methanol/water five times. An off-white powder was gained after drying in a vacuum oven at 60°C.

Yield: 76.5%, FT-IR (Golden gate ATR, 4 cm<sup>-1</sup>):  $\nu = 650, 960, 1257, 1522, 1623, 3300$ . Element Analysis for Lap-APES, Found: N, 0.67; C, 2.99; H, 2.53.

*Synthesis of naphthalene diglycol monoimide modified Laponite (Lap-NDI2O)<sup>3</sup>*

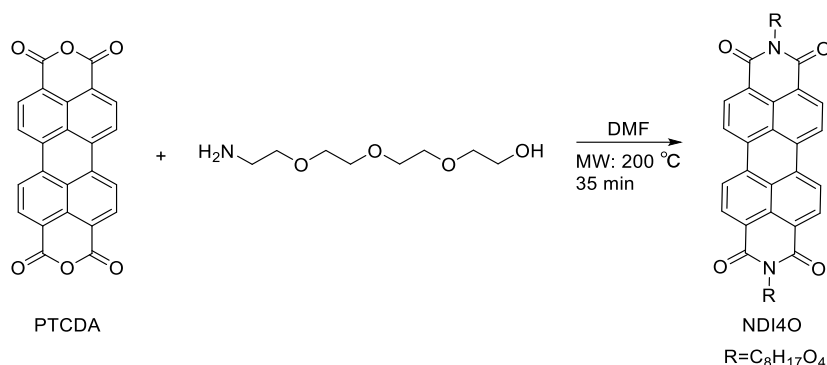


**Scheme S3.** synthesis route of Lap-NDI2O

Lap-APES (0.1 g) and compound 1, NMI2O (7.46 mg, 0.021 mmol), were dispersed in 5 mL methanol in a pyrex microwave reactor tube. The mixture was stirred for 5 min at 25 °C followed by sonication for 30 min. Once placed in the microwave reactor (CEM Discover, Matthews, NC, USA), the mixture was stirred for 2 min before irradiation at 100 W to achieve 100 °C for 1 min, followed by 140 °C for 10 min and then cooling of the tube. The resulting product was centrifuged for 10 min at 7500 rpm. The crude product was purified by washing it with methanol and water 3 times. The product was dried in a vacuum oven at 60 °C overnight.

Yield: 80%, FT-IR (Golden gate ATR, 4 cm<sup>-1</sup>):  $\nu = 650, 768, 796, 960, 1250, 1346, 1380, 1460, 1578, 1638, 1701, 3300$ . Element Analysis for Lap-NDI2O, Found: N, 0.88; C, 5.68; H, 2.42.

### Synthesis of perylene tetraethylene glycol diimide (PDI4O)<sup>4</sup>

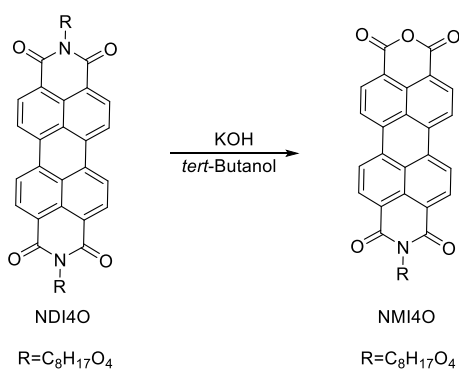


**Scheme S4.** synthesis route of PDI4O

Perylene-3,4,9,10-tetracarboxylic dianhydride (PTCDA, 0.1 g, 0.2549 mmol), tetraethylene glycol monoamine (92  $\mu$ L, 98 mg, 0.5098 mmol) and 8 mL anhydrous DMF were to a microwave reactor tube. The mixture was sonicated for 10 min prior to being placed in the microwave reactor. The dispersion was stirred for 30 seconds and heated with 100W to 200  $^\circ$ C for 35 min. After cooling down, DMF was removed via rotary evaporation. The crude product was purified via column chromatography (DCM: CH<sub>3</sub>OH = 9:1). The purified product was obtained as a red powder after removal of solvent by rotary evaporation.

Yield: 84%, <sup>1</sup>H NMR (400 MHz, CDCl<sub>3</sub>, 298.15 K, **Fig. S3**):  $\delta$  (ppm) = 8.65 (d,  $J$  = 8.0 Hz, 4H, aromatic), 7.56 (d,  $J$  = 7.8 Hz, 4H, aromatic), 4.48 (t,  $J$  = 5.9 Hz, 4H, CH<sub>2</sub>N), 3.88 (t,  $J$  = 5.9 Hz, 4H, CH<sub>2</sub>OH), 3.63 (m,  $J$  = 5.9 Hz, 24H, CH<sub>2</sub>O). FT-IR (Golden gate ATR, 4 cm<sup>-1</sup>):  $\nu$  = 3360, 2927, 2867, 1691, 1651, 1591, 1573, 1508, 1436, 1400, 1360, 1342, 1246, 1183, 1110, 1090, 1024, 991, 931, 857, 809, 794, 741, 715, 632, 587. LC-MS (ESI): 742.273 [M]<sup>-</sup>, calculated for C<sub>40</sub>H<sub>42</sub>N<sub>2</sub>O<sub>12</sub><sup>-</sup> [M]<sup>-</sup>: 742.274.

### Synthesis of perylene tetraethylene glycol monoimide (PMI4O)<sup>5,6</sup>

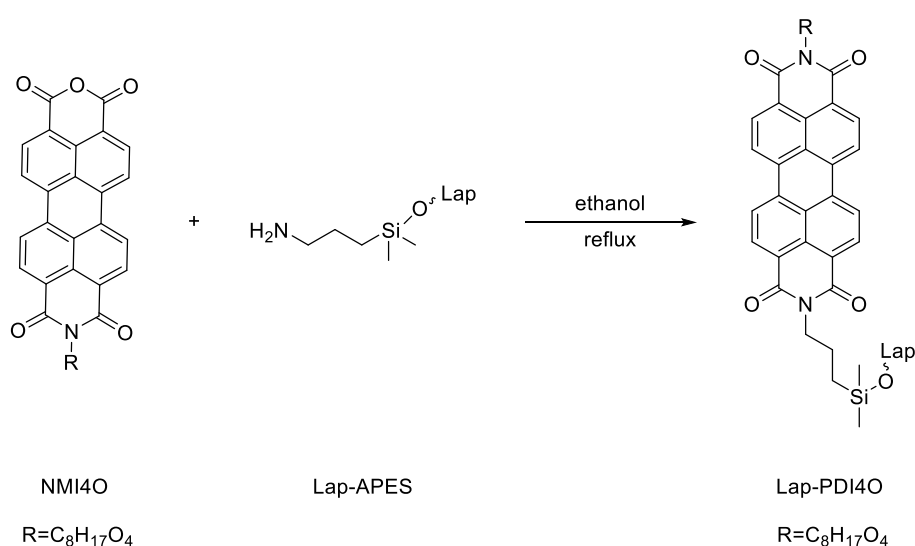


### Scheme S5. synthesis route of PMI4O

Perylenetetraethyleneglycol diimide (PDI4O, 0.1074 g, 0.14 mmol) was dispersed in 30 mL *tert*-butanol, and potassium hydroxide (KOH, 48 mg, 0.72 mmol) was added into the dispersion. The reaction was stirred under reflux for around 2 hours. The reaction was controlled by thin-layer chromatography (DCM: methanol = 9:1) till all PMI4O reacted. 20 mL glacial acetic acid and 20 mL 1M hydrochloric acid (HCl) was added to the cooled reaction mixture. The acidified reaction mixture was stirred at room temperature for 18 hours. Solids were filtered out on filter paper (Whatman<sup>®</sup> qualitative filter paper, Grade 1) and the filtrate was extracted in chloroform three times. The combined organic phases were dried over anhydrous magnesium sulfate followed by filtration. The product was obtained as a violet powder after removing the solvent by rotary evaporation.

Yield: 78%, <sup>1</sup>H NMR (300 MHz, CDCl<sub>3</sub>, 298.15 K, **Fig. S4**):  $\delta$  (ppm) = 8.61 (m, 6H, aromatic), 8.18 (d,  $J = 7.0$  Hz, 2H, aromatic), 4.48 (t, 2H, CH<sub>2</sub>), 4.20 (m, 4H, CH<sub>2</sub>), 3.88 (d,  $J = 5.5$  Hz, 2H, CH<sub>2</sub>), 3.65 (m, 8H, CH<sub>2</sub>). FT-IR (Golden gate ATR, 4 cm<sup>-1</sup>):  $\nu = 3370, 2927, 2850, 1734, 1719, 1691, 1649, 1598, 1578, 1489, 1461, 1441, 1400, 1365, 1345, 1246, 1099, 1052, 928, 885, 857, 809, 794, 746, 713, 635, 604$ . LC-MS (ESI): 567.153 [M]<sup>-</sup>, calculated for C<sub>32</sub>H<sub>25</sub>NO<sub>9</sub><sup>-</sup> [M]<sup>-</sup>: 567.153.

*Synthesis of perylene tetraethylene glycol monoimide modified Laponite (Lap-PDI4O)<sup>7,8</sup>*



### Scheme S6. synthesis route of Lap-PDI4O

Perylene tetraethylene glycol monoimide (PMI4O, 11.92 mg, 0.021 mmol) and Lap-APES (0.1g) were dispersed in 30 mL absolute ethanol. The reaction dispersion was stirred under

reflux for 18 hours. After cooling down, the dispersion was centrifugated at 7500 rpm for 15 min followed by washing with chloroform and water three times. The resulting product was dried in a vacuum oven at 60°C.

Yield: 85%, FT-IR (Golden gate ATR, 4 cm<sup>-1</sup>):  $\nu = 3330, 2957, 1689, 1641, 1593, 1575, 1513, 1494, 1446, 1406, 1370, 1352, 1260, 960, 806, 747, 647$ . Elemental Analysis for Lap-PDI4O, Found: N, 1.03; C, 7.11; H, 2.35.

**Methods.** Lap-NDI2O and Lap-PDI4O were dispersed in DMF as stock solutions with concentrations of 1 mg/mL. A 2 mM stock solution of CTAB was used for pillaring of the clay. 0.778  $\mu\text{mol}$  of CTAB (1.2x CEC of Laponite) was added to 0.1 mg/mL of the Lap-NDI2O. Fluorescence lifetime measurements were carried out at room temperature 1.5 hours after adding CTAB. To ensure complete pillaring fluorescence spectra were taken after 24 hours in the dark.

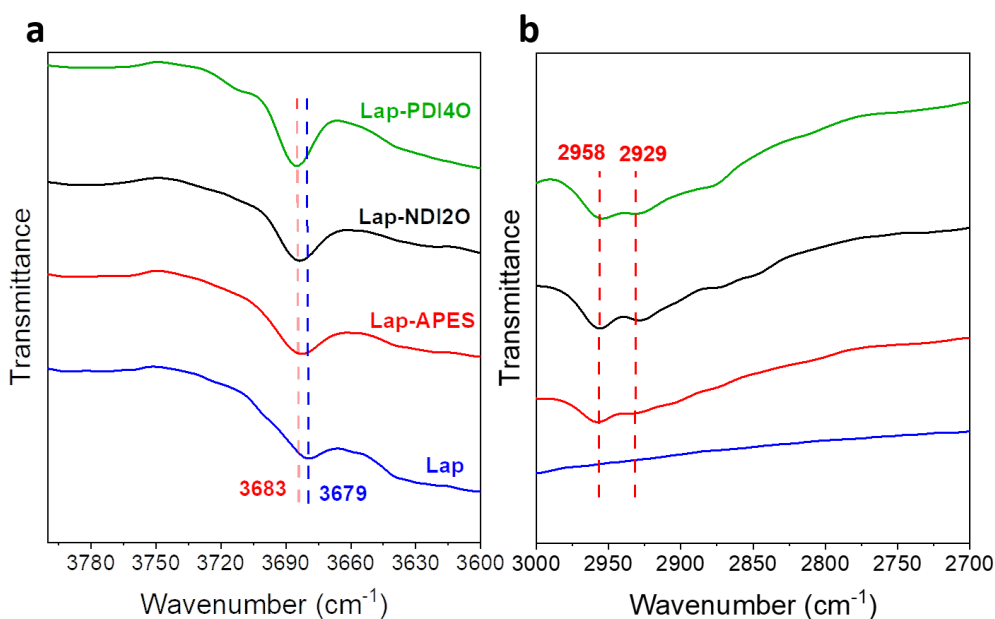


**Figure S1.** FT-IR spectra of Laponite (Lap), perylene diimide modified Laponite (Lap-PDI4O), naphthalene diimide modified Laponite (Lap-NDI2O), and aminosilane modified Laponite (Lap-APES)

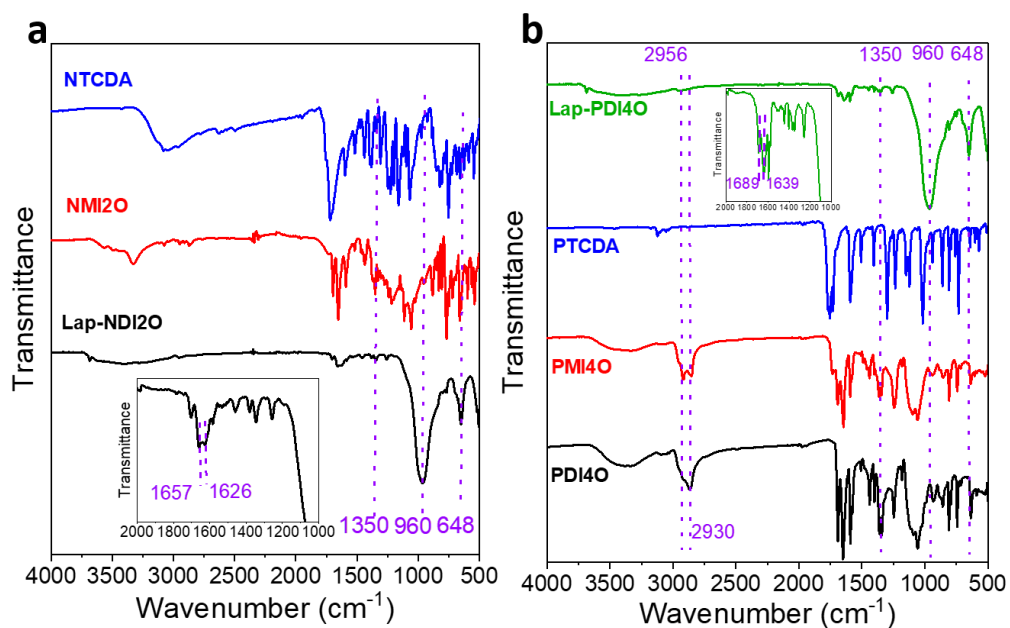


**Figure S2.** FT-IR spectra of naphthalene and perylene modified Lap and precursors/intermediates: naphthalene tetracarboxylic dianhydride (NTCDA), naphthalene monoimide (NDI2O), naphthalene diimide modified Laponite (Lap-NDI2O), perylene tetracarboxylic dianhydride (PTCDA), perylene monoimide (PMI4O), perylene diimide modified Laponite (Lap-PDI4O).

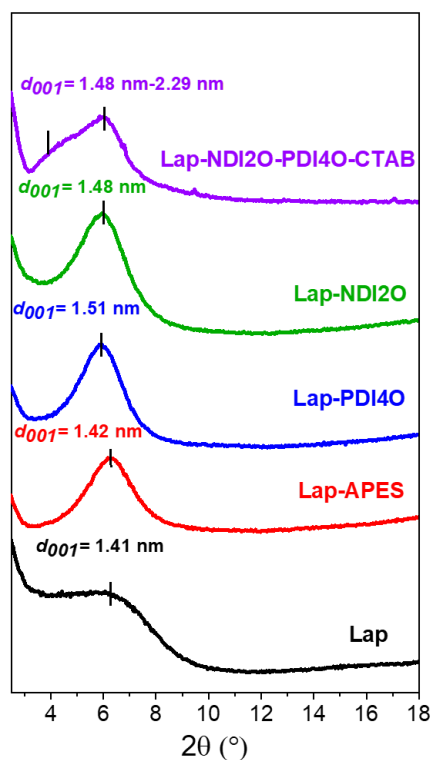


**Figure S3.** X-ray diffractograms of pristine Laponite (Lap), perylene diimide modified Laponite (Lap-PDI4O), naphthalene diimide modified Laponite (Lap-NDI2O), aminosilane modified Laponite (Lap-APES), CTAB pillared mix of Lap-NDI and Lap-PDI hybrid (Lap-NDI2O-PDI4O-CTAB).

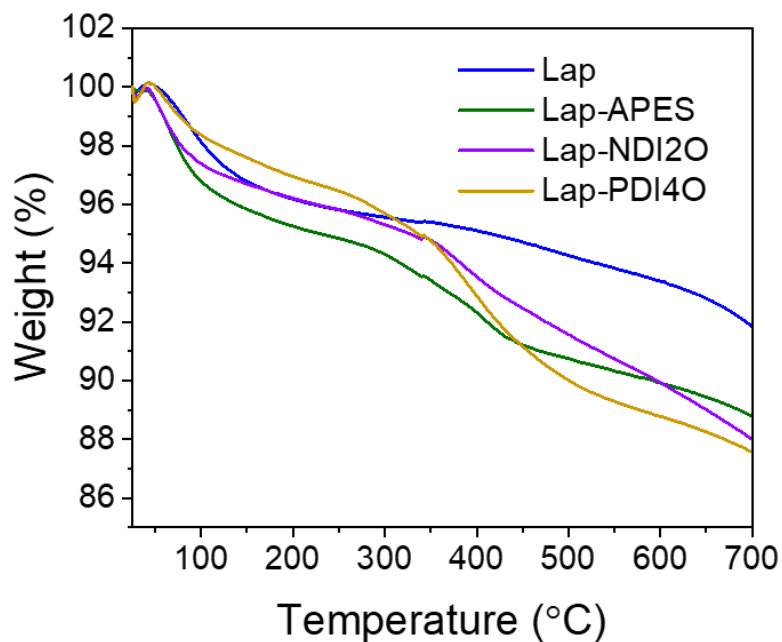


**Figure S4.** TGA curves of pristine Laponite (Lap), perylene diimide modified Laponite (Lap-PDI4O), naphthalene diimide modified Laponite (Lap-NDI2O), and aminosilane modified Laponite (Lap-APES).

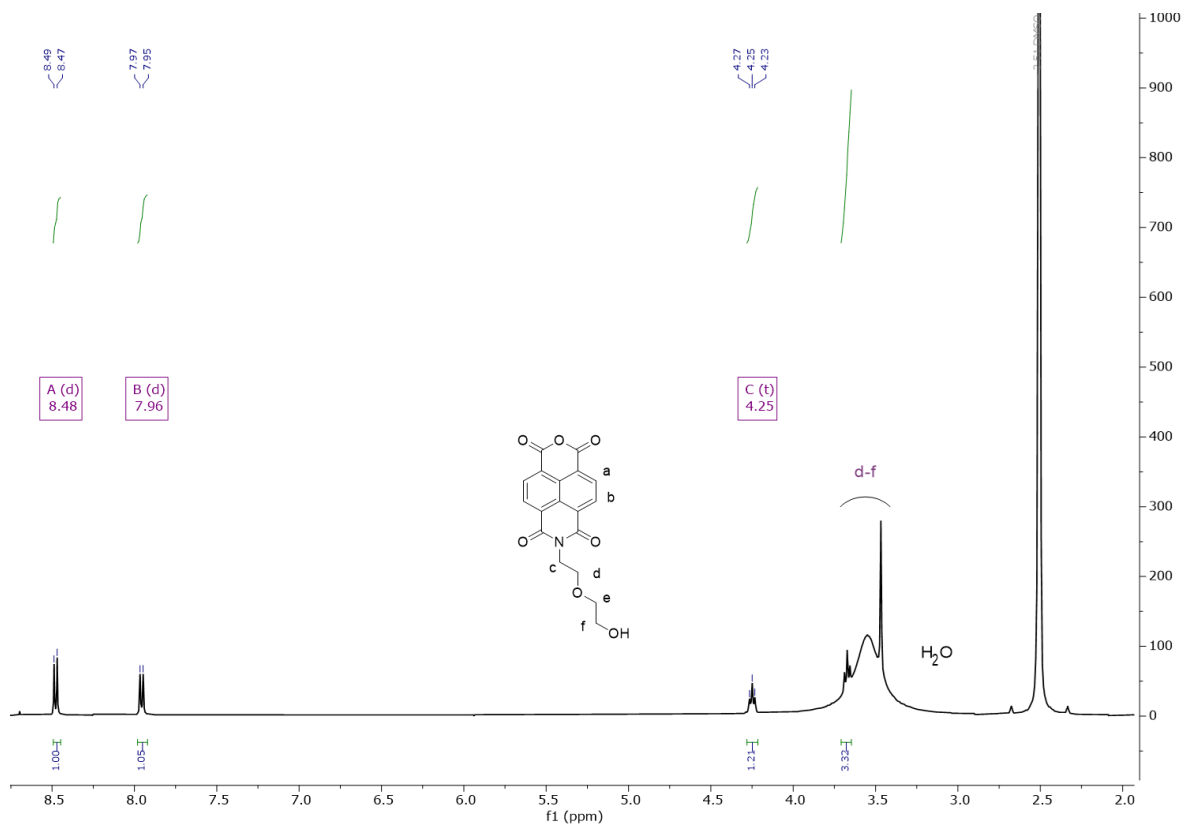


**Figure S5.**  $^1\text{H}$  NMR spectrum of naphthalene monoimide (NMI2O, 400 MHz,  $\text{DMSO-}d_6$ , 298.15 K)

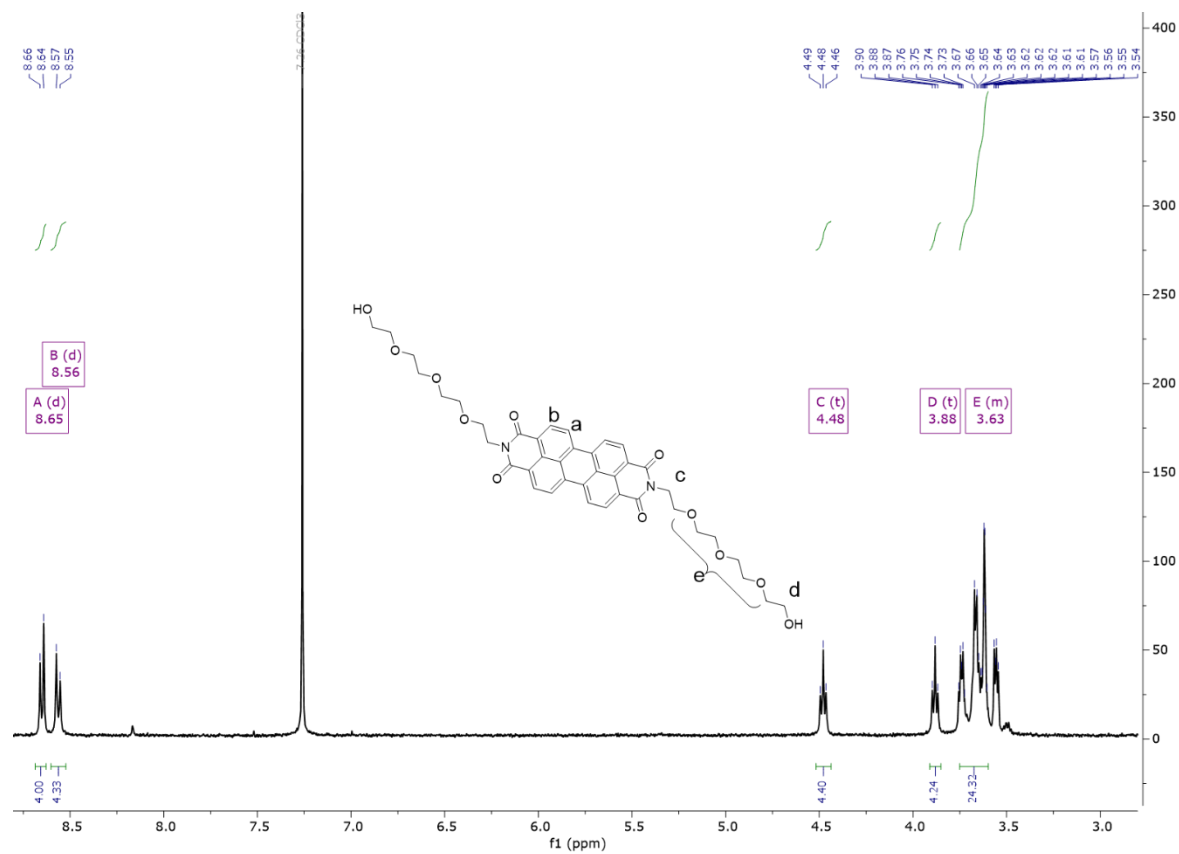




**Figure S6.**  $^1\text{H}$  NMR spectrum of perylene diimide (PDI4O, 400 MHz,  $\text{CDCl}_3$ , 298.15 K)

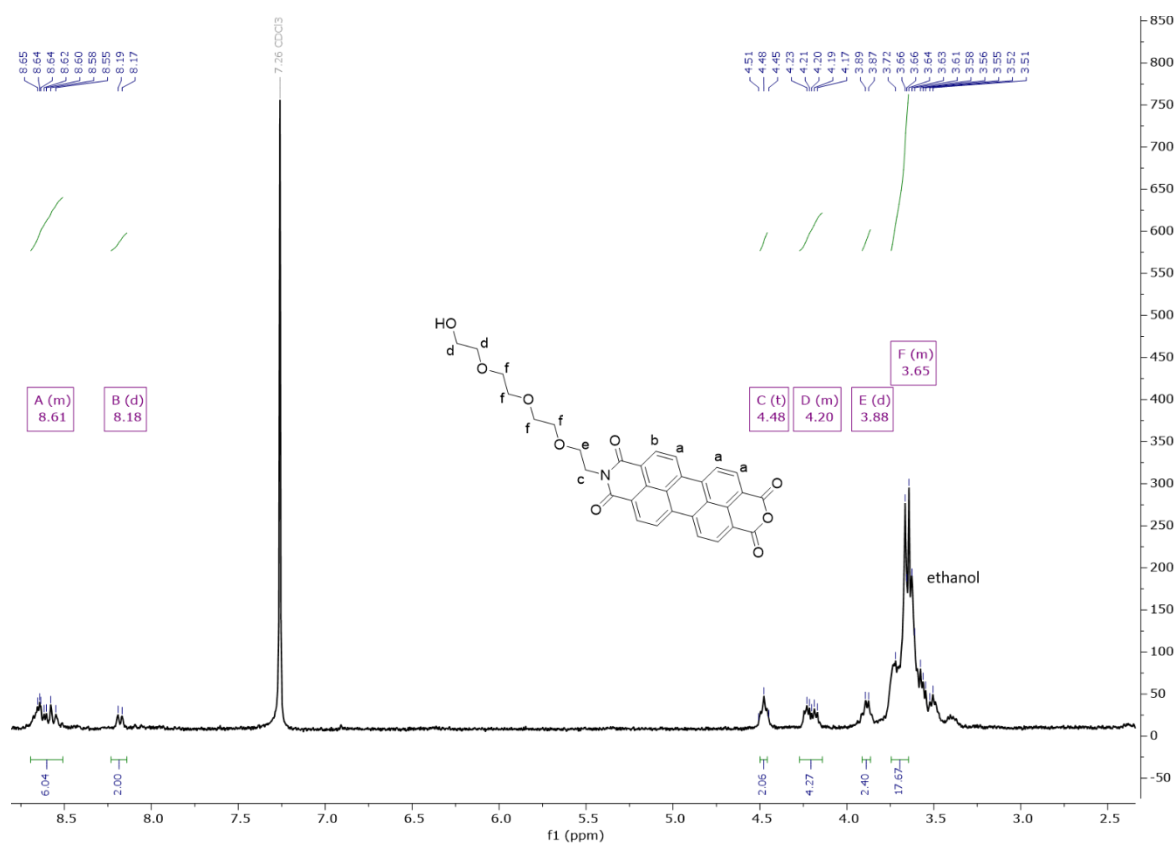


**Figure S7.**  $^1\text{H}$  NMR spectrum of perylene monoimide (PMI4O, 300 MHz,  $\text{CDCl}_3$ , 298.15 K)

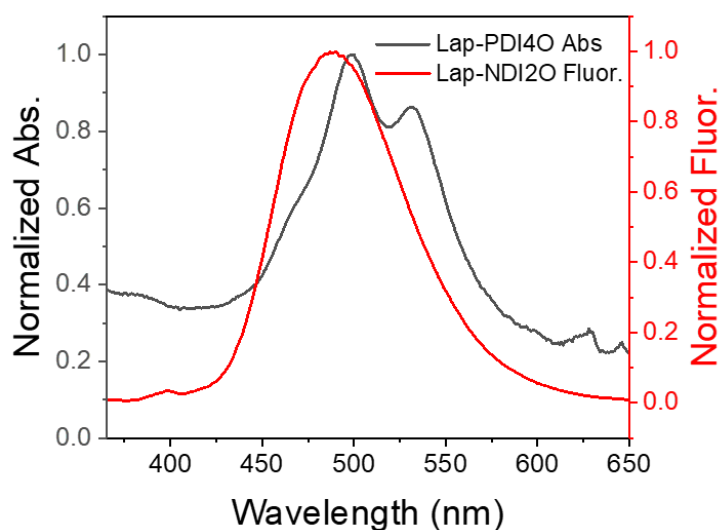


**Figure S8.** Normalized UV-Vis spectrum of acceptor (Lap-PDI4O, black, 0.01 mg/mL in 90% water) and normalized fluorescence spectrum of donor (Lap-NDI2O, red, 0.1 mg/mL in 90% water,  $\lambda_{ex}=350$  nm)

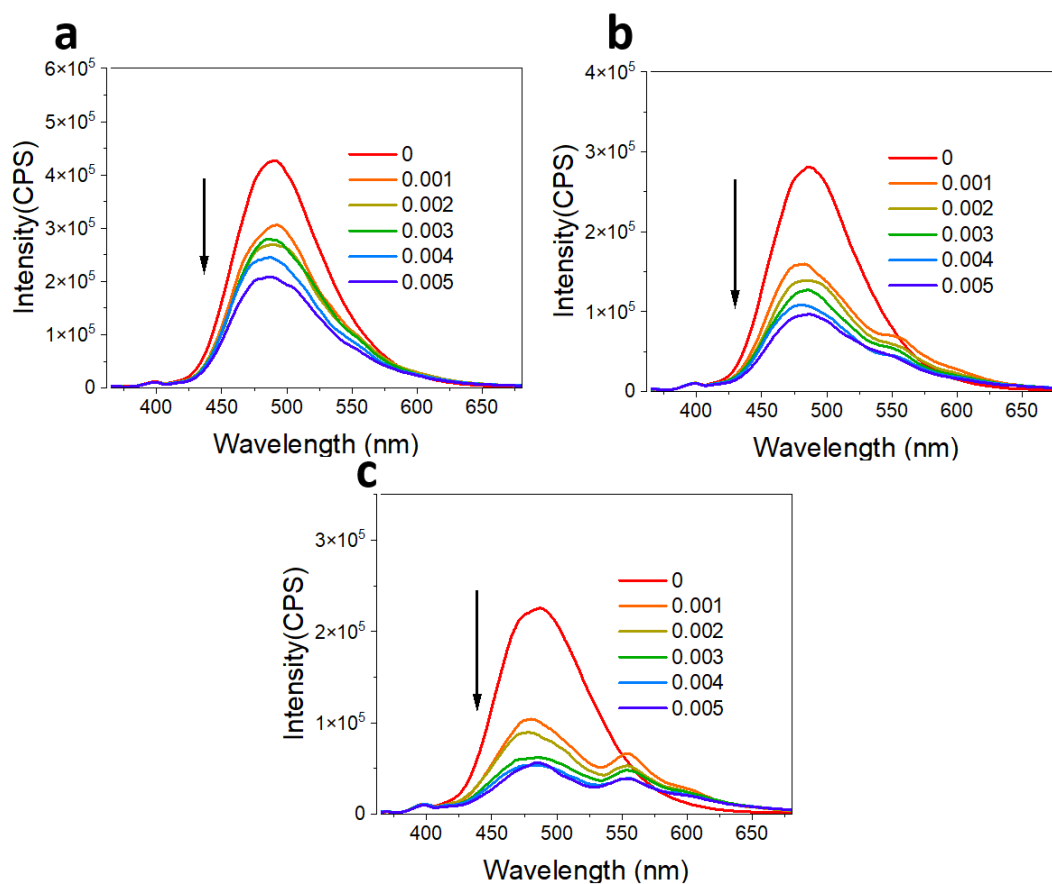


**Figure S9.** Fluorescence emission spectra of donor (Lap-NDI2O, 0.1 mg/mL,  $\lambda_{exc}$  = 350 nm) with increasing concentration of acceptor (Lap-PDI4O, mg/mL) in different DMF/water mixtures (a) 90% water and (b) 82.5% water and (c) 75% water. Arrow indicates increasing acceptor (Lap-PDI4O) concentration.

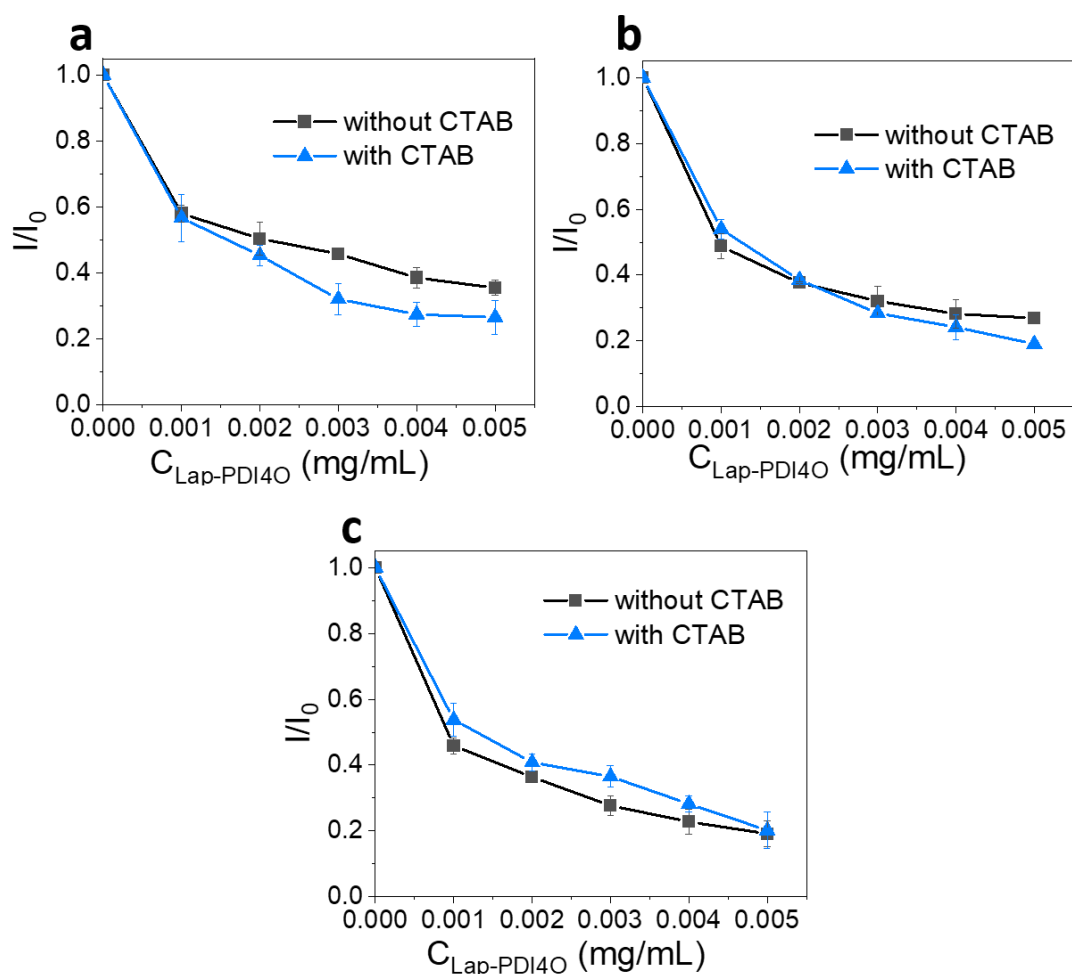


**Figure S10.** Fluorescence intensity relative to donor (Lap-NDI2O) alone at 485 nm as a function of the concentration of acceptor (Lap-PDI4O) in different DMF/water mixtures with and without CTAB. (a) 82.5% water and (b) 75% water and (c) 67.5% water.

**Table S1.** Fluorescence Lifetimes of Lap-NDI2O (0.1 mg/mL) pillared with 0.778  $\mu\text{mol}$  CTAB in 90% water with different concentrations of Lap-PDI4O, measured at 490 nm ( $\lambda_{ex} = 345$  nm).

[Lap-PDI4O] ( $\mu\text{g/mL}$ )	$\tau_1$ (ns)	$\tau_2$ (ns)	$\tau_3$ (ns)	$\tau_{\text{avg.}}$ (ns)
0	1.5 (0.47)	8.78 (0.28)	25.39 (0.25)	9.61
1	1.33 (0.56)	7.3 (0.26)	24.08 (0.18)	6.94
2	1.241(0.61)	6.76 (0.24)	23.45 (0.15)	5.91
3	1.153 (0.7)	6.3 (0.19)	22.697 (0.11)	4.471
4	0.994 (0.73)	5.34 (0.18)	21.07 (0.09)	3.575
5	0.982 (0.74)	5.65 (0.17)	21.54 (0.09)	3.54

## References

- (1) Imato, K.; Yamanaka, R.; Nakajima, H.; Takeda, N. Fluorescent Supramolecular Mechanophores Based on Charge-Transfer Interactions. *Chem. Commun.* **2020**, *56* (57), 7937–7940. <https://doi.org/10.1039/d0cc03126g>.
- (2) Wheeler, P. A.; Wang, J.; Baker, J.; Mathias, L. J. Synthesis and Characterization of Covalently Functionalized Laponite Clay. *Chem. Mater.* **2005**, *17* (11), 3012–3018. <https://doi.org/10.1021/cm050306a>.
- (3) Prentice, G. M.; Emmett, L. M.; Zhu, H.; Kociok-Köhn, G.; Pantoş, G. D. Thermally Stable Recyclable Naphthalenediimide-Siloxane Polymers. *Supramol. Chem.* **2016**, *28* (1–2), 161–167. <https://doi.org/10.1080/10610278.2015.1117085>.
- (4) Traeger, H.; Sagara, Y.; Kiebal, D. J.; Schrettl, S.; Weder, C. Folded Perylene Diimide Loops as Mechanoresponsive Motifs. *Angew. Chemie - Int. Ed.* **2021**, *60* (29), 16191–16199. <https://doi.org/10.1002/anie.202105219>.
- (5) Nagao, Y. Synthesis and Properties of Perylene Pigments. *Prog. Org. Coatings* **1997**, *31* (1–2), 43–49. [https://doi.org/10.1016/S0300-9440\(97\)00017-9](https://doi.org/10.1016/S0300-9440(97)00017-9).
- (6) Huang, C.; Barlow, S.; Marder, S. R. Perylene-3,4,9,10-Tetracarboxylic Acid Diimides: Synthesis, Physical Properties, and Use in Organic Electronics. *J. Org. Chem.* **2011**, *76* (8), 2386–2407. <https://doi.org/10.1021/jo2001963>.
- (7) Xu, L.; Manda, V. R.; McNamara, L. E.; Jahan, M. P.; Rathnayake, H.; Hammer, N. I. Covalent Synthesis of Perylenediimide-Bridged Silsesquioxane Nanoribbons and Their Electronic Properties. *RSC Adv.* **2014**, *4* (57), 30172–30179. <https://doi.org/10.1039/c4ra03260h>.
- (8) Xiang, H.; Valandro, S. R.; Hill, E. H. Layered Silicate Edge-Linked Perylene Diimides: Synthesis, Self-Assembly and Energy Transfer. *J. Colloid Interface Sci.* **2023**, *629*, 300–306. <https://doi.org/10.1016/j.jcis.2022.09.055>.

## **Appendix IV**

### **Supplementary Information for Chapter 4**

#### **Cascade Förster resonance energy transfer between layered silicate edge-linked chromophores**

## Supporting Information:

### Cascade Förster Resonance Energy Transfer Between Layered Silicate Edge-linked Chromophores

Hongxiao Xiang<sup>1</sup>, Eric H. Hill<sup>1,2\*</sup>

<sup>1</sup>Institute of Physical Chemistry, University of Hamburg, Grindelallee 117, 20146 Hamburg, Germany

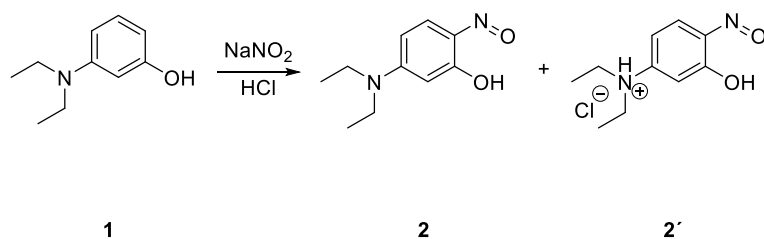
<sup>2</sup>The Hamburg Center for Ultrafast Imaging (CUI), Luruper Chausee 149, 22761 Hamburg, Germany

\*E-mail: [eric.hill@uni-hamburg.de](mailto:eric.hill@uni-hamburg.de)

#### Detailed Methods

**Materials.** All chemicals were used as received without further purification. Sodium ascorbate was purchased from Sigma-Aldrich (Germany). Concentrated hydrochloric acid (HCl, 37%) and sodium azide (NaN<sub>3</sub>) were purchased from ChemSolute. Potassium carbonate (K<sub>2</sub>CO<sub>3</sub>), sodium nitrite (NaNO<sub>2</sub>), *tert*-Butanol, and sea sand were purchased from Grüssing. Toluene, *n*-Hexan, and anhydrous *N,N*-Dimethylformamide (DMF) were purchased from Fisher Scientific. *N,N*-Dimethylformamide (DMF), and ethyl acetate were purchased from VWR Chemicals. Copper(II) sulfate (CuSO<sub>4</sub>) was purchased from Roth. (3-Chloropropyl)methoxydimethylsilane was purchased from ABCR. Thin Layer Chromatography (TLC) Silica gel 60 plates were purchased from Merck (Germany). Chloroform-*d* (CDCl<sub>3</sub>) and dimethylsulfoxide-*d*<sub>6</sub> (DMSO-*d*<sub>6</sub>) were purchased from Euriso-Top. Silica gel for column chromatography was purchased from Macherey-Nagel. Millipore-filtered water with a resistivity of 18.2 MΩ·cm was used for all reactions and preparation of dispersions.

**Synthesis.** Synthesis of 5-(Diethylamino)-2-nitrosophenol (**2**)[1,2]

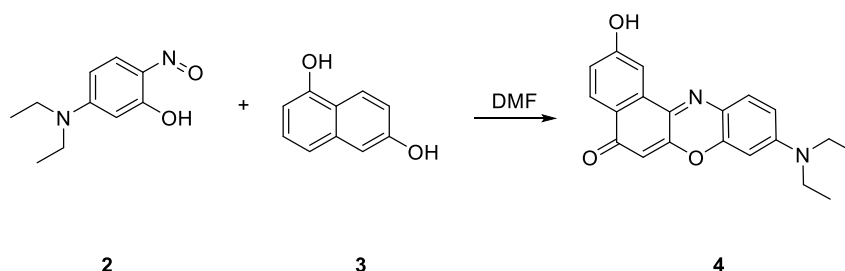


**Scheme S1.** synthetic route of compound 2

3-(Diethylamino) phenol (**1**, 40.36 mmol, 6.67 g) was dissolved in 8 mL water and 14 mL concentrated hydrochloric acid (HCl) under stirring. The solution was cooled down to 0°C in an ice bath. A solution of sodium nitrite (NaNO<sub>2</sub>, 36.52 mmol, 2.52 g) in 20 mL water was prepared in a separate flask. In the next step, the solution of sodium nitrite was dropwise added into the reaction solution within 30 minutes. The reaction mixture was stirred at 0°C-5°C for 4 hours. After the reaction, the formed solid was filtered out and dried at 60 °C overnight. For purification, the dried crude product was recrystallized in ethanol. A brown powder was gained as a mixture of **2** and **2'** by filtration and drying at 60°C in an oven.

Yield: 25%, <sup>1</sup>H NMR (300 MHz, DMSO-*d*<sub>6</sub>, 298.15 K, **Fig. S8**): δ (ppm) = 7.55 (d, *J* = 10.4 Hz, 1H, aromatic), 7.20 (d, *J* = 8.2 Hz, 1H, aromatic), 6.48 (s, 1H, aromatic), 3.58 (br, 4H, CH<sub>2</sub>), 1.29 (m, 6H, CH<sub>3</sub>). LC-MS (ESI): 195.114 [MH]<sup>+</sup>, calculated for C<sub>10</sub>H<sub>15</sub>N<sub>2</sub>O<sub>2</sub><sup>+</sup> [MH]<sup>+</sup>: 195.113.

#### Synthesis of 2-Hydroxy Nile Red (**4**)[1,3]

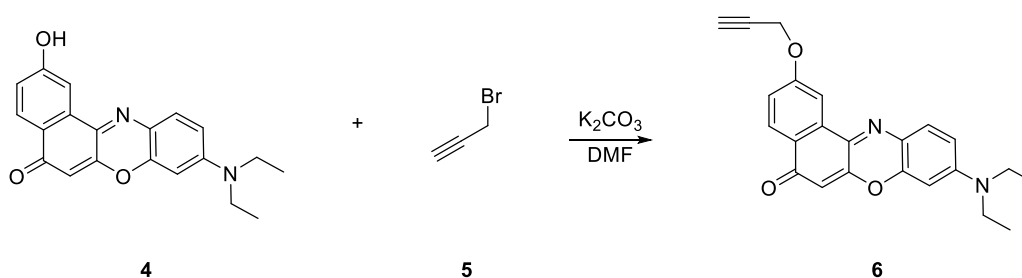


**Scheme S2.** synthetic route of compound **4**

5-(Diethylamino)-2-nitrosophenol (**2**, 4.33 mmol, 1 g) and 1,6-Dihydroxynaphthalene (**3**, 5.10 mmol, 0.75g) were weighed and dissolved 90 mL *N,N*-Dimethylformamide (DMF). The reaction mixture was stirred at 155 °C for 4 hours. After cooling down, the solvent was removed via a rotary evaporator. The gained crude product was poured into 200 mL brine and the precipitated solid was filtered out and washed with a mixture of dichloromethane and methanol with a ratio of 4: 1. A light brown powder was gained after drying in an oven at 60°C.

Yield: 29%, <sup>1</sup>H NMR (300 MHz, DMSO-*d*<sub>6</sub>, 298.15 K, **Fig. S9**): δ (ppm) = 10.43 (s, 1H, OH), 7.98 (d, *J* = 8.6 Hz, 1H, aromatic), 7.90 (s, 1H, aromatic), 7.60 (d, *J* = 9.0 Hz, 1H, aromatic), 7.10 (dd, *J* = 8.6 Hz, *J* = 2.5 Hz, 1H, aromatic), 6.82 (dd, *J* = 10.4 Hz, *J* = 1.6 Hz, 1H, aromatic), 6.67 (d, *J* = 6.8 Hz, 1H, aromatic), 6.17 (s, 1H, aromatic), 3.52 (q, *J* = 6.7 Hz, 4H, CH<sub>2</sub>), 1.17 (m, 6H, CH<sub>3</sub>). LC-MS (ESI): 335.141 [MH]<sup>+</sup>, calculated for C<sub>20</sub>H<sub>19</sub>N<sub>2</sub>O<sub>3</sub><sup>+</sup> [MH]<sup>+</sup>: 335.140.

Synthesis of 9-(Diethylamino)-2-(2-propyn-1-yloxy)-5H-benzo[a]phenoxazin-5-one (**6**)[4]

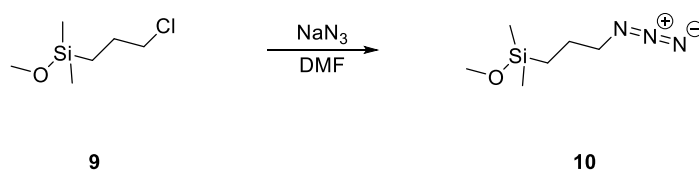


**Scheme S3.** synthetic route of compound **6**

2-Hydroxy Nile Red (**4**, 0.32 mmol, 0.1 g) was weighed and dissolved in 5 mL anhydrous *N,N*-Dimethylformamide (DMF) followed by getting cooled in an ice bath. Potassium carbonate (K<sub>2</sub>CO<sub>3</sub>, 1.29 mmol, 0.18 g) was added to the cooled solution. In the next step, propargyl bromide (**5**, 1.29 mmol, 0.1 mL) was added dropwise. The reaction mixture was stirred at 70 °C for 3 hours. After cooling down, the reaction solution was concentrated under reduced pressure and purified via column chromatography (*n*-hexane: ethylacetate = 4:1). The purified product was obtained as a brown powder after removal of the solvent via rotary evaporation and dried in an oven at 60°C.

Yield: 19%, <sup>1</sup>H NMR (300 MHz, DMSO-*d*<sub>6</sub>, 298.15 K, **Fig. S10**): δ (ppm) = 8.09 (d, *J* = 8.8 Hz, 1H, aromatic), 8.06 (d, *J* = 2.6 Hz, 1H, aromatic), 7.65 (d, *J* = 9.1 Hz, 1H, aromatic), 7.34 (dd, *J* = 8.8 Hz, *J* = 2.6 Hz, 1H, aromatic), 6.85 (dd, *J* = 9.1 Hz, *J* = 2.6 Hz, 1H, aromatic), 6.69 (d, *J* = 2.8 Hz, 1H, aromatic), 6.23 (s, 1H, aromatic), 5.04 (d, *J* = 2.4 Hz, 2H, OCH<sub>2</sub>), 3.68 (t, *J* = 2.2 Hz, 1H, ≡CH), 3.53 (q, *J* = 6.9 Hz, 4H, CH<sub>2</sub>), 1.18 (t, *J* = 7.0 Hz, 6H, CH<sub>3</sub>). FT-IR (Golden gate ATR, 4 cm<sup>-1</sup>): ν = 590, 638, 690, 756, 788, 806, 819, 844, 862, 892, 923, 925, 1006, 1080, 1114, 1147, 1176, 1193, 1209, 1247, 1265, 1334, 1373, 1404, 1467, 1490, 1517, 1548, 1589, 1639, 1672, 2108, 2850, 2871, 2925, 2964, 3190, 3286. LC-MS (ESI): 373.154 [MH]<sup>+</sup>, calculated for C<sub>23</sub>H<sub>21</sub>N<sub>2</sub>O<sub>3</sub><sup>+</sup> [MH]<sup>+</sup>: 373.155.

Synthesis of 1-Azido-3-(methoxydimethylsilyl)propane (**10**)[5]



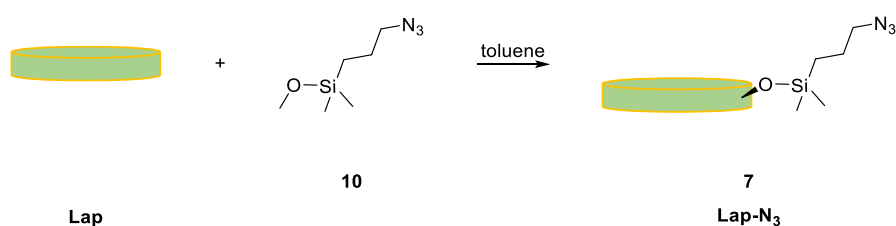


#### Scheme S4. synthetic route of compound **10**

Under the protection of nitrogen, (3-Chloropropyl)methoxydimethylsilane (**9**, 8 mmol, 1.06 mL) and sodium azide (16 mmol, 1.04 g) were added to 20 mL *N,N*-Dimethylformamide (DMF). The reaction mixture was stirred at 100 °C for 24 hours. After cooling down, the solid was filtered out and the filtrate was concentrated via a rotary evaporator. The product was gained as a pale yellow liquid.

Yield: 99%, <sup>1</sup>H NMR (300 MHz, CDCl<sub>3</sub>-d, 298.15 K, **Fig. S11**): δ (ppm) = 3.44 (m, 2H, N<sub>3</sub>CH<sub>2</sub>), 3.27 (m, 3H, OCH<sub>3</sub>), 1.64 (m, 2H, CH<sub>2</sub>), 0.64 (m, 2H, CH<sub>2</sub>), 0.12 (t, *J* = 11.0 Hz, *J* = 4.0 Hz, *J* = 2.2 Hz, 6H, CH<sub>3</sub>). LC-MS (ESI): 174.107 [M+H]<sup>+</sup>, calculated for C<sub>6</sub>H<sub>16</sub>N<sub>3</sub>OSi<sup>+</sup> [M+H]<sup>+</sup>: 174.106.

#### Synthesis of Lap-N<sub>3</sub> (**7**)[6]

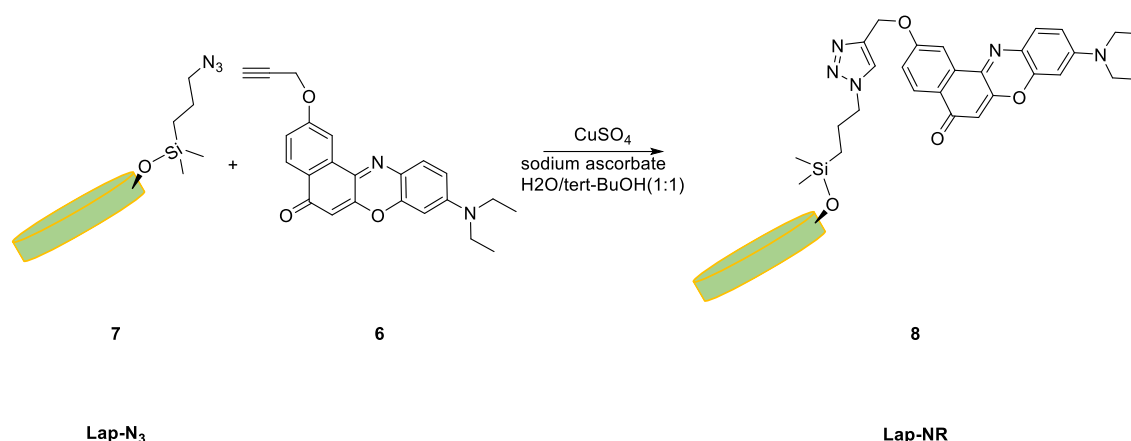


#### Scheme S5. synthetic route of Lap-N<sub>3</sub> (**7**)

Laponite (Lap, 0.5 g) was dried at 120 °C for 24 hours and transferred in a microwave reactor tube. Compound **10** (8.19 mmol, 1.42g) in 2 mL toluene was dropwise added. Another 8 mL toluene was added in the same tube, followed by 30 minutes of sonication. The reaction mixture was inserted in a microwave reactor and heated to 100 °C under stirring for 1 hour. In the next step, the solid was filtered off and rinsed with 50 mL methanol. The gained product was dried at 80 °C overnight in an oven.

Yield: 99%, FT-IR (Golden gate ATR, 4 cm<sup>-1</sup>): ν = 651, 794, 840, 960, 1253, 1656, 2106, 2879, 2933, 2954, 3107, 3681.

### Synthesis of Lap-NR (8)[1,6]



**Scheme S6.** synthetic route of Lap-NR (8)

Compound **7** (Lap-N<sub>3</sub>, 114.88 mg), compound **6** (10.73 mg, 29  $\mu$ mol), copper(II) sulfate (CuSO<sub>4</sub>·5H<sub>2</sub>O, 5.8  $\mu$ mol, 0.92 mg), and sodium ascorbate (5.8  $\mu$ mol, 1.14 mg) were weighed and dispersed in 5 mL mixture of *tert*-butanol and water with a ratio of 1:1. The reaction mixture was treated with 30 minutes sonication, followed by inserted in a microwave reactor. In the next step, the reaction dispersion was heated to 100°C under stirring and held for 10 minutes. As the reaction terminated, the product was washed with *N,N*-Dimethylformamide 5 times via centrifugation (7500 rpm, 10 minutes), followed by washing with water for another 3 times. The product was dried at 60 °C in an oven for 3 days and gained as a dark purple powder.

Yield: 97%, FT-IR (Golden gate ATR, 4 cm<sup>-1</sup>):  $\nu$  = 646, 960, 1253, 1384, 1413, 1438, 1496, 1595, 1660, 1822, 1978, 2011, 2034, 2048, 2069, 2812, 2885, 2933, 3107, 3625, 3687, 3712, 3784.

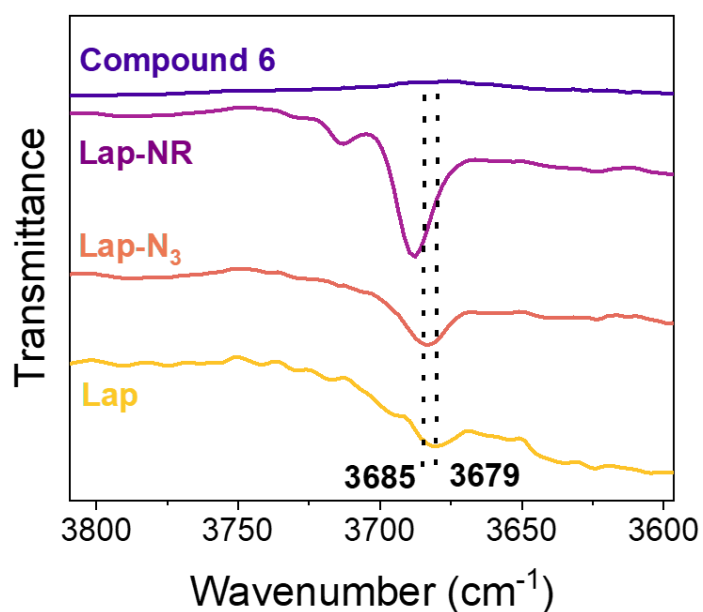


**Figure S1.** FT-IR spectra of compound **6** (purple), Nile red derivative modified Laponite (Lap-NR, purple-red), azide end group modified Laponite (Lap-N<sub>3</sub>, orange), and the pristine Laponite (Lap, yellow).

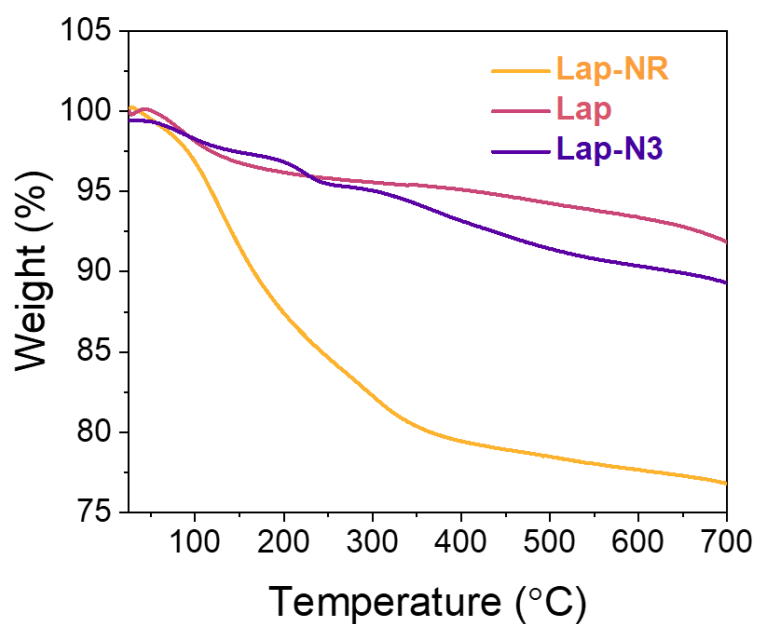


**Figure S2.** TGA curves of pristine Laponite (red, Lap), azide end group modified Laponite (purple, Lap-N<sub>3</sub>), and Nile red derivative modified Laponite (orange, Lap-NR).

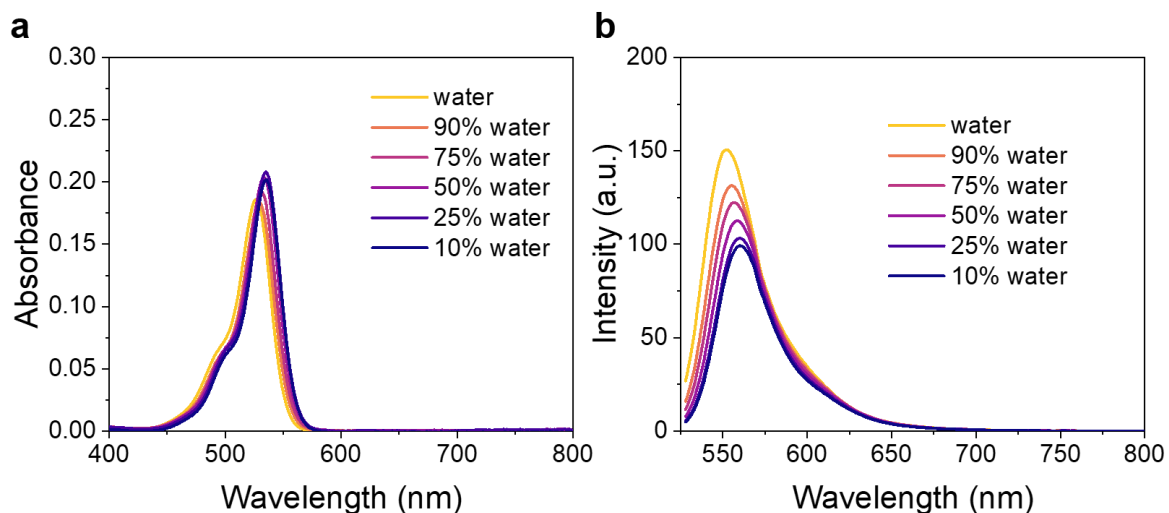


**Figure S3.** (a) UV-Vis absorbance spectra of rhodamine 6G (R6G, 20 μM) and (b) Fluorescence spectra of R6G (2 μM, λ<sub>ex</sub> = 520 nm) in various water/DMF composites.

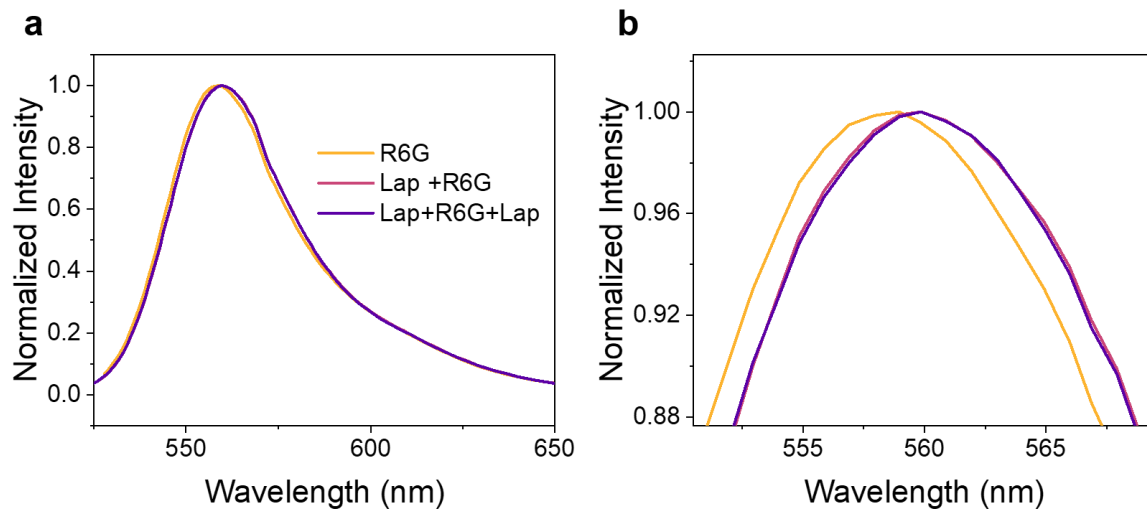


**Figure S4.** Normalized Fluorescence Spectra, λ<sub>ex</sub> = 350 nm (a) of R6G in 50% Water (2 μM), R6G (0.133 μM) on Lap (0.1 mg/mL), and R6G (0.133 μM) with increasing Lap concentration (0.13 mg/mL, Lap + R6G + Lap). (b) Zoomed-in wavelength ranges from 550 nm to 570 nm.

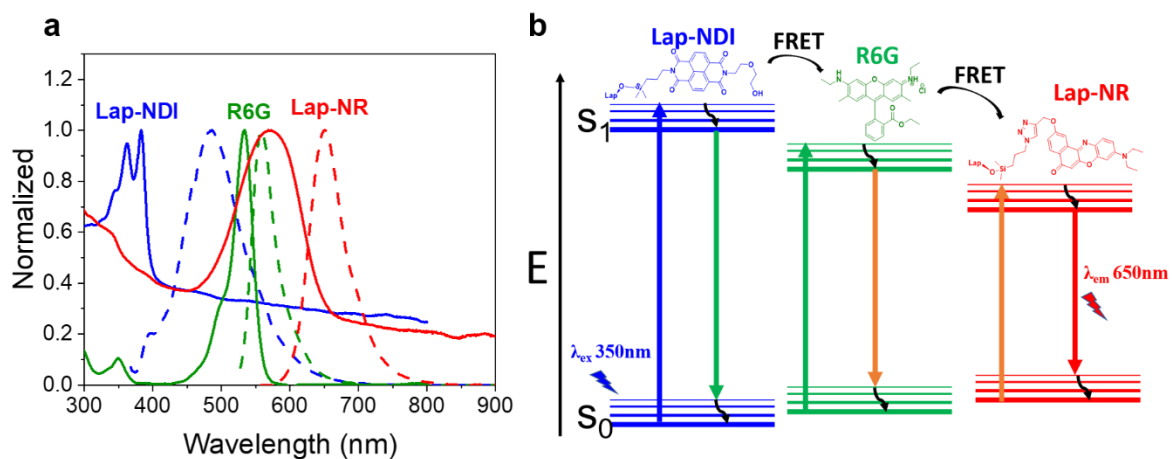


**Figure S5.** (a): Normalized UV-Vis spectra (solid lines) and Fluorescence spectra (dashed lines) of Lap-NDI (blue, 0.1 mg/mL,  $\lambda_{ex} = 350\text{ nm}$ ), R6G (green, 20  $\mu\text{M}$ ,  $\lambda_{ex} = 520\text{ nm}$ ), and Lap-NR (red, 0.1 mg/mL,  $\lambda_{ex} = 540\text{ nm}$ ); (b) Energy level diagram illustrating the cascade FRET process: upwards arrows refer to excitation, downwards arrows refer to fluorescence emission, and black curved arrows refer to internal conversion.

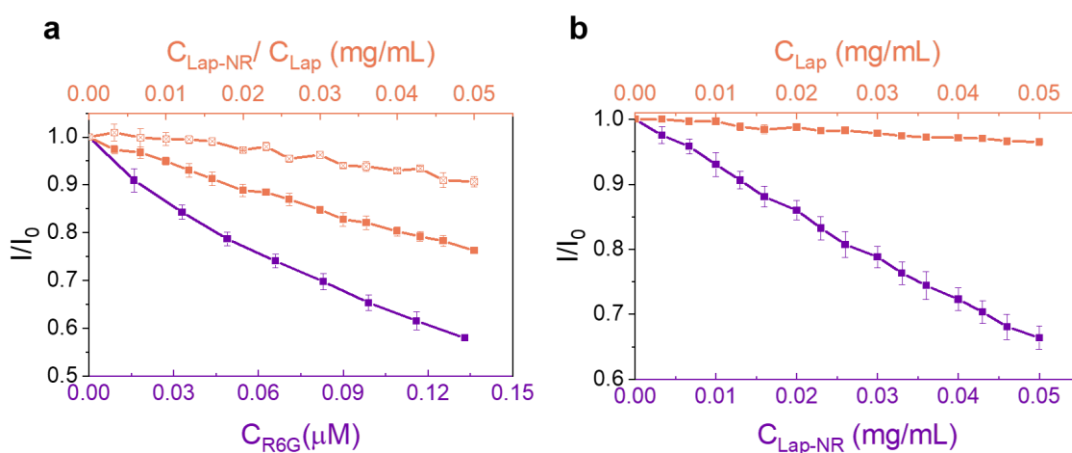


**Figure S6.**  $\lambda_{ex} = 350\text{ nm}$ ,  $I/I_0$  at 485 nm as a function of the concentration of R6G (purple square), Lap-NR (orange square), and Lap (orange crossing square) in 50% water (a), and  $I/I_0$  at 560 nm as a function of the concentration of Lap-NR (purple square) and Lap (orange square) in 50% water (b).

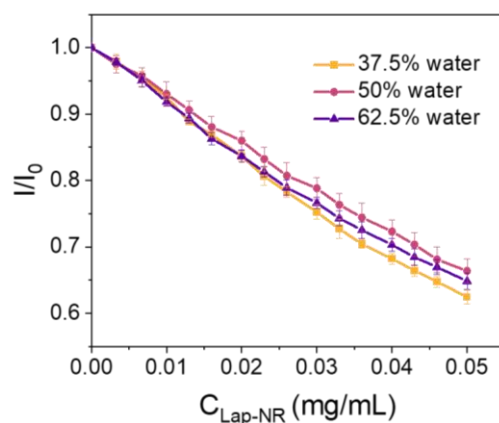


**Figure S7.**  $\lambda_{\text{ex}} = 350$  nm,  $I/I_0$  at 560 nm as a function of the concentration of Lap-NR in 37.5% water (orange square), 50% water (red circle), and 62.5% water (purple triangle).

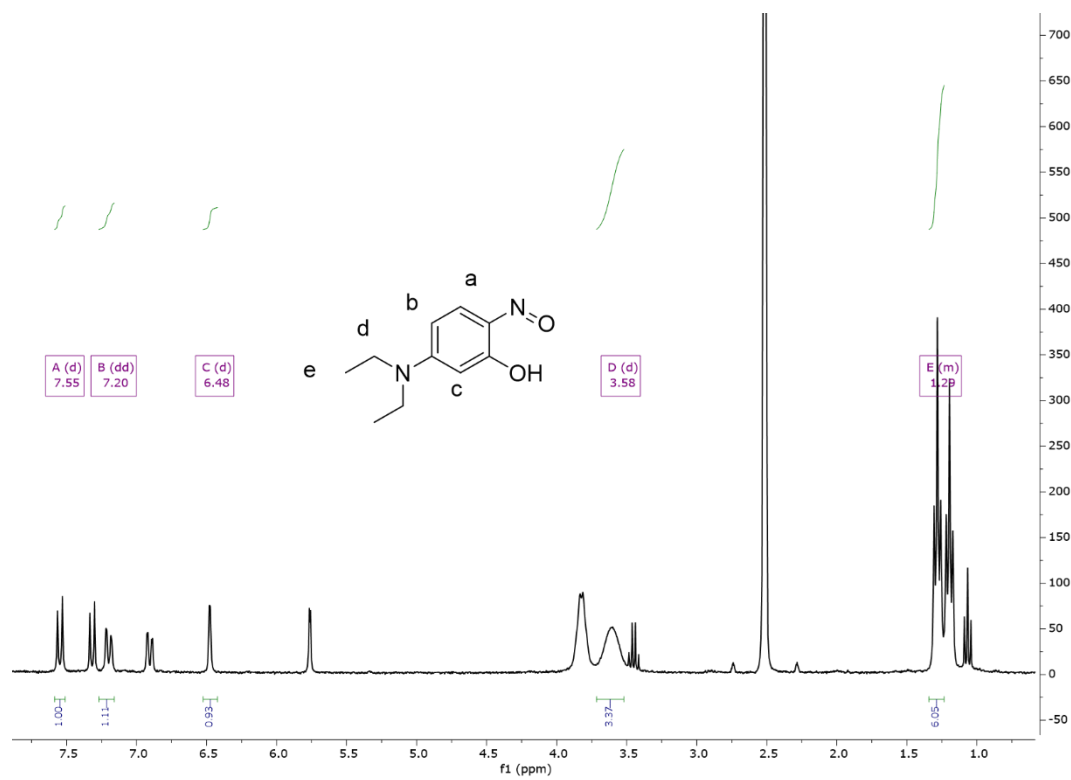


**Figure S8.**  $^1\text{H-NMR}$  of compounds **2** and **2'**.

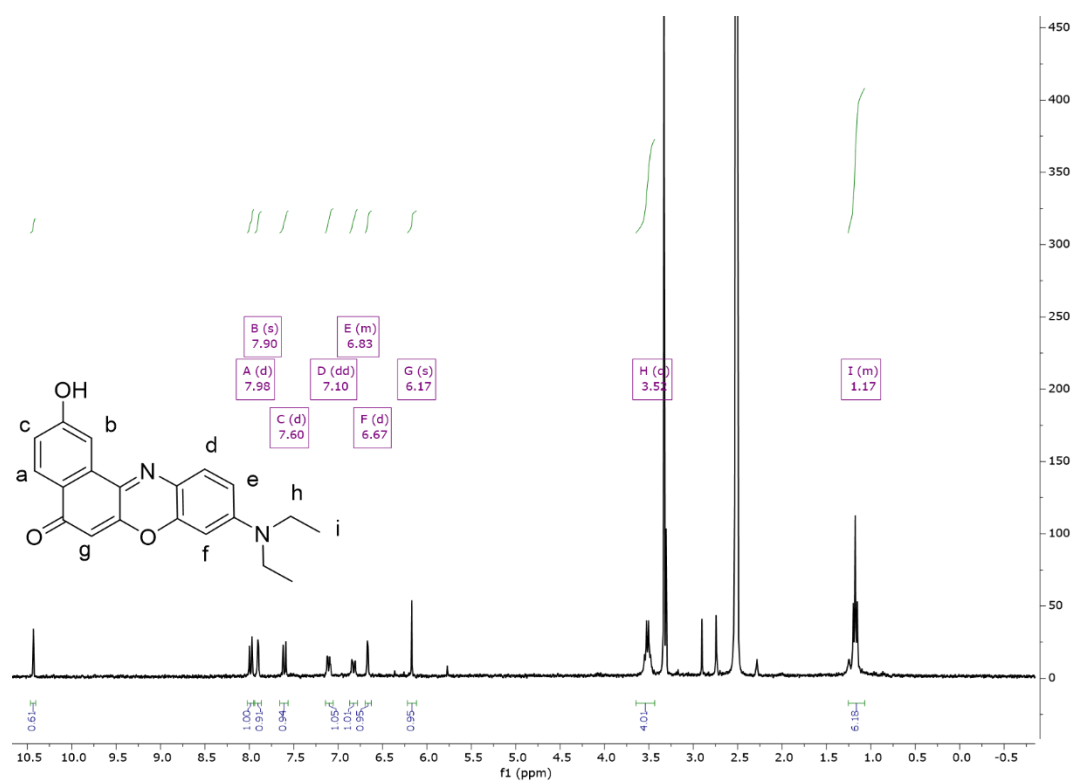


Figure S9. <sup>1</sup>H-NMR of compound 4.

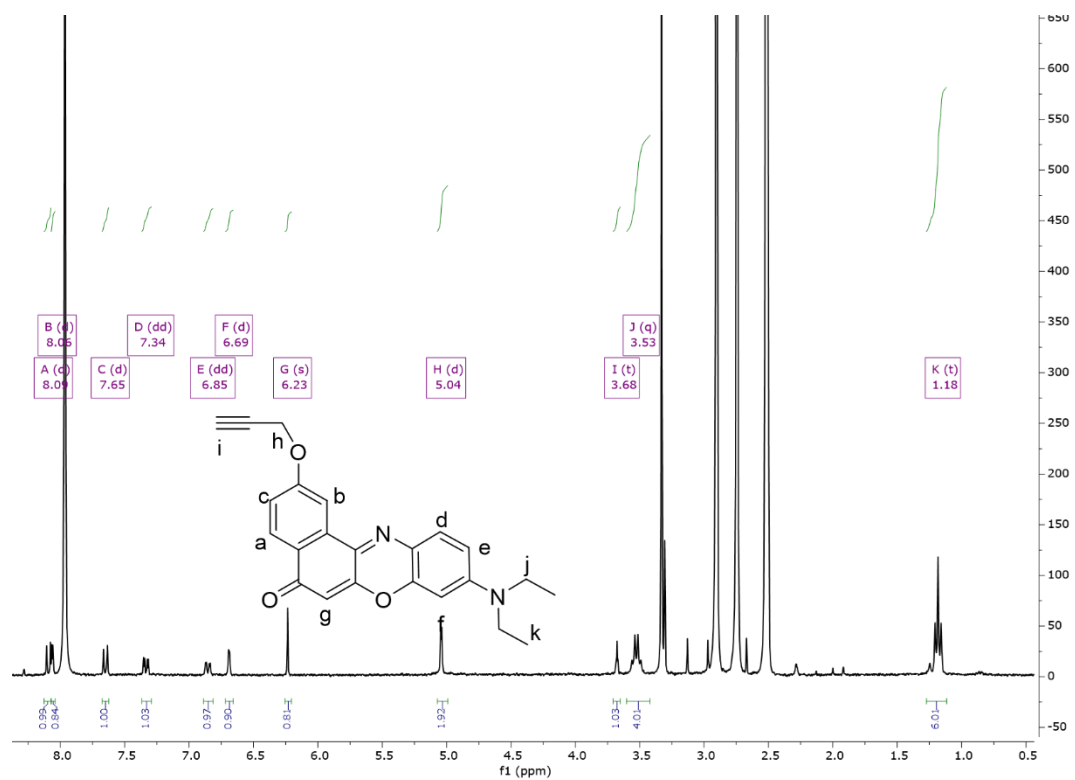
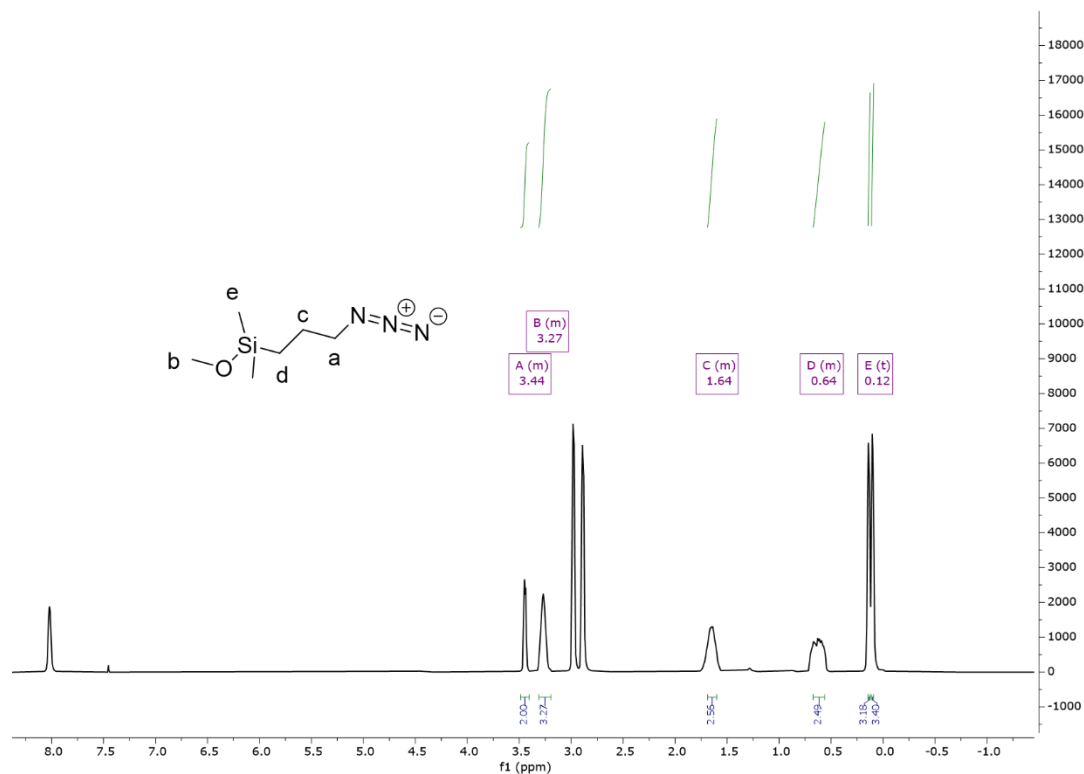


Figure S10. <sup>1</sup>H-NMR of compound 6.



**Figure S11.**  $^1\text{H-NMR}$  of compound **10**.

**Table S1.** Fluorescence Lifetimes of Lap-NDI (0.1 mg/mL) in 50% water with increasing concentrations of R6G and Lap-NR ( $\lambda_{em}$  = 480 nm,  $\lambda_{ex}$  = 345 nm).

[R6G] ( $\mu\text{M}$ )	$\tau_1$ (ns)	$\tau_2$ (ns)	$\tau_3$ (ns)	$\tau_{avg}$ (ns)
0	17.39 (17%)	3.74 (33%)	0.47 (50%)	4.46
0.016	16.96 (16%)	3.70 (32%)	0.47 (52%)	4.15
0.033	16.00 (15%)	3.33 (32%)	0.43 (53%)	3.66
0.049	15.49 (14%)	3.31 (31%)	0.44 (55%)	3.37
0.066	15.28 (13%)	3.30 (31%)	0.42 (56%)	3.23
0.083	14.71 (12%)	3.17 (31%)	0.40 (57%)	2.95
0.099	15.13 (13%)	3.24 (31%)	0.42 (56%)	3.15
0.116	14.78 (11%)	3.20 (31%)	0.42 (58%)	2.88
0.133	14.43 (11%)	3.08 (31%)	0.40 (58%)	2.77
[Lap-NR] (mg/mL)	$\tau_1$ (ns)	$\tau_2$ (ns)	$\tau_3$ (ns)	$\tau_{avg}$ (ns)
0.01	14.54 (11%)	3.14 (31%)	0.42 (58%)	2.82
0.02	14.62 (11%)	3.18 (31%)	0.43 (58%)	2.84



0.03	14.64 (11%)	3.16 (31%)	0.43 (58%)	2.83
0.04	14.64 (11%)	3.20 (30%)	0.43 (58%)	2.87
0.05	14.59 (11%)	3.12 (31%)	0.41 (58%)	2.81

**Table S2.** Fluorescence Lifetimes of R6G (0.133  $\mu\text{M}$ ) in 50% water in the presence of Lap-NDI (0.1 mg/mL) with increasing concentrations of Lap-NR ( $\lambda_{em}$ = 550 nm,  $\lambda_{ex}$ = 345 nm).

[Lap-NR] (mg/mL)	$\tau_1$ (ns)	$\tau_2$ (ns)	$\tau_{AvAmp.}$ (ns)
0	8.00 (10%)	3.23 (90%)	3.68
0.01	8.58 (10%)	3.26 (90%)	3.78
0.02	7.86 (12%)	3.12 (88%)	3.70
0.03	7.62 (14%)	3.06 (86%)	3.70
0.04	7.32 (16%)	2.93 (84%)	3.62
0.05	7.17 (17%)	2.89 (83%)	3.64

## References

- [1] M. Börgardts, K. Verlinden, M. Neidhardt, T. Wöhrle, A. Herbst, S. Laschat, C. Janiak, T.J.J. Müller, Synthesis and optical properties of covalently bound Nile Red in mesoporous silica hybrids-comparison of dye distribution of materials prepared by facile grafting and by co-condensation routes, *RSC Adv.* 6 (2016) 6209–6222. <https://doi.org/10.1039/c5ra22736d>.
- [2] A. Ionescu, N. Godbert, A. Crispini, R. Termine, A. Golemme, M. Ghedini, Photoconductive Nile red cyclopalladated metallomesogens, *J. Mater. Chem.* 22 (2012) 23617–23626. <https://doi.org/10.1039/c2jm34946a>.
- [3] S.-Y. Park, Y. Kubota, K. Funabiki, M. Shiro, M. Matsui, Near-infrared solid-state fluorescent naphthooxazine dyes attached with bulky dibutylamino and perfluoroalkenyloxy groups at 6- and 9-positions, *Tetrahedron Lett.* 50 (2009) 1131–1135. <https://doi.org/10.1016/j.tetlet.2008.12.081>.
- [4] N. Yotapan, C. Charoenpakdee, P. Wathanathavorn, B. Ditmangklo, H.A. Wagenknecht, T. Vilaivan, Synthesis and optical properties of pyrrolidiny peptide nucleic acid carrying a clicked Nile red label, *Beilstein J. Org. Chem.* 10 (2014) 2166–2174. <https://doi.org/10.3762/bjoc.10.224>.

- [5] P. Paoprasert, J.W. Spalenka, D.L. Peterson, R.E. Ruther, R.J. Hamers, P.G. Evans, P. Gopalan, Grafting of poly(3-hexylthiophene) brushes on oxides using click chemistry, *J. Mater. Chem.* 20 (2010) 2651–2658. <https://doi.org/10.1039/b920233a>.
- [6] C.G. Colletti, M. Massaro, G. Lazzara, G. Cavallaro, S. Milioto, I. Pibiri, R. Noto, S. Riela, Synthesis, characterization and study of covalently modified triazole LAPONITE® edges, *Appl. Clay Sci.* 187 (2020) 105489. <https://doi.org/10.1016/j.clay.2020.105489>.

## ACKNOWLEDGEMENTS

First and foremost, I would like to extend my deepest gratitude to Dr. Eric H. Hill, at the Institute of Physical Chemistry, University of Hamburg, for serving as my supervisor and providing me the opportunity to work with him. His unwavering support and guidance throughout my academic journey have been invaluable. Eric always keeps his office door open and has provided me with invaluable opportunities to ask his advice whenever necessary. I vividly recall the initial stages of my doctoral studies when I was still getting acquainted with my project; his patience and thorough explanations of key concepts, coupled with his guidance on beginning with simpler synthesis tasks related to my research, were instrumental in my development. His passion for research has been a constant source of inspiration, propelling me forward in my scholarly endeavors.

I am also deeply grateful to Prof. Dr. Volker Abetz at the Institute of Physical Chemistry, University of Hamburg for agreeing to be my co-supervisor and chair of my committee. Prof. Abetz consistently responds to my emails promptly and engages in discussions about the progress of my doctoral projects. I appreciate his patience and the critical feedback he provides from various perspectives, which has encouraged me to explore further potential within my research.

I would like to extend my sincere thanks to Prof. Dr. Alf Mews at the Institute of Physical Chemistry, University of Hamburg for agreeing to be my committee member and granting me access to facilities at his disposal. Prof. Mews provided critical comments and identified the overlooked areas of my research. This guidance drove me to a deeper understanding of both the theoretical and practical aspects of my work.

I would like to extend my heartfelt thanks to the past and present members of the Hill group, including Junying, Swetanshu, Christian, Silvano, Nina, Sanjay, Marcel, Ana, and Eike. Their immense support and the creation of an ideal work atmosphere have been invaluable, and without them, I would have faced significantly more challenges in reaching this point in my dissertation. A special thanks goes to Silvano, who has always been willing to offer support in my research and has provided me with sincere friendship. Without his support, this doctoral journey would have been far less remarkable.


Thanks should also be expressed to the members of the Mews group and Weller group at the Institute of Physical Chemistry, University of Hamburg. During my dissertation, they were always willing to provide technical support, and seeking assistance related to chemicals and administrative advice was a stress-free experience.

I would be remiss in not mentioning the assistance from the central measurement facilities of the Chemistry Department of the University of Hamburg. I acknowledge their support in mass spectroscopy, element analysis, and nuclear magnetic resonance.

Last but not least to express my gratitude to my family and my friends. Their support, understanding, and encouragement have been essential throughout this challenging journey. Without their love and support, this doctoral journey would not have been possible.

## DECLARATION

*„I hereby declare and affirm that this doctoral dissertation is my own work and that I have not used any aids and sources other than those indicated. If electronic resources based on generative artificial intelligence (gAI) were used in the course of writing this dissertation, I confirm that my own work was the main and value-adding contribution and that complete documentation of all resources used is available in accordance with good scientific practice. I am responsible for any erroneous or distorted content, incorrect references, violations of data protection and copyright law or plagiarism that may have been generated by the gAI.“*

19.08.2024, 

Date, Signature